



City Research Online

City, University of London Institutional Repository

Citation: González, T. (2023). Metal coating and embedding fibre optical sensors for industrial applications. (Unpublished Doctoral thesis, City, University of London)

This is the accepted version of the paper.

This version of the publication may differ from the final published version.

Permanent repository link: <https://openaccess.city.ac.uk/id/eprint/31894/>

Link to published version:

Copyright: City Research Online aims to make research outputs of City, University of London available to a wider audience. Copyright and Moral Rights remain with the author(s) and/or copyright holders. URLs from City Research Online may be freely distributed and linked to.

Reuse: Copies of full items can be used for personal research or study, educational, or not-for-profit purposes without prior permission or charge. Provided that the authors, title and full bibliographic details are credited, a hyperlink and/or URL is given for the original metadata page and the content is not changed in any way.



Metal coating and embedding fibre optical sensors for industrial applications.

Submitted by

Tania Grandal González

Thesis submitted for the degree of Doctor of Philosophy

Supervised by

Professor Tong Sun OBE

Professor Kenneth T.V. Grattan OBE

City, University of London

School of Mathematics, Computer Science and Engineering

EC1V 0HB, London, UK

March 2023

Table of Contents

Table of Contents.....	i
Table of Figures.....	iii
Table of Tables.....	xii
Acknowledgements.....	xiii
Copyright Declaration.....	xiv
Abstract.....	xv
Glossary of Symbols and Abbreviations.....	xvi
Chapter 1. Introduction.....	1
1.1 Motivation and objectives.....	1
1.2 Structure of the thesis.....	2
Chapter 2. Review of metallic coating and embedding of fibre optic sensors.....	4
2.1 Fibre Bragg Grating.....	5
2.2 Review of metallic coating and embedding of fibre optic sensors.....	8
2.2.1 Review of metallic coating of fibre optic sensor.....	9
2.3 Summary.....	27
Chapter 3. Metallic coating of Fibre Optic Sensors and their characterization.....	28
3.1 Coating techniques for generating a conductive layer.....	29
3.1.1 Electroless Ni deposition.....	29
3.1.2 Physical Vapor deposition of Ag, Au and Cr.....	33
3.1.3 Conductive Paint.....	37
3.1.4 Industrial technique Cu deposition.....	38
3.1.5 Sputter deposition of Au technique.....	40
3.2 Electroplating deposition technique.....	43
3.2.1 Characterization of electroplated Cu.....	45
3.2.2 Characterization of electroplated Ni.....	47
3.3 Thermal characterization of metallic optical fibre sensors.....	50
3.3.1 Thermal characterisation of coated optical fibres.....	50
3.3.2 Thermal characterization of metallically coated FBG sensors.....	53
3.4 Summary.....	59
Chapter 4. Sensor embedding process and characterization.....	61
4.1 Embedding process using the electroplating deposition technique.....	61
4.2 Embedding process by casting.....	63
4.3 Embedding process by Laser welding techniques.....	67
4.3.1 Laser embedding of sensors into tin alloy.....	68

4.3.2	Laser embedding using Ni-Cr alloy as embedded material	78
4.4	Embedding process by TIG welding	80
4.4.1	Embedding process by manual TIG welding	81
4.4.2	Embedding process using automatic TIG welding	88
4.5	Summary	94
Chapter 5. Experimental validation of FOSs embedded into metallic components		96
5.1	Introduction	96
5.2	Validation of the FOS monitoring system for antifriction material degradation	98
5.2.1	Sensorised antifriction specimens fatigue test	100
5.3	Validation of the FOS monitoring system for antifriction bearing operation	108
5.3.1	Results from the embedded FBGs	112
5.4	Summary	117
Chapter 6. Metal coated FOSs for monitoring Concentrated Solar Power Plants (CSP)		119
6.1	Introduction	119
6.2	FOS coating and packaging development	120
6.3	Validation on a laboratory scale	121
6.4	Validation on a medium scale	131
6.4.1	Manufacturing and validation of the mid-scale module	132
6.4.2	Manufacturing and validation of the mid-scale thermocline tank	139
6.5	NEWSOL prototype design and integration	144
6.6	Summary	149
Chapter 7. Conclusions and future work		150
7.1	Conclusions of the work carried out	150
7.2	Future work	152
7.3	References	153
List of Publications		161

Table of Figures

Figure 2.1: Representation of a single-mode optical fibre.	4
Figure 2.2: Schedule of an intrinsic (above) and extrinsic (below) FOS [4].	5
Figure 2.3: Schedule of a Fibre Bragg Grating fundamentals and operation.	5
Figure 2.4: Schedule of beam diffraction in hkl planes.	6
Figure 2.5: Schedule of multiplexed FBGs along one optical fibre.	7
Figure 2.6: Au coated FBGs from Technica. Picture of the frontier of the Au original coating of the optical fibre and, the re-coated section where the FBG was inscribed.	10
Figure 2.7: Schematic diagram of a typical metal-coating setup: a standard drawing tower equipped with a metallizer [14].	11
Figure 2.8: Simplified diagram for electroplating Nickle on a conductive optical fibre.	12
Figure 2.9: (a) Schedule of the metallic coating and electroplating bond. (b) Micro picture of the appearance of the metallic coated optical fibre after the electroplating process [16].	12
Figure 2.10: (a): Schedule of the FBGs coating developed by SHEN et al. [27]. (b): Schedule of the electroless procedure protected for coating an optical fibre by electroless deposition technique [42].	13
Figure 2.11 (a): special tool designed to continuously coat an optical fibre by sputtering. (b) Cross-section of the Pd and Ti optical fibre coated by sputtering [17].	14
Figure 2.12: View of LAMM workstation with rotational stage for grabbing and turning the FBG [20].	14
Figure 2.13: SEM micrograph of a bimetallic coating after the first heating/cooling cycle between room	15
Figure 2.14 (a): Arrangement for casting metal part. (b): Final appearance of the embedded sensor [50].	16
Figure 2.15: (a): Setup for the casting process with an RFBG strain sensor ($RFBG(T, \epsilon)$) and an RFBG temperature sensor $RFBG(T)$. (b): Picture of one arm of a cast part with the embedded FBG strain sensor after casting and machining [53].	17
Figure 2.16: (a): Cross-sections of a FBG sensor embedding test where the fibre is located along the melt flow direction. It is highlighted a non-bonded fibre-Al section (b): Cross-sections of three different probes where the fibre is located across the melt flow direction [52].	17
Figure 2.17: (a): Photograph of a flame spray setup. (b): Microscopic observation of the embedded optical fibre using the flame spray process [58].	19
Figure 2.18: (a) Embedded FBGs in the steel plates by the metallic based adhesive. (b): HVOF thermal spray coating application on the steel plates with the embedded FBGs [61].	19
Figure 2.19: (a): Schedule of the FOS embedded by HVOF spray coating and the expected thermal response of the embedded FOS. (b): Picture of the polymeric coated FOS embedded in a steel plate by HVOF spray coating [64].	20
Figure 2.20: Fibre embedded in a nickel-based brazing alloy with light coming out from the core of the fibres. (a): nickel-coated. (b): copper-coated single mode. (c): Bare fibre embedded, the brazing alloy is not in tight contact with the fibre. This surface was etched to show the microstructure [65].	21
Figure 2.21: (a): Cross-section of coated capillary embedded in stainless steel test component by SLM. (b) Cross-section of coated capillary brazed into the stainless steel test component. The capillary is damaged during the second SLM process [67].	21

- Figure 2.22: UAM process: (a) Fabrisonic SonicLayer™ 7200; (b) additive or ultrasonic welding stage of the process; (c) subtractive or machining stage of the process [72]. 22
- Figure 2.23: (a) Schematic diagram of the ultrasonic consolidation of fibre embedded aluminium structures. Embedding methods: (a) full load, (b) partial load, and (c) no load, respectively, on fibre [78]. (b): Schematic representations of the (a) UAM process and (b) fibre embedding steps (section view), which include building a few layers of material on the baseplate, machining a channel, laying the fibre optic in the channel, and layering foils on top to embed the fibre [77]. 22
- Figure 2.25: (a): Shape Deposition Manufacturing cycle for embedding fibre optic sensors. (b): Rotating part with embedded fibre optic sensor [16]. 23
- Figure 2.26: (a): Step by step of the casting and LSFF embedding procedure [19]. (b): Final appearance of the prototype sample with the FBGs embedded [83]. 24
- Figure 2.27: (a): Schematic cross section of the sample with embedded FBGs [84]. (b): Final appearance of the prototype sample with the FBGs embedded manufactured by electroplating and LSFF [83]. 24
- Figure 2.28: Schematic illustration of the embedding process with cross-sectional analyses of the individual steps [88]. 25
- Figure 2.29: (a) Schematic of turbine blade with an embedded Ni-FBG sensor fabricated by DED printing for high-temperature monitoring. (b): Photograph of a fully DED-printed miniature turbine blade with an embedded Ni-FBG sensor for high-temperature monitoring [93]. 26
- Figure 3.1: Diagram of the key objective of this chapter: a procedure for metallic coating FBGs. (a) standard FBGs with the polymeric protection removed. (b): metal coated fibre cut and with the metal removed from the extremes. (c) FBGs spliced to the metal coated fibre with a metallic coating thin layer on the FBGs section and a metallic coating layer on the whole fibre. (d) cross-section of the fibres for each coating step. 29
- Figure 3.2: Electroless Ni deposition process step by step. 31
- Figure 3.3: (a): Electroless Ni deposition set-up for coating optical fibre. (b): Ni coating layer, SEM picture. 32
- Figure 3.4: SEM images of the Ni coating layer made on the optical fibres by electroless deposition. (a) Ni coating fibre with grains on the surface. (b) Ni coating layer with adherence faults. (c) Ni coating layer with accumulations of Ni material forming clusters generating a non-uniform coating layer, (d) Ni coating layer presenting cracks and poor adhesion to the fibre. 33
- Figure 3.5: (a): PVD Balzer BAE 250 machine. (b): Optical fibres set-up to be coated in the PVD camera. (c): Optical fibres after Ag PVD coating. 34
- Figure 3.6: (a): PVD home-made machine. (b): Optical fibres before the PVD coating process bonded to the PVD machine cover. (c): Optical fibres after Au coating process bonded to the PVD machine cover. 35
- Figure 3.7: SEM images of the Ag coating layer made by PVD process. (a): Ag coated layer without defects, (b) Ag coated layer showing a scrape defect. 35
- Figure 3.8: Microscope images of the Au coating layer made by PVD process. (a) Au coated layer with low gold cover. (b) Au layer border showing poor adhesion to the fibre. 36
- Figure 3.9: Holder to fix the FBGs spliced to a Cu coated commercial optical fibre, during the Cr PVD process. (a): Before the PVD process. (b): after the PVD process. 36
- Figure 3.10: Response of the Ag coated FBG sensor for the thermal calibration. 37
- Figure 3.11: Photographic images of optical fibres coated with the Ni-based paint. (a): detail of the border section between the not coated and coated fibre. (b): detail of the fibre painted with the Ni based paint. 38

<i>Figure 3.12: Cu coated optical fibres by Inphotech. (a) detail of the Cu coating layer surface. (b): detail of the total diameter of the Cu coated fibre.</i>	39
<i>Figure 3.13: (a): Outline of sputtering process [100], (b): machine of sputtering [101], (c): detail of the sputtering process on the fibre with the fibre located in the frame.</i>	40
<i>Figure 3.14: Frame developed to fix the optical fibre on the sputtering chamber.</i>	41
<i>Figure 3.15: (a) 3D printed chamber with holes to allow the optical fibre that is not required to be coated to exit, from the sputter machine. (b) detail of the optical fibre coming out form the holes of the chambre, sealed with sticky tape.</i>	41
<i>Figure 3.16: SEM images of the Au coating layer obtained on the optical fibres made by sputter deposition technique. (a) detail of the Au coating layer for x140 magnifier, (b) detail of the Au coating layer for x700 magnifier.</i>	42
<i>Figure 3.17: (a) Electroplating Deposition scheme, (b) electroplating Ni deposition set-up.</i>	44
<i>Figure 3.18: Cross-section of a Cu commercial coated optical fibre re-coated with Ni by electroplating deposition technique. (a): Cross-section. (b): cross-section attacked with acid to reveal the structure.</i>	50
<i>Figure 3.20: (a): Cu re-coated FBG sensor response during the thermal calibration. (b): quadratic curve fitting to the sensor data for calculation of its the thermal sensitivity.</i>	53
<i>Figure 3.21: Cu re-coated FBG sensor appearance. Left: before the thermal test. Right: after the thermal test.</i>	54
<i>Figure 3.22: Ni re-coated FBG sensors wavelength variation during the annealing and thermal fatigue tests.</i>	55
<i>Figure 3.23: Response for the acrylate coated and encapsulated FBG sensors and, Ni re-coated FBG sensors during the thermal fatigue test.</i>	56
<i>Figure 3.24: FBG sensors response during the thermal calibration.</i>	57
<i>Figure 3.25: Response of FBG sensors tested front to temperature variation: (a) FBG1, (b) FBG2, (c) FBG3, (d) FBG4.</i>	58
<i>Figure 3.26: (a): Response of the Ni re-coated FBG sensor subjected to thermal fatigue between 650-1000°C. (b): Detail of the Ni re-coated FBG sensor response at 1050°C continuously.</i>	59
<i>Figure 4.1: Electroplating bonding strategies studied; (a): Cu re-coated optical fibre located on the surface of a Cu metal sheet (b): Cu re-coated optical fibre located in a groove made in the Cu metal sheet.</i>	62
<i>Figure 4.2: (a) unbonded Cu coated fibre to the Cu metal sheet after electroplating process. In this case, the metal sheet has no groove to locate the Cu coated fibre. (b): Cu coated optical fibre located in a groove made on the Cu metal sheet, before applying elelctroplating to embed the Cu fibre in the Cu metal sheet. (c): Cu coated optical fibre embedded in the Cu metal sheet after electroplating depositing of Cu. The fibre presented good bond with the Cu metal sheet.</i>	63
<i>Figure 4.3: (a) Tin alloy molten bath. (b) Cu re-coated optical fibre embedded in the tin alloy by casting. (c) red light emerging form the embedded fibre.</i>	64
<i>Figure 4.4: (a): Steel specimen made specifically with a centre groove for casting (b): Steel specimen after the casting process with the Ni re-coated FBG sensor embedded.</i>	65
<i>Figure 4.5: Experimental measured reflection spectrum of the Ni re-coated FBG sensor before and after being embedded by casting process.</i>	65
<i>Figure 4.6: (a) Tensile test set-up. (b) Ni re-coated FBG sensor embedded in a steel specimen by casting, after the tensile test; (c) The specimen is broken, but the Ni re-coated FBG sensor survived.</i>	66
<i>Figure 4.7: (a) Response of a Ni re-coated FBG sensor embedded by casting to the increase of tensile force applied. (b) Linear fitting between wavelength shift of the FBG sensor and the applied load.</i>	66

<i>Figure 4.8: Cross-section of the Ni re-coated FBG sensor embedded in the antifriction material by casting. (a): Ni re-coated FBG sensor picture of cross-section appearance in the antifriction material and steel base material. (b): Detail of the embedded Ni re-coated FBG sensor in contact with the antifriction material. (c) and (d): Cross-section detail for the frontiers bond between the antifriction material and the Ni re-coated FBGs.</i>	67
<i>Figure 4.9: Laser cladding set-up.</i>	68
<i>Figure 4.10: Embedding strategies studied to embed the Ni and Cu re-coated optical fibres by Laser Cladding process. (1): Embedding strategy based on the overlapping the recharge lines of tin deposition, transversal to the coating fibre. (2): Embedding strategy based on the overlapping the recharge lines of tin deposition, longitudinal to the re-coated fibre. (3): Embedding strategy based on the interlayer recharge lines, transversals to the re-coated fibre.</i>	69
<i>Figure 4.11: Steel-antifriction material sample appearance after the re-coated optical fibres laser cladding embedding tests.</i>	70
<i>Figure 4.12: (a): embedding strategy with a groove in the specimen. (b): Final steel-antifriction coated specimen appearance at the end of the laser cladding embedding tests.</i>	73
<i>Figure 4.13: Ni re-coated FBG sensor embedded by laser cladding into antifriction material.</i>	75
<i>Figure 4.14: Re-coated FBG embedded sensors response during the thermal tests. (a): Ni re-coated FBG sensor response and linear fit. (b): Cu re-coated FBG sensor response and linear fit.</i>	75
<i>Figure 4.15: (a): Ni re-coated FBG sensor embedded response during the tensile tests. (b): Cu re-coated FBG sensor embedded response during the tensile tests</i>	76
<i>Figure 4.16: (a): Strain characterization for embedded Ni coated fibre optic sensors. The sensitivities of each linear fit are: Up1: 0.0011 nm/$\mu\epsilon$, Up2: 0.0010 nm/$\mu\epsilon$, Up3: 0.0010 nm/$\mu\epsilon$, Down1: 0.0010 nm/$\mu\epsilon$, Down2: 0.0010 nm/$\mu\epsilon$ and Down3: 0.0010 nm/$\mu\epsilon$. (b): Strain characterization for embedded Cu coated fibre optic sensors. The sensitivities of each linear fit are: Up1: 0.0007 nm/$\mu\epsilon$, Up2: 0.0009 nm/$\mu\epsilon$, Up3: 0.0009 nm/$\mu\epsilon$, Down2: 0.0010 nm/$\mu\epsilon$ and Down3: 0.0010 nm/$\mu\epsilon$.</i>	77
<i>Figure 4.17: Cross-section of embedded FBG sensors after thermal and mechanical characterization. (a): Ni re-coated FBGs. (b): Cu re-coated FBGs.</i>	77
<i>Figure 4.18: Laser Additive Manufacturing embedding set-up.</i>	78
<i>Figure 4.19: Methodology for embedding Ni re-coated optical fibre by Laser AM process into a Cr-Ni alloy. (a): Ni re-coated fibre located in the AM made groove. (b): Ni re-coated fibre partially embedded. (c): Ni re-coated fibre totally embedded.</i>	79
<i>Figure 4.20: Cross-section detail for some of the Ni re-coated optical fibres embedded into Cr-Ni alloy by AM laser process. (a): Cross-section detail for a Ni re-coated optical fibre embedded into Cr-alloy structure. (b): detail of the Ni coating layer after being embedded. (c): Cross-section of a Ni re-coated optical fibre embedded into Cr-alloy structure, acid attacked to reveal the material composition and structure.</i>	79
<i>Figure 4.21: (a): Automatic TIG welding set-up. (b): Manual TIG welding set-up.</i>	80
<i>Figure 4.22: (a) Ni and Cu re-coated optical fibres on the tin-alloy steel substrate before being embedded. (b): Ni and Cu re-coated optical fibres after being embedded by manual TIG process.</i>	81
<i>Figure 4.23: (a): design of the machined grooves for the embedding tests. (b): picture of the sample during the embedding trials. (c): Sample with the optical fibres embedded after being machined to equalise the surface of the sample.</i>	83
<i>Figure 4.24: Cross-section of the re-coated optical fibres embedded in the groove sample. (a): Ni_004, (b): Ni_001. (c): Ni_002. (d): Ni_003.</i>	84

Figure 4.25: (a): Appearance of the Ni coated sensor after manual TIG welding embedding process. (b): Appearance of the Cu coated sensor after manual TIG welding embedding process. (c): Ni re-coated FBG sensor cross-section after embedding. (d): Cu re-coated FBG sensor cross-section after embedding.	85
Figure 4.26: FBG sensors spectrum before and after being embedded. (a): Ni re-coated FBG sensor. (b) Cu re-coated FBG sensor.	85
Figure 4.27: (a): Ni FBG sensor embedded, thermal response. (b): Linear fit for the Ni FBG sensor embedded thermal sensitivity. (c): Cu FBG sensor embedded, thermal response. (d): Linear fit for the Cu FBG sensor embedded thermal sensitivity.	86
Figure 4.28: (a) Load response of the Ni re-coated FBG sensor embedded by manual TIG welding process. (b) Load response of the Cu re-coated FBG sensor embedded by manual TIG welding process	87
Figure 4.29: Results of the calibration after the tensile tests on embedded FBGs for manual TIG. (a): Ni re-coated FBG. (b): Cu re-coated FBG. Up 1, 2 and 3 are for the cases where the strain is rising while Down 1, 2 and 3 are for the cases where the strain is falling.	87
Figure 4.30: Detail of the relative position of the torch to the fibre.	88
Figure 4.31: (a): appearance of the antifriction steel-based sample after embedding trials. (b): detail for one of the Ni re-coated optical fibres embedded by automatic TIG in a sample with a groove.	89
Figure 4.32: FBG sensors embedded by automatic TIG welding process. a): Ni re-coated FBG sensor, b): Cu re-coated FBG sensor.	90
Figure 4.33: FBG sensors spectrum before and after being embedded. (a): Ni re-coated FBG sensor. (b): Cu re-coated FBG sensor.	90
Figure 4.34: Cross-section of the re-coated FBG sensors embedded by automatic TIG welding process. (a): Ni re-coated FBG sensor. (b): Cu re-coated FBG sensor.	91
Figure 4.35: (a): Ni FBG sensor embedded, thermal response. (b): Linear fit for the Ni FBG sensor embedded thermal sensitivity. (c): Cu FBG sensor embedded, thermal response. (d): Linear fit for the Cu FBG sensor embedded thermal sensitivity.	92
Figure 4.36: Left: Ni embedded FBGs response for the tensile test. Right: Cu embedded FBGs response for the tensile test.	93
Figure 4.37: Linear fitting of the calibration after the tensile tests on embedded FBGs using automatic TIG. (a): Ni re-coated FBG. (b): Cu re-coated FBG. Up 1, 2 and 3 are for the cases where the strain is increasing while Down 1, 2 and 3 are for the cases where the strain is decreasing.	93
Figure 5.1: Typical hydrodynamic bearing for marine sector. (a) Bearing housing and (b) detail of the antifriction bearing located in the inner part of the bearing housing [3].	97
Figure 5.2: a) Bearing housing, b) and c) bearing shell, d) bearing on the shaft, e) antifriction bearing appearance on the shaft [3].	97
Figure 5.3: Some of the typical antifriction bearings defects due to particles: (a) inlay steel parts due to contamination of oil, (b) flakes due to wear and (c) tear [110].	98
Figure 5.4: (a) Components of the fatigue prototype test bench. (b): Detail of the fatigue machine structure.	100
Figure 5.5: (a): Detail of the pistons inside the fatigue machine to apply the pressure on the specimen through the lubricant oil. (b): antifriction specimen where the FOS was embedded.	100
Figure 5.6: Procedure to embed the metallic coated FBGs in the antifriction material specimens. Left: Detail of the metallic coated FBG located in the antifriction material groove and fixed by two tin weld spots points. Centre: Appearance of the specimen after having embedding the FBGs by automatic TIG welding. Right: Appearance of the specimen, with the embedded FBGs, after being machined to unify the specimen antifriction material surface.	101

<i>Figure 5.7 (a): Specimen with the FBGs embedded. (b): Detail of the specimen assembly on the test-bench machine top. (c): the sensorised specimen assembled.</i>	101
<i>Figure 5.8: Response of the Cu coated FBGs embedded in the antifriction coated specimen during some of the fatigue tests done. a) test 1, b) Test 14, c) Test 26.</i>	103
<i>Figure 5.9: Detail of the embedded FBG response for 1s of time at 667rpm and 35bar of pressure.</i>	104
<i>Figure 5.10: FFT of the embedded FBGs signal for some of the rotational speeds applied in the Tests done. a) FFFT comparative for 9 different tests done at 667rpm. b) comparison for the Test 20, made at 167 rpm applying different pressures. c) FFT made for Test 19, where the rotational speed was 83 rpm applying different pressures.</i>	105
<i>Figure 5.11: a) Appearance of the sensorised specimen before to be tested. b) Appearance of the sensorised specimen after 20 fatigue tests.</i>	105
<i>Figure 5.12: Appearance of the sensorised antifriction material specimen after 20 mechanical fatigue tests, inspected by penetrating liquids technique.</i>	106
<i>Figure 5.13: (a): Eddy current equipment and antifriction material samples with different thickness to calibrate the equipment. (b): Inspection of the sensorised antifriction material specimen by eddy current technique.</i>	106
<i>Figure 5.14: (a): Appearance of the sensorised antifriction specimen after 29 tests and detail of the artificial defects made: wear and two cracks. (b): Appearance of the specimen after the test 31.</i>	107
<i>Figure 5.15: Response of the Cu coated FBGs embedded in the antifriction coated specimen during the fatigue tests 31, carried out after the defects made on the specimen.</i>	108
<i>Figure 5.16: Detail of the embedded FBGs response for two different rotational speed and pressures applied on the sensorised specimen during the test 31.</i>	108
<i>Figure 5.17: (a) Antifriction coated bearing to be sensorised. (b): Machining drawing, for the integration of FBG and distributed fibre optic sensors.</i>	109
<i>Figure 5.18: Design of the metallic re-coated FOS to be embedded in the antifriction material coating of the bearing.</i>	110
<i>Figure 5.19: Embedding FOS procedure and final antifriction bearing appearance. a) Antifriction bearing shell with the machined grooves, b) detail of the groove with one Ni metallic coated distributed FOS located in the groove, c) distributed FOS embedded and FBGs array located and started to be embedded by manual TIG welding, d) image during the manual TIG welding embedding process of one of the metallic coated FBGs array, e) two half shells after the manual TIG embedding process.</i>	110
<i>Figure 5.20: (a): Sensorised antifriction bearing shells appearance after the surface machined. (b): FOS exit.</i>	111
<i>Figure 5.21: Final appearance of the FOS sensorised antifriction bearing installed in the test-bench.</i>	111
<i>Figure 5.22: Appearance of the two half shells of the sensorised bearing after the eleven tests made. (a): below part. (b): above part.</i>	112
<i>Figure 5.23: Response of the Ni re-coated FBGs embedded in the antifriction bearing during some of the tests carried out in the test-bench. a) test 2, b) test 6, c) test 7, d) test 11.</i>	114
<i>Figure 5.24: Detail of the embedded FBGs response for the test 6, front to: (a): pressure variations in static (no rotational speed applied), and (b): rotational speed and pressure variations.</i>	115
<i>Figure 5.25: (a): Conventional strain gauges response for the test 2. (b): Detail for the static pressure variation.</i>	116
<i>Figure 5.26: FFT response for some of the embedded FBGs. a) FFT response for the FBGs embedded in the below half shell bearing. Test 6 applying 250rpm and 250bar. b) FFT response for the FBG 1 embedded in</i>	

the above half shell bearing, during the test 2 applying 250bar and different pressures (150rpm, 200rpm and 250rpm). c) FFT response for the FBGs embedded in the below half shell bearing during the test 2 applying 250rpm and several pressures between 250bar to 80 bar. 117

Figure 6.1: NEWSOL concrete prototypes final design. a) Thermocline tank, b) energy storage module. 120

Figure 6.2: Design of the mini-modules developed at laboratory scale. 121

Figure 6.3: FBGs location for the mini-module 1. 122

Figure 6.4: Mini-module sample manufacturing process. a) preparation of the core formwork and placement of the core FBGs, b) core concrete filled, c) insulating concrete formwork preparation, d) integration of the FBGs located in the insulating concrete, e) insulated concrete filled, f) final appearance of the mini-module concrete sample with the embedded FBGs. 123

Figure 6.5: a) FBGs location in the insulating concrete layer. b) Response of the A, C and D FBGs embedded in the insulating layer, in wavelength shift values during the 28 days after filling the insulating layer. c) Response of these strain and temperature FBG sensors in strain and temperature values after decoupling temperature from strain. 124

Figure 6.6: a) Temperature FBGs location. b) Response from the temperature FBG sensors embedded in the core concrete of the specimen along the 28 days. 125

Figure 6.7: Strain H FBGs location. b) Response from the strain H FBG sensors embedded in the core concrete of the mini-module specimen, for the 28 days after the core concrete filled. 125

Figure 6.8: Experimental set-up for heating the mini-module: a) Machine to apply the heat through Joule's effect connected to the mini-module specimen. d) mini-module connected to the electrical connection cable through the both extremes of the steel pipe remarked in the c) picture. 126

Figure 6.9: a) FBGs location for the mini-module 1. b) FBG response during first heating for temperature sensors, c) FBG response during first heating for strain sensors. 127

Figure 6.10: Diagram representing the three different stages applied to carried out the heating test of the mini-module. 128

Figure 6.11: Thermocouple distribution for the mini-module heating test. 128

Figure 6.12: Thermocouples response during the thermal cycles. 128

Figure 6.13: a) Temperature FBG and thermocouple sensors location b) Temperature FBGs response during the thermal fatigue tests. c) Comparison between E, L and M temperature FBGs and the thermocouples. 129

Figure 6.14: a) Strain FBGs location, b) Response of the strain embedded FBGs during the thermal cycles in wavelength variation. b) Response of the strain embedded FBGs during the thermal cycles in strain. 130

Figure 6.15: Pictures of the Mini-Module 1 after the thermal cycles test. 131

Figure 6.16: a) Mid-scale module design, b) final appearance of the mid-scale module. 131

Figure 6.17: a) Mid-scale first concrete layer tank section design, b) final appearance of the mid-scale first concrete layer tank section. 132

Figure 6.18: FBG and thermocouples sensors distribution in the Mid-scale Module prototype. 133

Figure 6.19: FBG and thermocouples sensors position in the prototype along the mid-scale module prototype. Only FBGs reference is included. 134

Figure 6.20: a) Mid-scale module representation with the temperature FBGs embedded in the core layer. Graphs representing the temperature FBG sensors response during the core and insulating layers hardening and curing process: b) comparison for the temperature FBGs embedded at 300mm of height, c)

<i>comparison for the temperature FBGs embedded at 400mm of height, d) comparison for the temperature FBGs embedded at 550mm of height.</i>	135
<i>Figure 6.21: Representation of the FBG sensors for the insulating (top) concrete and their response after the third step manufacturing: insulating layers hardening and curing process.</i>	135
<i>Figure 6.22: a) Mid-scale module representation with the strain FBGs embedded in the core layer. Graphs representing the response of some strain FBG sensors vs. temperature FBGs embedded in the core concrete layer during the core and insulating layers hardening and curing process: a) design of the strain FBGs embedded in the core concrete, b) comparison between the FBG strain1_13 and the temperature FBGs A4_1, c) comparison between the FBG strain1_4 and the temperature FBGs A2_1, d) comparison between the FBG strain1_9 and the temperature FBGs A5_1.</i>	136
<i>Figure 6.23: Schematic of the heating process stages.</i>	137
<i>Figure 6.24: Temperature response for the temperature FBGs located in the insulating layer (top and bottom) for 2nd and 3rd heating phases.</i>	137
<i>Figure 6.25: Temperature response for the temperature FBGs located in the core concrete. a) Represents the response for the FBGs located at a height between 45-55cm, b) represents the response for the FBGs located at a height between 39-43cm and c) represents the response for the FBGs located at a height between 29-33cm.</i>	138
<i>Figure 6.26: Response oof the strain FBGs embedded in the core concrete material.</i>	139
<i>Figure 6.27: Table with the locations of the FBGs embedded and design of the mid-scale tank section.</i>	140
<i>Figure 6.28: Temperature FBG sensors response during the hydration and the first hours of hardening process for the FBGs located at: a) 250mm of height, b) 500mm of height, c) 750 mm of height.</i>	141
<i>Figure 6.29: Strain FBG sensors response during the whole curing concrete process. a) Raw data in wavelength variation. d) response in strain values after temperature decoupling.</i>	141
<i>Figure 6.30: a) Charge and discharge processes and program of the heating source and b) thermal cycle applied.</i>	142
<i>Figure 6.31: Detail of the temperature measured by the temperature FBGs at different heights: a) comparison for the FBGs located at 750mm of height; c) comparison for the FBGs located at 500mm of height; c) comparison for the FBGs located at 250mm of height.</i>	143
<i>Figure 6.32: Detail of the temperature measured by the temperature FBGs at different locations: a) comparison for the FBGs located in the left section of the mid-scale tank, FBG sensors B,D and G; b) comparison for the FBGs located in the central part of the mid-scale tank, FBG sensors C; c) comparison for the FBGs located in the right section of the mid-scale tank, sensors A and F.</i>	143
<i>Figure 6.33: Representation of the temperature distribution in the concrete layers through the interpolation of the measured data. a) representation of the temperature gradient for the left side, sensors D, G and B. b) representation of the gradient temperature along the central part of the concrete, sensors G,C and F.</i>	144
<i>Figure 6.34: Comparison for the strain FBGs S4 and temperature C2 FBGs.</i>	144
<i>Figure 6.35: Design of the FOS distribution in the different layers of the TT tank. a) Design of the FOS distribution to monitor the temperature of the molten salts (inside the tank), b) design of the FOS distribution to monitor the temperature on the air gap, between the molten salts and the concrete, c) design of the FOS distribution to monitor the temperature and the strain in the high performance concrete, d) Design of the FOS distribution to monitor the temperature on the rockwool layer, e) Design of the FOS distribution to monitor the temperature on the foundations layer.</i>	146
<i>Figure 6.36: TT demo CAC formwork and FOS integration before pouring the CAC.</i>	147
<i>Figure 6.37: Representation of the CAC pouring and FBG sensors embedding.</i>	147

Figure 6.38: Response of the temperature FBG sensors embedded in the CAC layer, after the first CAC pouring. a) shows the response of the temperature FBGs placed in the side of the TT exit S3, at the internal side of the CAC, close to the air gap. b) shows the response of the temperature FBGs located in the side of the TT exit S1, at the internal side of the CAC, close to the air gap. c) shows the response of the FBGs located in the side of the TT exit S3, at the external side of the CAC, close to the rockwool layer. d) shows the response of the FBGs located in the side of the TT exit S1, at the external side of the CAC, close to the rockwool layer.

148

Figure 6.39: Response of the strain FBG sensors embedded in the CAC layer, after the first CAC pouring. a) shows the response of the strain FBGs placed in the side of the TT exit S3, at the internal side of the CAC, close to the air gap. b) shows the response of the strain FBGs located in the side of the TT exit S1, at the internal side of the CAC, close to the air gap. c) shows the response of the FBGs located in the side of the TT exit S3, at the external side of the CAC, close to the rockwool layer. d) shows the response of the FBGs located in the side of the TT exit S1, at the external side of the CAC, close to the rockwool layer.

149

Table of Tables

<i>Table 3.1: Summary of the slides coating tests for the optimization of Ni electroless plating deposition process.</i>	31
<i>Table 3.2: Comparison table for all the coating techniques studied to generate a conductive layer on the optical fibre.</i>	42
<i>Table 3.3: Cu re-coated optical fibres by electroplating deposition technique, varying intensity or exposition time.</i>	46
<i>Table 3.4: Cu re-coated optical fibres by electroplating deposition technique, varying intensity and maintaining constant time.</i>	47
<i>Table 3.5: Ni re-coated optical fibres by electroplating deposition technique, varying intensity for 30 min of exposure.</i>	48
<i>Table 3.6: Ni re-coated optical fibres by electroplating deposition technique, varying exposure time at 0.5A of intensity.</i>	49
<i>Table 3.7: Coated commercial fibre optic specifications.</i>	51
<i>Table 3.8: losses of optical fibres during tests at different temperature.</i>	52
<i>Table 3.9: Quadratic coefficients and quadratic adjusted coefficient obtained for the quadratic fit of each calibration made for each FBGs tested.</i>	58
<i>Table 4.1: Main results of electroplating bonding study.</i>	63
<i>Table 4.2: Left: Ni coating fibres embedded unsuccessfully by Laser brazing using 1.6mm of diameter tin-alloy wire. Right: Ni coating fibres embedded successfully by Laser brazing using 1.6mm of diameter tin-alloy wire.</i>	70
<i>Table 4.3: Results for laser brazing with the tin-alloy wire of 2.4mm diameter.</i>	72
<i>Table 4.4: Cross-sections of the embedded Ni and Cu re-coated optical fibres into sample grooves.</i>	74
<i>Table 4.5: Ni and Cu optical fibres embedded by manual TIG welding and their cross-section details.</i>	82
<i>Table 4.6: Linear fit parameters from the tensile test of the Ni and Cu re-coated FBG sensor TIG embedded by manual TIG welding process.</i>	87
<i>Table 4.7: Cross-section detail of Ni and Cu optical fibres embedded by automatic TIG welding.</i>	89
<i>Table 4.8: Linear fitting parameters from the tensile test of the Ni and Cu re-coated FBG sensor embedded by automatic TIG welding process.</i>	93
<i>Table 5.1: Summary of the mechanical tests carried out and the parameters applied in each one.</i>	102
<i>Table 5.2: Summary of the tests made in the test-bench.</i>	112
<i>Table 6.1: Distribution of FOS sensors in the TT.</i>	145

Acknowledgements

First and foremost, I would like to express my heartfelt gratitude to my supervisors, Professor Tong Sun and Professor Kenneth Grattan, for their excellent SUPPORT (in all respects), for being there over these years and to make me believe I could do it. It was an honour and a privilege to work under such professional and kind-hearted experts in the field. I could never have imagined better professionals and, above all, better people to support and accompany me on this journey. I will be forever grateful.

How you will see this is not an individual work, I could never have done it without my AIMEN-FOS colleagues, specially, Sergio Fraga and Rubén Ruiz. Thank you for always being there, for the extra hours to complete the work, for the patience and constancy in the day to day work. Definitely, this would not be possible without you.

Additionally, I would like to express my gratitude to two people who are no longer working in AIMEN but played a significant role in the work presented. Firstly, I would like to thank you Enrique Piñero because this could have been your thesis; , showed me the way, and had faith in me. My professional career owes a lot to you. Also, I would like to extend my thanks to Ander Zornoza for generating the ideas behind NEWSOL and NEXT-BEARINGS and for providing the opportunity to apply our developments.

In addition to the technical support from my colleagues, I would like to thank AIMEN, particularly to Félix Vidal and Fernando Sánchez, for enabling me to continue growing and dreaming. I also want to express my appreciation to Elena Rodriguez for offering her support throughout this adventure.

Finally, I would like to express my gratitude to my family and to Pedro for always being there for me, for supporting me, for the immense patience and understanding, even if you did not fully comprehend it at times, and also for showing me the harsh realities of life. These experiences have shaped who I am today, providing me with a solid foundation for personal growth.

Sen esfuerzo non hay nada.

This is not just a motivational phrase; it is a way of life instilled in me by a very special person, my grandpa, whom I miss dearly. Thanks to you, Grandpa.

Copyright Declaration

The author hereby grants powers of discretion to the City, University of London Librarian to allow the thesis to be copied in whole or in part without further reference to the author. This permission covers only single copies made for study purposes, subject to normal conditions of acknowledgements.

Signed:

Tania Grandal.

Abstract

This thesis documents the development of two monitoring systems based on metal-coated Fibre Bragg Grating sensors, which are to be validated in two distinct industrial applications within harsh environments. One is intended for the naval sector as part of the NEXT-BEARINGS project, while the other is designed for the energy sector within the framework of the NEWSOL project.

The objective of the first application, within the NEXT-BEARINGS (Development of a new generation of naval components for the ship shaft line) project, was to monitor the degradation of antifriction materials in bearings for the naval sector using embedded FBGs with metal coating to measure strain and temperature. The second application, within the framework of the NEWSOL (New StOrage Latent and sensible concept for highly efficient CSP Plants) project, aimed to monitor the performance and operation of novel concrete energy storage components using metallicly coated FBGs for Concentrated Solar Power (CSP) plants, which operate at temperatures of up to 550°C. Despite their differences in industrial settings, both applications share similar harsh environments and high temperatures. Therefore, the FOS monitoring solutions developed in this work are all based on metal-coated FBGs as strain and temperature sensors.

In this thesis, a metallic coating procedure based on a combination of sputtering and electroplating deposition techniques was developed to apply metallic coatings of Ni and Cu to the FBGs and optical fibres. This procedure allows for the coating of longer lengths of fibre (hundreds of meters) and various thicknesses ranging from a few microns to hundreds of microns. Furthermore, after coating the sensors, a procedure was developed to embed these coated sensors into the antifriction bearing material, which is a tin alloy base, using various techniques such as laser cladding and TIG welding.

To verify the research, the metallic coated and embedded FBGs were validated under operational conditions for each use-case.

In the case of the NEXT-BEARINGS project, validation was carried out using two distinct test benches adapted to fulfill different technical objectives. On one hand, the response of the embedded FOS within the antifriction material was analysed using a dedicated fatigue machine developed for this purpose. On the other hand, to validate the embedded FOS response for bearing condition monitoring, a test bench designed for testing antifriction bearings in a real vessel was used. During these validations, the metallic-coated embedded FBGs were subjected to pressures up to 250 bar, rotary speeds up to 667 rpm, and temperatures up to 65°C for more than 5500 hours, providing a stable response throughout the tests.

In the case of the NEWSOL project, three different validations at laboratory scale, mid-scale, and real scale were conducted. The metallic-coated FBGs were embedded in various thermal storage components made using novel high thermal resistant concretes, and they were tested at temperatures up to 550°C. The embedded FBGs were capable of monitoring the concrete curing process, the operation of the storage components, and the degradation of the concrete.

The research concludes by considering future directions for the work in these and other industry sectors.

Glossary of Symbols and Abbreviations

Abbreviations:

3D	Three Dimensional
AE	Acoustic Emission
Al	Aluminium
AM	Additive Manufacturing
APPD	Atmospheric Plasma Powder deposition
Au	Gold
AWS	American Welding Society
BDS	Brillouin Distributed Sensor
C	Carbon
CRC	Canadian Communication Research
CSP	Concentrated Solar Power
CSP	Concentrated Solar Power
CTE	Coefficient of Thermal Expansion
Cu	Copper
CVD	Chemical Vapour Deposition
DED	Direct Laser Deposition
EFPI	Extrinsic Fabry-Perot Interferometer
FBG	Fibre Bragg Grating
FBGs	Fibre Bragg Grating sensor
FFPI	Fabry-Perot interferometer
FMW	Fronius Multi-Welding
FO	Fibre Optic
FOS	Fibre Optic Sensor
Fs	femtosecond
HVOF	High Velocity Oxigen Fuel
IR	Infrared
LAMM	Laser-Assisted Maskless Microdeposition
LENS	Laser Engineered Net Shaping
L-PBF	Laser based powder Bed Fusion
LSFF	Laser Solid Freeform Fabrication
MIG	Metal Inert Gas

MLD	Laser Metal Deposition
MWIR	Midwave Infrared
NDT	Non Destructive Testing
Ni	Nickle
OFDR	Optical Frequency Domain Reflectometer
P	Pressure
PCM	Phase Change Materials
PLD	Pulsed Laser Deposition
PVD	Physical Vapour Deposition
SDM	Selective Deposition Manufacturing
SEM	Scanning Electron Microscope
SHM	Structural Health Monitoring
SHM	Structural Health Monitoring
SiO ₂	Silicon Oxide
SLM	Selective Laser Melting
SM	Single-Mode
SS	Stainless Steel
SS316	Stainless Steel 316
TES	Thermal Energy Storage
TIG	Tungsten Inert Gas
UAM	Ultrasonic Additive Manufacturing
UV	Ultraviolet
WAAM	Wire and Arc Additive Manufacturing
WC-Co	carbide Cobalt

Symbols:

n_c	cladding refractive index
n_{eff}	effective refractive index
n_f	refractive index
ϵ_z	longitudinal strain of the grating
Λ	grating period
α	thermal expansion of silica
η	thermo-optic coefficient
λ	wavelength

λ_B *Bragg wavelength*
 ρ_e photo-elastic coefficient

Chapter 1. Introduction.

1.1 Motivation and objectives

The manufacturing industry is under a digital transformation to achieve the interconnection of the entire production chain and make decisions based on the real data obtained. The main value from this is the *data*, which must be available, reliable, accurate, up-to-date and simple. Therefore, the correct selection and installation of the sensors to obtain the data is crucial. This is not only essential to achieve the objectives of Industry 4.0, but also for *Condition Monitoring* of any component or structure in a non-industrial environment.

There are many industrial components and structures which are very difficult to monitor in a continuous and multipoint way to know their real status in real-time, because factors such as high temperature, difficulty due to remote access, and harsh environments (high temperature >350°C, corrosion, etc) where they operate, which makes it very expensive and/or difficult, if not impossible, to integrate commercial or standard sensors for monitoring. Such industrial sectors, including steelmaking, ceramic manufacturing, power plants, fuel combustion machinery, oil and gas, aircraft engines, shipbuilding components, etc., still require sensors to be developed, integrated and validated for better condition monitoring.

It is within this framework that the work presented in this thesis was developed, in order to develop a monitoring solution for two different applications in a harsh-environment. On the one hand, there is a strong need to develop a sensor for monitoring the real-status of antifriction material in ship bearings components. On the other hand, a novel monitoring system is required to monitor a new energy storage solution provided for a Concentrated Solar Power (CSP) plant. The ship bearing monitoring system was developed under the Galician regional project NEXT-BEARINGS [1]. And the monitoring solution developed for the CSP application was developed under the framework of the NEWSOL European project [2].

Although, they are totally different applications with different requirements, the proposed and developed monitoring system for both, was based on the same technology: Fibre Optic Sensors (FOSs).

FOS was the monitoring technology selected because it possesses the key features that are required in both applications, for example, their ease of integration into structure/materials and their high thermal sustainability.

To address the above challenges arising from two different applications, a FOS network has been carefully designed and developed to be integrated and validated in different industrial settings. The developments were primarily based on Fibre Bragg Grating (FBG) sensors, although distributed Rayleigh and Brillouin technologies were also tested in each case study for multi-parameter (strain, temperature, vibrations, load, etc) and multi-point (distributed or quasi-distributed) measurement.

The objectives required to be achieved by the two case studies are defined below.

In the first case study, ***NEXT-BEARINGS project***, the aim is to develop new advanced in-service monitoring solutions, based on sensors embedded into the antifriction coating material of a ship bearing to monitor its degradation and, alert and prevent potential failures. The antifriction material is a metal used as a coating in the bearings of the ships, to protect the bearing from friction with the axis of the ship during its operation [3]. The antifriction material wears over time and has to be repaired or replaced several times during its working life. The thickness of the antifriction material is around 3-5mm, and its

decrease of a few microns indicates that the material is required to be repaired. With the course of time, cracks and even flakes may appear in the coating. The aim of embedding sensors in the antifriction material is to know, in real time, the antifriction material condition of the bearing, and detect any defect or failure of the antifriction coating before it occurs. Given the limited access to the bearings due to the space constraints in the machine room of a ship, their condition is not reviewed very often. Even during the inspection period, the antifriction coating material of each bearing can only be inspected by dismantling the bearing(s).

In the second case study, **NEWSOL project**, the main objective of the project is to develop advanced materials solutions based on innovative storage media for CSP, from concepts to validation in the field, by monitoring their performance in real-time. This was supported by an innovative thermal energy storage design based on the combination of new functional and advanced materials, like heat thermal fluid, sensible and latent energy storage media and insulating materials, into two innovative Hybrid and Thermal Energy Storage system architectures: a novel thermocline tank concept for new CSP plants and an advanced concrete module for retrofitting existing CSP plants. In order to obtain information about these novel storage components and about the behaviour of the materials, an integrated monitoring system based on FOS (FBGs and Brillouin distributed sensors) was developed to monitor the thermocline and module operation, as well as their Structural Health Monitoring (SHM).

The FOS monitoring systems developed for both case studies are based on metallic coated fibres and FBGs because in the NEXT-BEARINGS case study, the FOS has to be embedded in the metallic antifriction material by welding processes and in the NEWSOL case study, the FOS has to withstand high temperatures (up to 550°C) and corrosive environments (CSP molten salts).

The focus of this thesis is on the development of the metallic coating for the FOS, to be applied on each case study. The thesis presents the detailed study carried out both to apply the metallic coating of different materials on optical fibres and FOS using different coating techniques, and to characterise and analyse the performance of coated FOS. Extensive research was also undertaken to embed the metallic coated FOS in different housing materials under both circumstances before their validation under real operation conditions.

1.2 Structure of the thesis

The work presented in this thesis is divided into seven chapters, starting from a review of the state-of-the-art technologies in Chapter 2, to Chapter 7 summarising the contributions made within the framework of this work.

This first chapter is an introduction to the thesis, highlighting the motivation and objectives of the work and the structure of the thesis.

The second chapter presents a review of state-of-the-art metallic coating techniques used to coat optical fibre in general or FOS in particular. Commercially available metal-coated FOS are also discussed in this Chapter. In addition, a study of embedding processes for fibre optic sensors in metallic structures or components is presented.

The third chapter includes detailed technical developments. In this chapter, several metallic coating techniques were tested to apply a metallic coating layer on FOS. Coating techniques, such as electroless deposition, Physical Vapor Deposition (PVD), sputtering deposition, metallic-based paint and electroplating deposition were studied to define the best procedure and select

Metal coating and embedding fibre optical sensors for industrial applications.

Chapter 1: Introduction.

the optimum metallic coating material or combination of materials to coat the FOS which will be applied in both case studies. Following the metallic coating procedure, a thermal characterization of metallically coated commercial and developed optical fibres and FBGs is made and presented. Thermal cycles between room temperature to 1000°C were carried out to analyse the sensitivity and performance of the metallic coated FOS developed.

The fourth chapter presents the developments to embed the metallic coated FOS into metallic materials. In this chapter, techniques including electroplating deposition were used to embed the metallic coated FOS into Cu structures. Also, casting, Laser Cladding and, manual and automatic, Tungsten Inert Gas (TIG) welding techniques were studied to embed the metallic coated FOS into the antifriiction bearing coating materials, defined for the NEXT-BEARING case study. Their corresponding thermal and mechanical response of the embedded FOS was analysed in detail in the Chapter. This Chapter also includes laser cladding embedding tests, with a high melting point material, such as a Ni-Cr alloy, which were carried out to explore the potential of the developed metal coated sensors.

The fifth chapter presents the validation of the metallically coated and embedded FOS discussed in the previous chapters, through monitoring the antifriiction material of vessels/ship bearings. The validation was carried out using two different test-benches. On the one hand, in order to analyse the response of the embedded FOS front to the antifriiction material degradation (e.g. appearance of defects, cracks, flakes, erosion, etc), a mechanical fatigue machine was specially designed and developed to test steel specimens of 3-5mm antifriiction material coating, simulating an antifriiction bearing section, with accelerated deterioration generated in the antifriiction material to monitor it and to analyse and characterise the embedded FOS response. On the other hand, to validate the embedded FOS for monitoring the bearing condition, a test-bench to test a real vessel antifriiction bearing was used.

The sixth chapter presents the integration and validation of the Ni coated FOS in concrete storage components for CSP plants. In this chapter the development of the Ni coated FOS is presented from laboratory scale up to prototype scale. Key aspects such as the embedding strategy, the durability of the embedded Ni coated FOS front to concrete thermal dilatation tests from room temperature to 700°C and the design and integration of the FOS monitoring system into the final thermocline tank prototype were covered in the Chapter.

The final chapter, Chapter 7, summarises the key achievements made from Chapters 3 to 6 and proposes a future work plan to advance further the research in this field.

Chapter 2. Review of metallic coating and embedding of fibre optic sensors

Silica fibre optic is a waveguide with a cylindrical symmetry, consisting of a core, with a refractive index n_f , surrounded by a concentric cladding with a slightly lower refractive index n_c , which causes the light to be guided within the core. Although there are many types of fibre optics, the most typically used for long-distance data transmission is the *single-mode fibre* with a core diameter of $8\mu\text{m}$ and a cladding of $125\mu\text{m}$ of diameter, which, in turn, is the focus of the work presented in this thesis. Figure 2.1 shows the schematic representative and dimensions a typical single-mode optical fibre.

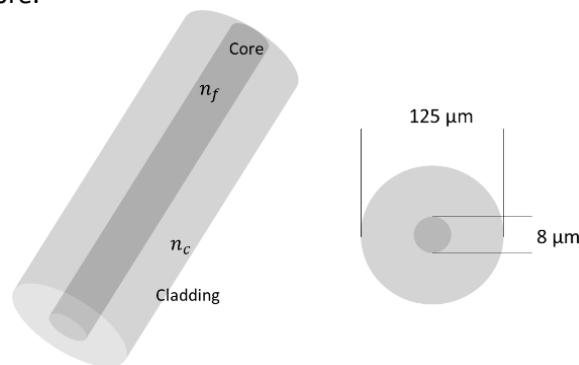


Figure 2.1: Representation of a single-mode optical fibre.

The optical fibre allows light, and therefore data, to be transmitted over long distances with minimal losses. The cost per metre is lower than that of traditional copper cable, thus lowering the cost of data transmission installations. Moreover, the optical fibre is made of dielectric material, silica (SiO_2), not metallic, which offers a perfect isolation between transmitter and receiver and prevents earth leakage, avoiding interference across lines, minimizing potential for eavesdropping or tapping of communications. Despite the fact that optical fibre is fully functional without any coating, the coating, however, gives extra protection both mechanically and chemically, thus minimising the losses which may occur when they are exposed to the harsh conditions. The typical coating materials used to coat and protect the optical fibres are polymers, e.g. acrylate or polyimide.

In addition to data transmission, optical fibres are also used as sensors in which the fibre coating materials could play a role in sensing by inducing a modification on the guided light when they respond to change, e.g. in the external environment.

A Fibre Optic Sensor (FOS) is a device based on the detection of changes in optical fibre-guided light due to external influences. These external influences can be physical, chemical, biomedical, etc. Fibre optic sensors possess inherent advantages, such as small size, light weight, ease for being embedded into materials/structures, immunity to electromagnetic interferences, resistance to corrosion, multiplexing and remote sensing capabilities. All these advantages make FOS technology an excellent solution to some real-world problems, e.g. in harsh environments and/or for applications where multi-parameter, multi-point measurement is required. They offer the possibility of measuring several parameters in a direct or indirectly way: strain, temperature, vibration, electric current, leakage, pressure, gas concentration, load, corrosion, etc.

FOS can be classified according to a variety of criteria. One of the most commonly used criteria is the classification according to the role of the optical fibre. According to this criterion, they are classified as extrinsic and intrinsic. Extrinsic sensors are usually defined as those sensors in which

Metal coating and embedding fibre optical sensors for industrial applications.

Chapter 2: Review of metallic coating and embedding of fibre optic sensors.

the light is guided by the fibre but the interaction between the light and the parameter, to be measured, occurs before a rate element outside the fibre. Although, it can be attached to it by fusion, bonding or mechanical connections, e.g. fluorescence or reflection sensors. While in the intrinsic sensors the interaction takes place inside the fibre, so the fibre is an active part of the sensing process, e.g. micro-curvature sensor, Bragg gratings. Figure 2.2 shows a scheme of the intrinsic and extrinsic FOS concept.

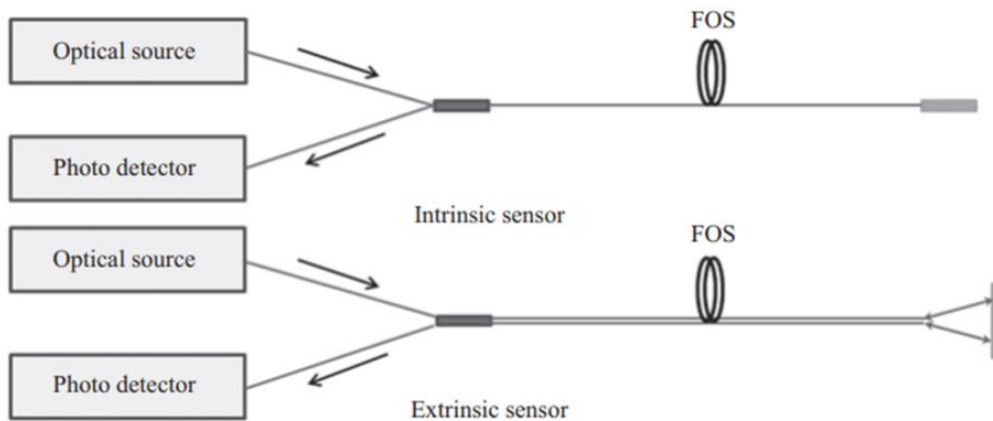


Figure 2.2: Schematic of an intrinsic (above) and extrinsic (below) FOS [4].

The work presented in this thesis is based, principally, on the development of one of the intrinsic types of FOS, namely Fibre Bragg Grating (FBG) optical sensors, to develop a real-time and multiparametric monitoring system for use in harsh environment applications.

2.1 Fibre Bragg Grating

Fibre Bragg Grating sensors are the most widely used FOS in the world due to their versatility, multiplexing capability and their mechanical and thermal properties. A FBG sensor is manufactured by exposing a small segment of optical fibre to a laser light in a periodic pattern, using on ultraviolet (UV) excimer laser or infrared (IR) femtosecond laser typically, to induce a change of the index of refraction of the fibre core along the longitudinal direction. This alteration acts as a filter, reflecting a narrow band of wavelengths guided by the optical fibre and transmitting all others, with the peak wavelength of the narrow band, called the Bragg wavelength. Figure 2.3 is a representation of the fundamentals and operation of a FBG for an optical fibre. The reflected light is analysed and monitored because it is dependent on the strain and temperature variations, is therefore the one that contains the relevant information.

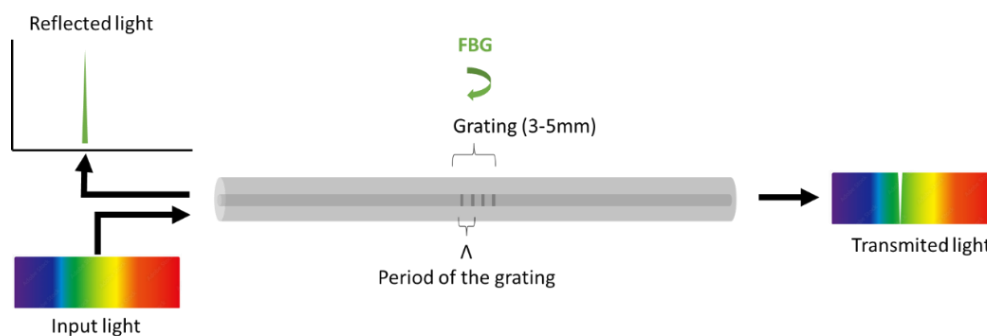


Figure 2.3: Schematic of a Fibre Bragg Grating fundamentals and operation.

The Bragg law of X-ray diffraction, was discovered in 1912, by Sir William Lawrence Bragg, a British physicist and X-ray crystallographer. Sir Bragg, together with his father, won the Nobel

Metal coating and embedding fibre optical sensors for industrial applications.

Chapter 2: Review of metallic coating and embedding of fibre optic sensors.

Prize for Physics in 1915 for an important step in the development of X-ray crystallography [5]. The formation of the gratings in an optical fibre to induce the Bragg reflection, was first demonstrated by Hill et al. in 1978 at the Canadian Communications Research Centre (CRC), Ottawa, Ont., Canada [6][7].

Bragg discovered that the X-rays scattered by all lattice points in a plane must be in phase by the Laue equations (the Max von Laue equations describe the behaviour of waves that are diffracted when incident on a crystal lattice), which describe the behaviour of waves that are diffracted when incident on a crystal lattice. Furthermore, the scattering from successive planes must also be in phase. For a phase difference equal to zero the laws of simple reflection must hold for a single plane and the path difference for reflections from successive planes must be an integer number of wavelengths [8]. Figure 2.4 shows how an incident beam is diffracted by two successive hkl planes with interplanar spacing $dhkl$. The path difference travelled by the two successive plane beams is given by equation (2.1), and hence the condition for maximum diffraction derives to the equation (2.2).

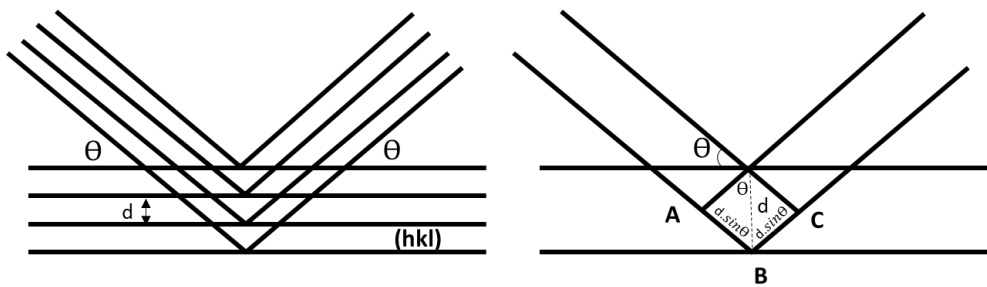


Figure 2.4: Schedule of beam diffraction in hkl planes.

$$AB + BC = 2d\sin\theta \quad (2.1)$$

$$2d\sin\theta = n\lambda \quad (2.2)$$

Where θ is the incident angle, n is the order of reflection, and λ is the wavelength. A diffraction pattern is obtained by measuring the intensity of the scattered radiation as a function of the angle θ . Whenever the scattered waves satisfy the Bragg condition it is observed a strong intensity in the diffraction pattern, known as Bragg peak [5].

When in the core of an optical fibre where a periodic modification is made, as a grating, $\theta=90^\circ$ and d is the distance between the *strips* of the grating, from equation (2.2), $\lambda=2d$ for $n=1$ which is the approximate wavelength of the reflection peak. The fibre therefore acts as a dichroic mirror, reflecting part of the incoming spectrum.

Equation (2.2), has to be adapted for silica, since the distances travelled by light are affected by the index of refraction of the optical fibre.

$$\theta(\lambda) = \beta\Lambda = \frac{2\pi}{\lambda}n_{eff}\Lambda \quad (2.3)$$

Where Λ is the grating period, which is the distance between the gratings of the core and n_{eff} is the effective index of the fibre. For $\theta=90^\circ=\pi$ and, combining equation 2.2 and 2.3 results the equation (2.4) is the one that governs the behaviour of the FBG sensors.

$$\lambda_B = 2n_{eff}\Lambda \quad (2.4)$$

The Bragg wavelength (λ_B) of a FBG, made on a silica monomode fibre, is a function of the effective refractive index of the fiber (n_{eff}) and the periodicity of the grating (Λ) and, therefore a

Metal coating and embedding fibre optical sensors for industrial applications.

Chapter 2: Review of metallic coating and embedding of fibre optic sensors.

FBG sensor is naturally sensitive to temperature and strain variations on the grating. The temperature variations cause the n_{eff} variation, hence the Bragg reflection peak variation, and the strain sensitivity cause a perturbation on the grating period, Λ , which also causes a change in the Bragg reflection peak.

The equation to calculate the dependence and sensitivity of the Bragg wavelength on the temperature and strain is expressed in (2.5) and (2.6) respectively, where T represents time and L length.

$$\frac{\Delta\lambda_B}{\Delta T} = 2n_{eff} \frac{\partial\Lambda}{\partial T} + 2 \frac{\partial n_{eff}}{\partial T} \Lambda \quad (2.5)$$

$$\frac{\Delta\lambda_B}{\Delta L} = 2n_{eff} \frac{\partial\Lambda}{\partial L} + 2 \frac{\partial n_{eff}}{\partial L} \Lambda \quad (2.6)$$

Combining both makes it possible to obtain the equation of sensitivity of the Bragg wavelength with temperature and strain (2.7):

$$\frac{\Delta\lambda_B}{\lambda_B} = (\alpha + \eta)\Delta T + (1 - \rho_e)\epsilon_z \quad (2.7)$$

Where α represents the thermal expansion of silica, η is the thermo-optic coefficient (representing the temperature dependence of the refractive index), ρ_e is the photo-elastic coefficient (the variation of the index of refraction with strain) and ϵ_z is the longitudinal strain of the grating.

One of the principal advantages of the FBGs, and many FOS in general, is that the strain variation could be due to different external events: pressure, load, vibration, expansion, contraction, corrosion deformation, chemical reaction, etc. This offers the advantage to indirectly monitor many other parameters from strain monitoring with these sensors. A major advantage of FBGs, is their multiplexing capability. It is possible to obtain several gratings along one optical fibre with different Bragg wavelengths reflected, by inscribing gratings with different periods along the same fibre, as shown in Figure 2.5.

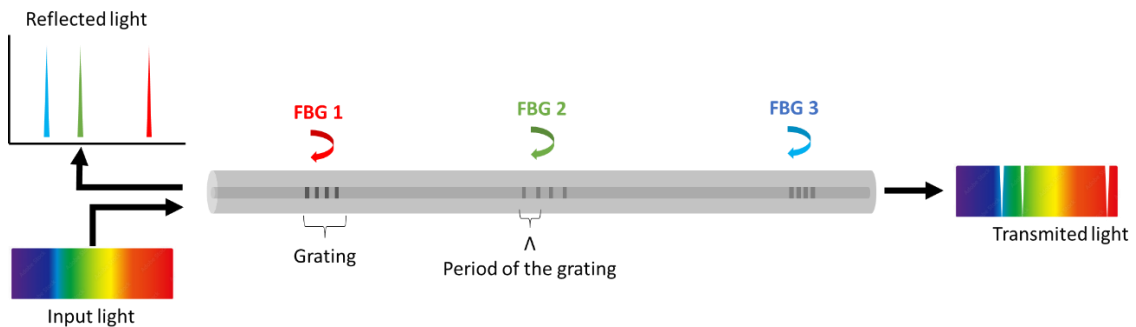


Figure 2.5: Schedule of multiplexed FBGs along one optical fibre.

Given the cross-sensitivity of a FBG, it is important to decouple the effect induced by temperature change from that by strain, for example, by adding a second FBG as a temperature reference. The temperature FBGs can be isolated from the strain variations, for example through sensor packaging or not being bonded to the medium being monitored.

Metal coating and embedding fibre optical sensors for industrial applications.

Chapter 2: Review of metallic coating and embedding of fibre optic sensors.

To apply FBG sensors in high temperature environment (e.g. $>400^{\circ}\text{C}$), three main aspects have to be considered:

1. How a grating is inscribed into an optical fibre.
2. What is the coating material of the fibre?.
3. What is the optimum packaging or embedding process required by the application?.

The grating is made by laser inscription into the core of a fibre. Typically, a UV laser is used to induce a semi-permanent change in the refractive index of the fibre core. This grating is named Type I and when is exposed to temperatures $>450^{\circ}\text{C}$ for a long time, the grating disappears. To use a Type I grating for higher temperatures a re-generation process is needed [9] which weakens the fibre. For high temperature applications, gratings inscribed by femtosecond (fs) laser or Type II gratings which have a permanent micro-structural change in the fibre core can survive up to 1000°C [10].

Knowing the type of grating that needs to be selected according to the type of application, the next step is to choose the most suitable coating or packaging for it. In high temperature and/or harsh environments, as is the case in both use cases of this thesis, FBGs are typically either metallized or encapsulated to ensure their long-term resistance in such applications. This chapter provides a review of existing technologies for coating, packaging or embedding FOS, including FBGs, for their use in harsh environments, such as high temperature environments. This paves the way for the further developments as detailed in the following chapters.

2.2 Review of metallic coating and embedding of fibre optic sensors

The unique characteristics mentioned of fibre optic sensors, specially of FBGs, drive the concept of using metallic coating, different from the typical polymeric coatings (acrylate, polyimide), to sense the change in parameters, to which they are not intrinsically sensitive, or, to protect the sensors from the environment, to which they are exposed in operation.

Embedding FOS within materials, components or structures adds *intelligence* and enables real-time monitoring at some critical locations that are impossible or difficult for retrofitting. Sensors hold great promise for increasing the safety of components, but their reliability and that of the process itself can reduce maintenance and operating costs. The integration protects the sensor from damage and isolates it from environmental disturbances. At the same time, it avoids or greatly reduces the visual inspection functions traditionally performed and provides real-time information in the event of a failure in the structure or component.

The embedding process can be carried out during the manufacturing of the structure or tool or after completion. The packaging material must to maintain the integrity of the sensor, so it is often necessary to coat the sensor with a specific material, prior to being embedded, to act as a transducer.

The integration of these sensors is not a trivial task and raises questions as to whether they may compromise the integrity of the structure/component. Generally, in the industry, traditional sensors should not be embedded in the components or structures, they are usually integrated around the target component. However, FOSs, and particularly FBGs, have been embedded into the structure or component for monitoring their structural integrity, e.g. in the aviation industry, due to their inherent advantages [11]–[13] .

The process for embedding and/or integrating FOS becomes more complicated when the application involves high temperatures ($>350^{\circ}\text{C}$) or, the structure or the component to be monitored, is at high or cryogenic temperature or in a harsh environment (corrosion, difficult

access, presence of dirt or oil, etc.). When the typical FOS polymeric coatings do not resist or, it is not possible to use glues or adhesives to make the bond because they became degraded. In these cases, there is a need to protect the optical fibre with a robust coating or packaging and find the most appropriate embedding method for the durability of the FOS monitoring system. The FOS developed in this thesis are in this context. Metallic coating FOS monitoring systems were developed for being integrated in the two different harsh environment applications mentioned in the chapter 1.

In the sections below the state of the art technologies, reported for metallic coating and metallic embedding of FOS, are presented.

2.2.1 Review of metallic coating of fibre optic sensor

The standard optical fibre coating is a polymeric material (acrylate or polyimide). This material acts like as a shock absorber to minimise attenuation caused by possible micro-flections, and protect the fibre from mechanical damage and/or moisture ingress (although not totally hermetically sealed). This type of coating does not withstand temperatures above 350°C, therefore in high temperature environments, the coating is required to be resistant to the operation temperatures as well as hermetic to assure the seal of the optical fibre from hydrogen penetration [13]. The hydrogen molecules are able to enter the silica of the optical fibre causing surface degradation at room temperature, which causes strength degradation of the fibre because it generates cracks on the surface. This effect is minimized by the typical polymeric coating. Also, at high temperatures, the hydrogen is diffused into the core of the fibre which causes faster core degradation, increasing the optical losses up to cause the optical fibre fault. For these environments, other resistant coatings are applied, like carbon (C), metallic or ceramic coating or packaging.

Carbon coated optical fibres are made by depositing a thin carbon (C) layer onto the surface of the silica during the fibre draw manufacturing process. The final carbon layer is around 20-50 nm, sufficient for protecting against both water and hydrogen diffusion, without causing micro-bend losses. However, it is thin and brittle, which cannot protect the fibre from mechanical damage such as scratches. For this reason, C coated fibres are always protected by additional polymer coatings, which are applied using standard coating applicators located below the hermetic coating reactor on the drawing tower [14]. But the polymeric coating makes it non-resistant to temperatures over 350°C.

In contrast with the carbon coated optical fibres, another way to obtain a sealed optical fibre to avoid their degradation due to hydrogen exposure and to obtain a high resistance at high temperatures (>350°C), is to use a metallic coating optical fibre. Metallic coating is hermetic and robust enough for protecting the optical fibres mechanically and thermally. They are widely used for high temperature environments due to their thermal properties. They have a high thermal conductivity and high capacity which favours an effective transfer of thermal energy from the coating to the sensor, thus increases the thermal sensitivity and thermal response.

Optical fibres coated with Cu, Al and Au are commercially available. Some fibres include a carbon layer sandwiched between the fibre cladding and the metallic coating to improve their bonding. All of them can be used as distributed FOS, with a maximum coating thickness of 25µm (for a single-mode fibre) and able to operate at a maximum of 400°C for Al coating, 450°C for Cu coating, and 600°C for Au coating, for long-term exposure application. In the case of FBG sensors, there are many limitations when it comes to acquiring metal coated FBG sensors. Only a few FBG sensor suppliers are capable of providing them, with limitations on the number of sensors per fibre and the coated length. These suppliers primarily use two methods to obtain metal coated FBG sensors. On one hand, they employ a metal coated fibre into which they

Metal coating and embedding fibre optical sensors for industrial applications.

Chapter 2: Review of metallic coating and embedding of fibre optic sensors.

inscribe an FBG sensor after removing the metal coating from that specific area. After manufacturing the FBG sensor, they reapply a layer of the same metal used in the metal coated fibre to cover that section of the fibre. Figure 2.6 shows a Au coated FBG sensor manufactured by this procedure. On the other hand, another method they commonly employ is to create FBG sensors in an optical fibre covered with a *soft* polymer coating. They then send this fibre to the company that manufactures the metal coated fibre and apply the metal coating to this fibre, having previously removed the soft polymer coating from it.

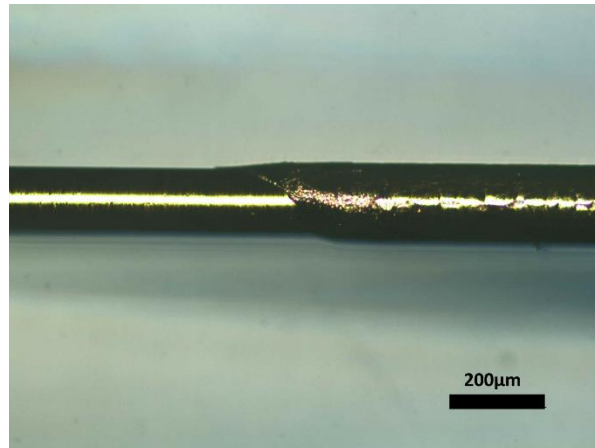


Figure 2.6: Au coated FBGs from Technica. Picture of the frontier of the Au original coating of the optical fibre and, the re-coated section where the FBG was inscribed.

The commercially available thickness of the metallic coating of optical fibres and FBGs is in the range of a few tens of microns, which does not provide sufficient protection to withstand the embedding process and operation conditions in the thermal concrete tank for the Concentrated Solar Plant (CSP) or in the antifriction metallic material by welding process, as detailed in the following chapters. Furthermore, it is not certain that the gold, with melting point at around $\sim 1064^{\circ}\text{C}$, could withstand the high temperature at around $700\text{--}1600^{\circ}\text{C}$ in soldering, depending of the technique and material. For these reasons, this thesis has developed a procedure for metal coating optical fibre and FBG sensors with a coating metal of Ni and/or Cu with sufficient thickness to withstand long term exposure to high temperatures, as well as the metal embedding process under laser embedding or Tungsten Inert Gas (TIG) welding techniques.

There are a wide variety of coating techniques reported to apply a metallic coating on an optical fibre. The Freezing technique is the most widely used by industrial manufacturers. As shown in Figure 2.7, this in-line coating is completed while passing the optical fibre through a molten metal in a drawing tower. If the temperature of the melt metallic material is close to the melting point of the metal and the temperature of the fibre is relatively lower (but close), a layer of the metal can freeze on the surface of the optical fibre. To obtain a stable uniform metal film, the duration of the contact of the fibre with the molten metal in the metallizer should be shorter than the time of fibre heating to the metal melting point [14]. The thickness of the metallic coating layer depends on the optical fibre diameter and its temperature. For a typical single-mode optical fibre of $125\ \mu\text{m}$, the maximum thickness obtained with this technique is around $25\ \mu\text{m}$.

This technique allows the use of a wide variety of metallic materials with a melting point up to $\sim 1500^{\circ}\text{C}$. However, the thickness of the coating layer is limited (tens of microns). Furthermore, it is not possible to manufacture a FBGs through the metallic coating and, also, it would be only possible to manufacture the FBGs, e.g. by fs laser, previously to the freezing metallic coating for metallic materials with a melting point lower than 1000°C , otherwise the sensor and/or the fibre would be damaged.

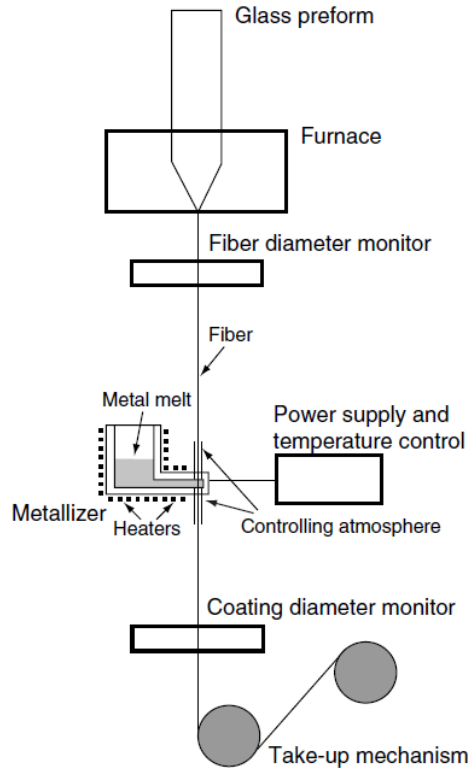


Figure 2.7: Schematic diagram of a typical metal-coating setup: a standard drawing tower equipped with a metallizer [14].

There are other coating techniques which are reported to apply a metal coating layer on an optical fibre, but they do not require such a sophisticated and expensive set-up, nor the metal coating being part of the fibre manufacturing process. Most importantly, they allow the use of metals with a high melting point and, achieve greater coating thicknesses than those obtained with the freezing technique, which is required for the use-cases studied here. These techniques are able to be applied at low temperature, so the fibre optic or sensor does not suffer any damage during the coating process.

The Electroplating Deposition technique is the most used to obtain a metallic coated optical fibre. The metallic coating procedure developed in this thesis is based on this technique (combined with sputtering technique), because it perhaps to apply multiple metals with a variable thickness, from a few microns to hundreds of microns.

As shown in Figure 2.8, electroplating process consists of an electric current flowing between two electrodes that are immersed in a solution rich in metal salts. The current flowing through the anode passes into the solution, causing the ions in the solution to follow the direction of the current and adhere to the surface of the cathode. The optical fibre here is used as the cathode and the released metal ions will adhere to it, producing metallic coating. This technique allows the use of a large amount of metals as coating material, the process is conducted at around 55°C which does not represent any danger to the fibre and, it is possible to achieve coating thickness from tens of microns to a few mm. Most of the bibliographical references about FOS metallic coating focus on the use of electroplating technique to coat the optical fibres, especially for coating FBG, Fabry-Perot sensors, or other types of point sensors FOS, due to its simplicity and flexibility. However, the section to be coated using this technique requires to be electrically conductive so that it can act as a cathode in a closed electrical circuit. FOS is made of silica, which is dielectric. Therefore, in order to be able to apply the electroplating process, an electrically conductive layer must be applied beforehand.

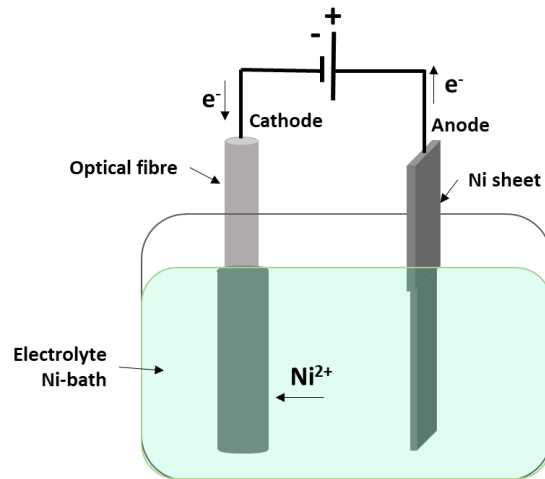


Figure 2.8: Simplified diagram for electroplating Nickel on a conductive optical fibre.

It is possible to use metallic coated optical fibres as a cathode. However, there are some other techniques which do not require the conductivity of the sections to be coated, such as Electroless Deposition, Sputtering Deposition, Physical Vapor Deposition (PVD), Chemical Vapor Deposition (CVD), Pulsed Laser Deposition (PLD), etc. But in any of these cases, prior to applying a metallic coating over the optical fibres, it is required that their original polymeric coating be removed.

Li et al. [15], [16] were the first to report metallic coating using sputtering deposition of $1\mu\text{m}$ of Ti and then $2\mu\text{m}$ of Ni, on a FOS, which is shown in orange in Figure 2.9.a. This was followed by applying electroplating deposition of Ni (green layer) to embed the coated optical fibre in a steel substrate (blue sheet) as illustrated in Figure 2.9.a and Figure 2.9.b.

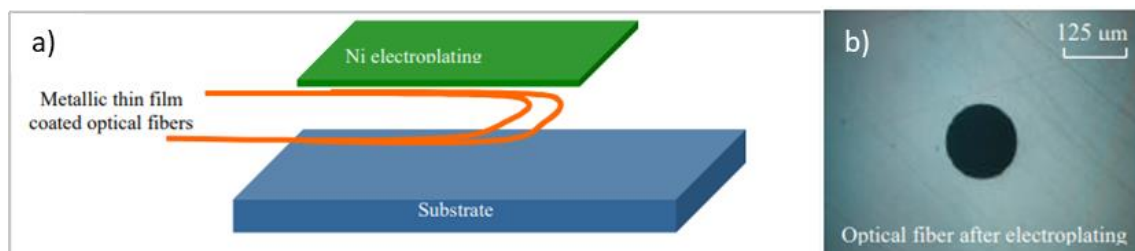


Figure 2.9: (a) Schedule of the metallic coating and electroplating bond. (b) Micro picture of the appearance of the metallic coated optical fibre after the electroplating process [16].

In the following years there have been numerous studies where other coating techniques have been developed [17]–[24], among which Li's approach (as discussed above) dominates due to minor variations required, unlike the others which require significant variations to apply the conductive layer [25]–[34]. Among these the most widely used approach is to generate the first coating layer using Electroless [21], [22], [26], [27], [29] and then Sputtering Deposition technique [35], [36].

Electroless deposition is a layer-by-layer coating technique which immerses an optical fibre in a chemical solution rich in metallic salts, similar to that of electroplating, but the reaction in this case is autocatalytic. To produce the autocatalytic reaction, the optical fibre has to be cleaned thoroughly, etched, sensitised and activated by passing through different solutions. This technique is of low-cost and can be implemented, at low temperature ($<90^\circ\text{C}$) without specific equipment, for coating with many different metals. It is, however, very sensitive to even the slightest contamination of the fibre during processing, which can lead to defects in the final finish or adhesion. Shen et al. [27] used the electroless deposition technique, before

Metal coating and embedding fibre optical sensors for industrial applications.

Chapter 2: Review of metallic coating and embedding of fibre optic sensors.

electroplating, to generate a thin film of Ni metallic coating layer on FBGs to improve the thermal resistance and sensitivity of the FOS. Figure 2.10.a shows the reported schedule of coating a FBG by electroless deposition of Ni and electroplating deposition of Au. In addition to thermal protection, metallic coatings made by electroless technique are also used to develop other types of sensors, e.g. corrosion sensors. Wright et al. [22] used the electroless coating technique to apply a first layer of Ni and a second layer of Fe to develop a distributed FOS for corrosion detection, providing real-time monitoring of the mass loss in natural gas transmission pipelines.

As electroless deposition technique presents a great potential for coating optical fibres, the many patents have been generated to cover the specific procedures or set-ups for metal coating [37]–[42]. Figure 2.10.b shows a schedule of the electroless step-by-step procedure protected by the patent [38], where the optical fibre was passed through the different solutions for cleaning, sensitisation, activation and final plating. Therefore, the electroless deposition technique is an alternative to the Freezing technique. However, this technique requires working with uncoated, therefore very fragile, optical fibre, and also, as already mentioned, it necessitates passing the fibre through numerous solutions, which may result in fibre breakage if the process is not automated, requiring meticulous control to prevent contaminations and to adjust the state of each solution for the applied coating to be of high quality.

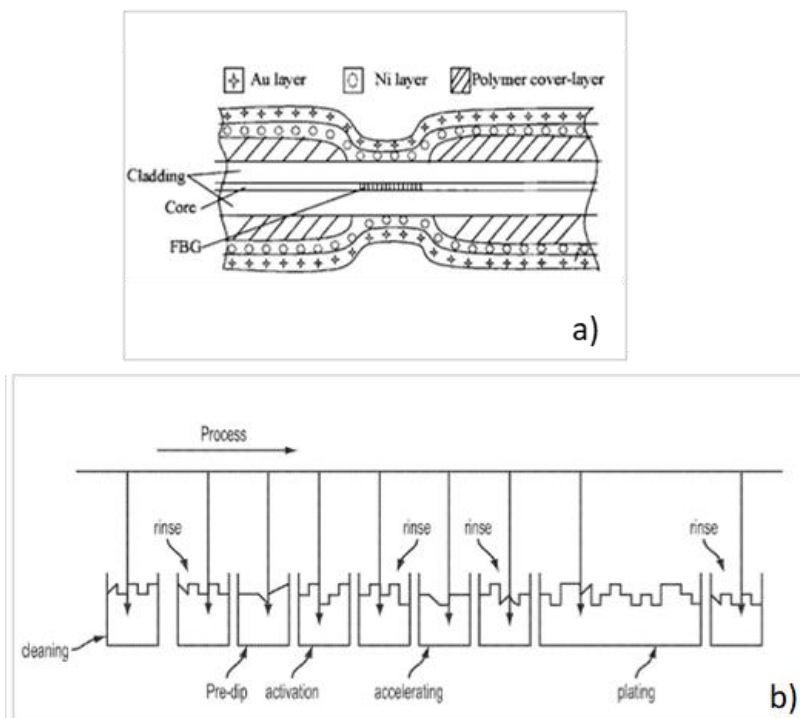


Figure 2.10: (a): Schedule of the FBGs coating developed by SHEN et al. [27]. (b): Schedule of the electroless procedure protected for coating an optical fibre by electroless deposition technique [42].

The second most used technique for generation of an electrically conductive layer, is the Magnetron Sputter deposition technique, as reported by Li et al. [15], [16] in 2000. This technique uses sputter equipment in which the optical fibre is placed in its vacuum chamber where the ions strike the metal target of which atoms are ejected (or sputtered) from the surface and adhere to the surface of the optical fibre. As the coating usually covers only one side of the fibre that is facing the metal target, it requires sputtering twice in order to coat the whole surface (diameter) of the optical fibre. Also, the vacuum chamber is small in size, it is not possible to coat long lengths or in a continuous way. Although commercial equipment is needed for applying this coating technique, it is widely used due to its relative low-cost (15000-30000 euros) compared with techniques as PVD (>60000 euros), relatively fast operation (~20 min.) and

Metal coating and embedding fibre optical sensors for industrial applications.

Chapter 2: Review of metallic coating and embedding of fibre optic sensors.

flexibility in the use of different metals as target material [17], [26], [32], [35]. Ke and Xu et al [17] designed a special tool, as shown in Figure 2.11.a, to coat long lengths of optical fibres using the sputtering technique. The optical fibre is roiled up inside and can be moved using a coil system during the sputtering process. Subsequent they tested the optical fibre, coated with a layer of Ti and of Pd, as shown in Figure 2.11.b for distributed hydrogen sensing.

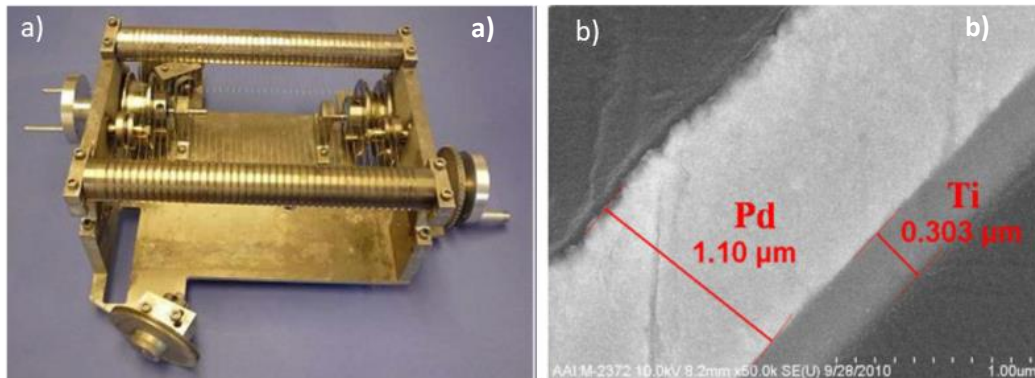


Figure 2.11 (a): special tool designed to continuously coat an optical fibre by sputtering. (b) Cross-section of the Pd and Ti optical fibre coated by sputtering [17].

The metal coating procedure developed in this thesis is based on a combination of sputtering deposition and electroplating deposition techniques, as will be detailed in Chapter 3. After studying different coating techniques, these were the most cost-effective and straightforward methods found for applying coatings of various metals and with different thicknesses, suitable for the requirements of the target applications.

Thin film coating techniques such as Physical Vapor Deposition (PVD), Chemical Vapor Deposition (CVD) or Pulsed Laser Deposition (PLD) are also used to coat the optical fibres with a thin metallic layer. These techniques, however, require specific and expensive equipment. More thin film coating techniques have been reported by the scientific community. For example, Hamidreza et al. [19], [20] developed a thin film metallic coating method based on Ag nanoparticles sintering deposition by laser-assisted maskless microdeposition (LAMM). Figure 2.12.a shows the LAMM set-up for making the Ag deposition and Figure 2.12.b shows the appearance of the Ag thin film layer deposited on the fibre.

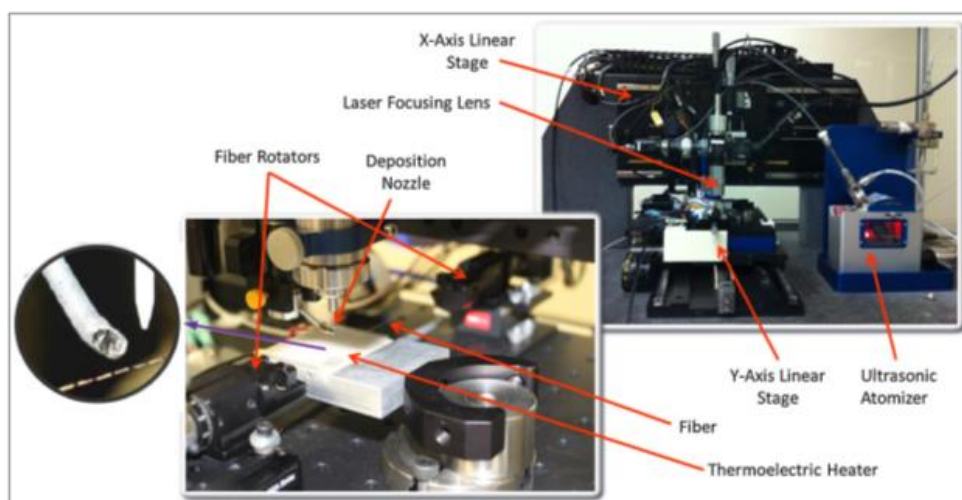


Figure 2.12: View of LAMM workstation with rotational stage for grabbing and turning the FBG [20].

A type of bi-coating technique has been developed to apply a conductive polymeric or a conductive paint layer over the layer coated using the electroplating technique to obtain a final

Metal coating and embedding fibre optical sensors for industrial applications.

Chapter 2: Review of metallic coating and embedding of fibre optic sensors.

metallic coating. This bi-coating, polymer-metal, is used in laser-applications to dissipate heat from the fibre laser [23] or to improve the sensitivity of chemical sensors [18].

Once the optical fibre has an electrically conductive layer, made by any of the above mentioned techniques, the electroplating deposition process makes it possible to grow the coating thickness up to the required thickness or to generate a bi-metal coating combining different metals. It should be noted that when the coating thickness is increased, fibre losses also increase due to the micro-bending stresses induced by the metallic coating [14], [43]–[46].

Another important factor influencing losses and, the strength and durability of metallic coated optical fibre is the Coefficient of Thermal Expansion (CTE) of the metals used for coating the fibre. On one hand, as the silica CTE is much lower than metals CTE, applying a bi-metal coating is better to avoid stress being concentrated at the silica-metal boundary because of the CTE differences. On the other, Kirkendall voids appear at the bi-metal boundary after the bimetallic structure is exposed to high thermal fatigue ($>700^{\circ}\text{C}$), causing coating degradation as shown in Figure 2.13 [47].

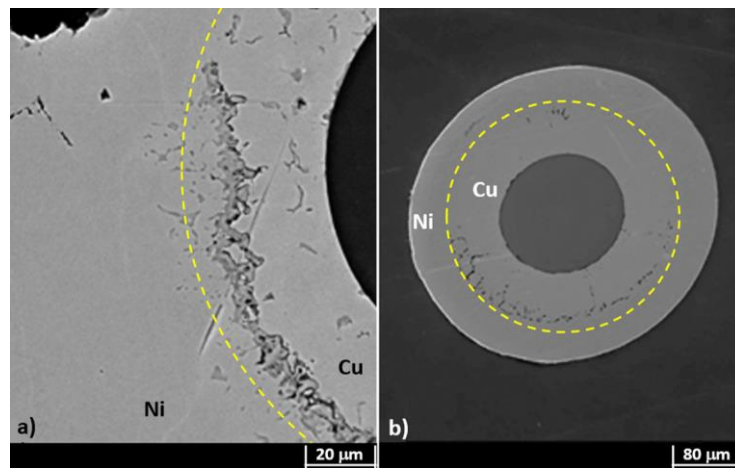


Figure 2.13: SEM micrograph of a bimetallic coating after the first heating/cooling cycle between room temperature and 800°C : (a) Cu coating thinner than the Ni one; (b) double layer with comparable thicknesses. Cu–Ni boundaries are highlighted by a yellow thin dotted line; it represents the region where the Cu–Ni alloy was formed [47].

In conclusion, FOS seem to be a good distributed or quasi-distributed solution for monitoring harsh environment applications, a specially in the case of high temperature applications because the silica can withstand harsh environments applications due to its intrinsic properties, but also, because it is receptive to coating by materials like metals which protects and seals the FOS from these environments and makes them more robust or even, sensitive to other parameters. In this section, the review of the techniques used to coat the FOS with metals was presented. There are many different options for applying a thin coating layer on the fibre and it is possible to apply many different metals, but for increasing the thickness of the coating, to protect the fibre front to embedding process, principally, there exists unanimity for the use electroplating deposition technique.

2.2.2 Review of metallic embedding of fibre optic sensors

Embedding the FOS into a metallic material, component or structure, is challenging because the metal is solid and not easily mouldable to integrate FOS. Thus to monitor a metallic structure or component the most commonly used approach is to bond or fix a FOS to the metallic surface. This, however, is not possible when it is in a harsh environment (e.g. high temperature, high corrosion, oily environment, etc), as neither the adhesives nor the fibre coating can withstand

Metal coating and embedding fibre optical sensors for industrial applications.

Chapter 2: Review of metallic coating and embedding of fibre optic sensors.

the condition in a safe and durable manner, as in the applications outlined in this thesis, such as the antifriction bearings and thermal storage components of a solar thermal power plant.

For high temperature monitoring there are some FOS packaging solutions which are able to sustain adhesion under some circumstances, but they have limitations (e.g. up to 700°C). The challenge lies in the requirement for monitoring strain in these structures and environments. One viable solution is to embed the FOS into a metallic structure to assure good strain transmission and durability, generating smart structure.

Many different procedures exist to embed a FOS (a FBG or any intrinsic FOS) into a metallic structure [48]. The most in common involves high temperatures (>450°C) and requires melting the metal to make the bond. Some of these techniques are: Casting, Spray Coating, Vacuum Brazing or Laser processing. In these cases, the polymeric coating of the optical fibres is removed and replaced by a heat resistant coating, typically metallic, which protects the optical fibre thermally and mechanically during the embedding process. There are methods for embedding FOS that do not require high temperatures, such as Electroplating Deposition or Ultrasound-based techniques.

The work presented in this thesis is based on metallic coating FOS embedded in a novel high thermal performance concrete during the concrete setting process. However, for the antifriction bearing use-case, embedding procedures were developed using TIG welding and laser cladding processes to embed the metallic coated FOS.

In this section a review of the reported techniques that have been carried out for embedding FOSs in metals is presented.

2.2.2.1 Casting embedding technique.

The first publication related with the FOS embedding into a metallic material is from Lee et al. in 1989 [49]–[51]. They reported embedding an optical Fabry-Perot interferometer (FFPI) sensor into Al by casting. To do so they used an un-coated optical fibre with its ends covered by a steel capillary tube, leaving the section of the FFPI sensor exposed to Al, as shown in Figure 2.14a. The capillary tube protects the air-metal junction, avoiding damage to it.

As Figure 2.14.a shows, the fibre optic sensor was placed inside a mould before pouring the melted Al material to fill the mould and embed the optical fibre. This marked the first successful embedding of an FOS into a metallic material, resulting in a new non-destructive sensor for monitoring internal perturbations in a structure as Figure 2.14.b shows.

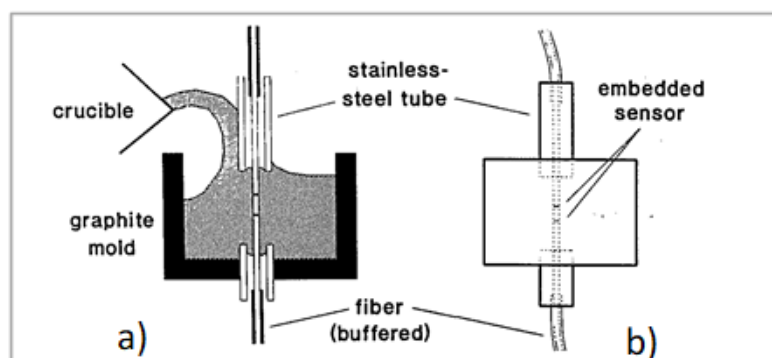


Figure 2.14 (a): Arrangement for casting metal part. (b): Final appearance of the embedded sensor [50].

The casting technique is a relatively easy and low-cost embedding technique. Nevertheless, it is only possible to use with metals with a relative low melting point, like Al, and requires a mould, so it is not a flexible process or adaptable to any existing structure. Only a few scientific papers reported the use of casting as a method for their sensor embedding. Werneck et al. [52], [53]

Metal coating and embedding fibre optical sensors for industrial applications.

Chapter 2: Review of metallic coating and embedding of fibre optic sensors.

embedded a FBG in an Al component by casting to monitor the internal stress during the casting solidification process [52], and then, in [53] to investigate the thermal and mechanical load response of different types of FBGs embedded in Al. Figure 2.15.a shows the schedule for the strain and temperature FBGs to be embedded by casting. Both FBGs are uncoated with the temperature sensitive FBG protected using a capillary tube, while strain sensitive FBG being unprotected to ensure a good thermal bond with the Al. Figure 2.15.b shows the final appearance of the strain FBGs after being embedded and Figure 2.16.a shows the cross-section of one of manufactured embedded probes. In this case, the fibre is located along the melt flow direction and some pores appear around the fibre. If the fibre is located transversely to the melt flow direction, the bond between the Al and the optical fibre is better as Figure 2.16.b shows.

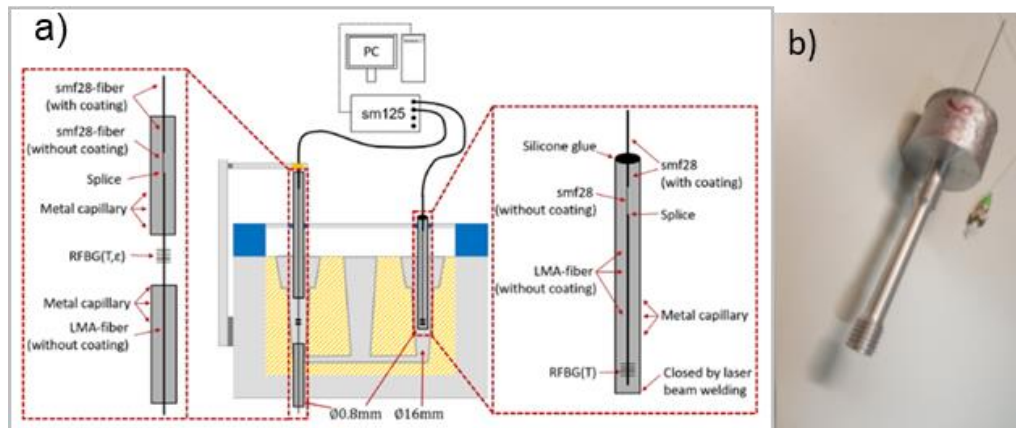


Figure 2.15: (a): Setup for the casting process with an RFBG strain sensor ($RFBG(T, \epsilon)$) and an RFBG temperature sensor $RFBG(T)$. (b): Picture of one arm of a cast part with the embedded FBG strain sensor after casting and machining [53].

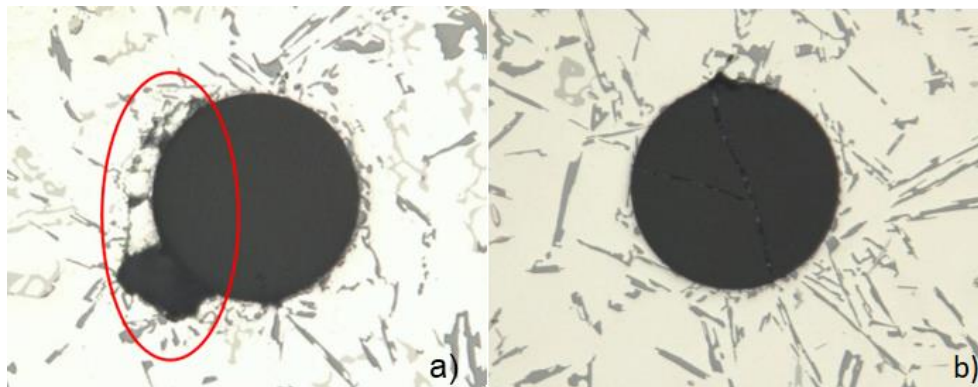


Figure 2.16: (a): Cross-sections of a FBG sensor embedding test where the fibre is located along the melt flow direction. It is highlighted a non-bonded fibre-Al section (b): Cross-sections of three different probes where the fibre is located across the melt flow direction [52].

In conclusion, the casting embedding technique could be useful for embedding FOS into Al or other metals with a low melting point to manufacture small pieces or to monitor the solidification casting procedure. This technique was studied to embed the metal coated FBGs in the antifriction material bearing, as detailed in Chapter 4, although in this case, a poor bond was found.

2.2.2.2 Electroplating deposition technique

Electroplating deposition is another simple and low-temperature metal embedding technique [15], [16], [24], [54]–[56]. This technique allows a metallic coated FOS to be embedded in the surface of a metallic structure or component, with almost no restrictions on material, i.e. multiple materials can be used as a base or added material to make the bond. This technique

Metal coating and embedding fibre optical sensors for industrial applications.

Chapter 2: Review of metallic coating and embedding of fibre optic sensors.

was the one used by Li et al. [15], [16] to bond the sputter-coated FBGs to the steel substrate, before embedded by Laser (which will be explained below). Following his approach, other researchers have used the electroplating deposition technique to embed FOS to components such as moulds or other structures. Jakka [24] and Zhuang [54], in their thesis, have presented a procedure to embed a fibre optic extrinsic Fabry-Perot interferometer (EFPI) by electroplating deposition onto a Cu substrate. Subsequently the embedded EFPI sensor was applied into a steel mould to monitor the strain and temperature of an Al casting process. Both researchers have evaluated different metallic techniques to coat the EFPI sensor and generate the coating layer: electroless Cu; Cu paint by dip coating and with Natural Beeswax before dip coating it with copper paint. The latter gave the best results when they were tested up to 700°C.

By contrast, Wang et al. [56] have developed metal-packaged strain and temperature FBG sensors for long-term structural health monitoring in cryogenic environments. They have coated FBGs using sputtering and then embedding the metallic coated FBGs into a steel metallic base-package, by electroplating deposition of Cu, to assure the joint resistance at cryogenic temperatures down to 80°K yet with a good and durable response.

This technique was also studied to embed the metallic coated FOS on metallic structures (detailed in chapter 4). It is slow and only allows embedding the fibre in relatively thin layers of added material, so the sensor remains superficially embedded. In the case of the antifriction bearing use-case, it would be necessary to combine this technique with another one such as laser cladding, TIG welding, or casting to achieve robust embedding of the sensor in the antifriction material layer that needs to be monitored, as if it remains superficially embedded, it is likely to degrade or even detach during operation.

2.2.2.3 Thermal spray coating technique.

Thermal spray coating technique is a technique used for applying a protective coating layer, metallic or ceramic, on a (metallic) material, to protect it from corrosion. This technique is to deposit a molten, semi-molten or powder material, onto almost any object by spraying to build up a thin layer of hard coating. Within this technology, the High velocity oxygen fuel (HVOF) spray is the most used for embedding FOS into metal [57]–[64]. In the HVOF technique, oxygen, fuel and the raw coating material powders are fed into a combustion chamber and are ignited using an electrical arc. The high pressure and high temperature generated in the chamber accelerate the particles through a nozzle at a high velocity. Finally, the particles are deposited on the substrate to form a physical coating [64]. This technique allows the coating of FOS with a wide variety of metal alloys which can operate from comparatively low temperatures to high temperatures, depending on the spray material to be applied.

Two different embedding strategies have been agreed in principle by the scientific community. The first strategy is based on the work reported by Baldini et al. [57] and Duo et al. [58]. They have used commercial metallic coated optical fibres of Au and Al (respectively) to embed them by spraying Ti and alumina (respectively). Figure 2.17.a shows a flame spray set-up by Duo et al. to apply the aluminium coating over the FOS, and Figure 2.17.b shows a microscopic cross-section of the metallic coated FOS embedded in aluminium, with which a good bond is shown. It is, however, reported that the commercial metallic coated optical fibre could withstand the spraying process for a few cms of length, but not for long lengths. To overcome this limitation it would be better to increase the metallic coating protection by encapsulating the optical fibre within a steel capillary tube or using a sapphire optical fibre for a safe longer length embedment.

Metal coating and embedding fibre optical sensors for industrial applications.
Chapter 2: Review of metallic coating and embedding of fibre optic sensors.

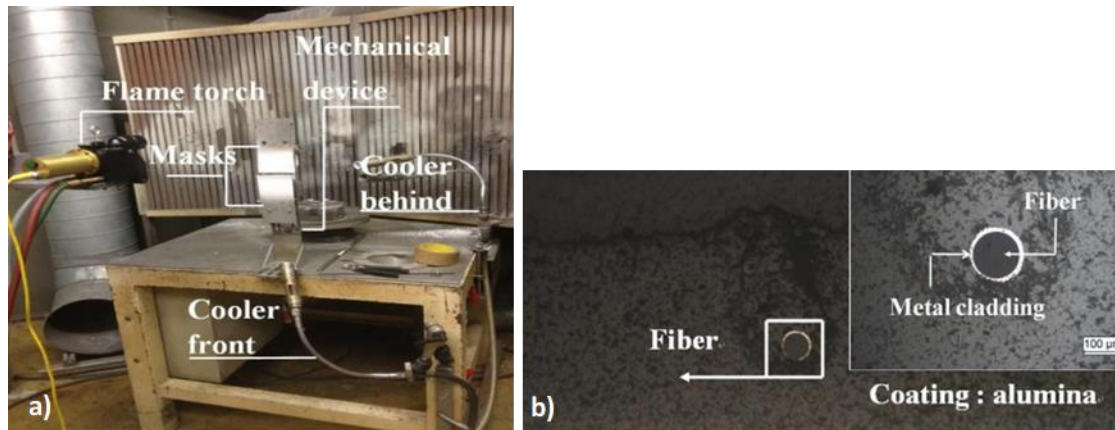


Figure 2.17: (a): Photograph of a flame spray setup. (b): Microscopic observation of the embedded optical fibre using the flame spray process [58].

The second embedding strategy is reported by researchers at North Dakota University. Over the last seven years they have published several papers [59]–[62] reporting different ways to embed FOS using an arc-spraying technique to monitor the corrosion distribution of steel pipes. They encapsulated the FO sensors in a hypodermic tube (the sensor section) and the rest of the optical fibre in a steel capillary tube. Then, they applied a high temperature adhesive on the encapsulated fibre and fixed it to a steel substrate to protect it from the spraying process. Finally, they applied thermal spray coating, of Al-Zn, over the glued and encapsulated fibre. Figure 2.18.a shows the FBGs embedded in the steel plates applying an adhesive based on stainless-steel, and Figure 2.18.b shows the HVOF thermal spray coating process during the Al-Zn application over the steel plates with the embedded FBGs. Sandlin et al. [65] used a similar strategy for embedding distributed FOS. They have embedded a commercial Cu coated optical fibre in a steel tube by spray coating of Ni20Cr. Before applying the spray, they glued the Cu coated optical fibre to the pipe by a ceramic adhesive to protect the fibre during the thermal spray coating process. In their work, only a maximum 3m is made possible due to the high attenuation of the embedded optical fibre.

In conclusion, this methodology is only valid for single-point FO sensors and could reduce the sensitivity of the sensors due to adhesive interference.

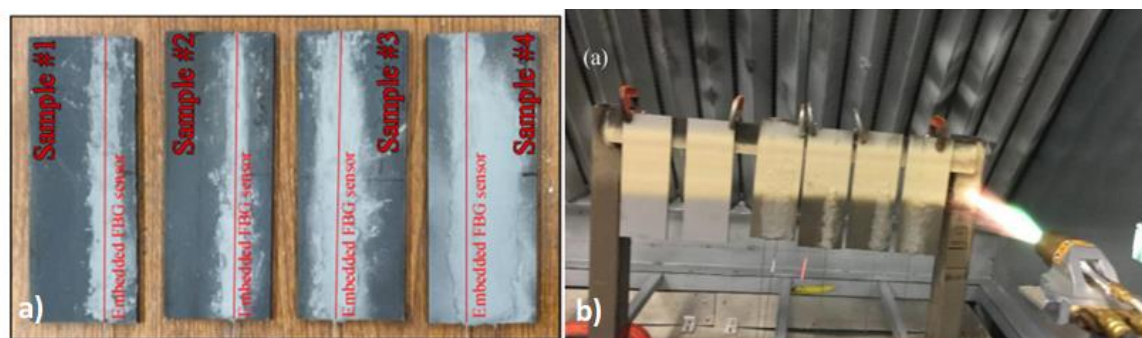


Figure 2.18: (a) Embedded FBGs in the steel plates by the metallic based adhesive. (b): HVOF thermal spray coating application on the steel plates with the embedded FBGs [61].

Lu et al. [64] recently published their work using a HVOF technique to spray zinc particles to embed optical fibres with standard and hard acrylate coatings onto a stainless-steel plate. They have demonstrated that it is possible to minimize the damage to the FOS by controlling the principal features of the spray process. They have selected pure zinc powders, with a low melting temperature of 420°C, to limit the heat energy acquired by the spray particles. The powder is of very small size (<30μm, diameter) and can be cooled down quickly before impacting the

Metal coating and embedding fibre optical sensors for industrial applications.

Chapter 2: Review of metallic coating and embedding of fibre optic sensors.

substrate. They have also applied a high scan speed for the spray to ensure a low deposition rate per area of substrate, allowing for rapid cooling. Figure 2.19.a shows the design of the embedded FOS by spray coating on the steel plate and the thermal response of it. Figure 2.19.b shows the real appearance of the standard polymeric coated FOS after being embedded by HVOF spray coating process.

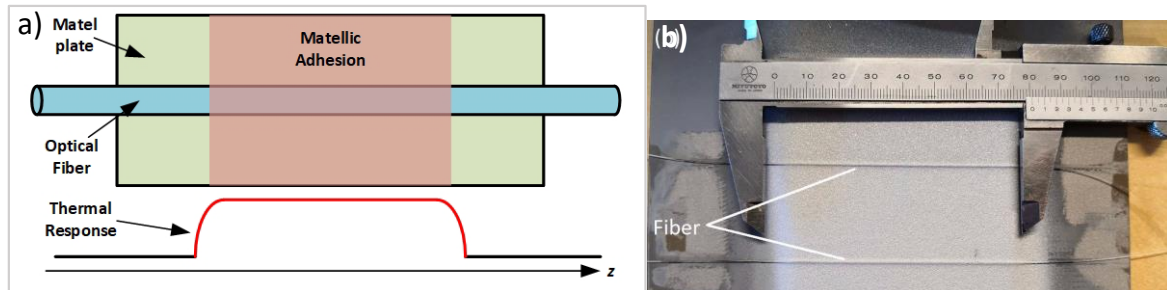


Figure 2.19: (a): Schedule of the FOS embedded by HVOF spray coating and the expected thermal response of the embedded FOS. (b): Picture of the polymeric coated FOS embedded in a steel plate by HVOF spray coating [64].

In conclusion the spray coating technique is useful for coating FOS with the metallic or ceramic materials. This technique is recommended to generate distributed or quasi-distributed corrosion monitoring systems for structures exposed to corrosive environments. In the case of the antifriction bearing use-case, applying this technique requires further development to enable the application of antifriction metal material onto the steel bearings and embedding the metal coated FOS during the embedding process. This technique will result in an increase in production time compared to the current techniques used (TIG welding, laser cladding, and casting), as well as a cost increase. Leaving aside the issue of developing and studying the feasibility of applying this technique.

2.2.2.4 Vacuum Brazing embedding technique.

Vacuum brazing is a joining process to join two or more parts of similar or dissimilar materials (metals or ceramics) by melting and flowing a filler material into the gaps between the parts by capillary action [66]. The process is carried out in a vacuum furnace with a clean atmosphere. The braze filler metal or ceramic must have a lower melting point than the adjoining parts and embedding is achieved by heating the joint to a temperature above the liquidus temperature of the filler, but below the solidus temperature of the parent materials. A strong joint can be achieved using this method. The main advantages of using vacuum brazing include achieving high integrity hermetic joints with minimal distortion.

Sandlin et al. [25], [65], [67], [68] reported to have embedded FBGs into a nickel alloy (Inconel 600) using vacuum brazing to generate resistant long-term FBGs for monitoring high service temperatures. In their earlier work, they placed commercial bare, Ni and Cu coated FBGs in a small groove machined in an Inconel piece. Then, they applied a silver-based brazing paste material and a nickel-based brazing foil, over the FBGs. The specimen was brazed using silver paste at a temperature of 900°C for 15 minutes and nickel-based foils at a brazing temperature of 1050°C for 15 to 25 minutes. After being embedded, the FBGs were subjected to long-term stability testing at high temperatures (68 hours at 600°C and six months of cyclic testing at 550°C). The authors report achieving good results with this method. Figure 2.20 shows the cross-section of the embedded Ni coated (a), Cu coated (b) and bare FBGs (c), respectively. The bare FBGs show cracks and pores around the fibre, this is because of the differences in thermal and mechanical properties between the metal and the silica. However, the metallic coated FBGs have shown good adherence to the metal brazing material, especially in the case of the FBGs coated with Ni. Therefore, the metallic coated FBGs are better to be embedded in a metallic structure by vacuum brazing technique. That is why in their work [25] Sandlin et al. have developed a new method for metal re-coating a Fabry-Perot FOS using a combination of

Metal coating and embedding fibre optical sensors for industrial applications.

Chapter 2: Review of metallic coating and embedding of fibre optic sensors.

electroless Ag and electroplating of Ni. It was necessary for them to develop this coating methodology because the Ni coated optical fibre used in their previous work was purchased from a company that does not exist anymore.

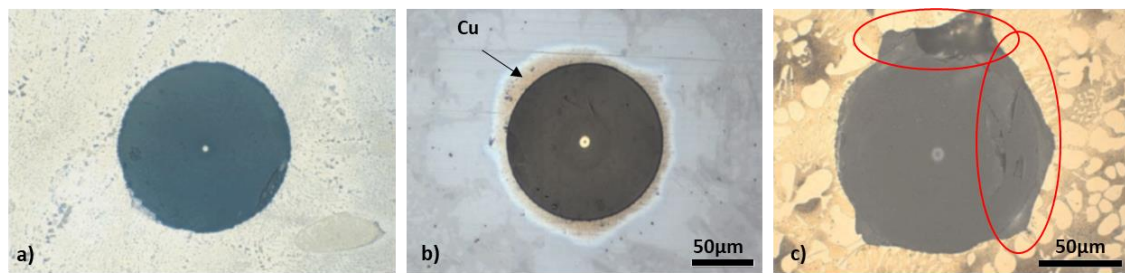


Figure 2.20: Fibre embedded in a nickel-based brazing alloy with light coming out from the core of the fibres. (a): nickel-coated. (b): copper-coated single mode. (c): Bare fibre embedded, the brazing alloy is not in tight contact with the fibre. This surface was etched to show the microstructure [65].

Mathew et al. [67] combine vacuum brazing and SLM (Selective Laser Melting) techniques to embed a Fabry-Perot (FP) FOS in a SS316 piece. The FP sensor is packaged in a metallic coated capillary tube (with an external diameter of 315µm), then, the capillary tube is positioned in a groove made in the SS316 piece. The Ni-Cr-Si-B-Fe filler metal powder is placed on an end-face of the capillary tube and vacuum brazing is used to bond the capillary tube to the SS base material. Finally, the FP sensor is completely embedded by adding more SS316 material over the brazing material using SLM. In this case, the vacuum brazing process is used to improve the bond, and avoid the appearance of pores, between the FP-capillary tube and the SS316 material deposited by SLM. Figure 2.21.a shows the cross-section of a FP sensor packaged in the coated capillary tube, embedded directly using SLM. Figure 2.21.b shows a cross-section of the FP sensor packaged in the coated capillary tube, embedded by a combination of vacuum brazing of Ni and SLM of SS316. It is clear that the combination of vacuum brazing and SLM gives a better bond for embedding the FOS [67].

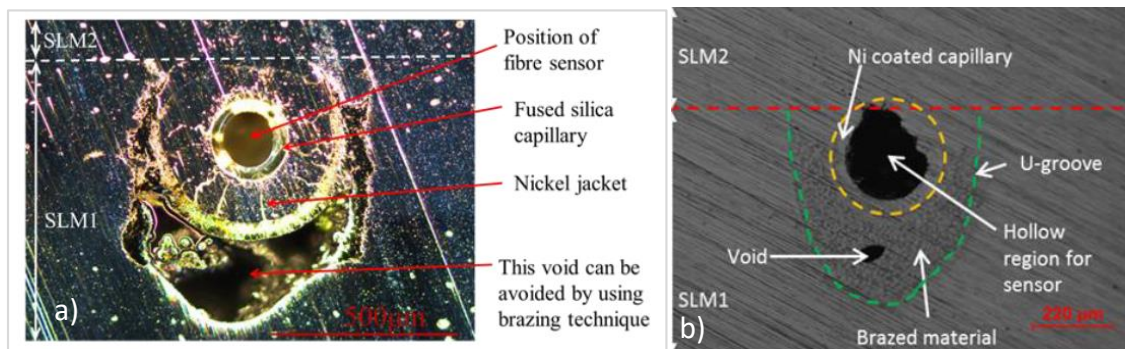


Figure 2.21: (a): Cross-section of coated capillary embedded in stainless steel test component by SLM. (b) Cross-section of coated capillary brazed into the stainless steel test component. The capillary is damaged during the second SLM process [67].

In conclusion, this technique offers the possibility to apply multiple metals for embedding the FOS, achieving high-quality embeddings. However, on the other hand, this technique requires expensive equipment (over €100,000) and has limitations in terms of the size and geometry of the components where the FOS will be embedded. In the case of antifriction bearings, this technique may only be viable for embedding FOS in small-sized bearings, which results in a significant increase in costs. It must also be used in conjunction with existing antifriction material deposition techniques to achieve the required antifriction layer thickness.

2.2.2.5 Ultrasonic additive manufacturing embedding technique.

The ultrasonic additive manufacturing (UAM) embedding technique, together with Laser-based embedding techniques, are the most used for embedding FOS in metallic structures. In this review it is only possible to include a few of the many reported techniques [51], [69]–[77]. UAM is a suitable technique for embedding fibre optics because it allows fibres to be embedded in metals without melting and without the use of epoxy. UAM is a three-dimensional (3D) printing technology which uses ultrasonic energy to produce metallurgical bonds between layers of metal foils near room temperature and enables the FOS integration during the UAM process. Despite the fact that the UAM can be used for many metals, such as stainless steel and Ni [77] or Cu [70], the most used is the Al, because of their thermal and mechanical properties, for ease of consolidation by UAM process [69]–[76], [78]. Fabrisonic [79] has patented a UAM procedure to embed FOS in reference [80]. Figure 2.22.a shows the UAM system developed by Fabrisonic the ultrasonic consolidation and, Figure 2.22.b and Figure 2.22.c shows the two high power ultrasonic transducers actuating the weld tooling, commonly called the sonotrode.

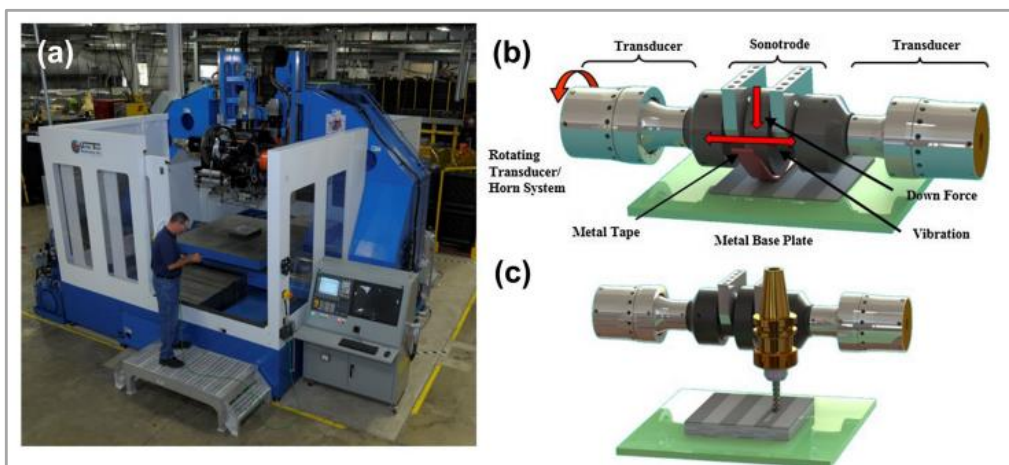


Figure 2.22: UAM process: (a) Fabrisonic SonicLayerTM 7200; (b) additive or ultrasonic welding stage of the process; (c) subtractive or machining stage of the process [72].

The procedure to embed FOS using the UAM process is detailed as follows. First, the FOS is placed between foils before being consolidated using a sonotrode. Figure 2.23.a shows the UAM embedding method used by Kong et al. [78] where the FOS is placed in between the Al foils to be bonded, while, Figure 2.23.b shows the method used by Hyer et al. [77], where Al foils were consolidated by UAM, leaving a groove for the FOS to be placed and embedded.

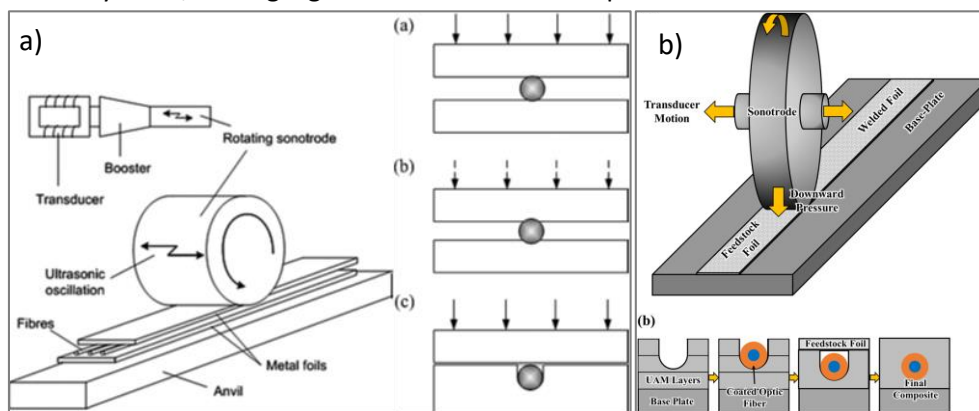


Figure 2.23: (a) Schematic diagram of the ultrasonic consolidation of fibre embedded aluminium structures. Embedding methods: (a) full load, (b) partial load, and (c) no load, respectively, on fibre [78]. (b): Schematic representations of the (a) UAM process and (b) fibre embedding steps (section view), which include building a few layers of material on the baseplate, machining a channel, laying the fibre optic in the channel, and layering foils on top to embed the fibre [77].

In addition to the strategy for embedding the sensors, the scientific community is divided on whether it is better to use metal coated fibre optic sensors [69], [70], [74], [77], [80] or sensors with standard polymer coatings [72], [73], [75], [77], [78] for embedding a FOS using the UAM technique. Li et al. [70], Hehr et al. [72] and Hyer et al. [77] have included, in their respective work, a comparative study between metallic coated and polymeric coated FOS embedded using UAM in Al, Cu, SS and Ni. They claim to have obtained better results from the metallic coated FOS embedded than the polymeric coated, especially in the case of using embedding metals different from Al.

In conclusion the UAM technique shows great potential for embedding FOS into different metal structures, generating smart pieces able to be monitored in real time. It is also a suitable technique to bond FOS in structures exposed to harsh environments, despite its limitation to allow embedding FOS in complex geometries and it has a relatively high cost.

2.2.2.6 Laser-based embedding technique.

The laser-based technique is probably the most widely used technique for embedding FOS in metals. There is a multitude of different laser technologies which can be selected or adapted to meeting the requirement, geometry, material, application, etc. Furthermore, laser-based technologies allow a high degree of control over the parameters used to melt or deposit the bonding material, which minimizes the damage to the fibre. The materials used can be diverse and in different formats (powder, wire, etc.). Laser manufacturing enables integrating metallic-coated FOS during the production of tooling and structural components. The Laser-based embedding technique, however, usually requires costly equipment and skilled operators.

There are three representative research groups, who have developed and matured laser-based embedding procedures to embed a FOS in metallic structure.

The first group used laser technology for embedding FOS as reported by Li et al. [16], [81], [82]. They were the pioneers not only in the development of a metallic coating for fibre optics, but also in embedding FOS using a laser technique. After the completion of metallic coating of the optical fibre by sputtering and bonding to a steel substrate by electroplating deposition as discussed in section 2.2.1 and shown in Figure 2.9, they used Shape Deposition Manufacturing (SDM), based on a Laser Cladding process to embed the FOS in the internal structure of a rotating tool, simulating the blades in gas turbine engines, for self-monitoring. Figure 2.24.a shows the SDM manufacturing process developed to embed the electroplated and bonded metallic coated FBGs in the rotating tool structure. They machined a groove in the first part of a rotating tool for easy bonding with the metallic coated FBGs. The rest of the rotating tool is finished by laser Cladding to complete the embedding of the FBGs. Figure 2.24.b shows the final appearance of the smart rotating tool with the FBGs embedded in it.

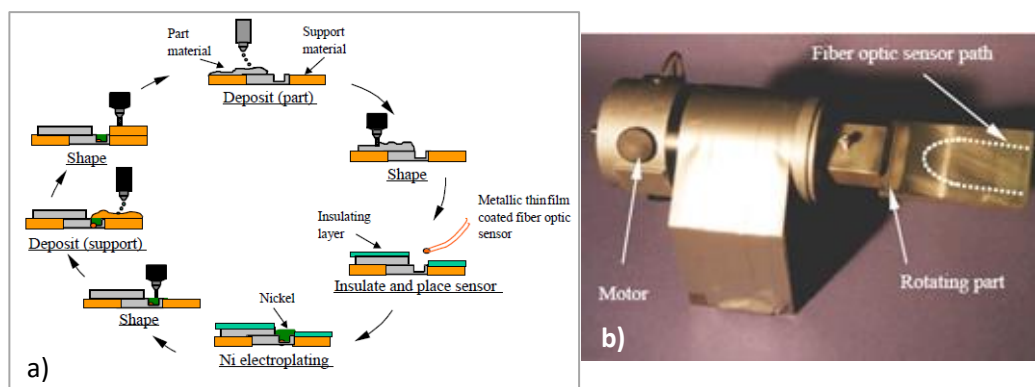


Figure 2.24: (a): Shape Deposition Manufacturing cycle for embedding fibre optic sensors. (b): Rotating part with embedded fibre optic sensor [16].

The work from the second group was reported by Alemohammad et al. [19], [20], [83], [84]. In addition to the development of a novel metallic coating technique based on the Ag nanoparticles sintering deposition by Laser-Assisted Maskless Micro-deposition (LAMM), as explained above, the group have developed two techniques based on a combination of Electroplating or Casting followed by laser solid freeform fabrication (LSFF) process to deposit layers of tungsten carbide-cobalt (WC-Co) on a steel base, to develop a smart cutting tool with the FOS (FBGs) embedded.

The embedding procedure was based on the combination of casting and LSFF. Figure 2.25.a shows the step-by-step procedure. First, the optical fibre with FBGs was placed in a block of steel within a machined channel. Then an alloy of tin-lead (Sn-Pb, melting point of 185°C) was cast around the fibre. To compensate the effect of residual thermal stresses on the optical response of the FBG, a constant tensile stress of 80 MPa was applied on the optical fibre during the embedding process. Finally, the embedding process was completed by LSFF of WC-Co layers. Figure 2.25.b shows the appearance of the final prototype made using the FBGs embedded in the metallic structure.

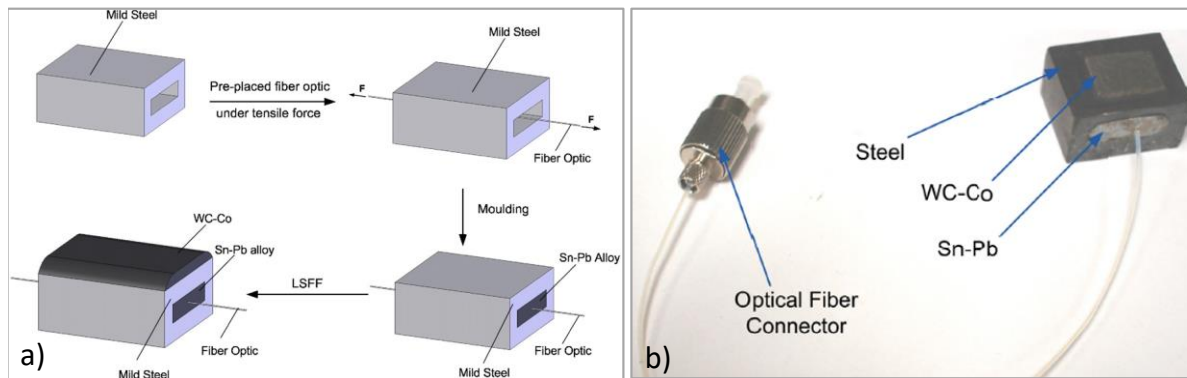


Figure 2.25: (a): Step by step of the casting and LSFF embedding procedure [19]. (b): Final appearance of the prototype sample with the FBGs embedded [83].

The second approach reported by the same group involves a combination of Ni electroplating deposition and LAMM. The schedule of the manufacturing process is shown in Figure 2.26.a. The Ag coated FOS is placed in a groove machined in a steel base structure, and then the Ag coated FBGs is bonded to the steel structure using electroplating of Ni. Before electroplating, the recipient surfaces were polished, and the surfaces that did not need nickel plating were covered by Kapton tape. The electroplating process takes 14-16h, resulting in a plated nickel layer with a thickness of 230 μm . To complete the manufacture of the smart cutting tool with the embedded FBGs, a layer of WC-Co material was deposited over the steel part by LSFF process. Figure 2.26.b shows the final appearance of the prototype sample with the embedded FBGs.

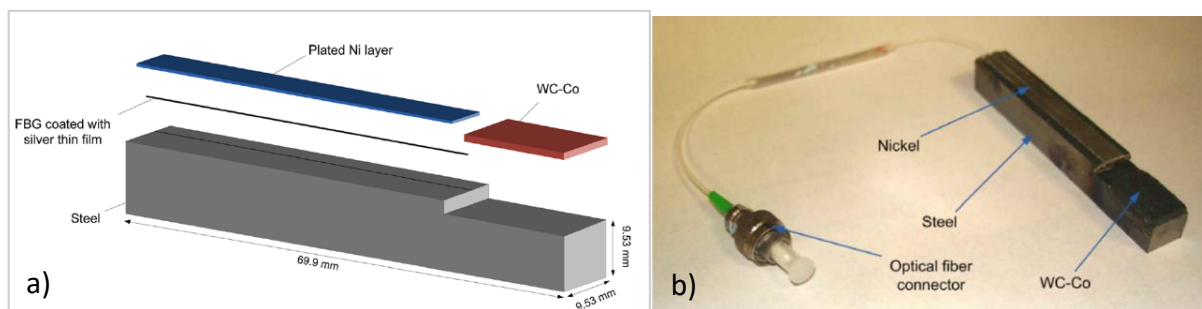


Figure 2.26: (a): Schematic cross section of the sample with embedded FBGs [84]. (b): Final appearance of the prototype sample with the FBGs embedded manufactured by electroplating and LSFF [83].

Metal coating and embedding fibre optical sensors for industrial applications.

Chapter 2: Review of metallic coating and embedding of fibre optic sensors.

The work from the third group was reported by Mathew et al. [85]–[91]. They have developed a procedure based on Selective Laser Melting (SLM) or a combination of SLM and Laser Metal Deposition (LMD) processes, to deposit new materials and to embed FOS to monitor the strain and temperature during the laser additive manufacturing processes.

They used metallic FBGs or in the case of the FP sensors, they encapsulate them in a metallic capillary tube [88]. The procedure they used to embed the FBG or FP sensor using SLM manufacturing of SS316 is described as follows. As shown in Figure 2.27.a, a metallic coated FOS is placed in a machined groove before being embedded by SLM or a combination of SLM and LMD. Figure 2.27 shows the SLM embedding procedure as well as the air gaps under the embedded FOS. These gaps could cause a loss of strain transmission and possible detachment from the bonding material, when the piece is subject to thermal or mechanical fatigue. Therefore, they tested different strategies to improve the bond using different geometries of grooves, adjusting the size of the groove to the diameter of the fibre or of the encapsulating tube, so that no gaps are left. In addition, they have tested different laser embedding directions or laser polishing to improve the surface of the piece and the bond of the FOS. They have obtained the best result creating ridges on top of the SLM-base part at either side of the U-groove to prevent brazing material from flowing out of the cavity during brazing process. These ridges are cut down to restart the SLM and complete the FOS embedding process.

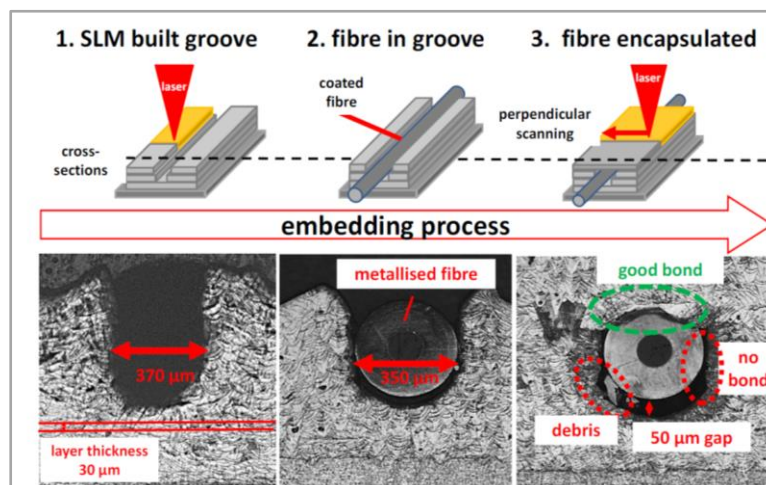


Figure 2.27: Schematic illustration of the embedding process with cross-sectional analyses of the individual steps [88].

In addition to these three research groups, there are other researchers and FOS companies working on the FOS embedding into metallic structures using laser technologies for developing smart components or structures or for monitoring the laser additive manufacturing process. Zou et al. [92] have embedded a metallic coated distributed optical fibre by laser to monitor the residual strains of the additive laser manufacturing process. They have used a commercial Cu coated optical fibre, to which a Ni coating has been applied by electroplating to increase its coating thickness and make it more resistant to the laser process. Then, they have been placed in a groove, made during the laser process manufacturing, and finally, the Cu-Ni re-coated optical fibre has been embedded into an Inconel power alloy by the Laser Engineered Net Shaping (LENS®). The embedded re-coated optical fibre was used as a distributed FOS and monitored using Rayleigh scattering Optical Frequency Domain Reflectometer (OFDR) to capture the strain and temperature variation during the LENS manufacturing process. The work from Hehr et al. [73] is also oriented towards this objective. They have embedded a distributed fibre optic sensor in an Al base-plate by UAM, to monitor the Laser-Powder Bed Fusion (L-PBF) process made over this Al plate by printing problematic components using AlSi10Mg powder.

Metal coating and embedding fibre optical sensors for industrial applications.

Chapter 2: Review of metallic coating and embedding of fibre optic sensors.

The embedded FOS provided information on delamination initiation and growth during the L-PBF print at the lower layers, while external-based indicators showed no defects.

In addition to monitoring the process, the laser embedded FOS are able to generate smart components. Kim et al. [93] has demonstrated the manufacturing of a smart mini turbine blade by Direct Laser Deposition (DED) with an embedded FBGs for high temperature monitoring. They have used of a Cr-Ni re-coated optical fibre manufactured by a combination of sputtering (Cr and Ni) and electroplating of Ni processes. Then, they have located the Cr-Ni coated FBGs in a groove and apply DED of Inconel 718 to complete the FOS embedding.

Figure 2.28.a shows the design of the smart miniature blade with the strategy to embed the Cr-Ni coated FBGs and Figure 2.28.b shows the final appearance of the miniature blade prototype manufactured and tested up to 500°C.

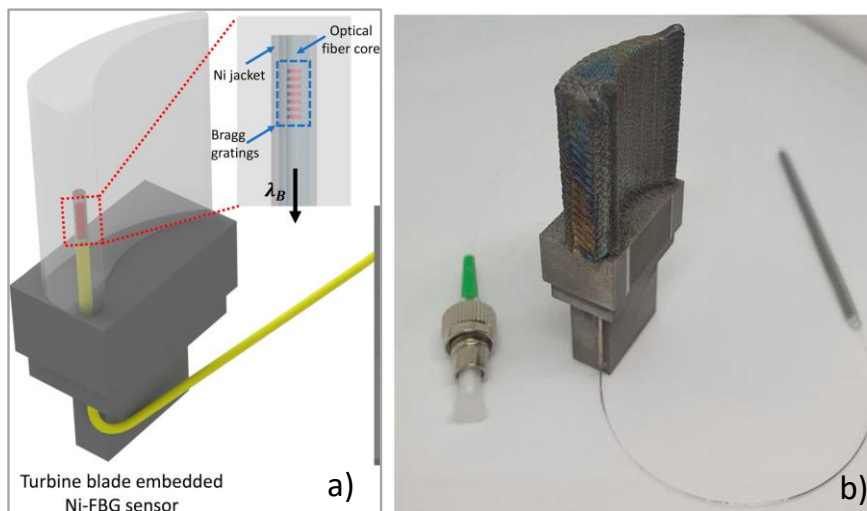


Figure 2.28: (a) Schematic of turbine blade with an embedded Ni-FBG sensor fabricated by DED printing for high-temperature monitoring. (b): Photograph of a fully DED-printed miniature turbine blade with an embedded Ni-FBG sensor for high-temperature monitoring [93].

In light of the above, it can be concluded that the laser process offers a multitude of possibilities to embed FOS in a myriad of different processes, using a myriad of materials and flexibility when working on complex geometries or large workpieces. In addition, its high precision guarantees the repeatability of the process and ensures the correct embedding of the FOS. The FOS embedding could be used to monitor and feed the process manufacturing modelling, as well as to generate smart pieces to be monitored in real-time during operation. Due to these advantages, this technique was one of the focuses of the embedding work carried out in this thesis. Laser cladding was studied for embedding metallic coated FOS in antifriction bearings, as well as for embedding FOS in other metals with a higher melting point, such as Inconel. This work is detailed in Chapter 4.

To finalize the FOS embedding review, one last work needs to be mentioned, which uses an embedding technique that had not been used previously, Wire and Arc Additive Manufacturing (WAAM) or even a combination of WAAM and Atmospheric Plasma Powder Deposition (APPD). This technique was used recently by the partners of the MULTI-FUN project [94]. They have embedded metallic coated distributed FOS to monitor strain and temperature of critical components, providing data for Structural Health Monitoring (SHM). They are looking for a new predictive maintenance strategies lowering the safety margins, reducing the part's weight and reducing maintenance costs.

2.3 Summary

In this chapter a comprehensive review of the FOS coating and embedding technologies is presented, coupled with their corresponding response in harsh environments, especially for high temperatures $>350^{\circ}\text{C}$. It is clear that the moisture ingress and hydrogen penetration in the silica degrade the FOS silica, and the process is accelerated when the fibre is exposed to high temperatures. It is therefore necessary to apply a coating on the silica FOSs to make them hermetically sealed and avoid the hydrogen penetration. The coatings most used are metallic, because of their mechanical and thermal properties, which also makes the FOS more robust for use in harsh environments.

In this chapter the most common techniques used to apply a metallic coating layer over the silica optical fibre were reviewed and discussed. Among the coating techniques reported, the Electroplating Deposition technique stands out as the most widely used. This technique can only be applied on electrically conductive substrates, therefore it must be applied after a preliminary thin film coating process is completed. Electroless and Sputtering deposition are considered to be the most widely deployed techniques for metallic coating.

The metallic FOSs can be directly embedded in metallic structures by casting or welding, because the metallic coating acts as a protection during the embedding process. In this way, it is possible to be able to monitor strain, in addition to temperature, to assess the status of the metallic structure. In this chapter, a review of techniques for embedding FOS in metallic structures is given. The most used techniques are UAM, specially for Al structures, and laser techniques, for high temperature melted materials. However, as outlined in this review each technique has advantages and disadvantages in terms of cost, piece size or complex geometry, material application, precision, final embedding quality, etc. Therefore, no single technique fits all applications.

After conducting this review and taking into account the requirements of each use case defined in this thesis, some of the review FOS coating and embedding techniques were selected for further study to develop the most suitable metal coating and embedding procedure for each use case. For FOS coating, techniques such as PVD, sputtering, electroless, and electroplating, among others, were chosen. Meanwhile, for sensor embedding, techniques such as laser cladding, TIG welding, or casting, among others, were explored.

Chapter 3. Metallic coating of Fibre Optic Sensors and their characterization.

As explained in Chapter 2, optical fibres have shown a high level of resistance to harsh environments, but need hermetic protection, e.g. at high temperatures ($>350^{\circ}\text{C}$), from hydrogen penetration or diffusion which weakens the optical fibre even to the point of failure. One of the solutions to protect the optical fibre from H_2 penetration is to coat the optical fibre with a thin metal layer. This also enhances the resistance of the optical fibre to high temperatures and increases its thermal sensitivity.

Optical fibres are made of silicon oxide (SiO_2), which is a dielectric material, and the coating techniques used for coating in this investigation are primarily focused on thin metallic films. In this chapter, some of the most popular coating techniques, used for optical fibres, are further studied to optimise the coating of optical fibre sensors with different metals. This study was made to select and modify an existing coating process, previously designed for the electroplating deposition (explained below). It is of critical importance not just to consider the quality of the final coating film, but also other key factors, such as cost, simplicity of the process, coating speed, maximum coating length, preparation of the fibre, material deposition flexibility, etc.

The key objective of this chapter is to develop a standardised procedure, allowing for effective coating of an optical fibre (more specifically inscribed with FBGs), using an electroplating deposition technique, forming a metallic layer thick enough to withstand harsh environments (high temperature, corrosion and embedding processes based on welding techniques). The coating procedure will be based on the same principle as represented in Figure 3.1, focused on metallic coating of FBGs. On the one hand, it will be based on FBGs inscribed using a fs laser, with a typical polymeric coating, which is to be removed in the FBG section, as Figure 3.1.a shows. On the other hand, a metallic coated optical fibre will be cut and the metallic coating will be removed from the extremes of the fibre, as depicted Figure 3.1.b. In this figure, the metal coated fibre is represented as a Cu coated fibre, because Cu has a high melting point and this fibre is relatively affordable in terms of cost. Then, the FBG section (without the polymeric coating) is spliced to the Cu coated fibre, and the FBG section is coated with a metal by one of the metallic coating techniques that are presented in the first section of this chapter. The optimum technique to coat the FBGs is selected after having evaluated the advantages and disadvantages of each of the coating techniques tested. Finally, a Ni or Cu coating layer is applied, by electroplating deposition, to strengthen and increase the thickness of the fibre, as Figure 3.1.c depicts. Figure 3.1.d shows the fibre cross-section for each one of the coating steps.

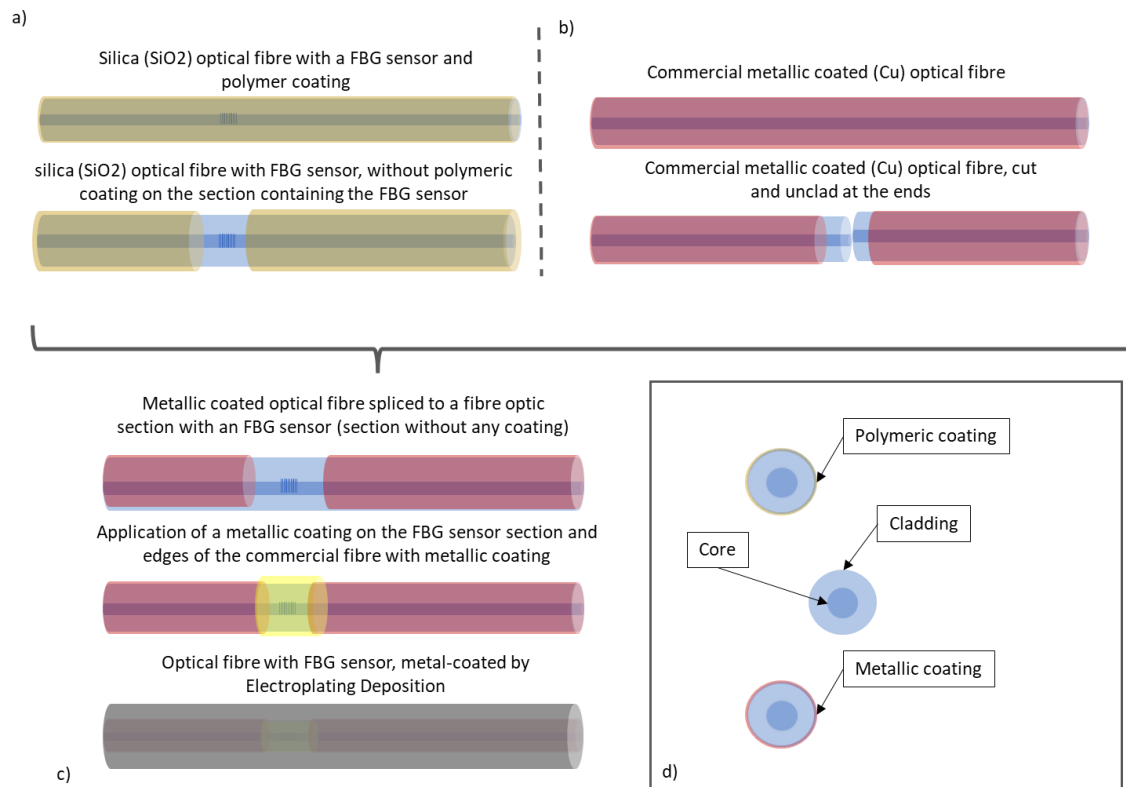


Figure 3.1: Diagram of the key objective of this chapter: a procedure for metallic coating FBGs. (a) standard FBGs with the polymeric protection removed. (b): metal coated fibre cut and with the metal removed from the extremes. (c) FBGs spliced to the metal coated fibre with a metallic coating thin layer on the FBGs section and a metallic coating layer on the whole fibre. (d) cross-section of the fibres for each coating step.

From the state of the art review, it was concluded that the most popular technique to apply thicker metallic coating layers with several metals is the electroplating deposition process. It is only possible to use this technique for applications on electrically conductive materials. FBGs must be coated using the electroplating deposition process to obtain a thick metallic coating, able to withstand high temperatures and the embedding process, a primary metallic coating layer must be applied on the silica fibre. As there are many different thin coating layer techniques to make this, in this chapter, five different coating techniques are studied to determine the more suitable one to apply the conductive layer prior to electroplating coating. In addition, for each studied technique, a simple characterization was made based on their respective microscopic, optical and/or thermal properties.

3.1 Coating techniques for generating a conductive layer

3.1.1 Electroless Ni deposition

The first thin metallic film coating layer studied was electroless Ni plating. This technique is based on an autocatalytic reaction that does not require a specific machine, anodes, electrical current or power supply to deposit metallic layers on non-metallic substrates. The process consists in several *layer by layer* steps to achieve a thorough clean, activation and sensitisation of the optical fibre surface, and to finally immerse it in an autocatalytic dissolution based on a metallic salt to generate a coating thin layer on the optical fibre surface of a few microns. The electroless plating deposition process is a relatively simple process but very strict in terms of following the defined process step by step. It is also very sensitive to contaminations that may

occur during the process and with little tolerance in its application parameters. It is essential to adhere to the times of each step, and carefully monitor the required temperature and pH.

The principal elements for the electroless plating process are a metal source, in this case Ni sulphate, a reducing agent that provides the electrons necessary for the reduction of the metal. It also requires an energy source (heat), complexing agents that control the free metal available for reaction, a buffering agent to withstand pH changes caused by hydrogen generation during deposition, an accelerator to increase the speed of the reaction and an inhibitor to control it and other reaction by products [95].

The purpose of the activation process is to generate a thin catalytic surface on the optical fibre surface, to reduce the metal palladium by sensitizing the surface adsorption, thus forming a palladium catalytic centre.

The process used in this section was inspired by the reported work from Shen et al. [27], Shiue et al. [21] and Pinto et al. [96]. The methodology and components for each dissolution involved are explained below and represented in Figure 3.2. It has the following steps:

1. Optical fibre cleaning:
 - Removal of the polymer coating.
 - Rinse the optical fibre with deionized water or acetone.
 - Clean and degrease the optical fibre by immersing it in a Sodium hydroxide solution (NaOH 15%) dissolved in deionized water for 20 min at 20-25°C.
 - Rinse the optical fibre with deionized water in an ultrasound bath for 10 min at 20-25°C.
 - Immerse the optical fibre in a solution of V(HF):V(H₂O):V(HNO₃)=2:1:1, HF concentration 40%, for 10 min at 20-25°C.
 - Rinse the optical fibre with deionized water in ultrasound bath for 15 min at 20-25°C.
 - Dry the optical fibre using compressed air or heat (120°C for 20 min.)

2. Sensitization and activation process:
 - Sensitization: Immerse the optical fibre in a bath composed of 3g/l de SnCl₂ and deionized water for 30 min. at 20-25°C.
 - Rinse the optical fibre with deionized water.
 - Activation: Immerse the optical fibre in a bath composed of 1g/l de PdCl₂ and deionized water for 30 min. at 20-25°C.
 - Rinse the optical fibre with deionized water.

3. Electroless plating process:

The activated optical fibre should be immersed for a few minutes in the Ni plating bath (composition described below), which needs to be at 87°C and have a pH of 4.8.

Ni bath composition:

 - 6.4 g NiSO₄·6H₂O
 - 5 g NaH₂PO₂·H₂O
 - 2.63 ml lactic acid (85%)
 - 2.5 g H₃BO₃
 - 0.2 g NaF
 - Ammonia solution (28% concentration) for adjusting the pH to 4.8.

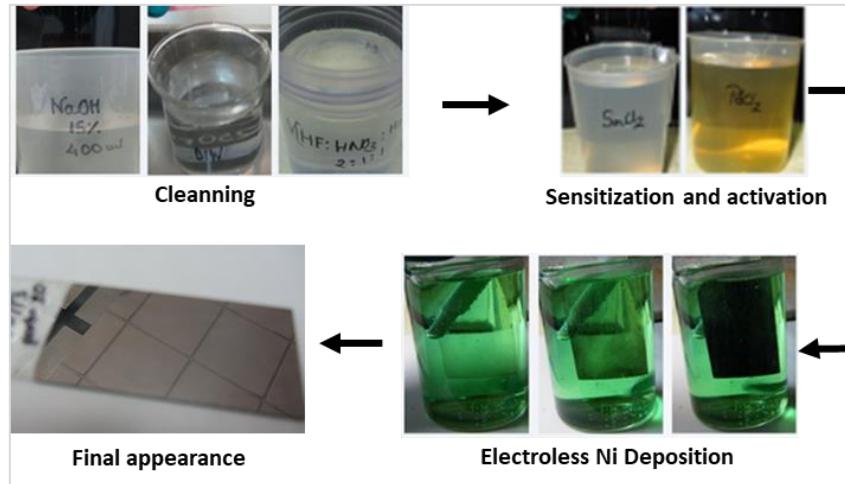


Figure 3.2: Electroless Ni deposition process step by step.

To optimize the Ni electroless deposition process, for the first test, silica slides were used. The tests were carried out through combination of optimised parameters and conditions, aiming to obtain a high quality Ni coated layer on the slides: homogeneous, bright and with good adhesion. Table 3.1 summarises the results obtained from this study. Although the Ni electroless step-by-step deposition process is well defined, more tests varying immersion time (from 10s to 1 min.), temperature (85 - 90°C) and pH (8.5 - 9) were necessary to obtain the appropriate process parameters until the required coating quality and adhesion were achieved.

Picture	Time (min.)	T (°C)	Events	Cause
	15	87	Non homogeneous coating, It shows flaking and por appearance	No well rinsed from PdCl ₂ to the bath inmersión, high pH (5.05) and insuficient slide cleaning.
	1.5	87	Uncoated sections and “ripple” appearance	The time is less than the above care.
	10	50-87	Non homogeneous coating layer, flaking appearance	No constant temperature
	4	87	Ripples in the lower part of the deposition slide,	Too much time immersed in the solution
	3	85-86	Matte color and sections without Ni deposition material	One of the SnCl ₂ and/or PdCl ₂ solutions is depleted and the pH is low.
	2	90	Matte color and sections without Ni deposition material	Ni bath depleted, high temperature
	2	88	Watermarks on the Ni coating layer	Insuficient drying process
	5	87-89	Good appearance and bond	No comments

Table 3.1: Summary of the slides coating tests for the optimization of Ni electroless plating deposition process.

It was found that the outcome is largely determined by how well the process is implemented and minor variations in the process or in the state of the solutions can cause severe defects in the final coating layer.

The best conditions to obtain the required results are the use of all solution new and fresh, an exhaustive clean and dry process, with the Ni bath set at a temperature between 87-89°C with a pH of 4.8 (Figure 3.2).

The metallic coating layer bonding test was made through pulling using a tape, which adheres to the thin coated layer surface. If the coating material is not peeled off when the tape is removed immediately with a sharp jerk its bond is good.

The Ni electroless deposition process, optimised through the use of glass slides, was subsequently applied to (glass) optical fibres (single-mode with a diameter of 125µm) and Figure 3.3.a shows the experimental set-up. The total length of an optical fibre coated was around 250mm as this is the maximum length of the measuring cylinder, which was used for the optical fibre plating process. The resulting thickness of the Ni coating layer, which depends on the immersion time, was between 2µm to 5µm. Figure 3.3.b shows a sample of a Ni coated optical fibre by electroless technique with a final diameter of 132µm which represents a Ni coating layer of 3.5µm.

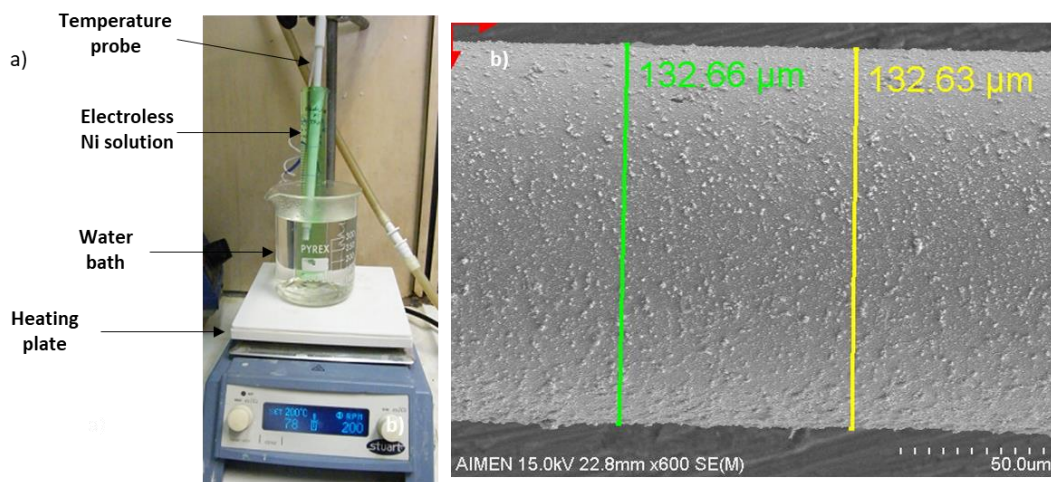


Figure 3.3: (a): Electroless Ni deposition set-up for coating optical fibre. (b): Ni coating layer, SEM picture.

Figure 3.4 shows some further SEM images of the Ni coating layer applied on the optical fibres. As observed, the final appearance of the coating Ni layer is very variable, despite the fact that, they were manufactured under the same procedure, parameters and conditions. Figure 3.4.a exhibits the Ni coated fiber with the highest quality coating obtained, as it doesn't present any kind of defect, although, some *grains* appear on the fibre surface. For the rest of pictures presented in Figure 3.4, it is clear that there show some major defects. Figure 3.4.b and Figure 3.4.d show cracks and adherence faults. Figure 3.4.c shows many accumulations of Ni material forming *clusters* generating a non-uniform coating layer, which is likely to cause major problems or defects when a second deposition process would be applied to increase the coating thickness on the surface of this fibre.

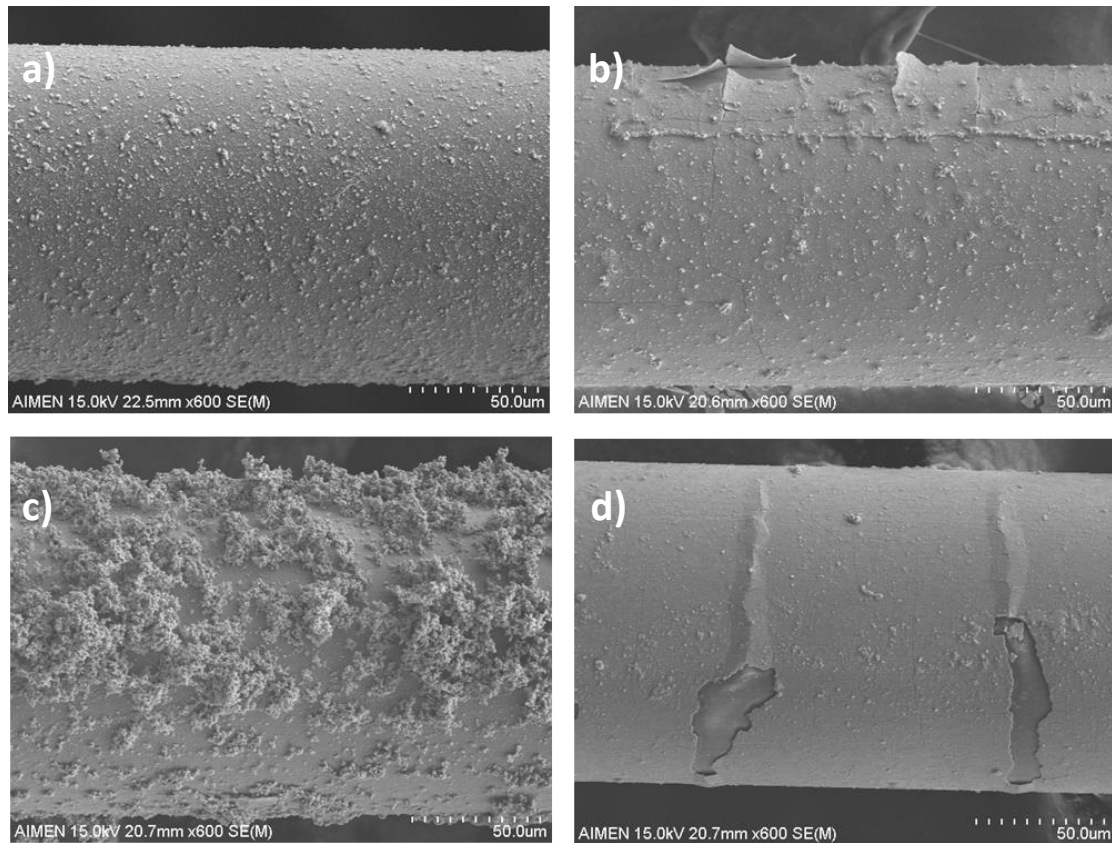


Figure 3.4: SEM images of the Ni coating layer made on the optical fibres by electroless deposition. (a) Ni coating fibre with grains on the surface. (b) Ni coating layer with adherence faults. (c) Ni coating layer with accumulations of Ni material forming clusters generating a non-uniform coating layer, (d) Ni coating layer presenting cracks and poor adhesion to the fibre.

After analysing different parameters involved in the electroless process, it was concluded that the defects in the Ni coating were mostly due to contamination produced during the tedious electroless process. The set-up developed for the electroless process was carried out in a common laboratory, not in a cleanroom. In addition, the ultrasonic cleaning and drying processes were carried out in another room, so no matter what level of care was undertaken with handling and transport of the samples, there exists an increased likelihood of contamination.

In conclusion, the Ni electroless plating process for coating optical fibre is a low-cost and effective process, as long as the process are well controlled and carried out in a cleanroom. However, it is not straightforward to achieve a high-quality coating layer, especially over long fibre lengths. Therefore, this technique was ruled out for inclusion in the coating procedure that was developed, as a preliminary step before electroplating.

3.1.2 Physical Vapor deposition of Ag, Au and Cr

Physical vapour deposition (PVD) is a vacuum coating processes in which material is physically removed from a source by evaporation, transported through a vacuum or partial vacuum by the energy of the vapour particles, and condensed as a film on the surfaces of appropriately placed parts or substrates.

Two different cathodic arc deposition machines were used to coat the optical fibres with Ag, Au and Cr. One of the PVD machines used was the Balzer BAE 250 system (Figure 3.5.a) and the second was in house developed equipment (Figure 3.6.a) developed by the quantum materials

Metal coating and embedding fibre optical sensors for industrial applications.
Chapter 3: Metallic coating of Fibre Optic Sensors and their characterization.

and photonics group of the Universidade de Santiago de Compostela (USC), where these coating trials were carried out. The PVD equipment was used to achieve a thickness of approximately 1 μm for Ag, Au, and Cr, as they were the metals available with good compatibility to bond with silica in the case of Ag and Au, and/or due to their high melting points, for Au and Cr. The thickness was monitored in real time by means of ultrasonic piezoelectric transducer on the top of the vacuum chamber. A shift of the resonance frequency of the piezoelectric transducer is directly related with the thickness of silver deposited on substrate [97].

An optical fibre was attached at one of its ends on the rotor cover (Figure 3.5.b and Figure 3.6.b); meanwhile the other end was free, thus fibre is disposed vertically in the vacuum chamber. The rotor applies a rotation during the process assuring homogenous deposition across whole length of the fibres. The fibres with sensors were glued to the holder and the rest of the optical fibres were rolled on themselves. To ensure a homogeneous coating over the entire surface of the fibres which were attached to the lid, once a deposition was finished, the fibre segments were flipped over and the process was repeated. Figure 3.5.c and Figure 3.6.c show the final appearance of the coated fibres attached to the top of the chamber.

In the first case (Balzer, Ag coating) several single-mode (SM) optical fibres and some FBGs, having had the acrylate coating removed by a mechanical stripper, were fixed to the top cover, as shown in Figure 3.5.b. For the Au and Cr coating trials, the home-made PVD system was used. Additionally, some Cu commercial coated optical fibre segments with a FBG sensor spliced in the centre of the fibre were also included.

This process is very sensitive to any contamination or dirt on the optical fibre surface, therefore, the surface of all fibres were thoroughly cleaned with acetone prior to coating.

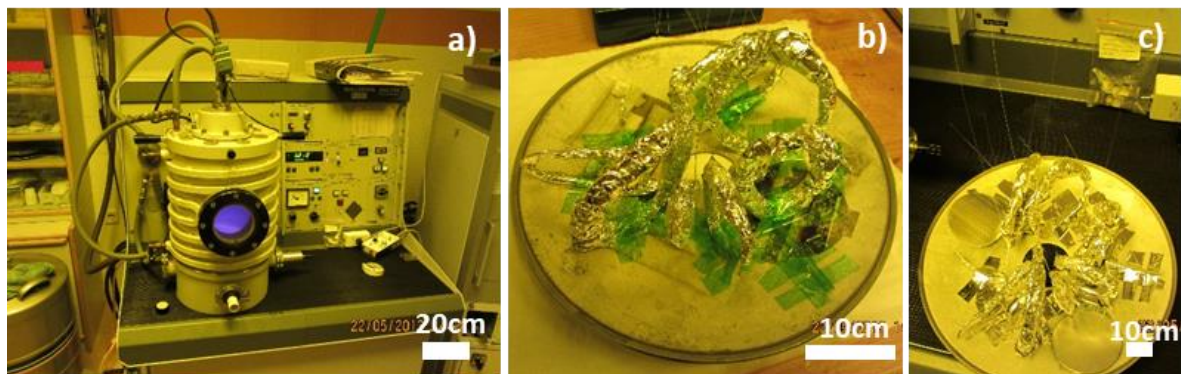


Figure 3.5: (a): PVD Balzer BAE 250 machine. (b): Optical fibres set-up to be coated in the PVD camera. (c): Optical fibres after Ag PVD coating.



Figure 3.6: (a): PVD home-made machine. (b): Optical fibres before the PVD coating process bonded to the PVD machine cover. (c): Optical fibres after Au coating process bonded to the PVD machine cover.

The Ag coating layer obtained exhibited a very good uniform appearance in general (Figure 3.5.c), although some minor defects were detected as shown in Figure 3.7.b. It was assumed to be caused by the manipulation of the optical fibre after the PVD coating deposition because it looks like a scrape. Otherwise, the Ag coating appearance, as shown in Figure 3.7.a, is better than that obtained using the Ni plating, described in the previous section.

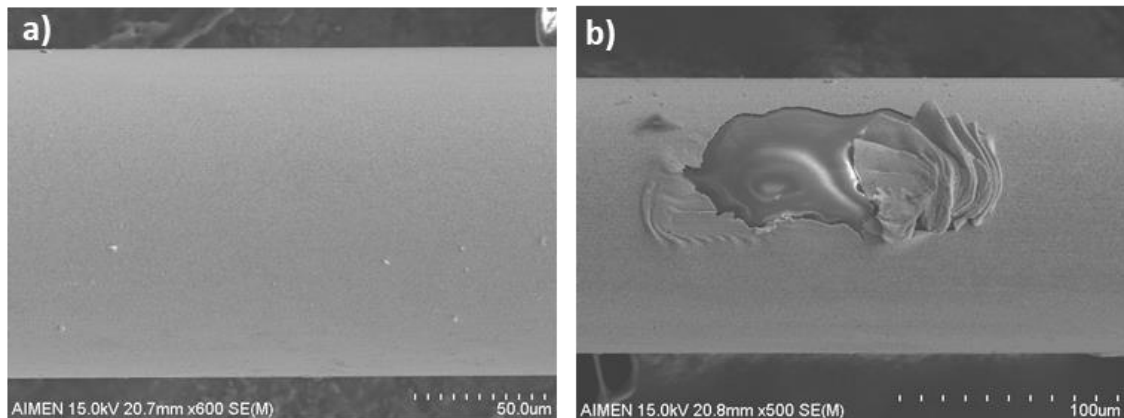


Figure 3.7: SEM images of the Ag coating layer made by PVD process. (a): Ag coated layer without defects, (b) Ag coated layer showing a scrape defect.

However, the Au coating layer obtained also, by PVD process, presents a poor quality. It presents a non-uniform coating layer (Figure 3.8.a) with many bond defects (Figure 3.8.b). In this case, it could be due to a contamination or non-uniform optical fibres distribution in the chamber, but also, due to a low-quality Au target used, as it was a recycled *scrap* gold, which was the material available because of the high cost of the gold.

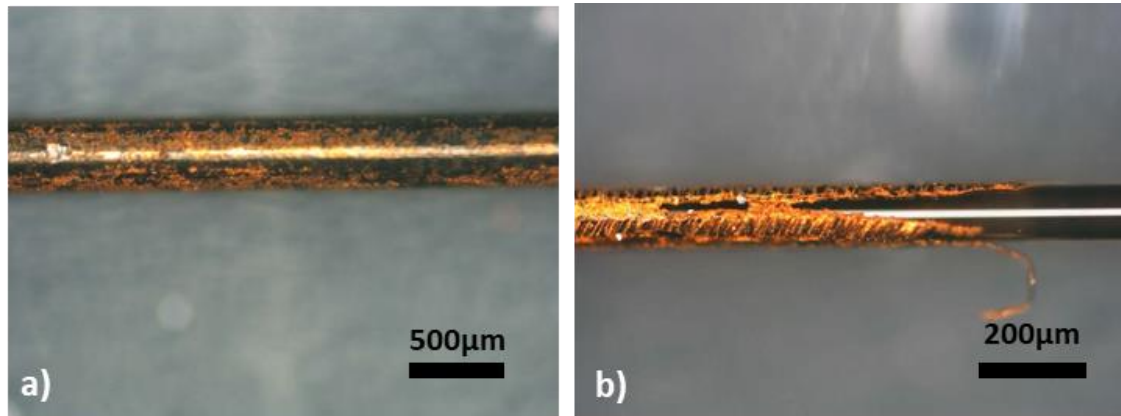


Figure 3.8: Microscope images of the Au coating layer made by PVD process. (a) Au coated layer with low gold cover. (b) Au layer border showing poor adhesion to the fibre.

A third coating test was done. In this case, Cr was used as coating metal. This material was selected because, in general, it has good adhesion to glass but also has very good thermal and mechanical resistance properties. To avoid potential damage caused by the optical fibres distribution or attachment in the PVD chamber, fewer fibres were put in for coating each time, giving more space between fibres, and the FBGs, spliced to the Cu coated optical fibre, were fixed in a holder as shown in Figure 3.9.a. The section of the fibre containing the FBG sensor, which has no coating, is exposed to the PVD process, while the rest of the fibre, which already has a commercial Cu coating, is rolled on the sides of the holder. The top of the holder was fixed to the cover chamber.

In this case, to ensure a thorough coating of the entire optical fibre, two PVD coating processes are required, as only one side of the fibre is exposed to the metal vapor at a time. Unfortunately, as Figure 3.9.b shows, the polymeric holder was deformed and peeled off from the PVD chamber cover. In addition, a good adhesion between the Cr and the optical fibre surface was not obtained. The optical fibres were not coated.

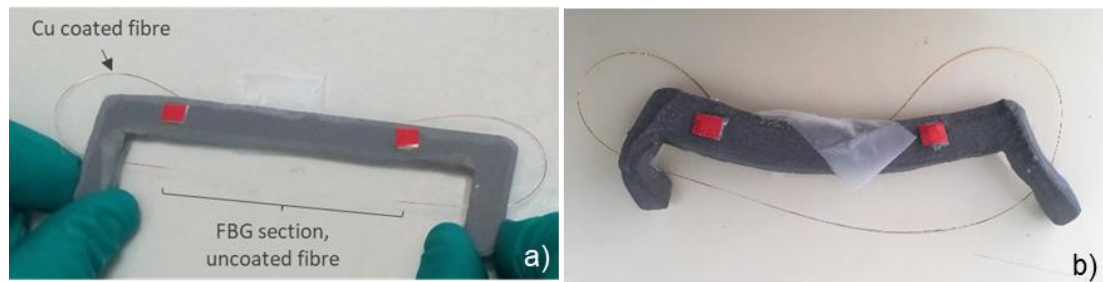


Figure 3.9: Holder to fix the FBGs spliced to a Cu coated commercial optical fibre, during the Cr PVD process. (a): Before the PVD process. (b): after the PVD process.

Finally, one FBG coated by PVD with 1.4µm of Ag was subjected to a thermal calibration from 50°C to 550°C to obtain the thermal sensitivity of the Ag coated FBG sensor. The results obtained are shown in Figure 3.10 where a good linear fit response ($r^2 = 0.99$) is observed with the thermal sensitivity of 0.011nm/°C, which is 10% more than the typical thermal sensitivity of existing commercial polymeric coated FBGs (HBM-Fibersensing). The improved sensitivity obtained can be attributed to the fact that the FBGs was coated with 1.4µm of an Ag layer.

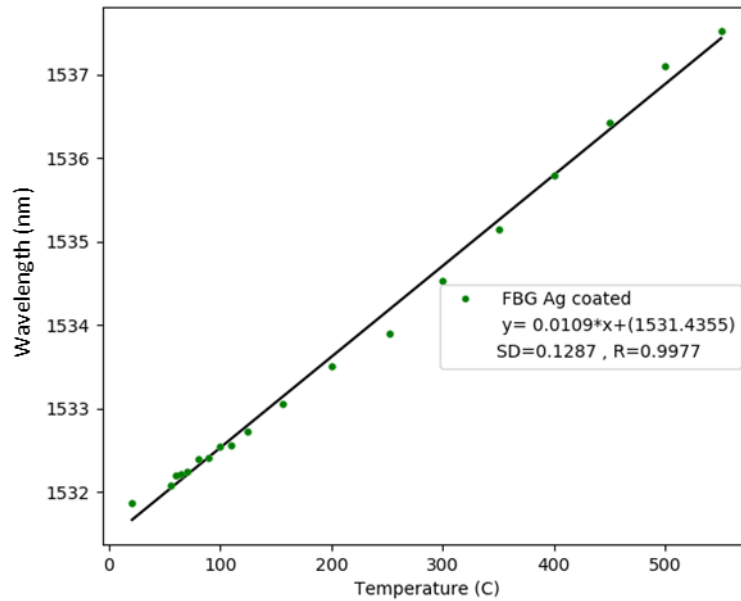


Figure 3.10: Response of the Ag coated FBG sensor for the thermal calibration.

In conclusion, in the case of the Ag material, the PVD technique studied presented a very high quality coating layer for the optical fibres as well as a good thermal response for the FBGs coated. The limitation is that the Ag melting point, which is lower than that of the optical fibre and of the other metals such as steel, Ni, Cu, etc, may restrict the fibre applications and provide limited protection of the fibre in embedding processes, such as welding or casting with molten metals with a melting point higher than that of silver.

Furthermore, during the PVD study, it was found that this technique presents many problems of adherence, principally associated with difficulties for fixing the optical fibres in the PVD conventional chambers, which restrains their manipulation and increases the likelihood of defects appearing in the final coated layer. Moreover, this technique requires expensive equipment or subcontracting the PVD coating process to a third party. The limited chamber size also limits the optical fibre coated length and the process is slow, because a very high vacuum is needed which requires 2-5 hours to achieve.

3.1.3 Conductive Paint

Another technique studied was to apply an electrically conductive coating on the optical fibre, using a nickel-conductive water-based paint (Super Shield™ Water Based Nickel Conductive Coating 841WB), coated directly on the surface of a non-conductive optical fibre. This paint, once dry, provides an electrically conductive film. This technique offers advantages, above all, for manufacture of arrays of several FBG sensors (one fibre with several FBG sensors), since the fibre hardly needs to be manipulated for painting. Ni was selected as the coating material, because of its high thermal and mechanical resistance.

The use of this metallic paint has no restrictions on the fibre length and allows the assembly and preparation of the entire sensor array. Subsequently, the application of the paint in the required sections of the optical fibre, including FBGs as non-conductive areas, to be metallised by electroplating.

This is a completely manual application technique. While the previous techniques presented a certain repeatability in the results, in terms of the surface finish and the thickness of the final

layer, in this case, it is very difficult to maintain repeatability and a completely homogeneous surface finish during application. This is reflected in the electroplating process, where irregularities or imperfections are accentuated when the Ni coating is regrown.

The procedure to paint (coat) the optical fibre with the Ni based-paint is described as follows. First, the polymeric coating of the optical fibre is removed using a mechanical stripper and then cleaned using acetone. Second, the optical fibre is passed through the paint and finally, it is placed upright to dry. Normally, with a single repetition of this procedure, the optical fibre is coated and a continuous but non-regular thickness layer is obtained. Figure 3.11 shows photographic images of the Ni-paint coated samples. The thickness of the layer varies in the range 10-150 μm .

Also, this technique has the problem to know how the Ni-based paint will behave in high temperature environments. Probably some organic components of the Ni-based paint will be degraded causing defects in the coating layer and potentially the optical fibre itself.

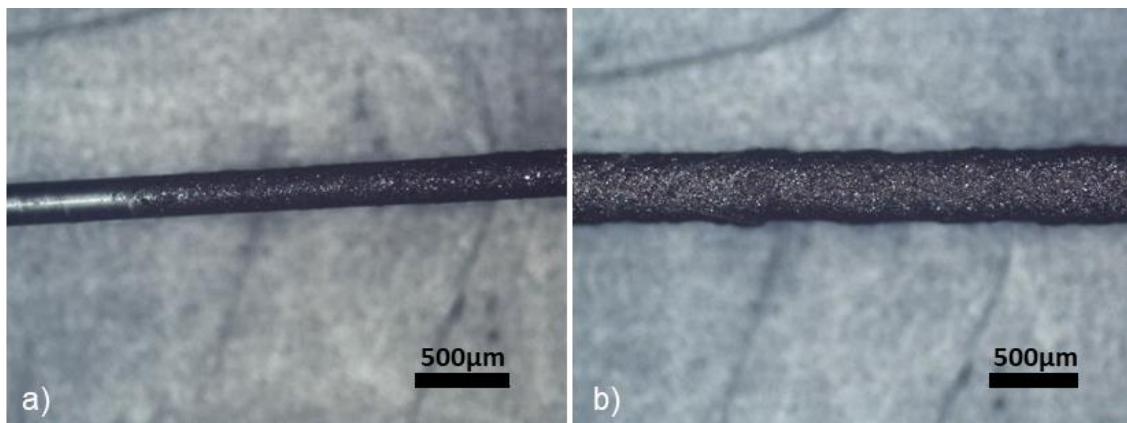


Figure 3.11: Photographic images of optical fibres coated with the Ni-based paint. (a): detail of the border section between the not coated and coated fibre. (b): detail of the fibre painted with the Ni based paint.

3.1.4 Industrial technique Cu deposition

In this section, a partnership in the form of subcontracting the company Inphotech [98] to coat and re-coat some FBGs is explained. This company operates in the field of photonics and fibre optics, providing tailor-made industrial solutions in cooperation with various companies and institutions in the field of research and development. Their commercial product range includes Cu-coated fibre optics.

This collaboration arises from the need to coat arrays of several FBGs along the same optical fibre, with a total coated length of 1.5m. These arrays are to be embedded in the antifriction material of a bearing by laser or TIG welding embedding processes, in order to monitor their Condition Monitoring status and operation (further details are included in Chapter 5). To ensure a good embedding process and to avoid any possible problems that may arise, the metallic coated optical fibre has to achieve a very good final quality. This means that there can be no defects, the thickness must be the same along the entire length of the optical fibre, because variations in thickness will affect the TIG process parameters. Additionally, the metallic coating materials must have the best possible thermal properties, with a high melting point to protect the optical fibre. At the same time, it must have a high thermal conductivity to help dissipate the heat generated, thus protecting the fibre from the thermal damage or being brittle.

As there are no customisable FBG sensors, in length or number of sensors, coated with metal on the market (at least at the time when this work was conducted). The easy way to generate a

relatively long FBG array was to splice the FBGs on the required sections along a Cu (commercial version) coated optical fibre, and then, re-coat the FBG sections to generate an electrically conductive layer. This enables the whole length of the optical fibre to be covered, including the re-coated FBG sections, with the same metal and thickness by electroplating deposition process (explained below).

Due to the ineffectiveness of in-house coating techniques, which failed to yield the desired results and imposed limitations on the total length of fibre to be coated, a decision was made to engage a commercial supplier specializing in metal-coated optical fibre to coat these arrays using their established industrial methodology, Inphotech was the provider selected.

Cu was selected as the coating material given the availability of their industrial set-up which can provide tailor-made service according to the requirements demanded by AIMEN. Two FBG sensors were spliced to a commercial optical fibre coated with Cu, like those used in the PVD technique explained above. These two commercial FBG sensors, sourced from Engionic [99], were fabricated using a femtosecond laser in a standard single mode optical fibre of 2m total length (i.e. FBG sensor fabricated in the middle of the SM optical fibre) Inphotech were responsible for coating the 2 uncoated sections, FBG sensor sections, of the first fibre and the 2m length of the second fibre, with a thin layer (about 20-60 μm) of Cu. The technique used from the company to apply the coating is confidential, but it is based on a cold coating technique.

Only one of the fibres from each configuration sent was successfully coated. The second commercial single FBG sensor fibre, with a total length of 2m, was damaged, and one of the sides of the commercial Cu-coated optical fibre attached to the FBG sensor section was also damaged. This was because their set-up is not optimized for this tailor-made work, which requires more optical fibre manipulation than the system allows. However, the quality of the optical fibres coated was very good, as Figure 3.12.a shows. And, the final coating thickness was around 60 μm , calculated from measured the total diameter of the fibre, as is depicted in Figure 3.12.b.

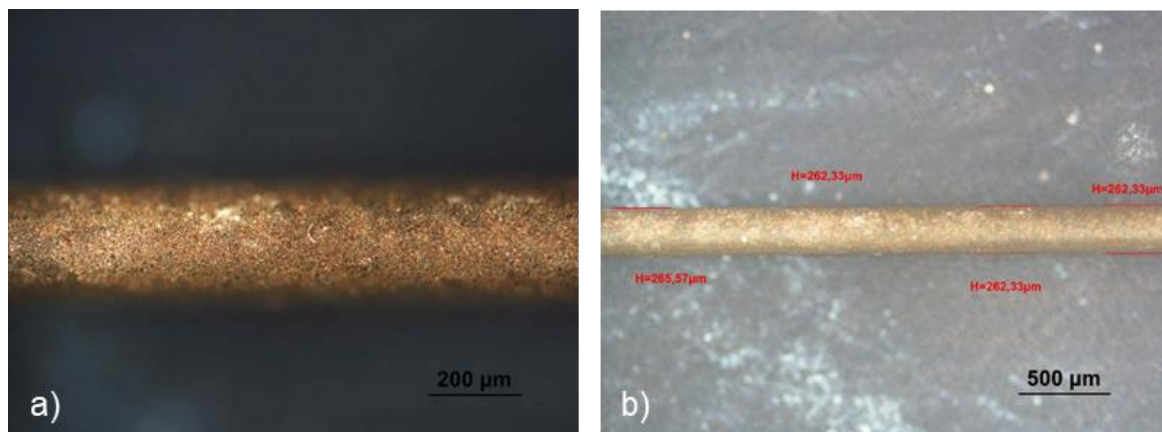


Figure 3.12: Cu coated optical fibres by Inphotech. (a) detail of the Cu coating layer surface. (b): detail of the total diameter of the Cu coated fibre.

In conclusion, for this technique high quality with good parameter control is obtained for the coating layer. Nevertheless, introducing this coating or re-coating process into an industrial system is not simple and a special optimization of the set-up must be carried out. In addition, this collaboration is expensive, taking time to prepare, deliver, coat and receive back the coated optical fibres. Therefore, it is not considered as an ideal coating process to apply the conductive layer on the fibres and establish as a step prior to the electroplating process.

3.1.5 Sputter deposition of Au technique

In this section, a sputter deposition technique is described. This process is based on the bombardment of a target material (Au wafer in this case), with high velocity positive ions (usually inert gas ions), to cause ejection of the surface atoms utilising a momentum transfer process between the sputter gas and target atoms. Argon is commonly used as the sputtering gas because of its inert properties which ensures an uncontaminated atmosphere. The ejected atoms can be made to condense on a substrate at an optimal distance from the target to form a film. Apart from the neutral atoms, charged atoms and electrons are also emitted from the surface. The sputtering yield 'S', i.e. the number of atoms ejected from the target surface per incident ion, depends on the target material composition, binding energy, characteristics of the incident ion and the experimental geometry. It also depends on the voltage and current (sputter power) at which sputtering takes place.

Figure 3.13 shows a schematic diagram and photographs of a conventional sputter deposition machine. As illustrated in Figure 3.13.a, a target is connected to a negative voltage supply (cathode) and the substrate holder along with the vacuum chamber is set at a ground potential, acting as the anode, and faces the target during sputtering. The plasma is maintained between the target and the substrate.

For this study, the sputter model SC7620, as the showed in Figure 3.13.b, was used.

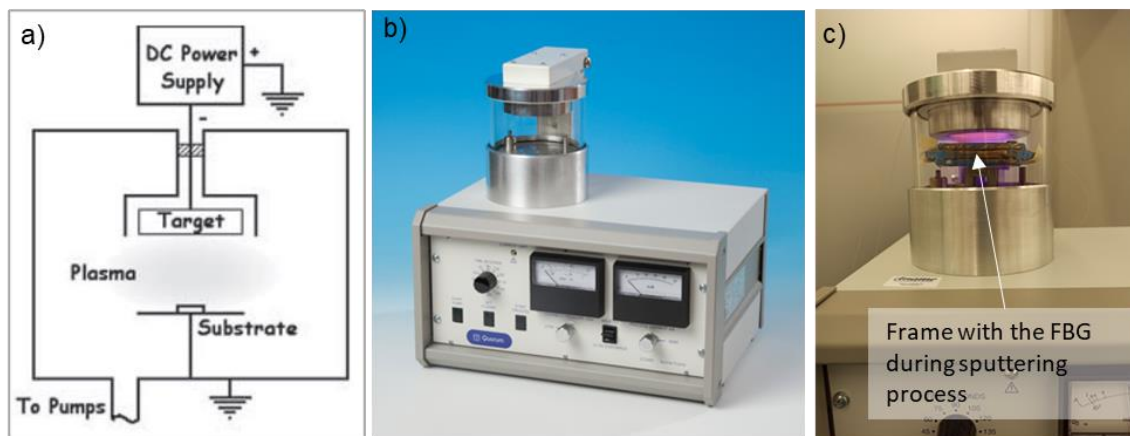


Figure 3.13: (a): Outline of sputtering process [100], (b): machine of sputtering [101], (c): detail of the sputtering process on the fibre with the fibre located in the frame.

The major limitation of this technique is the relative small size of the standard commercial equipment chamber. It is usually around 100mm in diameter, but the coated section is even smaller to ensure good coating quality to be obtained in the wafer area, which is usually around 30% of the chamber size. This limitation makes it difficult to coat a long optical fibre (longer than 50mm) due to the space constraint. In addition, the coating process has to be implemented twice to allow both sides of the fibre to be coated with uniform metal layer and thickness.

However, compared to the other techniques discussed earlier, this technique is more accessible and faster. It is because the vacuum needed to make it can be achieved within 10 minutes (depending of the equipment), and, different materials can be used as targets. Although it is necessary to purchase commercial equipment to perform this task, the cost is not very high compared with PVD or apply the metallic coating during the draw tower techniques.

Given the size limitation in this type of low-cost equipment discussed above, this machine was successfully used to coat the FBGs sections spliced to a Cu coated commercial fibre optic. These sections have a length between 30-40mm, which is well within 50 mm space limitation. To avoid damage on the fibre or on the Au coating layer during the manipulation of the fibre, e.g. when

inserting the fibre into the chamber; rotating the fibre inside the chamber and removing it from the chamber, an in house designed frame was developed as shown in and Figure 3.14, and Figure 3.13.c for working on the sputter machine.

The frame was designed to fix the un-coated section of an optical fibre (FBG section) so that there is no need to directly handle the fibre, but only the frame. To coat the whole fibre, two sputter coating layers had to be applied, one on each side of the cylindrical side of the fibre. Therefore, there are to turn the fibre. With the set-up described here in the frame (with the fibre fixed) can be removed from the chamber and turn it before being placed back inside. In the cases, where an array of several FBGs spaced along an optical fibre are required to be coated, the procedures is repeated for each FBG. First, the FBGs sections are spliced to the Cu coated fibre at the defined locations (lengths). Then, the first FBGs is located in the frame and it is positioned on the sputter chamber. The rest of the FBGs and fibre are outside of the chamber. Then, allowing application of the coating layer on the first FBGs, the frame is moved to the second FBGs section and the coating process is repeated and so on with each of the FBGs. Figure 3.14 described this process.

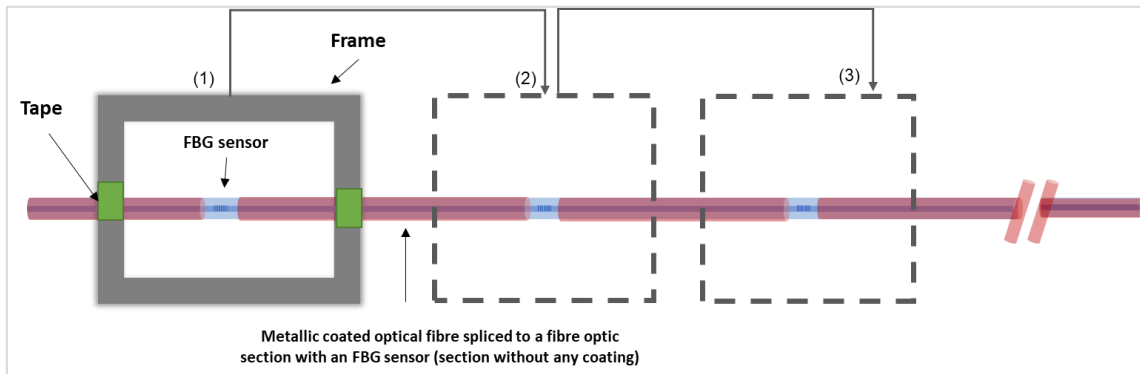


Figure 3.14: Frame developed to fix the optical fibre on the sputtering chamber.

Other strategies to fix the fibre were also explored. For example, using a 3D-printed special chamber, shown in Figure 3.15.a. This chamber has holes on the sides, as Figure 3.15.b shows, to enable pulling of the rest of the optical fibre, the Cu coated optical fibre, through it and sealing them with sticky tape. This solution served its purpose; however, for longer lengths, passing the fiber through the holes and sealing them posed a risk of damaging the fiber and/or sensor.

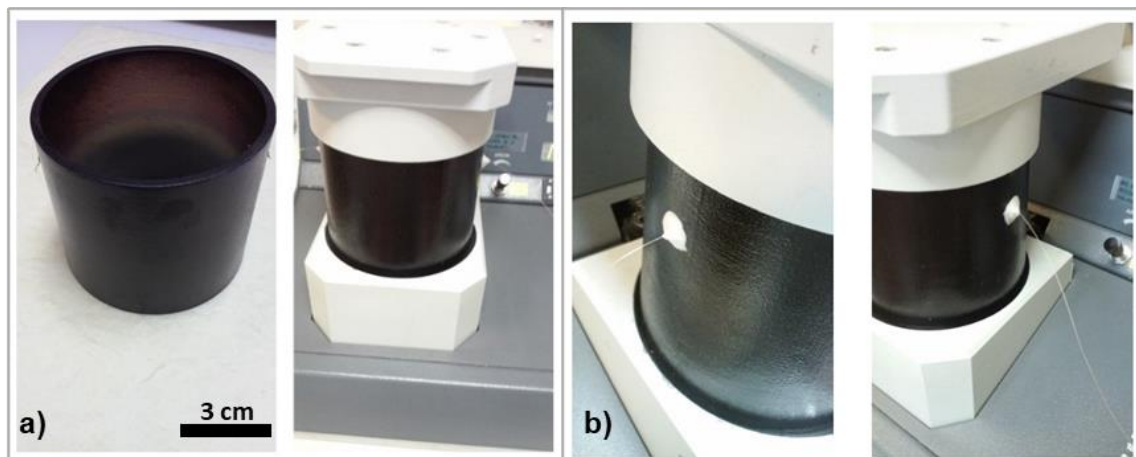


Figure 3.15: (a) 3D printed chamber with holes to allow the optical fibre that is not required to be coated to exit, from the sputter machine. (b) detail of the optical fibre coming out form the holes of the chamb्रे, sealed with sticky tape.

Finally, the control of the fibre-to-target distance is a significant factor to take into account. If this distance is not well adjusted, the erosion of the wafer from the target is greater, and hence its wear also influences the deposition layer that is obtained on the fibre, which will be thinner and more fragile.

In Figure 3.16 shows the Au coating layer for an optical fibre coated using the sputter deposition technique. The quality of the coating layer is good and the adhesion between the Au layer and the optical fibre was also good. The thickness of this technique varies between 1-10 μ m, depending on the vacuum level, Au target status, Ar concentration in the chamber and exposure time of the fibre. Prior to the deposition, the optical fibre was carefully cleaned using acetone to exclude the presence of impurities, dust or other kind of dirt on the fibre surface which could cause defects in the coating layer.

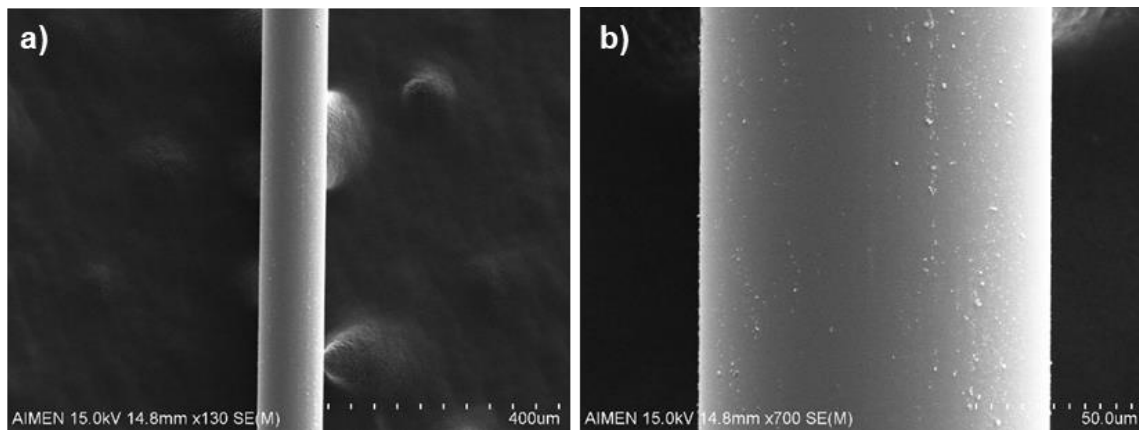


Figure 3.16: SEM images of the Au coating layer obtained on the optical fibres made by sputter deposition technique. (a) detail of the Au coating layer for x140 magnifier, (b) detail of the Au coating layer for x700 magnifier.

After the study of these five metallic coating techniques discussed above, the principal advantages and disadvantages studied are summarized in Table 3.2. Using the characteristics studied, the sputter deposition technique is seen to be the best option. Therefore, it has been selected as being the most suitable for applying the first conductive layer on the optical fibre, prior to the electrodeposition process.

Technique	Good adhesion from metallic coating to the fibre	Good quality of the coating layer	allows the use of several coating metals	Equipment required	Technique relatively fast	High cost	Repetitivity.
Electroless	✓ (but difficult to achieve)	✓	✓	✗	✗	✗	✓
PVD	✗ (Not in all the cases studied)	✓ (for Ag)	✓	✓	✗	✓	✓
Ni-based Paint	✓	✗	✓	✗	✓	✗	✗
Industrial process	✓	✓	✗	✓	✗	✓	✓
Sputtering	✓	✓	✓	✓	✓	✗	✓

Table 3.2: Comparison table for all the coating techniques studied to generate a conductive layer on the optical fibre.

3.2 Electroplating deposition technique.

The final aim of this work is, on the one hand to generate high temperature (>400-1000°C) and corrosion resistant fibre optic sensors, and on the other hand, to develop fibre optic sensors that are able to be embedded into metallic structures to monitor their operation and status and, detect and avoid potential failures like: cracks, corrosion, erosion, etc. To embed fibre optics in this kind of material, a protective coating on the fibre is needed, ideally incorporating a metal with a higher melting point than that of the metal piece or to at least withstand the embedding process for thermally and mechanically protecting the optical fibre. In this section electroplating deposition of Ni and Cu on optic fibres is studied and described as a conductive process. Using the electroplating deposition technique it was possible to achieve coating thicknesses from a few micrometres to thousands of micrometres. Copper (Cu) and Nickel (Ni) were the materials selected for electroplating deposition due to their high melting point and good adhesion with the silica.

In addition, a study of electroplating parameters, e.g. intensity, electrode material, state of reduction solution, and their correlation with the coating thickness and roughness has been made.

Figure 3.17.a shows a typical electroplating deposition scheme which consists of two electrodes that are immersed in an electrolyte, a conductive, aqueous solution of salts (Ni or Cu salts in this case) and other additives that provide ions to facilitate the flow of current between electrodes. A power source supplies direct current to the anode, which causes the oxidation of its atoms, causing them to dissolve in the electrolyte. At the cathode, the dissolved metal ions are reduced at the solution-cathode interface, so that the cathode is coated with a metallic layer. The rate of oxidation of the anode is equal to the rate of coating of the cathode, indicating that the electrolyte bath is continuously replenished by the anode. An inert, conductive electrode, such as graphite, can also be used instead of a metallic electrode of the same metal of the salts to avoid impurities on the coating layer. In the case of using an inert cathode, no ions are added to the solution, so the electrolyte bath is depleted as the cathode is coated and the solution needs to be renewed after some time of use.

Based on this scheme, Figure 3.17.b shows the experimental set-up to coat an optical fibre with Ni (in the case of this picture). A conductive fibre is immersed in a Ni bath solution and connected to the negative pole of the current source, acting as the cathode a conductive sheet was fixed in front and parallel to the fibre, connected to the positive pole, acting as the anode. Also, a heating plate and a temperature probe are used to heat the solution at the required temperature and control it. In this case, the electroplating process is made on a small glass chemical test tube, which was located in a water bath to better control the temperature.

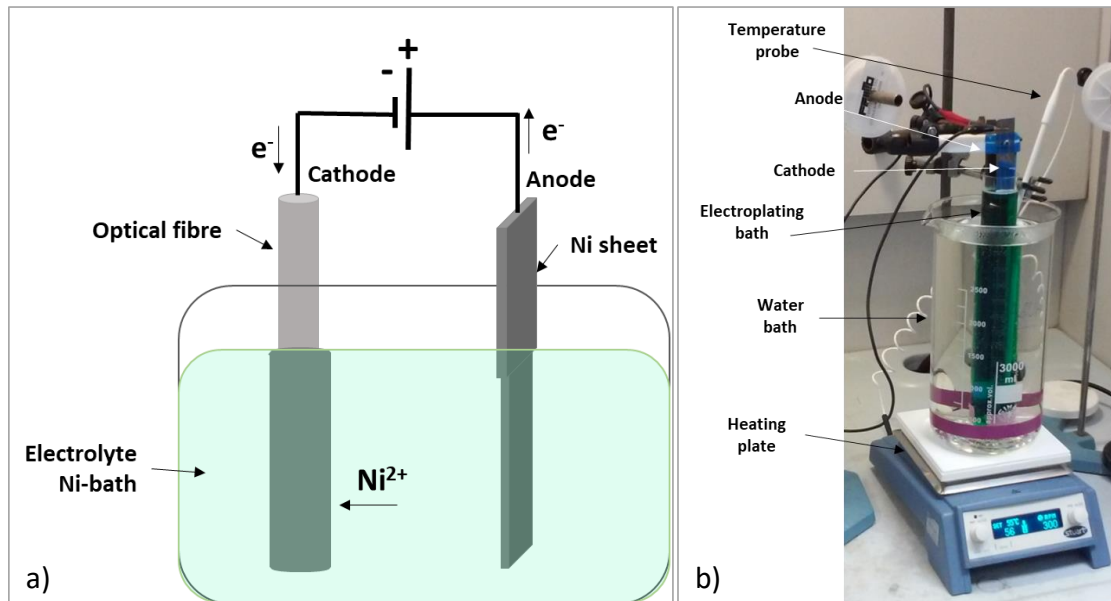


Figure 3.17: (a) Electroplating Deposition scheme, (b) electroplating Ni deposition set-up.

In this section, Cu and Ni electroplating deposition were studied. The composition of each electrolyte bath and the methodology used for applying this technique is described as follows:

1. Making the solution, composed by:
Electroplating of Copper:
 - 225 [g/l] CuSO₄
 - 50 [g/l] H₂SO₄Electroplating Deposition of Nickel:
 - 300 [g/l] NiSO₄·6H₂O
 - 20 [g/l] NiCl₂·6H₂O
 - 40 [g/l] H₃BO₃
 - 0.36 [g/l] Sodium Lauryl Sulphate
2. Heating the solution up to 55°C
3. The optical fibre with a previous conductive layer is cleaned by acetone and fixed using another tape on a cathode sheet.
4. When the solution reaches 55°C, the sheets for anode and cathode were placed in parallel into the dissolution bath.
5. Finally, the sheets (anode and cathode) are connected with the electrodes of the intensity source. The parameters (intensity and voltage) are pre-selected and the source is turned on.

To assure a good deposited coating layer there are to take know the solution status. The main indicators of the bath status are: pH, concentration of salts in the bath and density. The pH should be around 4.5. The salts concentration is directly related to the density of the bath. If the salts concentration is low, the density of the bath is also low, then, new concentrated components should be added. Conversely, if the density of the bath is high, deionized water should be added to adjust it. Finally, it is very important to maintain effective and continuous bath agitation to refresh and unify the solution, but above all, to avoid the generation of air bubbles around the substrate to be coated.

On the other hand, the main parameters involved in the electroplating deposition process are: anodes (electrically conductive material), current density (intensity and voltage) and temperature. The anodes should be made of the same material as the coating and be as pure as possible, so that impurities are not deposited on the substrate. The current density will depend on the bath conductivity and the size of the sample to be coated. The temperature should be set at 55°C, to maximise the solution conductivity and minimise the probability of *burning* the sample.

Using the methodology described above, different tests were conducted to study the dependence of the thickness coating layer on variations in the parameters or conditions of the solution. To make this study, Cu coated commercial optical fibre was used to simplify the conductive layer applied on the optical fibre. The Cu coated optical fibre was a standard single mode optical fibre with a total diameter of 165µm, with a coating thickness of 40µm, purchased from IVG Fiber® [102].

3.2.1 Characterization of electroplated Cu

To investigate the correlation between electroplating process parameters and the quality and thickness of the resulting Cu-coated layer, as well as to establish parameters for the Cu electroplating process, commercial optical fibre samples of identical length were used. These samples underwent electroplating with variations in either exposure time or applied intensity, specifically, the current density. The bath temperature was maintained at 55°C, graphite sheets served as the anode, and the optical fibre length remained consistent at 12 cm. Fresh dissolution was employed for each test.

Table 3.3 and Table 3.4 shows the results obtained for a representative sample of each time/intensity combination studied. The thickness of the final coating layer grows with both parameters, although the exposure time influences the thickness to a greater extent, than the current density because the coating rate is lower for a higher exposure time for the same intensity. In addition, the increase of intensity, which is an increase of the current density, affects the final quality of the coating, increasing the diameter and coating granules.

*Metal coating and embedding fibre optical sensors for industrial applications.
Chapter 3: Metallic coating of Fibre Optic Sensors and their characterization.*

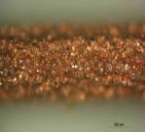
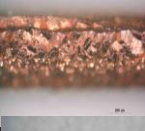
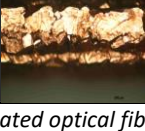
Intensity (A)	Time (min.)	Picture	Final fibre diameter (μm)	Coating rate ($\mu\text{m}/\text{min}$)	Intensity (A)	Time (min.)	Picture	Final fibre diameter (μm)	Coating rate ($\mu\text{m}/\text{min}$)
0.5	30		335	5.7	0.2	75		432	3.6
	45		551	8.6		75		426	3.5
	75		624	6.1		135		586	3.1
	75		676	6.8		135		556	2.9
0.15	75		406	3.2	0.3	75		518	4.7
	75		399	3.1		75		502	4.5
	135		480	2.3		135		649	3.6
	135		481	2.3		135		685	3.9

Table 3.3: Cu re-coated optical fibres by electroplating deposition technique, varying intensity or exposition time.

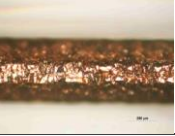
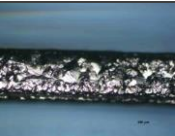
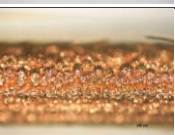
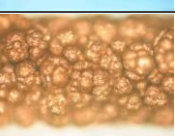
Time (min.)	Intensity (A)	Picture	Final fibre diameter (μm)	Time (min.)	Intensity (A)	Picture	Final fibre diameter (μm)
30	0.1		214	30	0.3		355
			288				328
			264				316
			255				408
			200				442
	0.2		309		0.5		481
			308				495
			294				616

Table 3.4: Cu re-coated optical fibres by electroplating deposition technique, varying intensity and maintaining constant time.

3.2.2 Characterization of electroplated Ni

A similar set-up was created for the characterisation of electroplated Ni by replacing the Cu bath dissolution discussed above with Ni.

In this case, the parametrization dependence study was made in two parts. First, some Ni electroplating samples were proposed by varying the intensity but maintaining an exposure time of 30 min (Table 3.5). For the second study, the intensity was keeping constant at 0.5A, and the exposure time for re-coating the optical fibres was varied (Table 3.6).

Intensity (A)	Time (min.)	Picture	Final fibre diameter (μm)	Intensity (A)	Time (min.)	Picture	Final fibre diameter (μm)
0.15	30		237	0.3	30		312
			252				614
			242				394
0.2			271	0.5			540
			228				492
			288				455
0.3			347	1			400

Table 3.5: Ni re-coated optical fibres by electroplating deposition technique, varying intensity for 30 min of exposure.

As in the case of the Electroplating Cu deposition, for Ni, the thickness of the coating grows with the increasing intensity and exposure time to the electroplating process. But in this case, the quality of the coating layer is better than Cu coating, because the grain size of the Ni coating is smaller. The Ni electroplating process, however, requires a higher current density to achieve the quality required.

At 0.5A of intensity (Table 3.6), the Ni coated layer presents uniformity without the granulated appearance as shown in Table 3.4 for intensities higher than 0.5A. This is an advantage when subjecting these fibres to high temperatures or embedding processes. Moreover, it is also observed that the deposition rate decreases more with increasing exposure time than in the case of Cu.

Time (min.)	Intensity (A)	Picture	Final fibre diameter (µm)	Tasa de Crecimiento [µm/min]	Time (min.)	Intensity (A)	Picture	Final fibre diameter (µm)	Tasa de Crecimiento [µm/min]
15	0.5		322	10.4	60	0.5		573	6.8
			348	12.2				551	6.4
			327	10.8				590	7.1
30			417	8.4	75			615	6.0
			413	8.3				596	5.7
			415	8.3				599	5.8
45			507	7.6	135			797	4.7
			475	6.9				838	5.0
			463	6.6				778	4.5

Table 3.6: Ni re-coated optical fibres by electroplating deposition technique, varying exposure time at 0.5A of intensity.

Finally, Figure 3.18 shows the cross-section appearance and structure of the Ni coated layer. Figure 3.18.a shows a Cu commercial coated optical fibre re-coated with Ni by electroplating deposition technique. The black circle on the centre of the picture is the silica optical fibre, the small cream circle around the silica is the Cu commercial layer and the grey bigger circle is the Ni re-coating layer. Figure 3.18.b shows the same fibre attacked with acid, revealing the polycrystalline structure of the Ni coating layer.

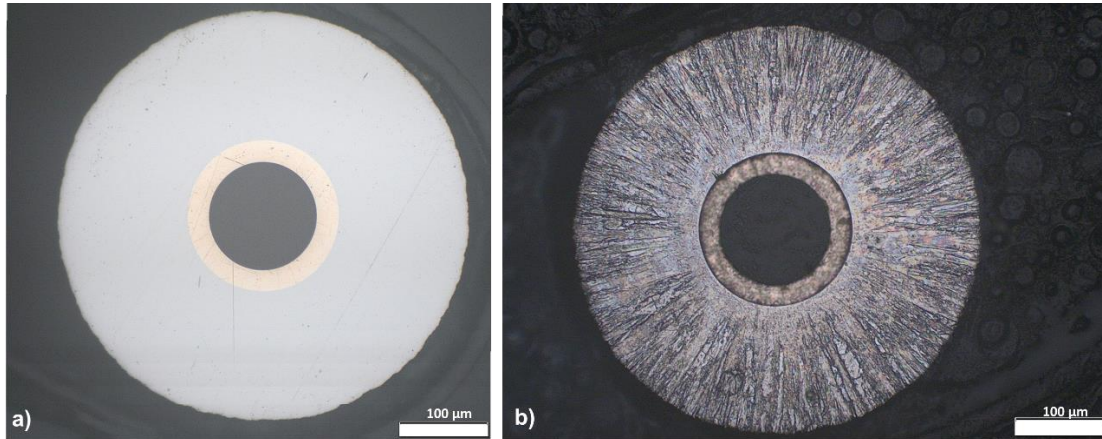


Figure 3.18: Cross-section of a Cu commercial coated optical fibre re-coated with Ni by electroplating deposition technique. (a): Cross-section. (b): cross-section attacked with acid to reveal the structure.

3.3 Thermal characterization of metallic optical fibre sensors

In this section, the spectra, losses and thermal resistance of some Ni and Cu coated fibre optic were analysed. It includes both the commercial coated optical fibres and point FBG sensors metallized with Ni and/or Cu using the techniques discussed above.

For the distributed sensors, several coated commercial optical fibres (Au, C and Cu) were acquired and while Ni coated optical fibre was obtained using electroplating a Cu coated commercial fibre. The metal coated FBGs were manufactured by the methodology shown in Figure 3.1. The techniques used were Au sputtering to apply a conductive layer on the FBGs section and Ni or Cu electroplating deposition along the entire optical fibre length, and not only to the FBGs section.

3.3.1 Thermal characterisation of coated optical fibres

Six different optical fibres, with different coatings were chosen for the thermal tests. Their technical characteristics and significations are shown in Table 3.7. The optical fibres were placed in an oven, where temperature cycles were applied. For each fibre, both ends were spliced to connectors outside the oven, so the loss of the fibres for each temperature cycle can be easily measured using a laser source (1550nm) and an optical power meter. The optical fibres tested are listed below:

- Au coated commercial optical fibre sourced from AMS technologies with coating thickness of 15µm on a 125µm diameter fibre and operation temperature up to 800°C.
- Cu coated commercial optical fibre sourced from IVG. The thickness of the Cu layer was 20µm on a 125µm diameter fibre and the fibre can operate up to 600°C, but at temperatures higher than 400°C the coating deteriorates by oxidation.
- Ni coated optical fibre using electroplating ~70µm longer of Nickel coated on the above Cu coated fibre from IVG.
- Carbon coated commercial optic fibre from IXBlue. The thickness of the Carbon layer was <1µm on a 245µm diameter fibre.
- Cu coated optical fibre with 316 steel capillary of 2 mm outer diameter and 1.5mm inner diameter, sourced from IVG. The thickness of the Cu layer is 20µm on a 125µm diameter fibre.
- Standard single mode optical fibre coated with polyimide with 316-steel capillary with 0.8mm outer diameter and 0.5mm inner diameter. The thickness of the polyimide layer is 62.5µm on top of a 125µm diameter fibre.

Primary coating	Additional layer	Temp range long term (°C)	Core diameter (µm)	Cladding diameter (µm)	Coating diameter (µm)	Provider
Copper alloy	Carbon	600	9	125	165	IVG Fiber
Au	-	700	9	125	155	Fiberguide
Acrylate	Carbon	-	7.5	125	245	IxBlue

Table 3.7: Coated commercial fibre optic specifications.

The temperature cycles are applied using the following pattern: each cycle consisted of increasing the temperature to be within 250°C to 800°C, keeping it constant for 2 hours, before dropping it to be between 20°C and 50°C for another 2 hours.

The losses for each tested fibre were measured before to start, during each step of temperature applied and after each cooling after each temperature step applied. Table 3.8 shows the losses at each loss measure carried out.

It was observed that the standard polyimide coated optical fibre with 316 steel housing shows significant loss at 400°C, around 38dB. The Ni-Cu coated fibre, at this temperature shows higher losses (4dB) than the C and other metallic coated optical fibres which show losses between 0.6 and 2.2 dB. At 700°C Cu and C coated fibres fail, showing losses over 55dB. Ni coated fibre degrades in the cycles of 800°C, triggered by a small defect during fabrication. While, gold coated fibre is the most robust, since it has withstand all the temperature cycles showing minor losses. Although, this fibre is too expensive for the final applications, then, this study will continue to be carried out, including also, re-coated fibres as it had the next best response.

Temperature of test set (°C)	Temperature (°C)	Loss in Cu coated optical fiber with 316 steel housing (dB)	Loss in Comercial carbon coated optical fiber (dB)	Loss in Comercial Au coated optical fiber (dB)	Loss in Cu coated comercial optical fiber (dB)	Loss in Ni coated optical fiber (AIMEN) (dB)	Loss in standard optical fiber with 316 steel housing (dB)
200	35	0	0	0	0	0	0
	25	-1,61	-2,87	-3,62	0,3	1,31	-3,54
	250	-2,3	-2,27	-2,77	-0,75	2,54	-6
	45	-0,99	-0,83	0,13	0,53	0,81	0,14
	250	-1,58	-2,15	-4,37	-0,94	2,37	-2,1
	45	-1,55	0	0,54	0,47	1,45	-0,07
300	28	-0,7	-0,03	0,01	0,33	0,46	-1,15
	300	-1,05	-0,48	-0,7	0,85	1,38	-2,04
	46	-0,67	-0,03	0,91	1,01	1,5	-0,93
	300	-0,96	-0,11	0,1	0,36	2,08	-1,15
	45	-0,88	0	0,57	0,98	1,69	-0,76
	28	-1,28	-2,23	-2,26	0,12	2,66	-1,59
	300	-1,25	-2,23	-2,04	0,36	2,81	-2,41
48	-0,93	-1,96	-0,28	0,21	1,04	-0,59	
400	400	-1,49	-1,42	-1,24	-0,03	2,86	-1,15
	26	1,03	-2,58	-1,39	-0,26	0,97	-0,07
	400	-0,64	-1,46	-2,26	0,88	3,54	-37,57
	50	-0,93	0	-0,01	0,39	1,55	-
	400	-1,37	-0,9	-1,33	0,42	4,08	-
	27	-1,31	-0,34	0,15	0,33	1,16	-
500	500	-1,61	-0,93	-1,66	0,03	2,9	-
	51	-0,83	-0,13	0,24	-0,39	1,93	-
	500	-1,16	-0,78	-2,98	-0,29	3,36	-
	25	-1,46	-2,27	-3,11	-0,76	3,12	-
	500	0,96	-1,46	-2,61	0,12	4,78	-
	51	0,69	-0,75	0,37	0,21	2,53	-
600	600	-1,07	-0,87	-1,66	0,64	4,2	-
	25	-0,88	-2,11	-0,47	-0,39	2,48	-
	600	-0,95	-0,84	-1,51	0,39	4,24	-
	55	-1,34	0,05	0,23	0,21	2,21	-
	600	-0,96	-0,69	-1,21	0,36	3,88	-
	25	-2,01	-2,11	-2,98	-2,73	1,43	-
700	700	-0,44	-58,45	-2,45	-1,52	4,05	-
	25	-3,76	-	-0,42	-23,72	-6,22	-
	700	-55,82	-	-3,08	-54,03	2,38	-
	50	-	-	0,66	-	-8,38	-
	700	-	-	-1,58	-	-0,55	-
	25	-	-	-1,21	-	-10,61	-
800	800	-	-	-1,31	-	-17,59	-
	55	-	-	0,25	-	-45,95	-

Table 3.8: losses of optical fibres during tests at different temperature.

3.3.2 Thermal characterization of metallically coated FBG sensors

As discussed above, Au commercial coated fibre and Ni re-coated optical fibre were proven to withstand prolonged exposure to high temperatures without affecting their response. In this section, FBG sensors spliced to Cu or Au commercial optical fibre and Cu and Ni re-coated, were also thermally tested to study their thermal behaviour at high temperatures (>400°C).

The interrogators used to monitor the FBGs were the FS22 from HBM-Fibersensing [103] and the s125 from Micron Optics [104].

3.3.2.1 Thermal characterization of Cu re-coated FBG sensor

In this section Cu re-coated FBG sensors were tested and calibrated at high temperature. The Cu re-coated FBG sensor was re-coated with Cu to reach a total fibre diameter of 711µm: 20µm of Cu from the commercial optical fibre and 273µm of Cu by electroplating deposition.

This sensor was heated in a furnace from room temperature to 1000°C in steps of 200°C, to determine its thermal resistance and the thermal sensitivity of the Cu re-coated FBG sensor.

Figure 3.19.a shows the FBG wavelength shift when temperature changes. At temperatures higher than 800°C, the sensor failed, but until then it shows a stable signal. Figure 3.19.b shows the quadratic curve fitting of the data collected up to 800°C, showing its thermal sensitivity about three times of that of an uncoated sensor.

After the thermal test, the Cu re-coated layer of the FBG sensor was analysed to determine the cause of the FBG sensor failure. Figure 3.20.a and Figure 3.20.b shows the Cu layer appearance before and after the thermal calibration test, respectively. A high level of Cu layer coating degradation was detected. The Cu of the coating layer has been oxidised which causes cracks which are visible on the optical fibre and that resulting in its eventual failure.

Other thermal tests using Cu re-coated FBG sensors were permitted to corroborate this behaviour of the Cu and it was found that the Cu coating layer works well for temperatures <400°C. For temperatures greater than 400°C, the Cu becomes oxidized, and the optical fibre eventually fails due to defects in the coated layer, which accumulate over time. Therefore, the Cu coating is not recommended to protect the fibre sensor to high temperature exposure. For this reason, no more temperature thermal studies were carried-out, including annealing studies.

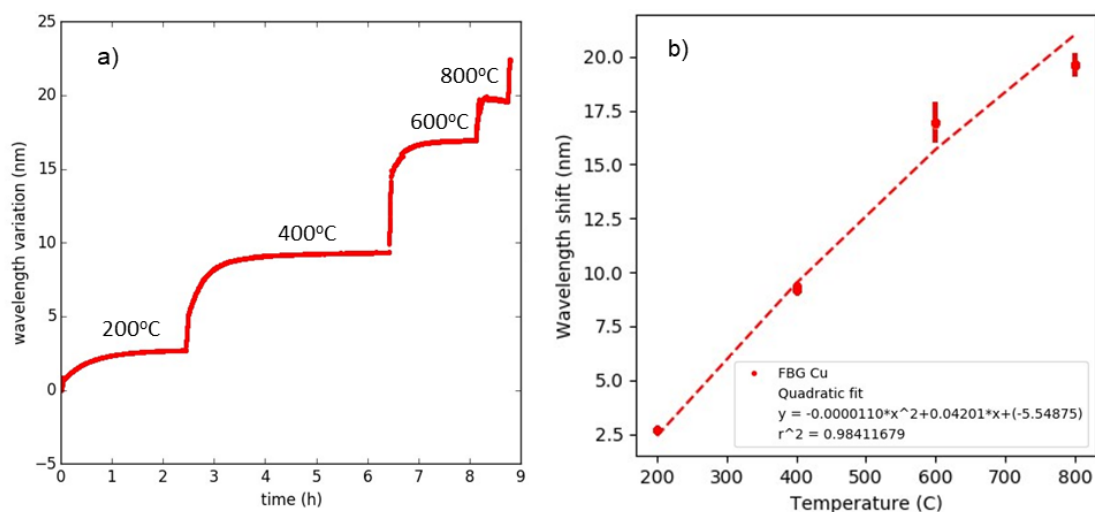


Figure 3.19: (a): Cu re-coated FBG sensor response during the thermal calibration. (b): quadratic curve fitting to the sensor data for calculation of its the thermal sensitivity.

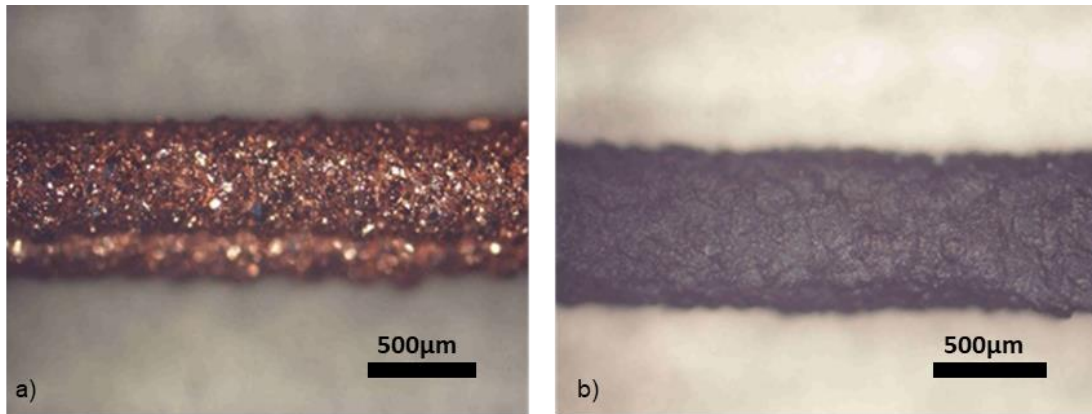


Figure 3.20: Cu re-coated FBG sensor appearance. Left: before the thermal test. Right: after the thermal test.

3.3.2.2 Thermal characterization of Ni re-coated FBG sensor

3.3.2.2.1 Annealing study

Annealing is a thermal procedure where the fibre is heated to a high temperature and held at that temperature for a relatively long time (>10h), and then cooled back to room temperature. The heating is usually carried out gradually, as is the cooling, so that the thermal contrast is not abrupt and does not cause unwanted defects in the material. After the annealing process, the internal structure of the optical fibre and then coated layer change permanently. For this reason, the temperature applied in this procedure must always be higher than the operation temperature, to which the sensor will be subjected, so that the structure is stable throughout the working temperature range and does not undergo variations in the internal structure that could affect its response. After the annealing process, the Bragg wavelength is shifted with respect to its original Bragg wavelength for a given temperature value [105]–[107].

For this purpose, three FBGs re-coated with Ni by electroplating were made. The process to re-coat was the explained in section 3.2. One FBG sensor silica section was spliced to an Au commercial coated optical fibre and then coated with Au and Ni. Also, two FBGs were spliced to a Cu commercial coated optical fibre and coating them with Au and Ni. The diameter of the silica fibre (single mode) was 125 µm. The total diameter of each re-coated FBG sensor was 530 µm for the Ni-Au FBG1, 345 µm for FBG2 with Ni-Cu coating, and 630 µm for FBG3 with Ni-Cu coating. This allows for the study of the influence of both the coating thickness and the base coating material of the fibre.

The annealing study involves a combination of continuous heating, to study the annealing effect on each FBG, and fatigue thermal test, to study the response and repeatability of each FBG. The Ni re-coated FBG sensors were located in a tube furnace and subjected to continuous heating (annealing) for >48h at temperatures of 250, 450, 650 and 850°C. After annealing (continuous heating), the sensor was cooled down to room temperature with the wavelength shift recorded, and then, the FBG sensors were subjected to a thermal fatigue test at a temperature close to, but lower than the annealing temperature (200, 400, 600 and 800°C) for 7-10 days to reach temperature, to study their behaviour and response. This thermal fatigue test was performed after the corresponding annealing test, so the fibre structure and coating layers would already have been modified during annealing at a higher temperature than the working temperature, and the sensor response should be stable.

In Figure 3.21 the Ni re-coated FBG sensors signal during the annealing and thermal fatigue tests is shown. Up to the annealing at 850°C, all the FBG sensors show good repeatability during fatigue test. During the annealing processes, the Ni-Cu coated FBG2 sensor is stable, the Ni-Au

coated FBG1, also shows a stable signal, except for the 450°C annealing, which could be due to a failure to place the sensor inside the oven during this test. However, the Ni-Cu coated FBG3 sensor is not stable during annealing at temperatures of 650°C and 850°C, even though its response remains stable and repeatable throughout all thermal fatigue tests. The Ni-Au coated FBG1 sensor also shows a good signal response during the fatigue tests at 800°C, after annealing at 850°C. However, the Ni-Cu coated FBG2 sensor signal exhibits some faults during the thermal fatigue tests at 800°C (highlighted in Figure 3.21).

Moreover, it was observed that the final wavelength after each annealing process is the same as that obtained at the end of the thermal fatigue test. At temperatures below the annealing temperature, the scale of the wavelength shift is related to the coating material and its thickness, for example, FBG3 (higher thickness) exhibits higher a wavelength shift than the other two FBGs tested.

Finally, the FBG sensor sing response to the fatigue tests is concluded to be stable after each annealing test made. It confirms that an annealing process at equal or higher temperature than the maximum operating temperature is needed, to ensure the repeatability of the sensor during its operation. In addition, it has been found that thicker coated FBG sensors exhibit greater robustness to exposure at high temperatures than the thinner coated FBGs.

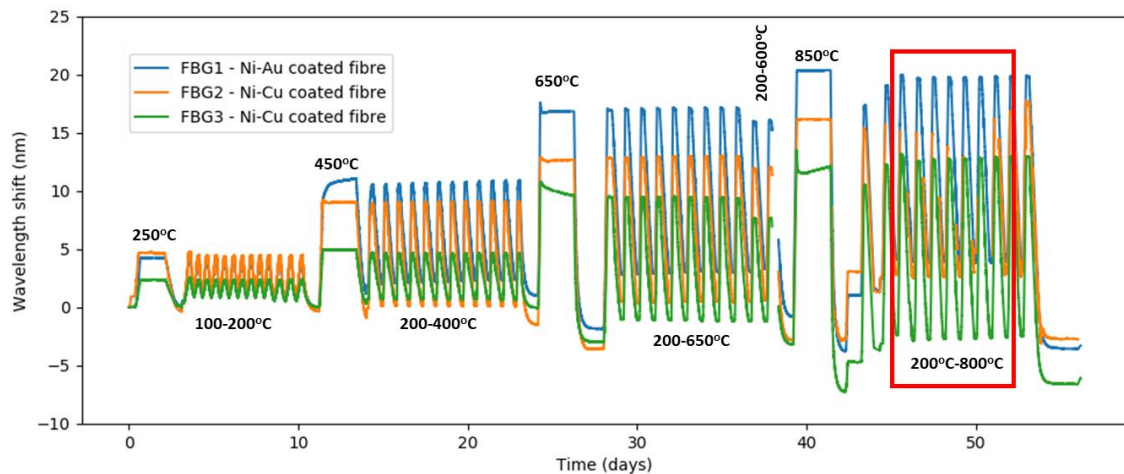


Figure 3.21: Ni re-coated FBG sensors wavelength variation during the annealing and thermal fatigue tests.

3.3.2.2.2 Ni re-coated FBG thermal response

In this section, different coated and non-coated FBG sensors were thermally fatigue tested up to 650°C, as well as being calibrated by applying a temperature variation from 50°C up to 650°C in steps of 100°C to determine the thermal sensitivity. In addition to the temperature sensors, some of the Ni re-coated FBGs were bonded to a steel pipeline to test them as strain sensors. To bond the FBG sensors to the steel structure a high resistance silicone (BISAN 1600°C) and metal based adhesive (Durabond 7032) were used.

The coated FBG sensors used for this study were follows:

- FBG1 and FBG2: Commercial standard FBG sensor with acrylate coating, encapsulated in stainless steel capillary tube of inner diameter of 2.7mm and external diameter of 3.2mm. Temperature sensor.
- FBG3: Ni re-coated FBG sensor. Commercial FBG sensor section spliced to a Cu commercial coated optical fibre. The Ni re-coated FBG sensor was made by Au sputtering + Ni electroplating and bonded to the steel structure with a Ni-based high temperature resistance adhesive. Strain & temperature sensor.

- FBG4: Ni re-coated FBG sensor. Commercial FBG sensor spliced to an Au commercial coated optical fibre. The Ni re-coated FBG was made by Au sputtering + Ni electroplating. Temperature sensor.

The acrylate coating of FBG1 and FBG2 is degraded during the thermal tests, but this test is also to study the thermal resistance of the silica optical fibres without any coating, compared to the Ni re-coated FBG sensors. FBG3 and FBG4 were coated with a similar coating thickness around 650µm.

Initially, the thermal fatigue test was performed, in order to stabilise the signal and avoid annealing effects during the thermal calibration. The FBG sensors were located in an oven set with thermal cycles between 100°C to 650°C with 2 hours heating (100°C - 650°C), 2 hours stabilizing (650°C), 10 hours cooling (650°C - 100°C). Figure 3.22 shows the FBG sensor sing response. At the beginning of the fatigue test, the sensors were heated to 650°C during 24h for annealing, and then, they were continuously cycled for 20 days.

In general, the FBG sensors tested show a stable and repeatable signal, although the type of coating and adhesive used play a role. The sensor with the highest sensitivity was FBG4 with the gold coated fibre bonded to the Ni coated FBGs. The other Ni re-coated FBG (FBG3) sensor exhibit a very similar response, the difference is very small and is due to an added strain component being bonded to the pipe structure. As expected, the standard FBG sensors (FBG1 and FBG2) with the polymeric coating exhibit significantly lower thermal sensitivity compared to the others.

Finally, it was observed that the annealing effect, the wavelength shift after the first heating of the optical fibre sensor, is higher for the Ni re-coated FBGs than for the acrylate coated FBG sensors due to the higher thermal expansion coefficient of the coated metal layer.

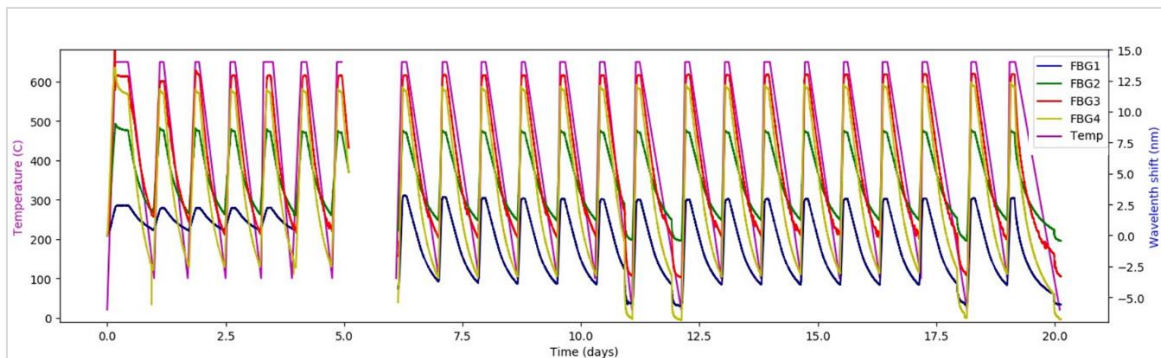


Figure 3.22: Response for the acrylate coated and encapsulated FBG sensors and, Ni re-coated FBG sensors during the thermal fatigue test.

The thermal sensitivity of each of the FBG sensors tested was calculated from the data obtained from the thermal ramp test shown in Figure 3.23. In this case, the temperature was increased from 50°C to 650°C in steps of 100°C, for the first cycle and from 250°C to 650°C for the following four thermal heating ramps, to accelerate the calibration by not having to wait for cooling down to 50°C.

There is hardly any difference between the response of each of the sensors for each applied cycle, the response of the sensors is overlapping, indicating that they are very stable and repetitive. Figure 3.24 shows the quadratic adjustment of each of the sensors, based on the data from this test and Table 3.9 shows the coefficients for the quadratic fit ($y = ax^2+bx+c$). With this adjustment, the characteristic sensitivity of each sensor is obtained.

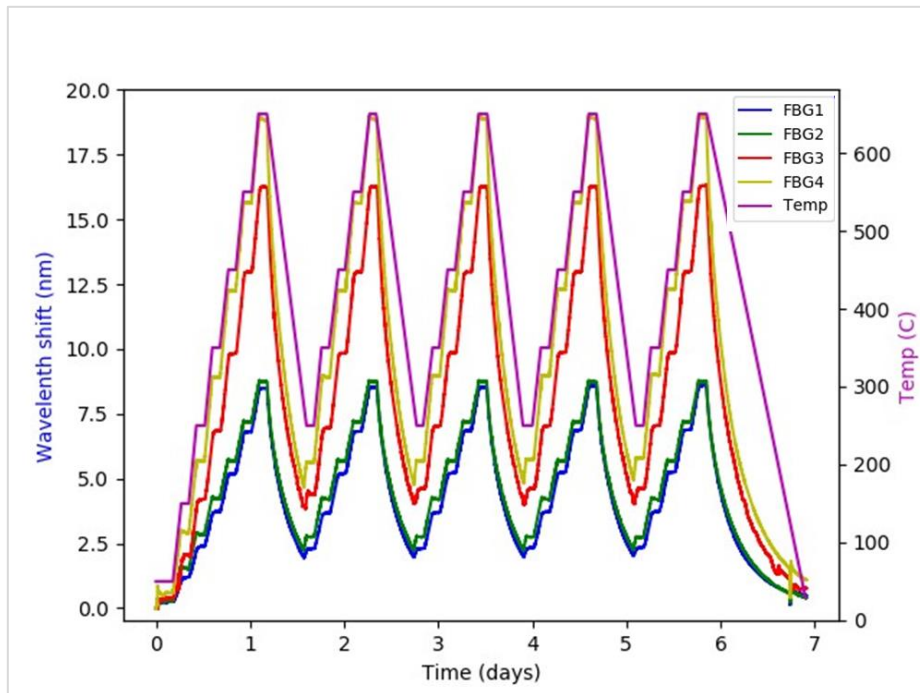


Figure 3.23: FBG sensors response during the thermal calibration.

FBG1 and FBG2 sensors exhibit very similar linear fit adjustment coefficients, as expected. They also show similar thermal sensitivity. The minor differences are attributed to the FBG sensors' placement within the oven, which can result in slight temperature variations between the setpoint temperature and the actual temperature. Regarding the sensitivity of FBG4 and FBG3, FBG4 demonstrates a higher thermal sensitivity than the FBG3 sensor. This is primarily due to the use of metallic-coated commercial optical fibre.

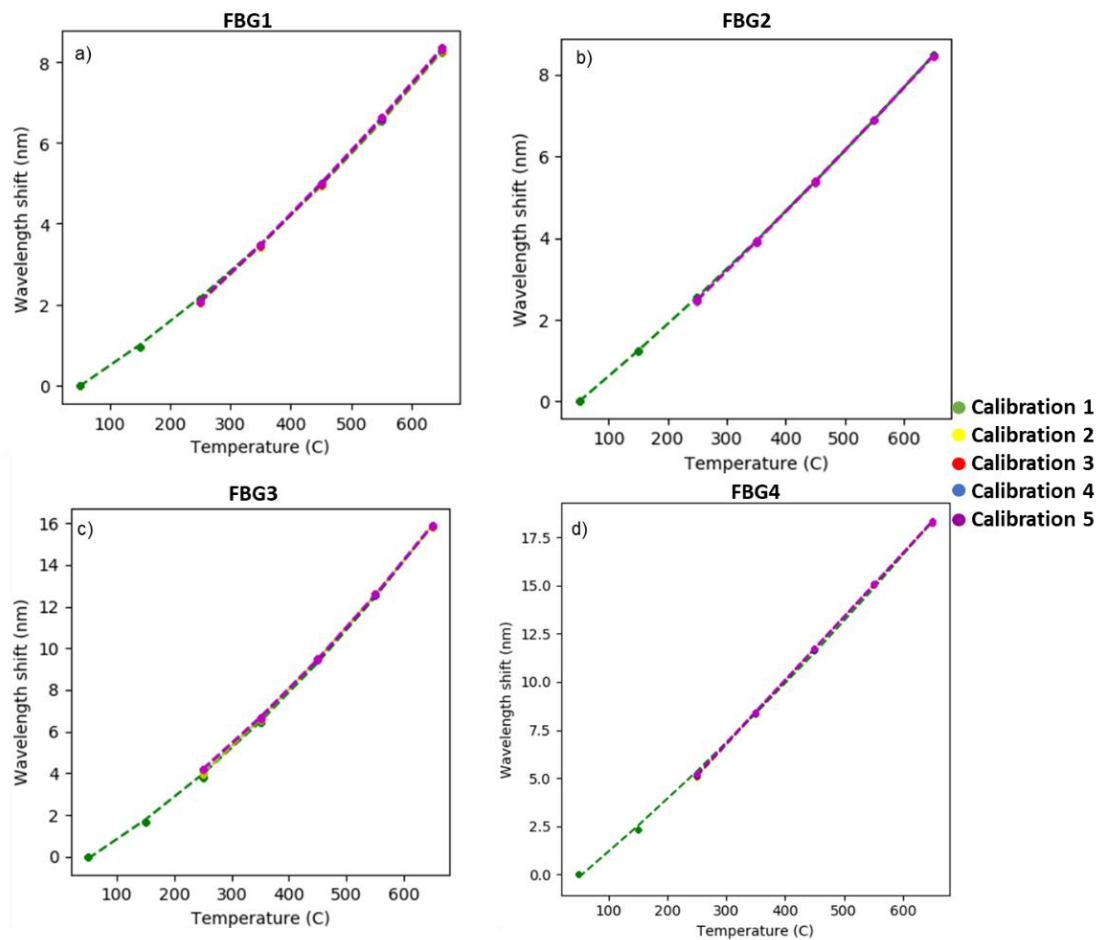


Figure 3.24: Response of FBG sensors tested front to temperature variation: (a) FBG1, (b) FBG2, (c) FBG3, (d) FBG4.

FBG1	a	b	c	r ²	FBG2	a	b	c	r ²
Calibration 1	0.000	0.012	-0.602	0.9999	Calibration 1	0.000	0.009	-0.490	0.9999
Calibration 2	0.000	0.013	-0.899	0.9999	Calibration 2	0.000	0.011	-1.027	0.9999
Calibration 3	0.000	0.013	-0.915	0.9999	Calibration 3	0.000	0.011	-0.999	0.9999
Calibration 4	0.000	0.013	-0.913	0.9999	Calibration 4	0.000	0.011	-0.974	0.9999
Calibration 5	0.000	0.013	-0.919	0.9999	Calibration 5	0.000	0.011	-0.971	0.9999
FBG3	a	b	c	r ²	FBG4	a	b	c	r ²
Calibration 1	0.000	0.016	-0.919	0.9999	Calibration 1	0.000	0.025	-1.418	0.9999
Calibration 2	0.000	0.019	-1.495	0.9999	Calibration 2	0.000	0.034	-3.396	0.9999
Calibration 3	0.000	0.016	-0.750	0.9999	Calibration 3	0.000	0.033	-3.163	0.9999
Calibration 4	0.000	0.016	-0.744	0.9999	Calibration 4	0.000	0.033	-2.997	0.9999
Calibration 5	0.000	0.016	-0.741	0.9999	Calibration 5	0.000	0.032	-2.885	0.9999

Table 3.9: Quadratic coefficients and quadratic adjusted coefficient obtained for the quadratic fit of each calibration made for each FBGs tested.

After annealing, acrylate-coated FBGs become more fragile and can be easily broken, but Ni-recoated FBG sensors have shown greater robustness. This is the major reason for developing a metallic coating to protect the fibre in these high-temperature environments, making it more robust.

3.3.2.2.3 Study of degradation of a Ni re-coated FBG sensor under extreme conditions

Finally, a Ni re-coated FBG sensor (Cu commercial fibre+ Au sputtering +Ni electroplating) was tested at extreme conditions, to know its behaviour and durability. The sensor was first annealed at 1000°C for 2 days, following this, continuous thermal fatigue tests between 650-1000°C were applied, as fast as the tube furnace used would allow. After 25 days of testing, the sensor was still responding to the cycles, so a new annealing temperature was raised to 1050°C continuously (no cycling). Figure 3.25 shows the response of the sensor, which shows a very stable and repeatable response during the heating cycles, but once the temperature was increased and heated continuously, after two days, it stopped giving a signal. It can be concluded that Ni re-coated FBG sensors can withstand extreme temperatures but if they are exposed continuously end up overheating and failing because of the 1000°C temperature exposure.

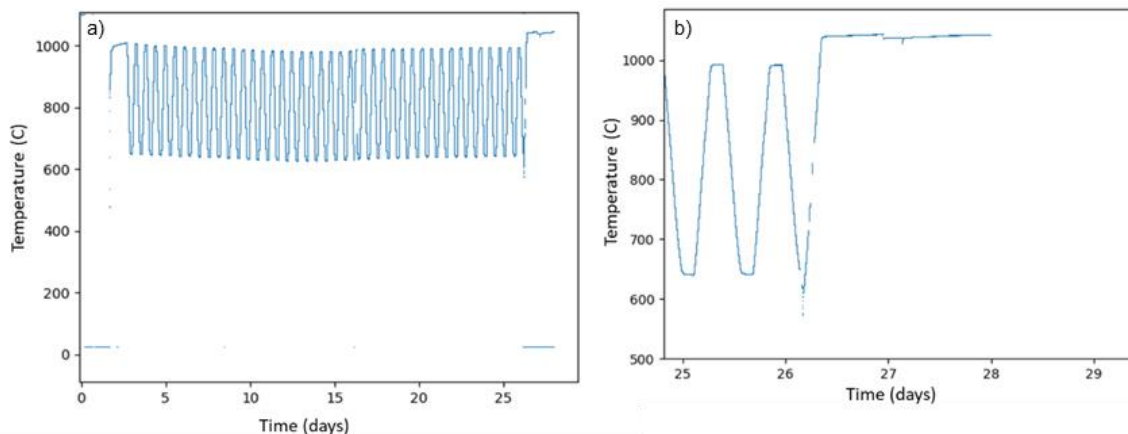


Figure 3.25: (a): Response of the Ni re-coated FBG sensor subjected to thermal fatigue between 650-1000°C. (b): Detail of the Ni re-coated FBG sensor response at 1050°C continuously.

3.4 Summary

In this chapter a procedure to coat and re-coat in fibre FBG sensors and connected optical fibre was developed. The coating procedure is based on a combination of two techniques, the first is to apply a conductive layer on the optical fibre and the second to generate a customized coating with flexibility to use different metals as coating material and to reach different thickness required by applications. The studied techniques to apply the first conductive layer on the fibre were: Electroless, PVD, Ni based-paint, an industrial optical fibre coating process and sputtering deposition, with particular attention trying placed on the FBG section. The sputtering technique of Au has resulted in the most suitable Au conductive layer of a few microns. The electroplating technique was used for a second layer coating as it allows applying a variable thickness using several materials, and has the advantage of being scalable to allow coating of long optical fibre lengths.

After the completion of this two-layer metal coating procedure, both the metallic fibres and metallic FBG sensors were thermally tested (between 650 to 1000°C) obtaining a very stable and repeatable response for the Au, Ni-Cu and Ni-Au coated optical fibres was subjected to fatigue tests. But for a continuous exposure at extreme temperatures (1050°C) the Ni re-coated FBG sensor was overheated, leading to failure. On the case of the Cu re-coated FBG sensors, it was found that the Cu layer at temperatures >400°C became oxidized, and it causes the degradation and ultimate failure of the optical fibre.

Metal coating and embedding fibre optical sensors for industrial applications.

Chapter 3: Metallic coating of Fibre Optic Sensors and their characterization.

Furthermore, a Ni re-coated FBG sensor was bonded to a steel pipeline and tested as a strain sensor up to 650°C for more than 20 days, a very satisfactory result has been obtained.

Annealing plays an important role in ensuring the repeatability of the sensor during its operation. In addition, it was determined from the thermal test made that thicker coated FBG sensors thicknesses better withstand higher temperatures.

Chapter 4. Sensor embedding process and characterization

Smart structures and materials offer a promising technological solution for online health monitoring. They are structures/materials embedded with sensors, which are minimally invasive and in many cases micrometrical fiber optic sensors (FOS). Smart composite structures with embedded FOSs already set a precedent, proven with extended functionality and reliability based on the provided accurate damage and lifecycle predictions. Embedding sensors in a composite fabrication process is relatively straightforward because the temperatures reached during the process do not damage the FOSs. Also placing and fixing the fibre is feasible: resin or concrete are easy to handle while in the liquid phase during infusion. This, however, is not the case in metallic structures, which requires welding, casting or other high temperature processes to embed the fibre optic into the metallic structure.

The aim of this chapter is to embed the metallic re-coated optical fibres and FBG sensors into metallic structures to generate a smart component in order to able to conduct real-time condition monitoring and thus have the ability to act preventively before component failures occurs.

To embed fiber optics into metallic materials, a protective coating on the fiber is needed. In Chapter 3, a detailed procedure to coat and re-coat the optical fibres, obtaining thicker metallic coatings, was explained. These coatings demonstrated good high temperature resistance and protection for the optical fibre sensors. Using electroplating deposition technique it is possible to achieve a coating thickness, ranging from a few micrometers to hundreds of micrometers for different metals.

For the embedding study described in this chapter, Copper (Cu) and/or Nickel (Ni) were the materials selected to from the electroplating deposition coating because of their respective high melting point. This property is very important to protect the fiber during the embedding process wherein high temperatures were reached (700°C ~1400°C, depending of the added material melting point).

In this chapter, results are included for Ni and Cu re-coated optical fibres and FBG sensors being embedded into metallic structures of several materials, such as Sn alloy, Cu and Inconel. Different techniques such as electroplating, TIG welding, casting and Laser Cladding were also studied to embed the coated optical fibres.

4.1 Embedding process using the electroplating deposition technique

The first technique studied for embedding Cu re-coated optical fibres was based on electroplating deposition. This technique is easy and non-obtrusive for bonding metallic coated fibre optic to metallic structures. It offers the possibility to apply different materials which is very useful for integrating the optical fibre in the metallic structure surface and protecting the sensor in harsh environments applications.

In this study, some commercial Cu coated optical fibres of diameter of 165µm and a total length of 50mm were fixed, at their extremes, on a Cu metal sheet of 40x20x2mm (length x width x thickness). The bond was made using adhesive tape (magic tape or insulating tape). Figure 4.1 shows the two strategies for bonding Cu coated optical fibre to the Cu metal sheet. Figure 4.1.a shows the Cu coated optical fibre bonded directly to the Cu metal sheet surface, while in Figure 4.1.b a small groove was made in the Cu metal sheet to accommodate the Cu coated optical fibre prior to bonding. In both cases, the surface of the metal sheet was sanded and cleaned

with acetone and the Cu coated optical fibre was also cleaned using acetone. Then, the Cu coated fibre and Cu metal sheet were immersed in the electroplating Cu bath and connected to the power source, acting as cathode and a Cu metal sheet as the anode.

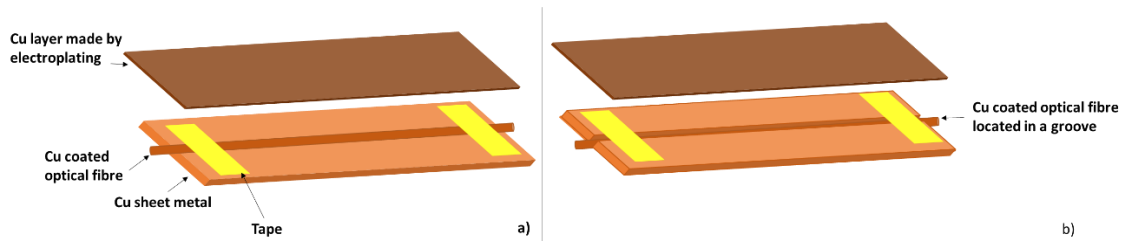


Figure 4.1: Electroplating bonding strategies studied; (a): Cu re-coated optical fibre located on the surface of a Cu metal sheet (b): Cu re-coated optical fibre located in a groove made in the Cu metal sheet.

For this electroplating fibre-sheet bonding study, different time and intensity parameters were tested, which are summarized in Table 4.1. It was observed that the best bonding was achieved when the current intensity was set at 0.25A and in most cases using the groove strategy. For these tests 0.25A was the optimum because the current density achieved was the ideal for this sample size. The grain of the deposited material was small, but sufficient to bond and embed the fibre into the sheet, while at 0.5A, the grain is larger and does not uniformly cover and embed the fibre. . Figure 4.2.a shows the result for a test conducted at 0.25A without the groove on the Cu metal sheet. It was observed that the Cu coated fibre protrudes above the Cu sheet surface. A thicker layer of Cu is required to bridge that *bulge* and correctly bond the fibre to the sheet surface. The deposited Cu is coating the fibre and the metal sheet but, it failed to embed the fibre in the deposited copper, so the bond was not good. However, for the second embedding strategy, with a groove on the Cu sheet surface as Figure 4.2.b shows a improvement compared to Figure 4.1.a. After electroplating deposition, the fibre is completely bonded to the Cu metal sheet and embedded in the deposited Cu, as Figure 4.2.c shows. In this case, the groove helps the fibre to be embedded in the deposited material because the Cu deposition completely covers it within the groove.

Although electroplating deposition represents a valid, simple, and cost-effective technique for both bonding and embedding, it requires proper 'shielding' of the areas that are not to be coated during the electroplating process. This becomes a major challenge when a bath deposit is required with the size of the component or part into which the optical fibre sensor is to be embedded, such as in the use-case of bearings. In this scenario, embedding the fibre in the bearing using electroplating deposition would necessitate locating and securing the sensor within the anti-friction bearing, while also protecting the conductive parts of the bearing that shouldn't be coated before immersion in the electroplating bath. This process leads to a significant increase in production time and requires specific training for the workers responsible for it.

Intensity (A)	Time (min)	Picture	Final diameter on the OF section (mm)	Sheet thickness (mm)	Adherence Cu OF and Cu sheet	Final thickness of Cu layer on the Cu sheet (mm)	Groove
0.25	60		280	0.53	Bad	0.05	No
	120		329	0.59	Bad	0.11	No
	420		517	0.89	Good	0.41	No
	120		296	0.60	Good	0.15	Yes
	300		476	0.88	Good	0.40	Yes
	420		379	0.84	Good	0.36	Yes
0.5	60		343	0.60	Bad	0.12	Yes
	120		446	0.68	Bad	0.20	No

Table 4.1: Main results of electroplating bonding study.

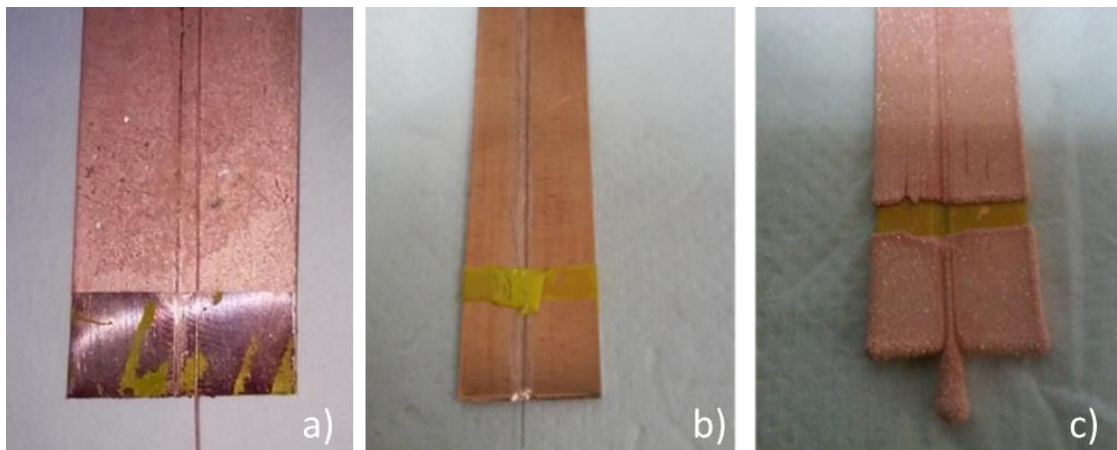


Figure 4.2: (a) unbonded Cu coated fibre to the Cu metal sheet after electroplating process. In this case, the metal sheet has no groove to locate the Cu coated fibre. (b): Cu coated optical fibre located in a groove made on the Cu metal sheet, before applying electroplating to embed the Cu fibre in the Cu metal sheet. (c): Cu coated optical fibre embedded in the Cu metal sheet after electroplating depositing of Cu. The fibre presented good bond with the Cu metal sheet.

4.2 Embedding process by casting

The second technique studied to embed the Cu or Ni re-coated optical fibres into metallic structures, was casting. Casting is a manufacturing process in which a metal is heated in a bath up to its melting point, then, the molten metal material is poured into a mold, which contains a hollow cavity of the desired shape, to solidify and subsequently demoulded. To do so it usually

requires the re-coated optical fibres to be exposed to a high temperature for a relatively long time (<700°C, >2h, depending of the casted material). But in this case, the metal material used to embed the optical fibres was an antifriction material based on a tin alloy, so it had a relatively low melting point (220°C-250°C), which makes it easier for casting. For ease of embedding the re-coated optical fibres, a hole was drilled in a steel piece. The steel piece, without the Cu re-coated fibre, was then inserted into a molten tin alloy bath (at 440°C), shown in Figure 4.3.a, for a few minutes, to temper it and to ensure a good bond between the steel and the tin alloy, during the casting process. Subsequently the steel piece was removed from the bath for insertion of the re-coated fibres through the hole as shown in Figure 4.3.b. Finally, the molten tin alloy was poured into the machined hole, where the Cu re-coated fibre was located, until completely filled as shown in Figure 4.3.c. Two fibres were casted using this method, one coated with Ni (total diameter of 462µm formed by 125µm of silica, 317µm of Ni, 20µm of Cu) and the other with Cu (total diameter of 560µm of which 220µm was of Cu). Both fibres survived the casting process as illustrated in Figure 4.2.c, where red light was transmitted through the casted fibres.



Figure 4.3: (a) Tin alloy molten bath. (b) Cu re-coated optical fibre embedded in the tin alloy by casting. (c) red light emerging from the embedded fibre.

After this validation, a specific specimen of steel, with a machined channel located in the centre as shown in Figure 4.4.a, was manufactured in order to embed a Ni re-coated FBG sensor using the casting technique. The embedded specimen was subsequently tested using a loading machine to analyse the embedding robustness and sensor response. The Ni re-coated FBG sensor with a total diameter of 442µm (and coating thickness of 158µm) was manufactured using a combination of Au sputtering and Ni electroplating, as detailed in Chapter 3.

The procedure to embed the Ni re-coated FBG sensor was the same as that explained above. First the steel specimen and the Ni re-coated FBG sensor were immersed in the melted tin alloy bath, it was heated to assure a good bond between steel and antifriction material, and then, the Ni re-coated FBG sensor was placed in the channel and the antifriction material was poured. Figure 4.4.b shows the Ni re-coated FBGs embedded in the specimen. The FBG sensor survived the embedding process. Figure 4.5 shows the near infra-red spectrum of the Ni re-coated FBG sensor before and after being embedded. As expected, the spectrum, measured with the Yokogawa-AQ6370D, has shown blue shift, confirming that the FBG sensor is contracts when the metal solidifies.



Figure 4.4: (a): Steel specimen made specifically with a centre groove for casting (b): Steel specimen after the casting process with the Ni re-coated FBG sensor embedded.

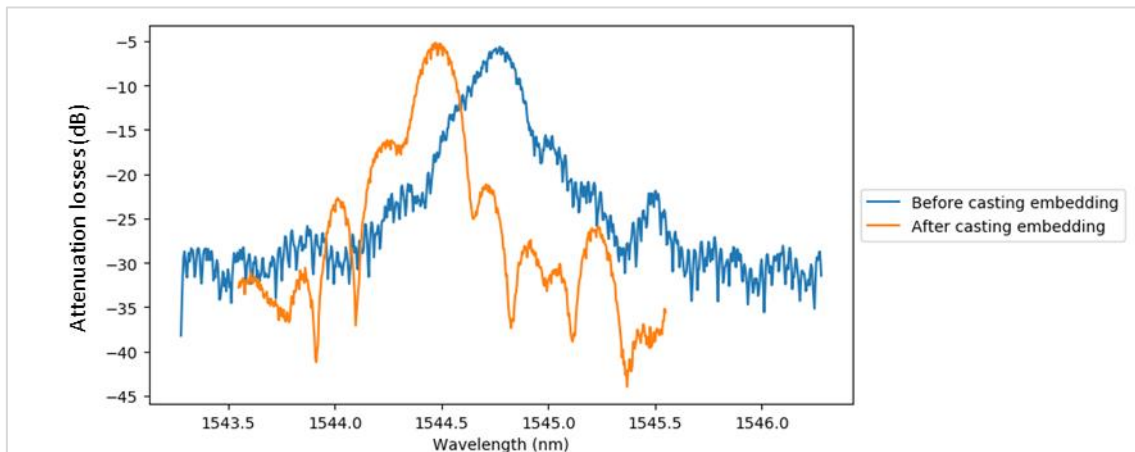


Figure 4.5: Experimental measured reflection spectrum of the Ni re-coated FBG sensor before and after being embedded by casting process.

Once embedded, this specimen was subjected to tensile tests using the universal testing machine shown in Figure 4.6.a. The sample was clamped to the tensile testing machine at both ends, where a longitudinal stretching force was gradually applied in steps, from 0 to 80 kN, which correspond to strains in the range from 0 $\mu\epsilon$ to 2000 $\mu\epsilon$. To avoid cross-sensitivity between strain and temperature, the laboratory temperature was constant during the tests.

The tensile force increases until the specimen breaks as shown in Figure 4.6.b. Figure 4.5.c shows the broken sample after a higher load than 80kN was applied. It is observed that the Ni re-coated FBG survived despite the steel and antifriction material breaking, this exhibiting a higher mechanical resistance than the specimen into which it was embedded.

Figure 4.7.a shows the response of the embedded Ni re-coated FBG sensor for each applied load and Figure 4.7.b shows the linear fitting between the wavelength shift of the embedded FBG and the applied load. The sign response of the FBG sensor to the applied load is linear during

the entire test, although it could be observed a subtle change of tendency after applying 40kN of load.



Figure 4.6: (a) Tensile test set-up. (b) Ni re-coated FBG sensor embedded in a steel specimen by casting, after the tensile test; (c) The specimen is broken, but the Ni re-coated FBG sensor survived.

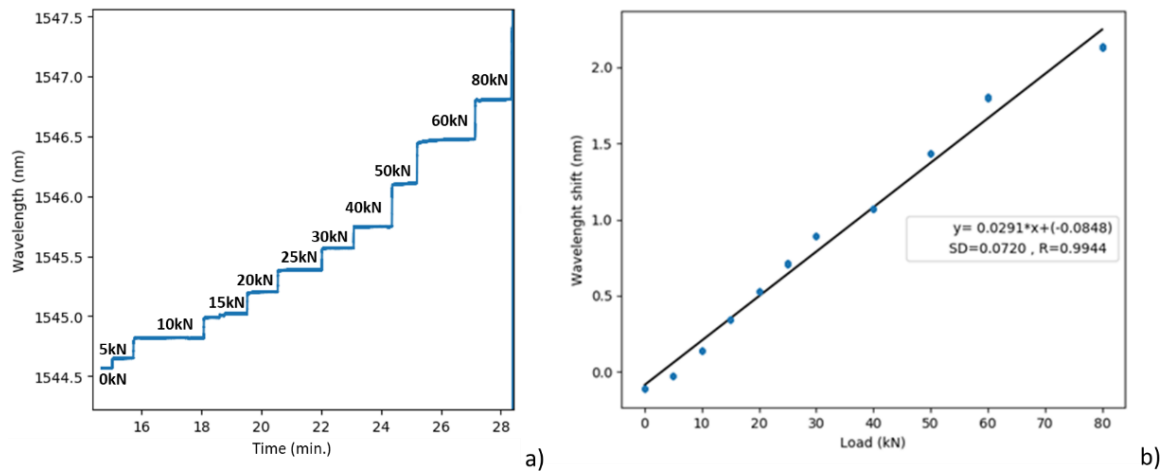


Figure 4.7: (a) Response of a Ni re-coated FBG sensor embedded by casting to the increase of tensile force applied. (b) Linear fitting between wavelength shift of the FBG sensor and the applied load.

Finally, the central part of the specimen, where the FBG sensor was located, was cut and its transversal section was analysed to determine the bond status. Figure 4.8 shows the cross-section of the Ni re-coated FBG sensor embedded in the antifriction material and the frontier interface between the steel and the anti-friction material bond.

The bond between the antifriction material and steel (straight line in Figure 4.8.a) exhibits good bond appearance at this section, with no evidence of cracking or voids. Figure 4.8.b, Figure 4.8.c and Figure 4.8.d, show the details of the bonding section between the Ni re-coated optical fibre and antifriction material surrounding. As shown in Figure 4.8.b and Figure 4.8.c, the antifriction material shows some cracks in the region of the upper area of the fibre and in Figure 4.8.c and Figure 4.8.d, a minor gap between them (black line) is observed. This gap could have been formed during the tensile test or could have occurred during the casting process due to the difference in temperature between the materials during the casting process.

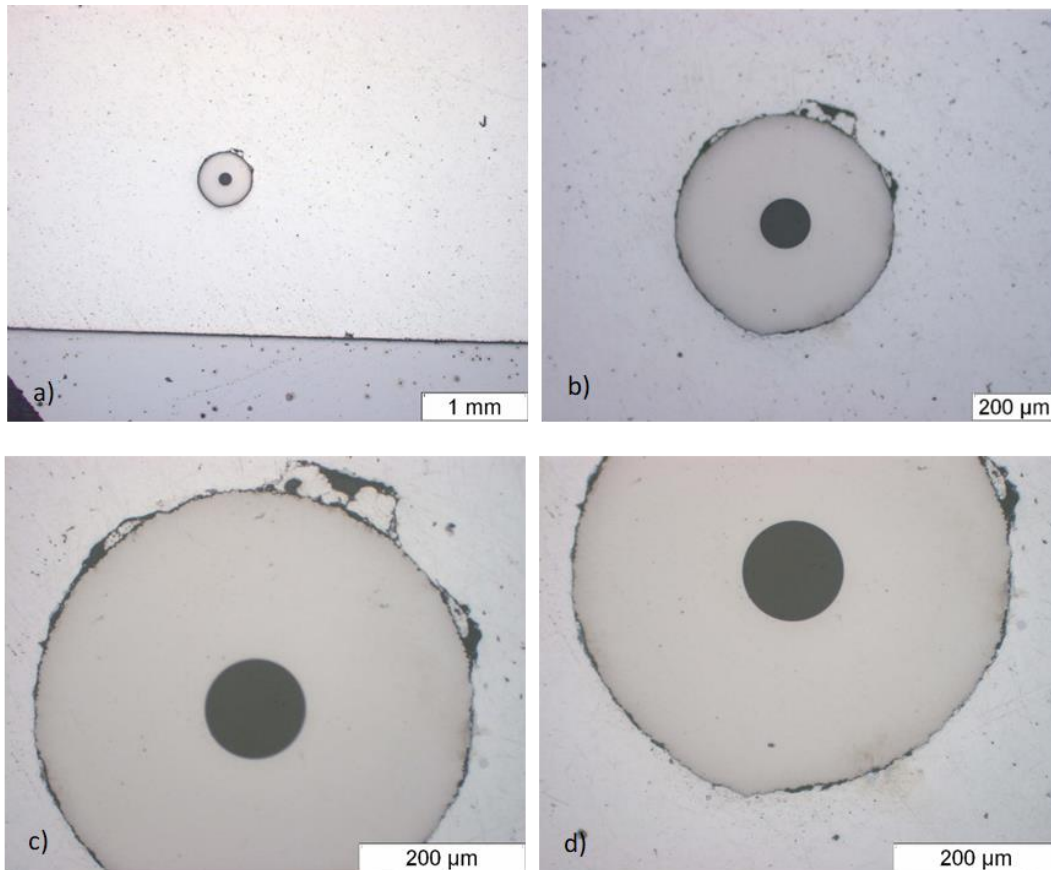


Figure 4.8: Cross-section of the Ni re-coated FBG sensor embedded in the antifriction material by casting. (a): Ni re-coated FBG sensor picture of cross-section appearance in the antifriction material and steel base material. (b): Detail of the embedded Ni re-coated FBG sensor in contact with the antifriction material. (c) and (d): Cross-section detail for the frontiers bond between the antifriction material and the Ni re-coated FBGs.

In conclusion, machining the steel specimen to generate a groove, for embedding sensors by casting, may have affected its mechanical strength, which contributes to its failure, as the antifriction material has lower mechanical strength than steel. This embedding technique, however, could be useful for embedding fibre optic sensors in structures where high mechanical requirements are not required, and where the melting point of the molten metal is relatively low (<800°C) to avoid affecting the optical fibre integrity.

On the other hand, the embedded FBG sensor has withstood the applied load with a linear response demonstrating its resilience.

4.3 Embedding process by Laser welding techniques

In this section, a laser cladding process is studied for embedding metallic re-coated fibre optic sensors. The laser cladding technology is a special welding technique in which the laser is the heat source of the welding process. Figure 4.9 shows the laser cladding set-up used for this study, comprising the laser head used and the main laser cell components. The aim of this process is to fuse and distribute the added material between the pieces to bond, without melting them. It is possible for the added material to be deposited layer-by-layer, generating an Additive Manufacturing (AM) process. The added material can be in either powder or wire format.

The laser cladding technology discussed offers several advantages over other welding techniques in terms of embedding FBG sensors, achieving both high accuracy and high efficiency as well as good repeatability and reproducibility. It is possible to control and adjust the key parameters, even during the embedding process, to achieve the highest bonding quality.

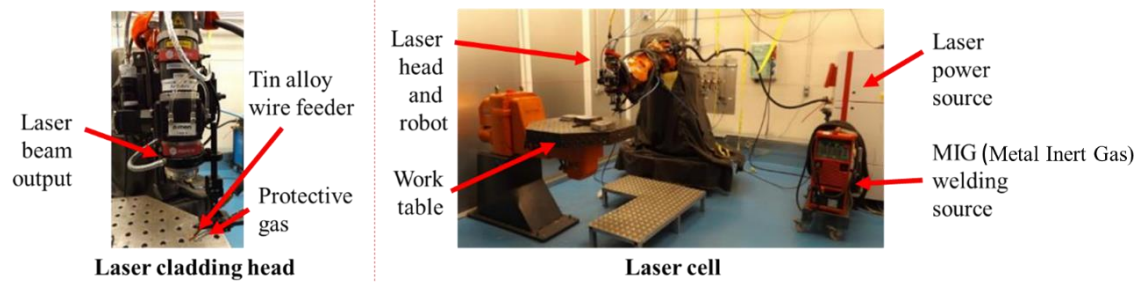


Figure 4.9: Laser cladding set-up.

In this section two different studies applying two different added materials to embed the re-coated fibre optic sensors is explained. In the first case, the added material was the same tin alloy, antifriction material, as those discussed in the previous section and the optical fibres were embedded into a steel piece with a tin coating layer of 3 mm thickness, simulating the same material composition of the antifriction material bearing (NEXT-BEARING use-case), which are the final intended product for FOS integration.

In the second laser embedding study, the re-coated fibre optic sensors were embedded into a Ni-Cr alloy, using Laser Cladding as an AM process. In this way, the potential of the laser process for embedding the re-coated fibre optic sensors in materials with high and low melting points is studied.

4.3.1 Laser embedding of sensors into tin alloy

In this first laser embedding study, Ni and Cu re-coated optical fibres and FBGs, with diameters between 200-900 μm (starting from silica fibres of 125 μm of diameter), were embedded using the Laser Cladding process. Two tin alloy wires of diameter of 1.6mm and 2.4 mm, respectively, were used as added material. The embedding tests were made on a steel specimen with a layer of antifriction material deposited by laser. To apply the antifriction material directly on the steel substrate with a good bond, a higher laser power was needed, because the steel has a higher thermal resistance than the antifriction material. This was followed by embedding the re-coated optical fibres into a steel substrate with a layer of a few millimeters (3mm) of anti-friction material, considered as a precursor research prior to the latter sensor being embedded into a bearing antifriction layer for long-term bearing condition monitoring.

In this study, a cross-comparison was made by using a laser with less power but using more added material or the other way around, i.e. with higher power but less added material. The laser used was the Laserline LDF 6000-40VGP diode laser with 6KW maximum optical power coupled to 0.4mm diameter optical fibre, and the parameters of the laser were: power between 1.2-2.1kW, head speed of the laser 50 mm/s and speed range of the wire 2.5-3.5 m/min.

To embed the Ni and Cu re-coated optical fibers, the following strategies are deployed as illustrated in Figure 4.10, aiming to identify the most suitable approach with the least heat generated during the embedding process.

1. Overlapping the recharge lines of tin deposition, transverse to the re-coated fibre. (a typical method to apply laser cladding)
2. Overlapping the recharge lines of tin deposition, longitudinal to the re-coated fibre. (a typical method to apply laser cladding)
3. Interlayer recharge lines, transverse to the re-coated fibre, aiming to minimize the thermal damage.

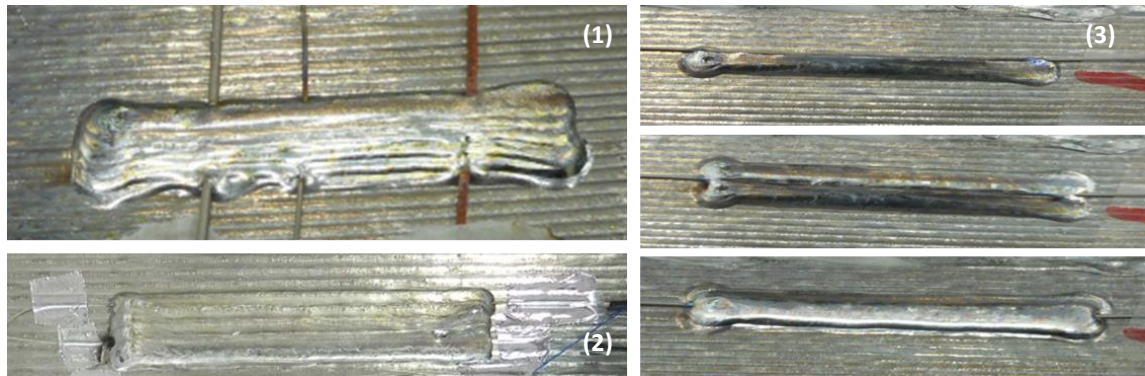


Figure 4.10: Embedding strategies studied to embed the Ni and Cu re-coated optical fibres by Laser Cladding process. (1): Embedding strategy based on the overlapping the recharge lines of tin deposition, transversal to the coating fibre. (2): Embedding strategy based on the overlapping the recharge lines of tin deposition, longitudinal to the re-coated fibre. (3): Embedding strategy based on the interlayer recharge lines, transversals to the re-coated fibre.

4.3.1.1 Results from the tin alloy with a diameter of 1.6 mm

In this case, only Ni re-coated optical fibres were tested. They were located on a steel specimen with an antifriction material (tin alloy based) surface. The fibre was of a total length around 250mm with both ends fixed to the antifriction layer using an Al tape, to prevent it from moving during the embedding process. After this, the laser line was programmed to embed the fibre using one of the strategies explained above and the laser power applied was the only configurable parameter changed during the tests. It is possible to determine the fibre survivability, either by using a red laser light transmission inside the embedded fibre or measuring the losses generated by the embedding process.

Using the above method, Table 4.2 (left columns) presents those unsuccessfully embedded Ni-recoated optical fibres while Table 4.2 (right columns) the successfully embedded sensor. The losses of N37 and N23 were measured and the N23 fibre which was embedded using the 3rd embedding strategy, shows minimal losses. Among the 'survival' fibres shown in Table 4.3, N23 has the minimal coating thickness with diameter of 507 μ m.

However, the cross-sections of all the successfully embedded fibres exhibits different degrees of thermal damage and surface degradation. This is, because the temperature can peak up to 700°C during the laser embedding process and, although, nickel has a higher melting point, with a very thin coating layer (<80 μ m), it can be thermally affected at lower temperatures.

Another issue detected, during the 1.6mm diameter tin alloy wire deposition tests, was that any defects or impurities intrinsic to the wire generated a defect in the bead of deposited material. Whereas with the 2.4mm wire, as shown in section 4.3.1.2, such impurities were not generated, since, having a larger diameter, the melted material of the wire itself was capable of absorbing the impurity without generating damage and making the embedding process safe and stable.

Reference	Picture	Fibre diameter (µm)	Losses (dB)	Embedding strategy	Laser power (W)	Reference	Picture	Fibre diameter (µm)	Losses (dB)	Embedding strategy	Laser power (W)	Cross-section
N27		573	-	1	2100	N40		621	-	3 and 4	2100 and 1800	
N17		394	-	4	2100	N42		739	-	1 and 4	2100	
N9		492	-	1	2100	N37		551	3.05	1 and 3	1500	
N10		312	-	1	2100	N25		838	-	4	2100	
N6		221	-	2	2100	N23		507	1.85	4	2100	

Table 4.2: Left: Ni coating fibres embedded unsuccessfully by Laser brazing using 1.6mm of diameter tin-alloy wire. Right: Ni coating fibres embedded successfully by Laser brazing using 1.6mm of diameter tin-alloy wire.

4.3.1.2 Results from the tin alloy with a diameter of 2.4 mm

In this subsection, laser cladding embedding of Ni and Cu re-coated optical fibres were done using a tin-alloy wire with a diameter of 2.4mm. Similar to the above, the 3rd embedding strategy was used, so do steel-antifriction coated specimens (with or without grooves of 1.5x1.5mm), into which the re-coated optical fibres were embedded. Figure 4.11 shows the final appearance of the antifriction coated steel-base sample, where the embedding re-coated fibres trials were carried out, without machined grooves. A length between 5-8cm of each tested fibre was embedded, weld seams show a good appearance without pores or non-uniformities.

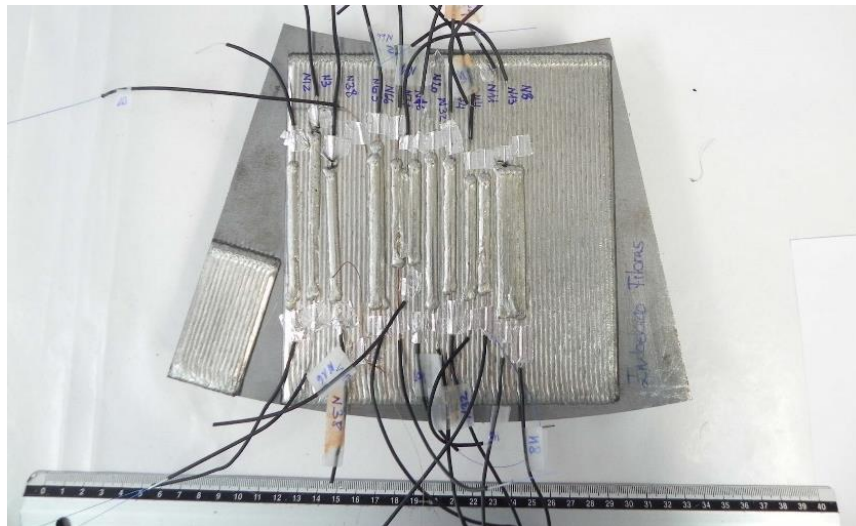


Figure 4.11: Steel-antifriction material sample appearance after the re-coated optical fibres laser cladding embedding tests.

Table 4.3 summarises the laser cladding results obtained from embedding Ni and Cu re-coated optical fibres in the specimens without any groove. Cu re-coated fibres with a diameter around 400µm and Ni re-coated fibres between 250-500µm were tested. In addition, laser powers of 1500W, 1800W and 2000W were applied to analyze the differences caused by the change in the laser power, coating material and coating thickness over the laser cladding process. The laser

Metal coating and embedding fibre optical sensors for industrial applications.

Chapter 4: Sensor embedding process and characterization.

power of 2000W, compared to 1500-1800W, is observed to be too strong as it melts the coating material of the fibre.

Regarding the coating material and coating thickness, lower losses were obtained from the embedded re-coated fibres of larger diameters (caused by the thicker coating), but the coating material, Cu or Ni, did not make any difference.

*Metal coating and embedding fibre optical sensors for industrial applications.
Chapter 4: Sensor embedding process and characterization.*

Coating	Fibre diameter (µm)	Loss before embedding (dBm)	Loss after embedding (dBm)	total LOSS (dB)	Laser Power (W)	Embedded length (cm)	Cross-section after embedding with laser
Cu	399	11.26	12.35	1.09	1500	6.3	
Cu	480	0.6	1.1	0.5	2000	1st step: 7,7	
						2nd step: 7,3	
Cu	481	2.18	2.18	0	1500	5	
Ni	237	2.08	3.6	1.52	1800	7.2	
Ni	242	2.87	broken	-	1800	7.1	
Ni	252	2.65	broken	-	2000	5.6	
Ni	271	2.41	23.9	21.49	1500	5.7	
Ni	347	2.54	3.44	0.9	1500	4.1	
Ni	348	3.92	5.58	1.66	2000	7.2	
Ni	400	14.67	17.25	2.58	1800	4.8	
Ni	413	4.98	6.02	1.04	1800	6.3	
Ni	455	20.63	39.33	18.7	2000	6.7	
Ni	495	6.37	6.93	0.56	1500	7.8	

Table 4.3: Results for laser brazing with the tin-alloy wire of 2.4mm diameter.

In summary, from this Laser embedding study demonstrated better results for the tests made using a tin-alloy welding wire of 2.4mm of diameter because it was possible successfully to embed Cu and Ni re-coated fibres with a lower thickness of coated layer than that required for the tests made with the 1.6mm of welding wire diameter. Although the losses measured were higher for the tests made with the 2.4mm of welding wire diameter.

The following laser embedding cladding tests were made on the specimen with the machined grooves. Figure 4.12.a shows the strategy used to embed the Ni and Cu re-coated optical fibres into a specimen with groove and Figure 4.12.b the final appearance of the specimen Ni or Cu re-coated optical fibres were placed in the groove with both ends fixed with Al tape. Then, the laser beam was delivered to the corner groove rather than directly onto the fibre, causing the molten material to drip onto it. As in the case of the tests carried out on the test piece without grooves, in this case a laser deposited track was applied on one side of the groove, and after this, a second track was applied on the other side of the groove, in order to embed the fibre indirectly, without passing the laser directly on the fibre. After the second laser track, the fibre was almost completely embedded. Finally, a last laser track was applied above the fibre to complete its embedding. These tests were carried out at 1500W as result of the previous trials show that the fibre was well embedded at this power.

Following these tests, optical fibre lengths between 4-9cm were embedded using different parameters of current and speed, and most have a good finish and embedding quality (Figure 4.12.b).

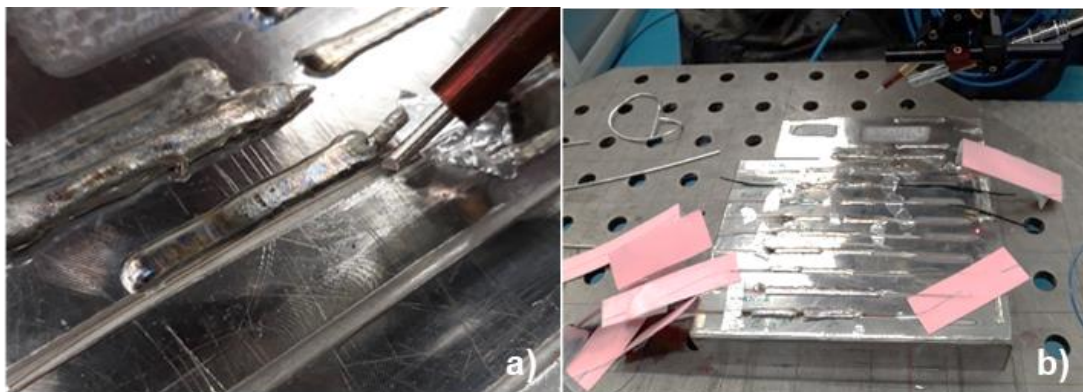


Figure 4.12: (a): embedding strategy with a groove in the specimen. (b): Final steel-antifriction coated specimen appearance at the end of the laser cladding embedding tests.

Table 4.4 shows the cross sections of the Ni and Cu re-coated optical fibres embedded using laser cladding into sample grooves. The first point noted is that the whole groove cavity is filled, meaning that the embedded optical fibre is well bonded to the antifriction material. The measured losses were lower compared to those without a groove. In addition, the Cu coated sensor with a minimum diameter of 375 μ m and Ni coating of 236 μ m were successfully embedded, which is comparable to the case without grooves. The Cu re-coated optical fibres with a diameter smaller than 600 μ m exhibit some thermal damage (i.e. pores from the molten material), but Ni fibres present a better appearance for all the coating thickness tested. It can therefore be concluded that this embedding strategy with groove, generates less thermal stress on the fibre, especially for the fibres coated with Ni.

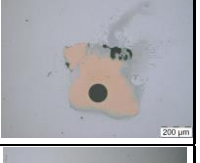
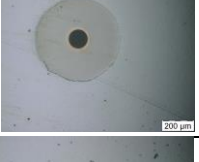
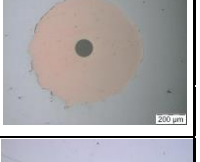
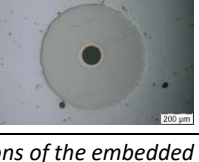
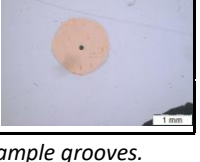
Coating material	Fibre diameter (μm)	Losses (dB)	Cross-section	Reference	Fibre diameter (μm)	Losses (dB)	Cross-section
Ni	236	-		Cu	375	-	
Ni	440	0.06		Cu	424	0.1	
		0.3				48	
Ni	520	-		Cu	600	-	
Ni	657	-		Cu	867	1	

Table 4.4: Cross-sections of the embedded Ni and Cu re-coated optical fibres into sample grooves.

In conclusion, it is possible to embed metal-coated optical fiber into the antifriction material using laser cladding. It is observed that, using this technique, the re-coated layer of the optical fiber suffers some thermal damage, especially for the Cu coating layer. The minimum diameter of a coated fiber for embedding is 236 μm using a 2.4mm wire diameter of added material and 507 μm using 1.6mm of added material, and the best results obtained were using the embedding strategy number 3. Regarding the laser parameters, the best embedding results were obtained using a power between 1500-1800W, with a laser speed of 50 mm/s and the wire speed of 3 m/min.

4.3.1.3 FBG sensors embedding by laser cladding and characterization

Following the feasibility study to embed re-coated optical fibres using laser cladding as discussed above, some Ni and Cu re-coated FBGs were subsequently manufactured and embedded using the same procedure. They were then mechanically and thermally tested to analyse their response and sensitivity.

Two metal re-coated FBG sensors were embedded by laser cladding, into a specimen of steel with an antifriction material coating of 3mm of thickness. The specimens had a specific geometry, shown in the Figure 4.13, for ease of tensile testing using the stressing machine described earlier (section 4.2).

One of the embedded FBGs was re-coated with Ni providing a total diameter of 398μm (Figure 4.13) and the second FBG was re-coated with Cu with a total diameter of 508μm. The tin alloy wire diameter used for these tests was 2.4mm and the laser power was set to 1800W.

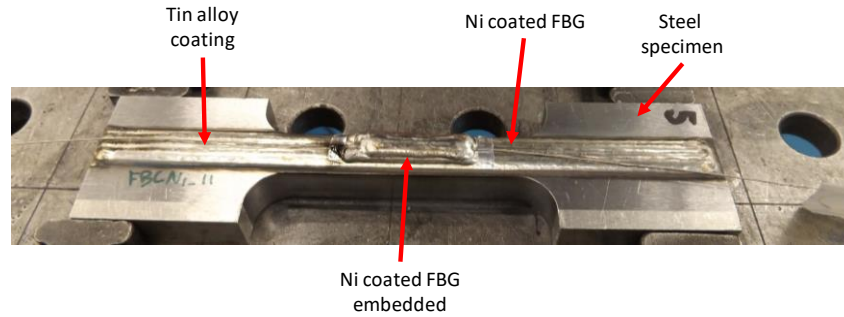


Figure 4.13: Ni re-coated FBG sensor embedded by laser cladding into antifriction material.

The thermal sign response of the embedded FBGs was recorded when both specimens were subjected to step temperature changes was in the range 50°C to 200°C in steps of 50°C. The maximum temperature reached was 200°C because the antifriction material melting point is around 250°C.

Figure 4.14 shows the thermal sign response and linear fit for each embedded FBG sensor tested. The embedded FBG sensors show a stable and repeatable response over all the thermal repetitions made. Using linear fitting, the thermal sensitivity of 0.23nm/°C is obtained for the embedded FBGs with Ni re-coating and 0.29nm/°C for the Cu due to its higher thermal coefficient. In both cases, little change in the thermal sensitivity is observed before and after embedding.

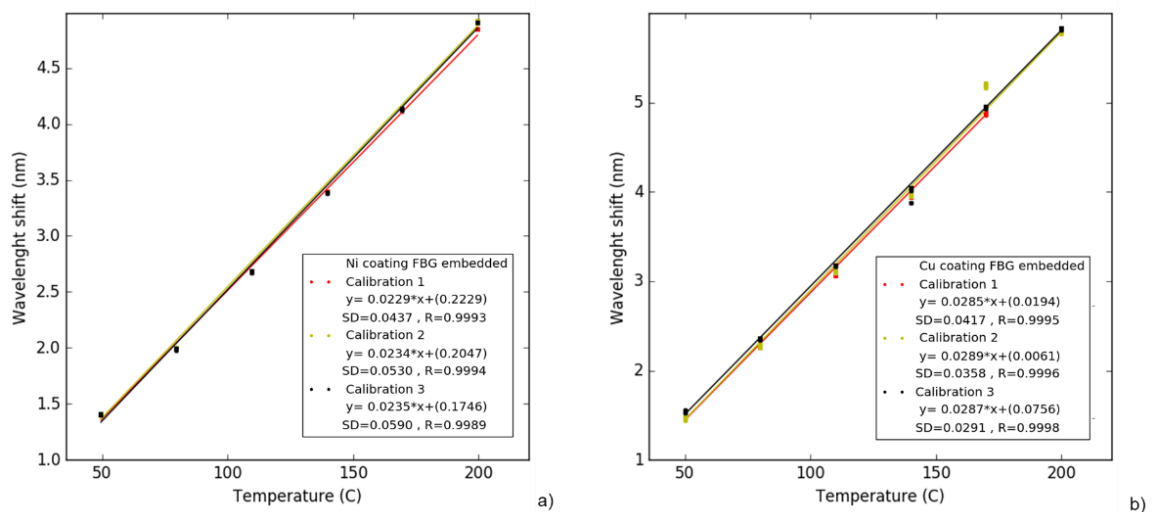


Figure 4.14: Re-coated FBG embedded sensors response during the thermal tests. (a): Ni re-coated FBG sensor response and linear fit. (b): Cu re-coated FBG sensor response and linear fit.

After the temperature calibration was completed, several repetitive tensile tests were carried out on the specimens. The first tensile test was undertaken by increasing the tension from 0 to 20kN, in steps of 2kN for the Cu embedded sensor (Figure 4.15.a) and in steps of 5kN for Ni (Figure 4.15.b). For these tests, conventional strain gauges were glued on the surface of each specimen (close to where the FBG was embedded) to allow for a direct comparison of their respective responses.

Figure 4.15 illustrates the regular 'steps' with the application of a load step changes over the total duration of the test (1600 seconds for Cu-recoated and 3500 seconds for Ni-recoated). It should be noted that the sensitivity to loading for both sensors is different. This arises from the different geometries of the samples, as the locations where the sensors were embedded were different and thus each cross-section was different as well.

The results of the investigation show that the response of both FBG sensors embedded is linear with the load and repeatable (as can be seen from Figure 4.16). The measured sensitivity of the sensors (determined from the slopes of the graphs) was shown to vary between $0.9\text{pm}/\mu\epsilon$ and $1\text{pm}/\mu\epsilon$, which is in accordance with the strain sensitivity measured for conventional, non-embedded FBG-based strain sensors. The graphs illustrated show three measurements for the strain increasing (Up 1 to Up 3, load increasing), followed by the strain decreasing (Down 1 to Down 3, load applied decreasing) for both Cu embedding (Figure 4.15.b) and Ni embedding (Figure 4.15.a) (it should be noted that the Down 1 steps for Cu coated FBG sensor was discarded because the response of the gauge was not linear). In both cases (Figure 4.16) the result from the first application of the strain (Up 1) varies most from the other calibrations because of the initial residual strain from relief at the beginning of the calibration process – it can be seen from the subsequent strain applications that this effect *settles*, for the Ni embedded fibre, as is seen in the other graphs (Figure 4.16.a), while in the case of the Cu embedded fibre, the wavelength for zero load shows a minor shift for each load cycle carried-out, which could be related with the strain relief.

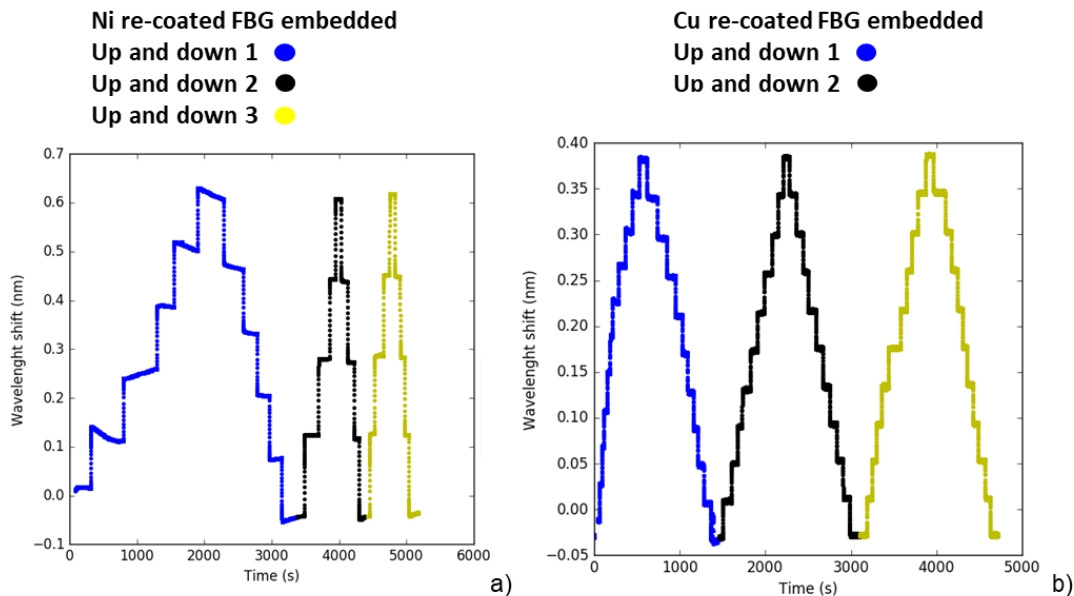


Figure 4.15: (a): Ni re-coated FBG sensor embedded response during the tensile tests. (b): Cu re-coated FBG sensor embedded response during the tensile tests

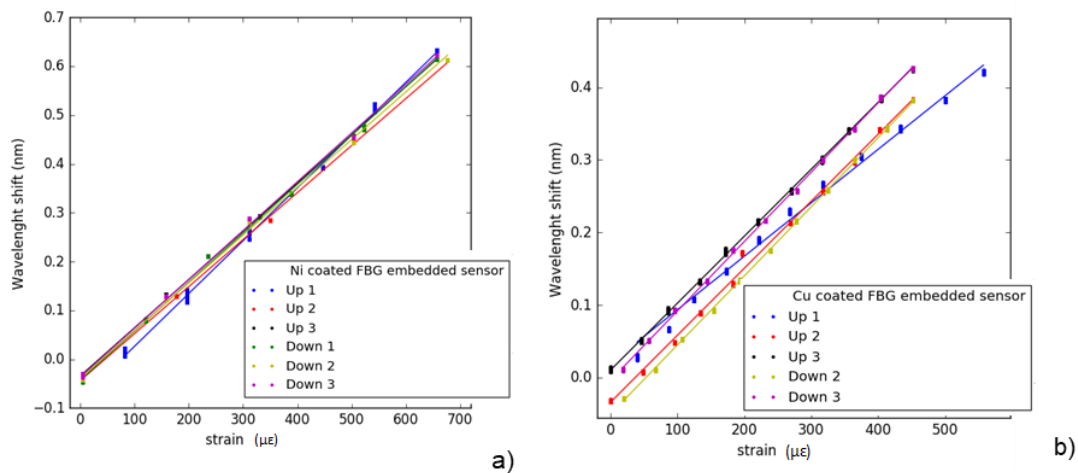


Figure 4.16: (a): Strain characterization for embedded Ni coated fibre optic sensors. The sensitivities of each linear fit are: Up1: $0.0011 \text{ nm}/\mu\epsilon$, Up2: $0.0010 \text{ nm}/\mu\epsilon$, Up3: $0.0010 \text{ nm}/\mu\epsilon$, Down1: $0.0010 \text{ nm}/\mu\epsilon$, Down2: $0.0010 \text{ nm}/\mu\epsilon$ and Down3: $0.0010 \text{ nm}/\mu\epsilon$. (b): Strain characterization for embedded Cu coated fibre optic sensors. The sensitivities of each linear fit are: Up1: $0.0007 \text{ nm}/\mu\epsilon$, Up2: $0.0009 \text{ nm}/\mu\epsilon$, Up3: $0.0009 \text{ nm}/\mu\epsilon$, Down2: $0.0010 \text{ nm}/\mu\epsilon$ and Down3: $0.0010 \text{ nm}/\mu\epsilon$.

Finally, after their thermal and mechanical characterization, the specimens were cut for analysing the embedding quality and the cross-section of each one. Figure 4.17.(a) shows the cross-section of the Ni re-coated FBG embedded and Figure 4.17.(b) the Cu re-coated FBGs embedded. The Ni coating layer presents some melted material in a small top section, due to the high temperatures reached during the embedding process. However, the rest of the fibre coating presents a very good bond to the antifriction material. For Cu embedded fibre, the cross-section presents some diffusion material, due to the fast thermal transfer of Cu, and more inhomogeneity geometry of the fibre. The inhomogeneity comes from Cu coating electroplating process, in which a higher roughness, than for NI coating, is generated. In both cases, despite these minor details, a high embedding quality with a good bond, has been achieved.

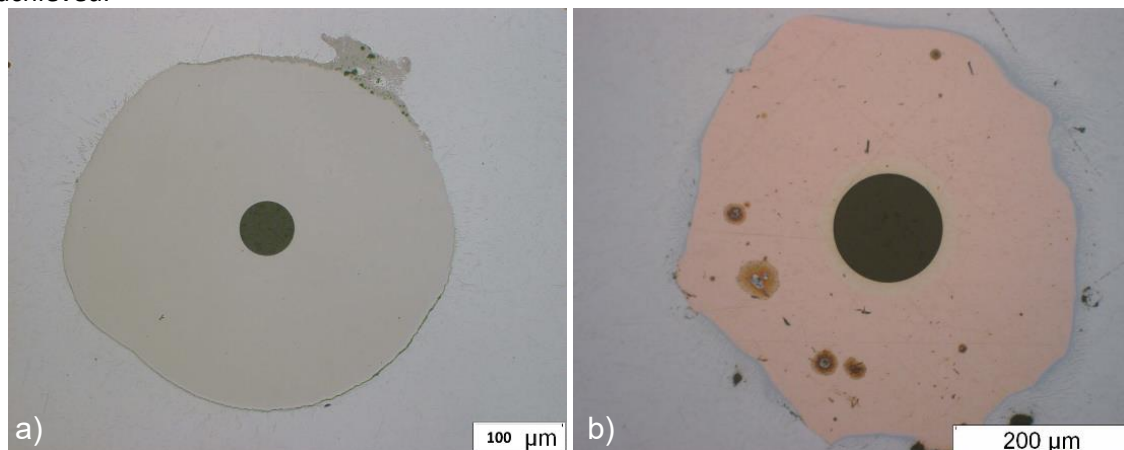


Figure 4.17: Cross-section of embedded FBG sensors after thermal and mechanical characterization. (a): Ni re-coated FBGs. (b): Cu re-coated FBGs.

In conclusion of the global laser cladding technique as embedding process study, the results obtained and the analysis carried out have shown the success of the laser cladding welding technology used, demonstrating its being successfully used for embedding FBG-based fibre optic sensors into metallic structures. The work done has shown that it is possible to embed Cu and Ni re-coated fibre optics containing sensors over $300\mu\text{m}$ of diameter with low losses, of between

0 and 1.5 dB and yet still enabling satisfactory strain and temperature measurement results. In the research carried out, both Ni and Cu re-coated FBG-based embedded fibre optic sensors give a similar mechanical and thermal response to similar non-embedded sensors and give good cross-comparison with the response of the conventional gauge used for that purpose.

4.3.2 Laser embedding using Ni-Cr alloy as embedded material

The tin alloy used, in the previous section, as added material to embed the Ni and Cu re-coated optical fibres and FBG sensors, has a relatively low melting point (250°C), although during the laser embedding higher peak temperatures were achieved (700°C). In this section, the laser embedding process is studied to embed Ni re-coated optical fibres into a Cr-Ni alloy, in powder form (not-wire), which has a melting point higher than 1300°C.

The laser technique used here is based on Additive Manufacturing (AM) by Laser. Figure 4.18 shows the laser cell set-up used. This technique is similar to the cladding process explained in the previous section, but in this case the laser head used is a little different and the laser AM process is close-loop controlled in real-time, using a technology developed by AIMEN named CLAMIR [110]. This technology is based on image monitoring in real-time linked to artificial intelligence algorithms. The monitoring system measures and maintains the melt pool geometry through a closed-loop control of the laser power using a 1000 image per second MWIR camera.

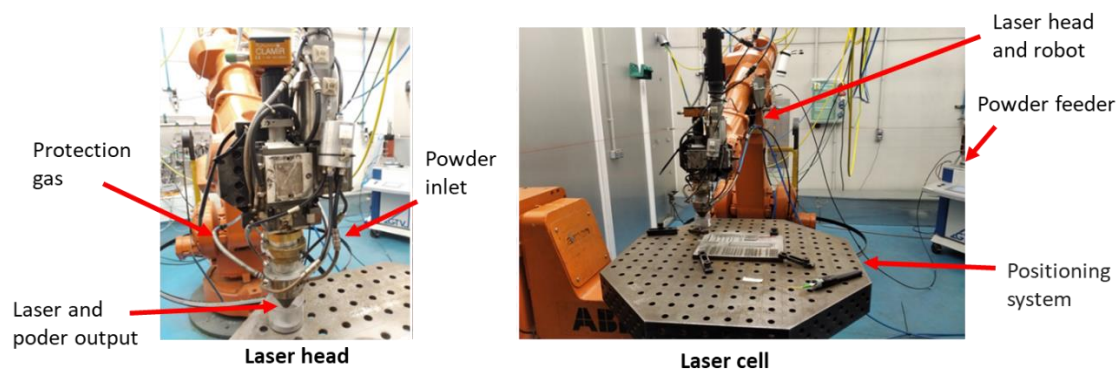


Figure 4.18: Laser Additive Manufacturing embedding set-up.

For this study, only Ni re-coated optical fibres were used, because of the material compatibility with the powder material alloy added and its higher melting point (>1400°C) compared to copper (1000°C). The diameter of the Ni re-coated optical fibres used here was around 900µm, which means 20µm of Cu (commercial coated optical fibre) and around 370 µm of Ni layer.

Stainless steel was used as the base material of the specimen substrate used to deposit the Cr-Ni alloy. A layer of Cr-Ni alloy was deposited over the stainless steel using Laser AM, generating a groove (1x1mm) to match the diameter of the Ni re-coated fibre. Then, the Ni re-coated optical fibres were located on the groove and the Cr-Ni alloy was added by Laser AM on either sides of the groove. Finally, a third recharge line was added on the top of the Ni re-coated fibre to complete the embedding process. The embedding strategy used and shown in Figure 4.19, was the one that gave the best results as discussed in previous sections: Figure 4.19.a shows the Ni re-coated fibre located in the AM made groove, Figure 4.19.b shows the Ni re-coated fibre partially embedded and Figure 4.19.c shows the Ni re-coated fibre totally embedded in the Cr-Ni alloy.

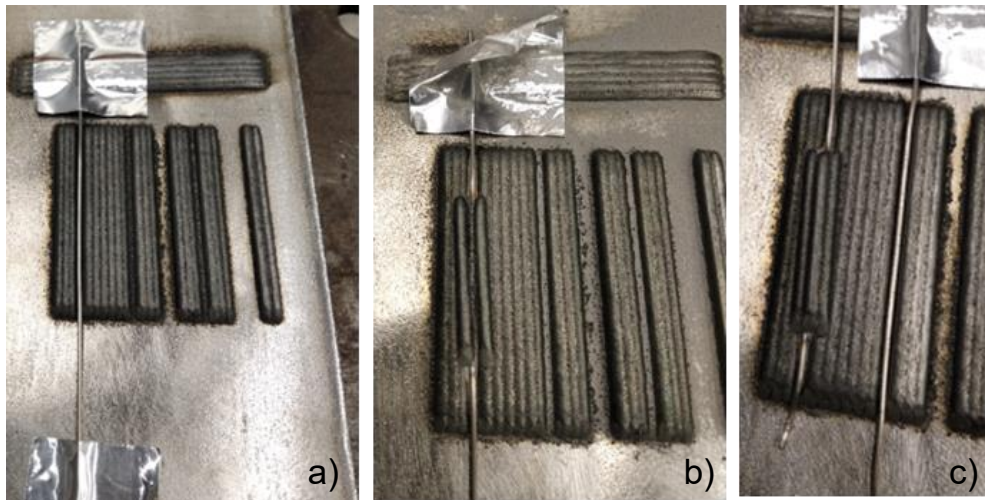


Figure 4.19: Methodology for embedding Ni re-coated optical fibre by Laser AM process into a Cr-Ni alloy. (a): Ni re-coated fibre located in the AM made groove. (b): Ni re-coated fibre partially embedded. (c): Ni re-coated fibre totally embedded.

Two of the three tested fibres were able to transmit the red laser light launched from one end of the fibre, confirming that the Ni re-coated optical fibre withstands the AM laser embedding process. Nevertheless, the cross-section of all optical fibres embedded show a hole between the base material and the embedded Ni coated optical fibre, as shown in Figure 4.20.a. This is because the groove made to match the Ni coated fibre was larger than the fibre diameter and the molten material (Cr-Ni alloy) during the laser deposition was not sufficient to cover these grooves. This could be a problem when measuring strain with these embedded fibres, because they are not fully bonded to the metallic structure. There may therefore be a lack of structural information from the sensor signal. However, the Ni re-coated optical fibre part which is well embedded with the Cr-Ni alloy, top part, is very well bonded and no pores or other defects were detected.

In addition, it was observed that the Cu layer (between silica and Ni layer) has melted during the laser embedding process and it was mixed with the Ni coating material. Therefore it is expected in Figure 4.20.b that a reddish ring (Cu layer) should be visible, around the fibre (black circle). But this layer is not visible in this, nor in the cross-sections of the other embedded fibres. Instead it is shown in Figure 4.20.c, the picture of the embedded fibre after acid attack, which reveals the embedded optical fibre borders.

The melted material mix could be good, because some scientific publications say that if a bimetal material is subjected to thermal fatigue at high temperatures, pores are generated at the frontier between the two materials [49]. Then, if the Cu and Ni are mixed due to the high temperatures reached during the AM laser process, these pores should not appear.

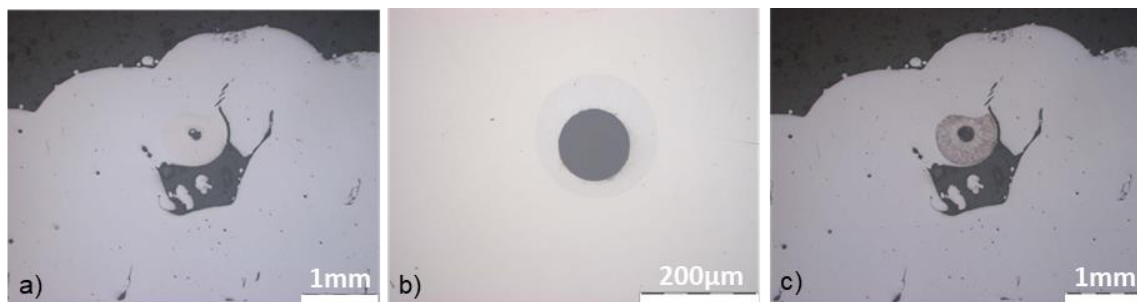


Figure 4.20: Cross-section detail for some of the Ni re-coated optical fibres embedded into Cr-Ni alloy by AM laser process. (a): Cross-section detail for a Ni re-coated optical fibre embedded into Cr-alloy structure. (b): detail of the Ni coating layer after being embedded. (c): Cross-section of a Ni re-coated optical fibre embedded into Cr-alloy structure, acid attacked to reveal the material composition and structure.

This work is still on-going and more work needs to be done to optimize the embedding process. It involves adjusting the groove size to the dimensions of the metal re-coated optical fibre dimensions, preparing new Ni re-coated optical fibres with different thicknesses to optimize the laser AM process and embedding metallic coated FBG sensors to study its response after being embedded.

Despite all the work that remains to be done, this small feasibility study proves that it is possible to embed re-coated optical fibres in high melting point materials using the laser embedding process.

4.4 Embedding process by TIG welding

It is clear that more cost-effective and simpler embedded techniques, better suited to use eventually in a production environment are required. In this last section of the chapter on embedding fibre optic sensors in metals, two processes based on Tungsten Inert Gas (TIG) welding are studied: manual TIG and automatic TIG welding processes.

TIG welding is an electric arc welding process, involving the use of a shielding gas and a non-consumable tungsten electrode. The arc is established between electrode and the piece to be welded, and filler metal can be added independently. Two different TIG welding variants were studied in this work to evaluate which is the most effective, these automatic and manual welding. Automatic and manual TIG welding set-ups used in this study are shown respectively in Figure 4.21.a and Figure 4.21.b.

In the case of the automatic TIG welding process, the parameters involved in the process were selected prior to the use of the welding process. By contrast, in the TIG manual process, it is only the current which is a priori defined, with all the other parameters for the welding conditions usually depending on the skills and experience of the technician undertaking the weld. Repeatable and high accuracy automatic TIG welding techniques are available, as is the less repeatable, yet highly-adaptable and portable manual TIG welding technique. Both techniques are low-cost in comparison to the other techniques used for FOS embedding and have the advantage of being familiar, being used in many industries in the metal-mechanic sectors, this being especially true of the widely-used manual TIG approach.

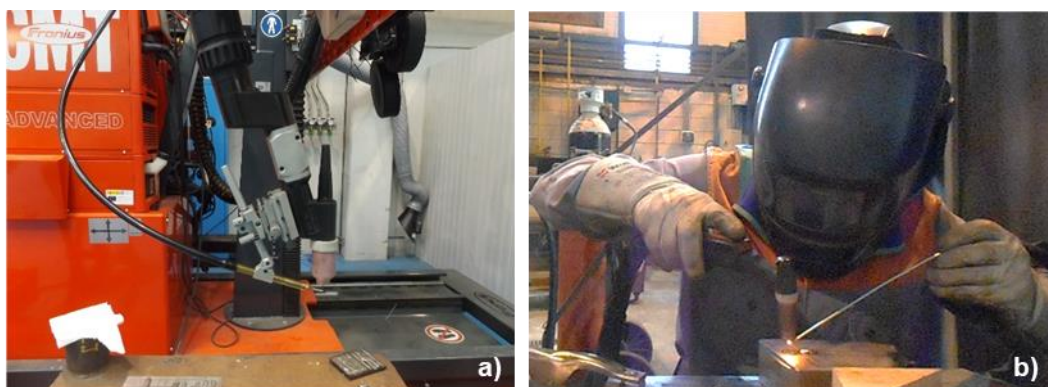


Figure 4.21: (a): Automatic TIG welding set-up. (b): Manual TIG welding set-up.

A tin-alloy wire of 2.4mm of diameter was used as welding filler material which is the same antifriction material discussed in the previous sections of this chapter. The samples on which the embedding tests were carried out were based on stainless steel with a thin tin-alloy layer as that previously used.

As in the studies explained above, in a first step, metal re-coated optical fibres of different thicknesses were produced and embedding tests were carried out, using the two TIG welding techniques, to optimise the process. Then, specific specimens and re-coated FBG sensors were manufactured, embedded, and thermal and mechanical tests were performed for fulling characterisation.

4.4.1 Embedding process by manual TIG welding

For the manual TIG welding, specific Ni and Cu re-coated optical fibres with a diameter between 165 μm to 1200 μm were manufactured (using the procedure developed and explained in Chapter 3) and tested using the manual TIG welding process. First, the manual TIG welding current was optimized for embedding the optical fibres by varying the current between 50A and 80A. It was observed that currents over 60A damaged the re-coated optical fibre and fibres with coatings under 500 μm (diameter of the coated fibre) could barely withstand the welding. Also, currents below 50A would result in poor welding quality. Therefore, coatings near 500 μm and currents of 60A were chosen as the best parameters to embed the optical fibres. It should be noted that the training acquired by the worker is essential for successful embedding. For example, it was important not to apply the arc directly on the coated fibre, but offset to one side. Cu re-coated fibres were also far more fragile than Ni re-coated, due to the lower melting point of Cu compared to Ni, and its high thermal transmission coefficient, which causes a rapid heat transfer to the fibre, which may damage it. Figure 4.22.a shows the Cu and Ni re-coated optical fibres located and fixed on the steel-base before being embedded. Figure 4.22.b shows the final sample appearance after embedding trials. Optical fibre lengths are around 5 cm were embedded. Upon inspection the weld seams looked good, continuous and without pores.

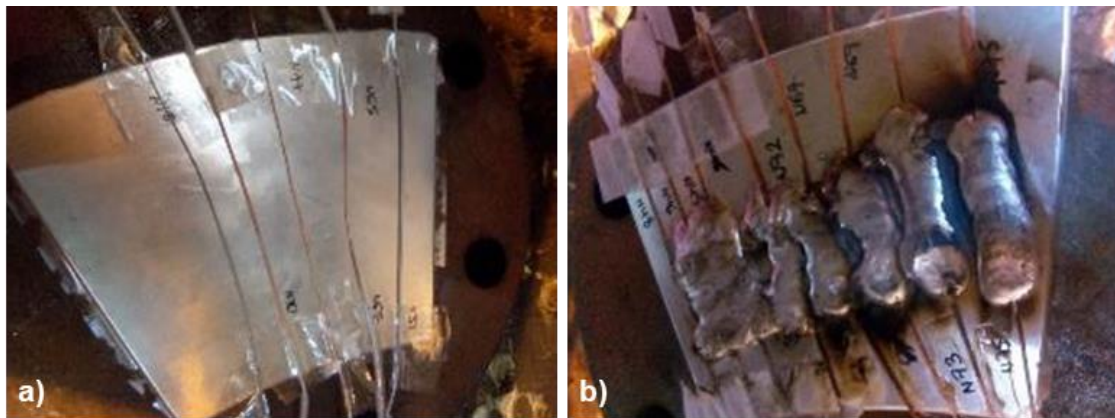


Figure 4.22: (a) Ni and Cu re-coated optical fibres on the tin-alloy steel substrate before being embedded. (b): Ni and Cu re-coated optical fibres after being embedded by manual TIG process.

Table 4.5 shows the results for Ni and Cu re-coated optical fibres embedded using manual TIG welding. Ni and Cu re-coated optical fibres with a diameter between 500-800 μm were tested. In general Ni coating fibers were well embedded in the antifriction material and show less re-coating material fusion or pores than Cu coating. Also, some of the embedded Ni re-coated optical fibres show material fusion, mixing of Ni and tin alloy, which appears when the tin-alloy wire was too close to the coating fiber and the arc damages the coating of the fiber. This means that this process depends heavily on the experience of the person who performs the welding. In addition, copper embedded fibres show losses around 3dB, while Ni losses for the embedded fibres were around 2dB, which means Ni fibres are more resistant to the embedding process.

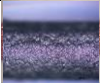
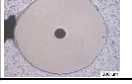
Coating	Fibre diameter (μm)	Loss (dB)	Embedded length (cm)	Coating fiber	Embedded cross-section	Coating	Fibre diameter (μm)	Loss (dB)	Embedded length (cm)	Coating fiber	Embedded cross-section
Ni	525	2.62	3.6			Cu	518	3.44	4.2		
Ni	590	2.44	3.5			Cu	586	20.2	3.5		
Ni	761	1.38	3.2			Cu	624	2.24	3.7		
Ni	778	4.58	4.6			Cu	685	14.6	4		

Table 4.5: Ni and Cu optical fibres embedded by manual TIG welding and their cross-section details.

Similar to the laser cladding embedding study, embedding tests on samples including grooves were performed on Ni re-coated optical fibres, because of their superior thermal resistance and bond with the antifriction material. The sample tested had a base material of steel and 5mm of antifriction material, with several grooves of different sizes as shown in Figure 4.23.a. It is designed to study the best for embedding the re-coated optical fibres in terms of protection and adhesion to the antifriction material. Grooves with a V shape of 3.5x2mm (depth x width) and 3.5x1.5mm and, grooves with a U shape of 3.5x2mm and 1.5x1.5mm, were machined. The sample length was around 350mm and the re-coated optical fibres tested had a total diameter around 600-700μm of Ni. The TIG process current applied was between 40-50A, because it was the coating with which the best results were achieved in the previous tests.

All the Ni re-coated optical fibres were successfully embedded, the resulting optical losses of the embedded fibres were around 0.1-0.3 dB and the minor losses were obtained for the Ni_002 fibre, which was embedded in the 3.5x2mm groove using only one weld seam. After embedding the re-coated FBGs, the weld seams were machined to even out the sample surface and study if any pore or defect appears in the embedded optical fibres sections. Figure 4.23.b shows the appearance of the sample after the TIG welding process and Figure 4.23.c shows a section sample after having been machined, which shows a very good appearance without any important defect on the surface of the embedded fibre optic regions.

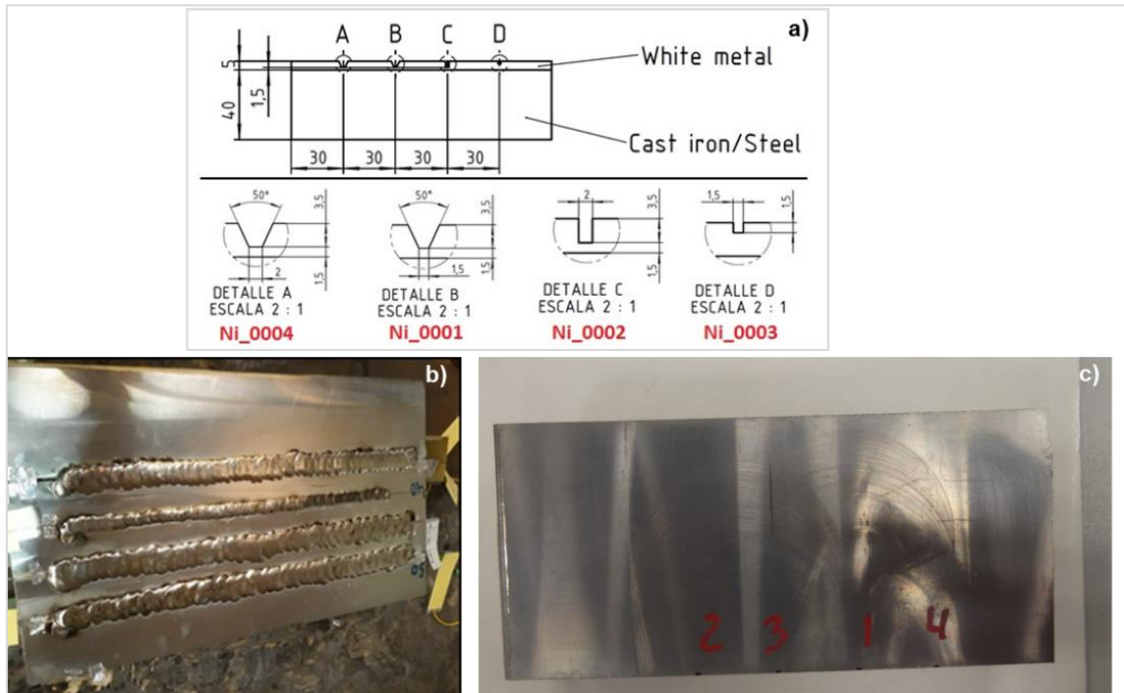


Figure 4.23: (a): design of the machined grooves for the embedding tests. (b): picture of the sample during the embedding trials. (c): Sample with the optical fibres embedded after being machined to equalise the surface of the sample.

Figure 4.24 shows the cross-section of each of the embedded Ni re-coated optical fibres on the grooves. The observed best bonds were obtained from Ni_002 (Figure 4.24.c) and Ni_003 (Figure 4.24.d) references, which were embedded on the 3.5x2mm and 1.5x1.5mm U shaped groove. The V shapes grooves, Figure 4.24.a and Figure 4.24.b, presents some gaps between the embedded fibre and the antifriction material. Furthermore, no melted coating material problems were observed in these tests, from which it can be concluded that the groove thermally protects the fibre during the manual TIG welding process.

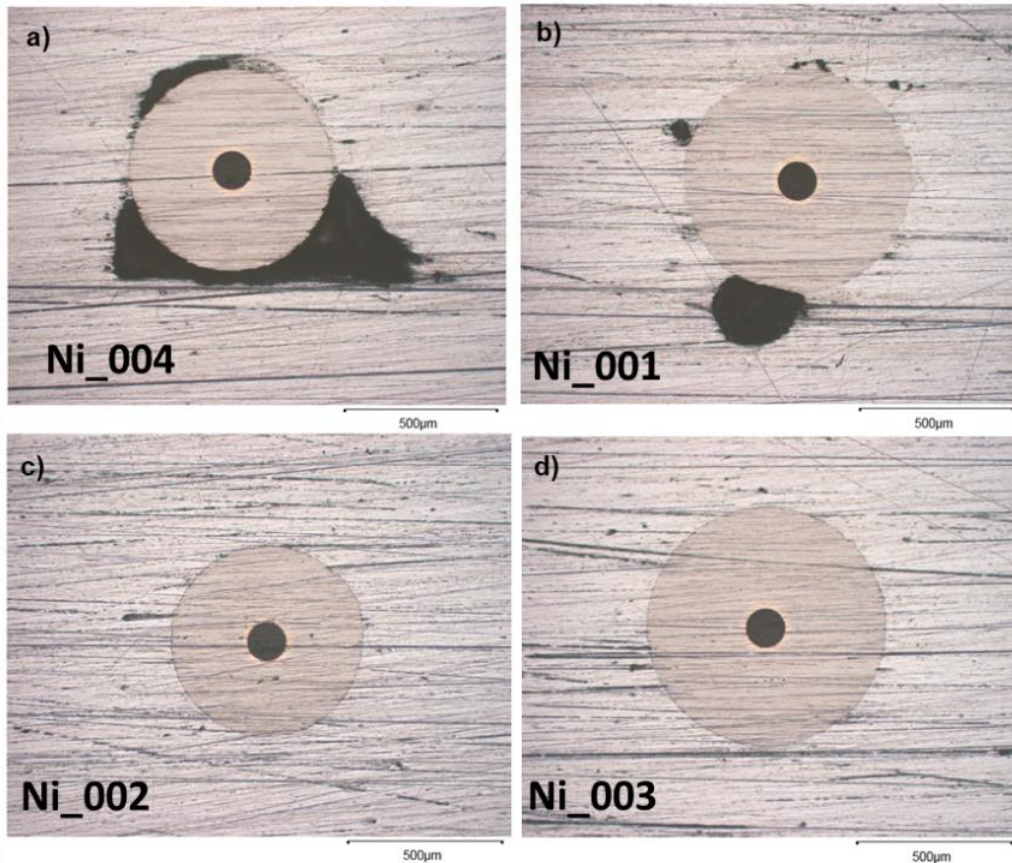


Figure 4.24: Cross-section of the re-coated optical fibres embedded in the groove sample. (a): Ni_004, (b): Ni_001. (c): Ni_002. (d): Ni_003.

Considering the optimization phase of the completed embedding process, Cu and Ni re-coated FBG sensors were manufactured and embedded using manual TIG welding. The specimens used to embed the FBG sensors were the same as those in the Laser Cladding embedding characterization.

One of the re-coated FBG sensors was coated with Ni up to a 526µm of diameter (20µm of Cu and 180µm of Ni thickness) and the other with Cu with a total diameter of 738µm (306µm of Cu thickness). This difference in thickness between the sensors is due to the fact that copper is a material with a higher thermal conduction coefficient than Ni and therefore, during the manual TIG process it was necessary to protect the fibre with a greater thickness, since part of this coating melts during the embedding process. Figure 4.25.a shows the appearance of the Ni re-coated FBG sensors embedded in the specimens using manual TIG welding process and Figure 4.25.b shows the Cu re-coated embedded FBG sensor. The manual TIG process is much more hostile towards the sensors than any other automatic process, since, being a slower process, the temperatures reached are much higher. This is the reason why, in the cross section (Figure 4.25.c and Figure 4.25.d), it can be seen that the Ni and Cu layer of the embedded sensors has been damaged by melting after embedding, although the Cu coating layer exhibits a larger amount of melted material.

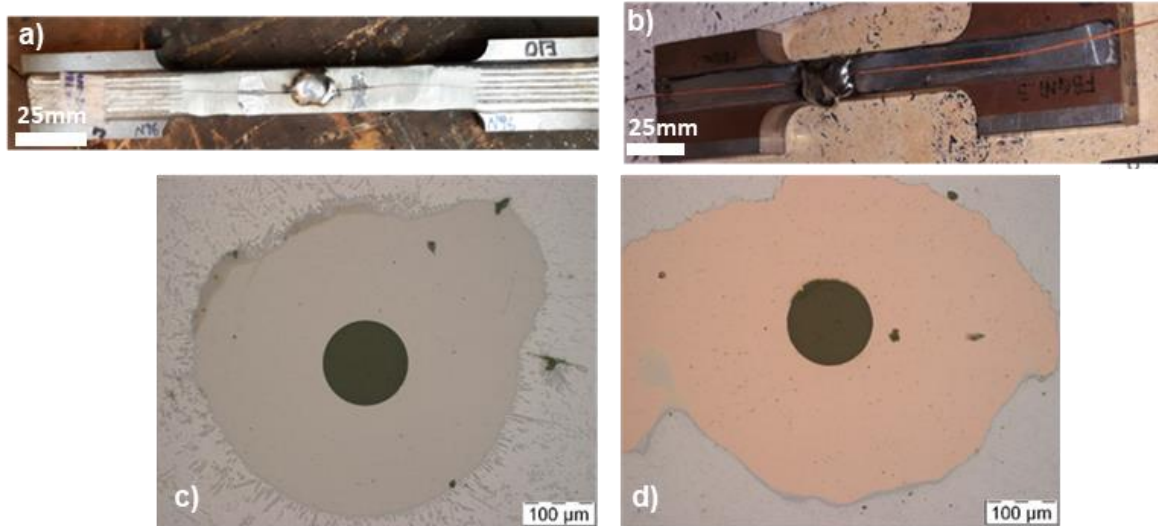


Figure 4.25: (a): Appearance of the Ni coated sensor after manual TIG welding embedding process. (b): Appearance of the Cu coated sensor after manual TIG welding embedding process. (c): Ni re-coated FBG sensor cross-section after embedding. (d): Cu re-coated FBG sensor cross-section after embedding.

The method used to initially evaluate the quality of the process of embedding of the FBG sensors was to analyse and compare the spectrum of the sensors before and after having been embedded. In Figure 4.25, the Bragg peak spectrum for the coated FBG sensors before and after being embedded by manual TIG welding process are shown. The wavelength peak variation for the Ni re-coated FBG sensor, after being embedded (Figure 4.26.a), is lower than that observed in the Cu re-coated FBG sensor (Figure 4.26.b). Also, the peak shape for the Cu re-coated FBG sensor, after the embedding process, was broader, which means that it has been deformed as it was subjected to a non-uniform strain, which is in accordance with the cross-section melting material appearance. In addition, in both cases, the signal amplitude of the FBGs changed, confirming that these sensors were thermally and mechanically affected. It is also possible to conclude that the Cu re-coated FBG sensor, embedded by using manual TIG welding, has a poor adhesion to the base-substrate and the added material or the coating layer.

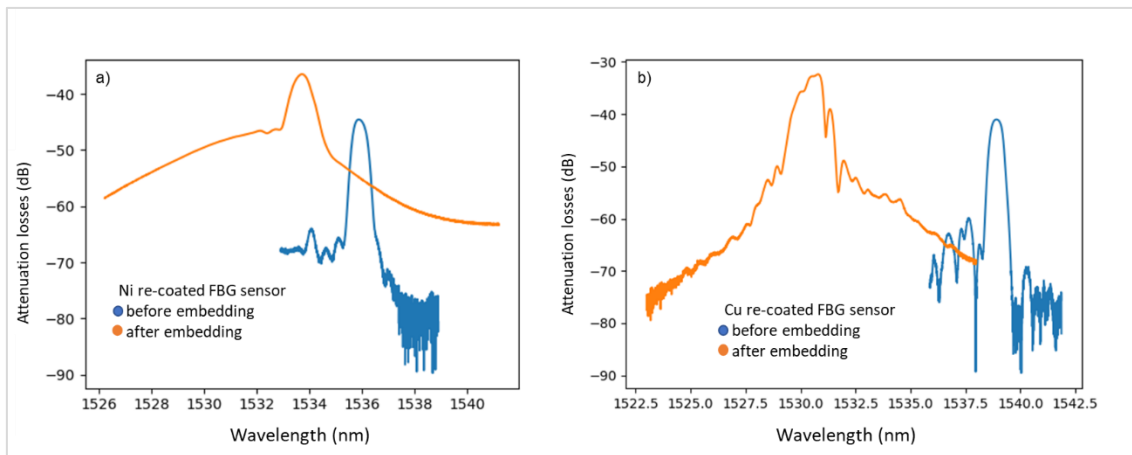


Figure 4.26: FBG sensors spectrum before and after being embedded. (a): Ni re-coated FBG sensor. (b) Cu re-coated FBG sensor.

The above was followed by laser embedding study, thermal heating and tensile tests. For the thermal characterization, these FBG sensors were subjected to three repetitions of a temperature up between 50-200°C in steps of 30°C. Regarding the tensile tests, they were subjected to a load between 0-30kN in steps of 5kN, where an additional strain gauge (Yokogawa

KFGS-5-120-C1-11 L1M2R) was attached to the specimen, allowing calibration of the response of the FBG sensors into strain.

Figure 4.27.a and Figure 4.27.c show the thermal response of Ni coated embedded FBGs and Cu coated embedded FBGs, respectively. Both embedded FBGs show a repeatable and stable thermal response. The Cu embedded FBGs exhibits a higher wavelength variation than that of the Ni embedded FBGs because of the greater coating layer thickness and the higher thermal coefficient of the copper material.

Figure 4.27.b and Figure 4.27.d show the linear fit of the embedded Ni and Cu FBG sensors thermal response, respectively. Even in the case of the Cu FBG sensor, which had a slightly deformed spectrum, because of the Cu melted material around the embedded fibre, the thermal response is linear. In the case of the Cu re-coated FBG sensor, the sensitivity is slightly higher (0.028nm/°C) than that of the Ni re-coated FBG sensor (0.025nm/°C), as expected.

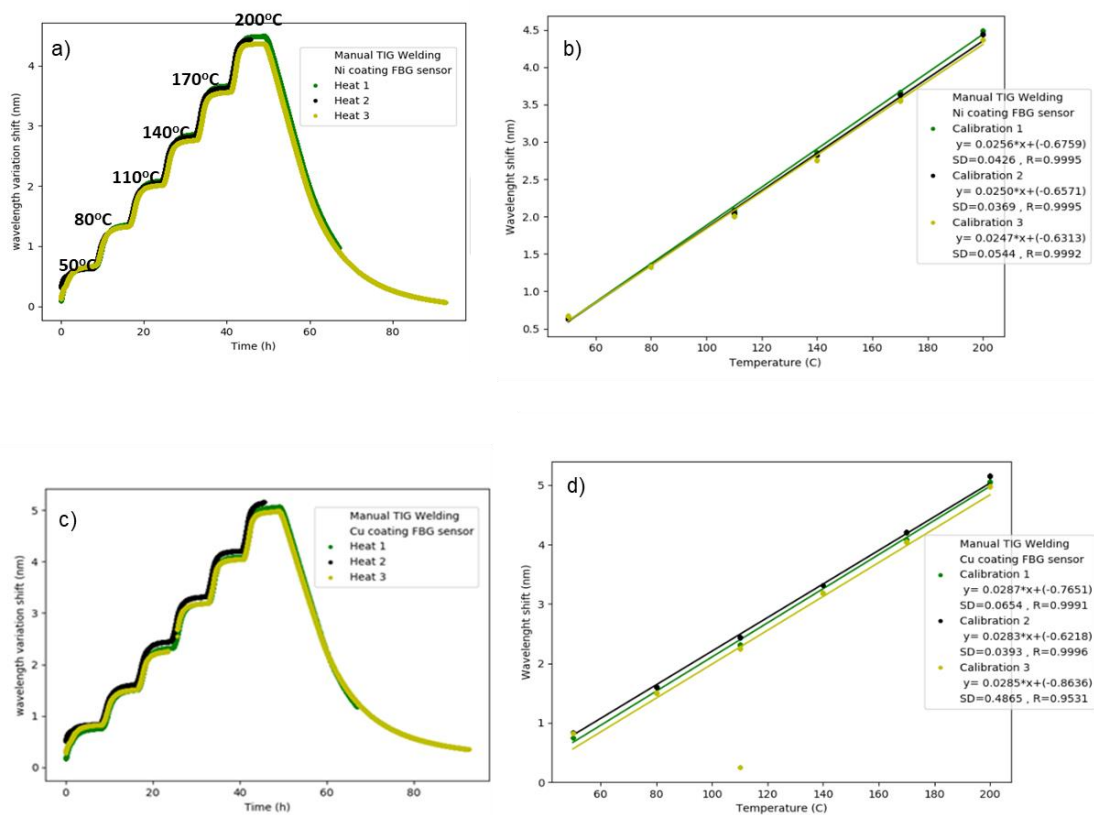


Figure 4.27: (a): Ni FBG sensor embedded, thermal response. (b): Linear fit for the Ni FBG sensor embedded thermal sensitivity. (c): Cu FBG sensor embedded, thermal response. (d): Linear fit for the Cu FBG sensor embedded thermal sensitivity.

Finally, tensile tests, from 0-30kN in steps of 5kN, performed in order to made to characterize the mechanical response of the embedded FBG sensors. Strain gauges (Yokogawa KFGS-5-120-C1-11 L1M2R) were also glued on the specimen surface, next to the FBG embedded sensors, to compare both responses. Figure 4.28 shows the response of the Ni (Figure 4.28.a) and Cu (Figure 4.28.b) re-coated FBG sensors embedded using manual TIG, subjected to tensile tests. In the case of the Cu re-coated and embedded FBG sensor shows a high noise rate and the wavelength variation for the loads applied is half of that for the Ni re-coated and embedded FBG sensor. This is because of the peak deformation of this sensor and poor quality of embedding resulting from the manual TIG welding process. However, the Ni re-coated embedded FBG sensor shows a stable and repeatable response except for the first load. Even, the wavelength at 0 after the first tensile test up to 30kN is different from the initial, due to the release of residual stresses in the

embedding material and the sensor, generated in the process manual TIG welding process. In the tests performed, it can also be seen that there is slippage of the specimen in the tensile test machine, since the strain gauge also shows a settling effect.

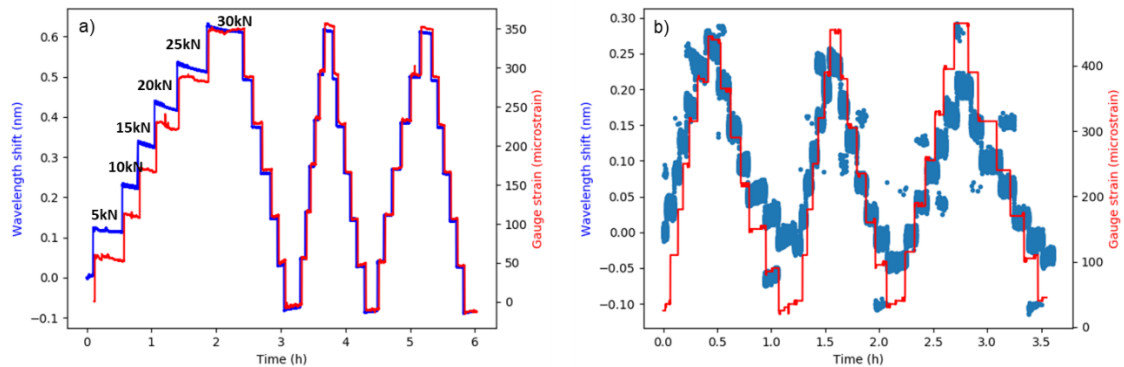


Figure 4.28: (a) Load response of the Ni re-coated FBG sensor embedded by manual TIG welding process. (b) Load response of the Cu re-coated FBG sensor embedded by manual TIG welding process

Other than that, the response of the embedded Ni re-coated FBG sensor is linear with load and strain for up and down tests, as can be seen in Figure 4.29, where the calibration of the Ni (Figure 4.29.a) and Cu (Figure 4.29.b) embedded FBG sensors, compared to that from a conventional strain gauges, have been performed. The sensitivities obtained from each embedded FBG sensor is detailed in Table 4.6. The Ni embedded FBG sensor shows a 0.0010 nm/ $\mu\epsilon$, which is in good agreement with the original FBG sensitivities i.e. those obtained before coating and embedding. In the case of the Cu re-coated FBG embedded by using the manual TIG method, the sensitivity is resulting low at 0.0003nm/ $\mu\epsilon$, because of some damage generated during the embedding process.

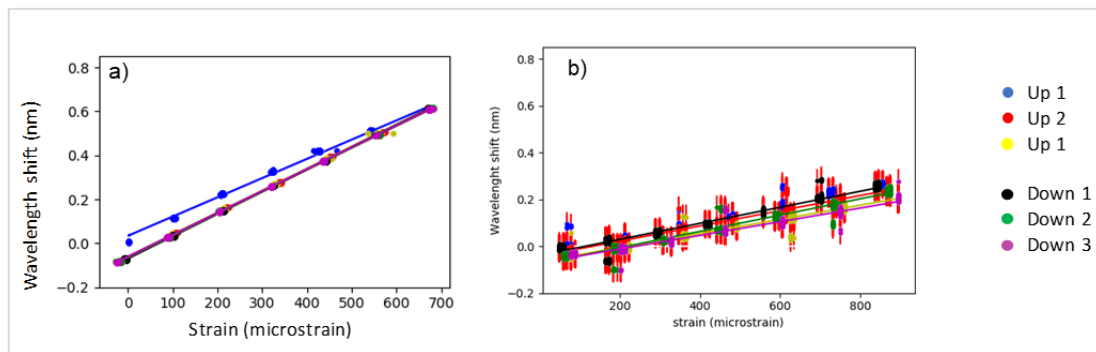


Figure 4.29: Results of the calibration after the tensile tests on embedded FBGs for manual TIG. (a): Ni re-coated FBG. (b): Cu re-coated FBG. Up 1, 2 and 3 are for the cases where the strain is rising while Down 1, 2 and 3 are for the cases where the strain is falling.

Linear fit parameters for the tensile tests ($y = ax+b$)

		<i>a</i>	<i>b</i>	<i>SD</i>	<i>r</i>	<i>a</i>	<i>b</i>	<i>SD</i>	<i>r</i>	
Manual TIG on Nickel coated FBG sensor	Up 1	0.0009	0.0337	0.0092	0.9988	Down 1	0.0010	-0.0688	0.0024	1.0000
	Up 2	0.0010	-0.0641	0.0033	0.9999	Down 2	0.0010	-0.0632	0.0032	0.9999
	Up 3	0.0010	-0.0620	0.0026	0.9999	Down 3	0.0010	-0.0614	0.0016	1.0000
Manual TIG on Copper coated FBG sensor	Up 1	0.0004	-0.0336	0.0090	0.9951	Down 1	0.0003	-0.0387	0.0142	0.9885
	Up 2	0.0003	-0.0429	0.0163	0.9871	Down 2	0.0003	-0.0755	0.0105	0.9941
	Up 3	0.0003	-0.0655	0.0068	0.9972	Down 3	0.0003	-0.0700	0.0108	0.9899

Table 4.6: Linear fit parameters from the tensile test of the Ni and Cu re-coated FBG sensor TIG embedded by manual TIG welding process.

The manual TIG welding process for embedding re-coated FBG sensors is therefore a difficult process to optimise because the success of the process depends largely on the operator's

judgement, experience and skill. In addition, it is a relatively slow process which results in the fibres being exposed to high temperatures for relatively long periods of time, and this affects the embedding result, and therefore, better results were obtained for the Ni coated sensors, because this material resists the high temperature better than the Cu. Furthermore, the embedding strategy using a groove (1x1mm) seems to reduce thermal damage to the fibre during the embedding process.

4.4.2 Embedding process using automatic TIG welding

This section describes the results of a new FBG sensors embedding technique, Automatic TIG welding. For this purpose, metal-coated optical fibres with different thicknesses have been embedded and the losses generated during the process have been measured to determine the minimum thickness that can be successfully embedded. Following this, the temperature and strain response of these embedded FBG sensors was calibrated, as in the case of the previous embedding techniques.

In this case, the TIG welding embedding process was carried out automatically using the Fronius Multi-Welding (FMW) system production cell, which is equipped with the Magic Wave 5000 welding machine. For the embedding of re-coated fibres, the same antifriction (tin-alloy based) metal wire was used as a filler material. The wire diameter was 1.6 mm, a lanthanum electrode (EWLa-1 according to American Welding Society (AWS)) with a diameter of 1.6 mm, argon as shielding gas and pulsed direct current with electrode to the negative were used to carry out the tests. Adjustment tests were performed to determine the optimal parameters, which were: current intensity (35-40A), displacement speed 0.4 m/min, wire feed speed 1.5 m/min and torch position relative to the optical fibre (1.5-2mm) as shown in Figure 4.30.



Figure 4.30: Detail of the relative position of the torch to the fibre.

Similar to the previous embedding studies, preliminary tests were carried out on Ni and Cu re-coated fibres with different thicknesses, to check the applicability of the automatic TIG for embedding in the antifriction material and to parameterise the process. After preliminary tests, it was found that it was feasible to embed both nickel and copper re-coated optical fibres using automatic TIG. Therefore, adjustment was made to optimise the embedding parameters and determine the minimum coating thickness necessary to avoid fibre breakage during the embedding process, from which it was found that it is possible to successfully embed fibres with Ni coatings $\geq 240\mu\text{m}$ and Cu coatings $\geq 280\mu\text{m}$, which are smaller thicknesses than in previous embedding techniques. The embedding strategy used in these tests was the same as that used in the previous embedding techniques. Furthermore, embedding tests on samples with and without grooves on the antifriction coating layer were performed.

Figure 4.31.a shows the appearance of the antifriction steel-based sample after the re-coated optical fibres embedding trials. Figure 4.31.b shows a Ni re-coated optical fibre embedded in a sample with a groove.

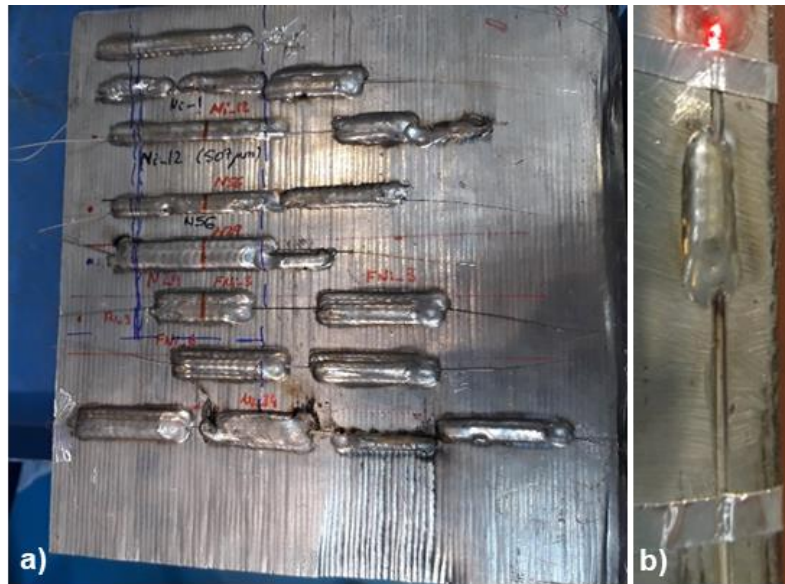


Figure 4.31: (a): appearance of the antifriction steel-based sample after embedding trials. (b): detail for one of the Ni re-coated optical fibres embedded by automatic TIG in a sample with a groove.

Table 4.7 presents the results obtained from some of the Ni and Cu re-coated optical fibres embedded by automatic TIG welding process in samples with and without grooves. Cu re-coated optical fibres present a large amount of Cu molten material, as well as large pores around the embedded optical fibres. While, for almost all, Ni coating fibres result in better bonding and lower thermal damage. The same TIG welding parameters were applicable for embedding the re-coated optical fibres in samples with groove or without, the only difference was in the torch programming, which could be closer to the fibre and thus ensure embedding in fewer passes.

The measured losses were small for both types of coating materials which is a great advantage of using the automatic TIG welding method compared with the manual counterpart.

The best results were obtained for 2mm of distance from the torch of the TIG to the fibre for Cu and 1.5mm for the Ni re-coated fibres.

Coating	Distance between torch and fibre (mm)	Fibre diameter (µm)	Losses (dB)	Cross-section
Ni	2.00	236	29	
Ni	1.50	305	0.17	
Ni	1.50	337	--	
Ni	2	435	-	
Coating	Distance between torch and	Fibre diameter (µm)	Losses (dB)	Cross-section
Cu	2.00	279	-	
Cu	2.00	381	0.23	
Cu	2.00	408	-	
Cu	2.00	550	44	

Table 4.7: Cross-section detail of Ni and Cu optical fibres embedded by automatic TIG welding.

After these tests, the next step was to embed two FBG sensors in tensile specimens and then calibrate them thermally and mechanically. One of the embedded sensors was re-coated with Ni, shown in Figure 4.32.a, and the other with Cu, shown in Figure 4.32.b. The total thickness of the Ni re-coated FBG sensor was of 464 μ m diameter and in the case of the Cu re-coated FBG sensor, it was 592 μ m. The embedding was carried out without a groove, positioning the fibre on the surface of the specimen, which had been coated with a layer of anti-friction material (1-2mm) of a around 30mm.

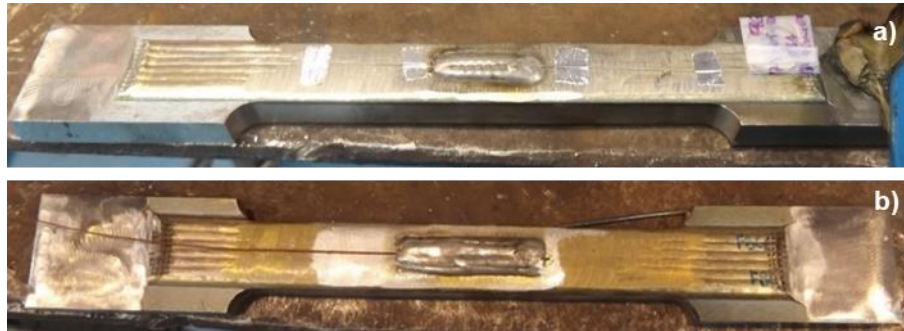


Figure 4.32: FBG sensors embedded by automatic TIG welding process. a): Ni re-coated FBG sensor, b): Cu re-coated FBG sensor.

As a first step, in order to determine the quality of the FBGs embedding and bond, it was possible to compare the spectrum obtained before and after being embedded. Figure 4.33.a shows the Ni re-coated FBG sensor spectrum before and after being embedded. A blue wavelength shift of 2nm was observed and this is due to the contraction of the FBGs after being embedded. Also, a slightly increased power loss intensity was observed. For the embedded Cu re-coated FBG sensor the power is similar before and after being embedded, a blue wavelength shift of 2nm resulted, as shown in Figure 4.33.b. In this case, the embedded FBGs show no distortion in their spectra shape after being embedded, which means that the automatic TIG welding process makes a homogeneous embedding process along the fibre. On conclusion, from the spectrum analysis it is possible to say that both re-coated FBGs were well embedded in the sample.

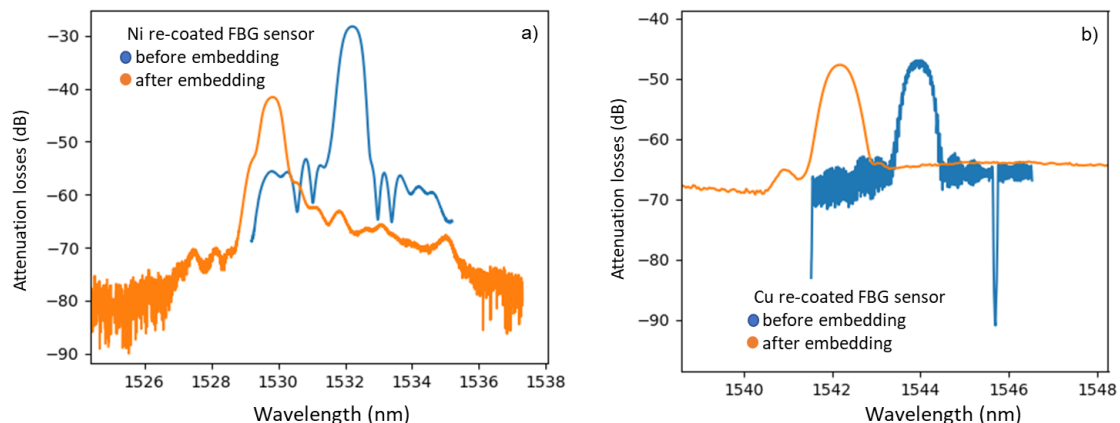


Figure 4.33: FBG sensors spectrum before and after being embedded. (a): Ni re-coated FBG sensor. (b): Cu re-coated FBG sensor.

To demonstrate empirically the conclusions drawn from the analysis of FBG spectra. Cross-section cuts and micro analysis were made. Figure 4.34.a and Figure 4.34.b show the Ni and Cu embedded cross-sections. These results show good agreement with the spectral analysis, and hence show a high quality bond to the antifricition material with no melted material or pores being observed.

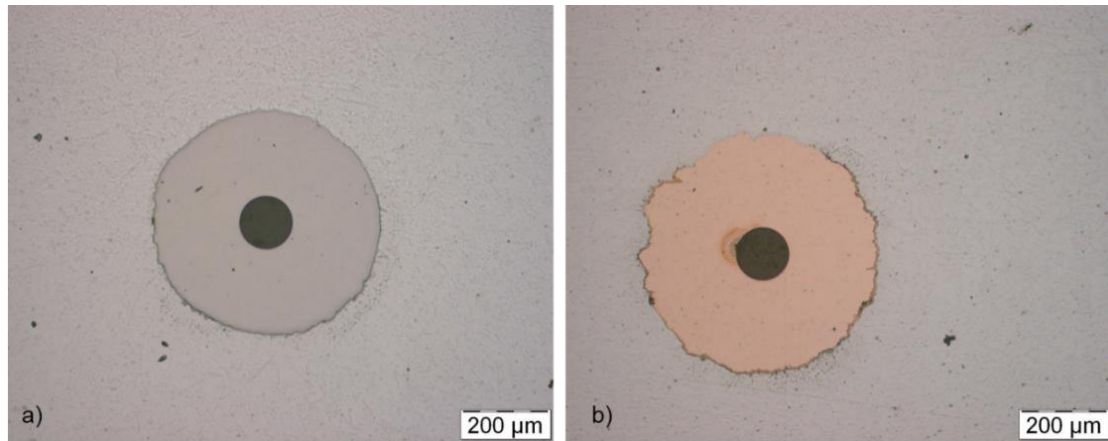


Figure 4.34: Cross-section of the re-coated FBG sensors embedded by automatic TIG welding process. (a): Ni re-coated FBG sensor. (b): Cu re-coated FBG sensor.

Before cutting the specimens, thermal and tensile tests were carried out. First, a temperature calibration of the embedded FBG sensors was made by placing the specimens in an oven and applying step temperature variations from 50°C to 200°C in steps of 25°C. Figure 4.35.a and Figure 4.35.c show the response of each embedded FBG sensor and, Figure 4.35.b and Figure 4.35.d show their respective linear fitting to obtain their corresponding thermal sensitivity. The response of the embedded FBG sensors is stable and repeatable for each thermal tests conducted. The sensitivity is very close for both embedded FBGs. For the Ni re-coated FBGs the value is 0.029nm/°C and for the Cu re-coated FBGs it is 0.027nm/°C. In this case, the Cu FBG sensor shows a lower thermal sensitivity than that of the Ni, which is unexpected as the Cu layer was thicker than the Ni. However, this could be caused by the amount of antifricition material, which is in greater volume are used the Ni FBG sensor than on the Cu embedded FBG sensor.

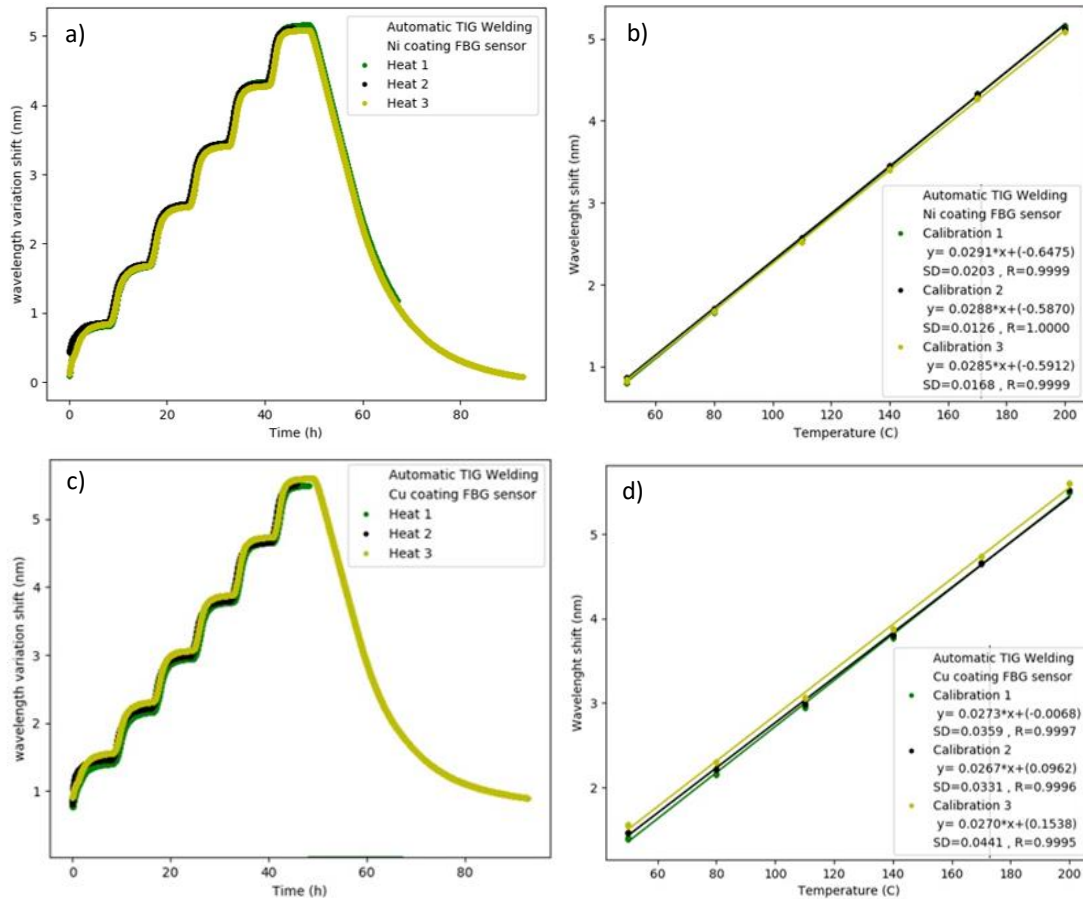


Figure 4.35: (a): Ni FBG sensor embedded, thermal response. (b): Linear fit for the Ni FBG sensor embedded thermal sensitivity. (c): Cu FBG sensor embedded, thermal response. (d): Linear fit for the Cu FBG sensor embedded thermal sensitivity.

The strain calibration of the embedded FBG sensors was carried out by performing tensile tests on the specimens, applying loads between 0-30kN in steps of 5kN. In this way, the specimen is deformed and the FBG sensor provides a response to this deformation. Strain gauges (Yokogawa, KFGS-5-120-C1-11 L1M2R) were also mounted on the specimens to compare the responses from both sensors during the strain tests. Figure 4.36.a and Figure 4.36.b show the response of the Ni and Cu embedded FBGs, respectively, for the tensile tests, compared with the glued gauges. The response of the embedded FBGs is equal to the strain gauges, in trend, but not in absolute values. In both cases, it was observed that for the first ramp-up, the sensitivity is different from the following ones, where the sensitivity is more repetitive and the response of the FBG sensor is faster and more stable. This is due to the residual stresses that are produced during the embedding process and that are eliminated in the first ramp up.

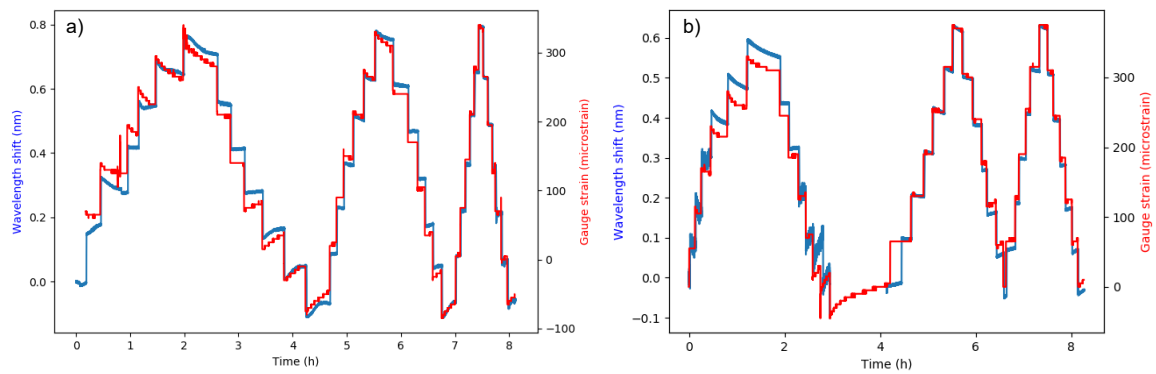


Figure 4.36: Left: Ni embedded FBGs response for the tensile test. Right: Cu embedded FBGs response for the tensile test.

Figure 4.37.a and Figure 4.37.b show the linear fitting between the wavelength shift of Ni/Cu embedded FBG and the strain gauge response for calculation of the strain sensitivity of each embedded FBG sensor. The sensitivity of the Ni embedded FBG sensor is around 0.0012nm/ $\mu\epsilon$, while for the Cu embedded FBG sensor 0.001nm/ $\mu\epsilon$, with more details shown in Table 4.8. The sensitivities obtained for each FBG is slightly different for Ni and Cu FBGs. This may be due to the mechanical behaviour of each material or because of a small misalignment of the strain gauges.

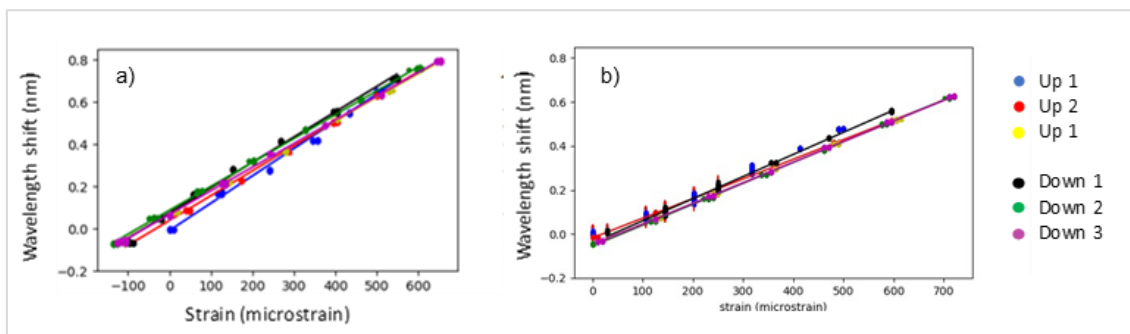


Figure 4.37: Linear fitting of the calibration after the tensile tests on embedded FBGs using automatic TIG. (a): Ni re-coated FBG. (b): Cu re-coated FBG. Up 1, 2 and 3 are for the cases where the strain is increasing while Down 1, 2 and 3 are for the cases where the strain is decreasing.

Linear fit parameters for the tensile tests ($y = ax+b$)

		<i>a</i>	<i>b</i>	<i>SD</i>	<i>r</i>					
<i>Automatic TIG on Nickel coated FBG sensor</i>	<i>Up 1</i>	0.0013	-0.0085	0.0189	0.9958	<i>Down 1</i>	0.0012	0.0746	0.0166	0.9981
	<i>Up 2</i>	0.0012	0.0390	0.0109	0.9994	<i>Down 2</i>	0.0011	0.0871	0.0075	0.9997
	<i>Up 3</i>	0.0011	0.0699	0.0065	0.9998	<i>Down 3</i>	0.0011	0.0669	0.0074	0.9997
<i>Automatic TIG on Copper coated FBG sensor</i>	<i>Up 1</i>	0.0010	-0.0201	0.0089	0.9985	<i>Down 1</i>	0.0010	-0.0331	0.0060	0.9995
	<i>Up 2</i>	0.0009	-0.0176	0.0031	0.9998	<i>Down 2</i>	0.0009	-0.0547	0.0040	0.9998
	<i>Up 3</i>	0.0009	-0.0471	0.0031	0.9999	<i>Down 3</i>	0.0009	-0.0488	0.0037	0.9999

Table 4.8: Linear fitting parameters from the tensile test of the Ni and Cu re-coated FBG sensor embedded by automatic TIG welding process.

After the trials and analyses carried out for automatic TIG welding, it can be concluded that this automatic process can be performed faster and therefore the fibre is potentially subject to less thermal damage. Also, it is a relative low-cost process and with greater access in the industrial sector to implement it. But above all, it has been found that the embedded FBG sensors have a high quality response to thermal and mechanical variations, showing their measurement/monitoring potential.

4.5 Summary

In this chapter, a number of techniques for embedding metallic coated optical fibres into metallic structures were studied. Ni and Cu re-coated optical fibres and FBG sensors were embedded into metallic materials, such as Cu, Sn alloy and Inconel (Ni-Cr alloy). Different techniques, such as electroplating, casting, Laser Cladding, Laser Additive Manufacturing and, manual and automatic TIG welding were studied to embed the re-coated optical fibres.

In general, for all techniques studied, the objective of embedding the fibres in the metallic material was achieved. However, each of them has advantages and limitations that must be taken into account depending on the final application.

The electroplating deposition process is relatively easy, cheap and simple to embed the re-coated FOS but, it presents many limitations regarding the thickness of the final embedding layer and the robustness of the bond. This method is recommended for applications with simple geometry, small size components and for FOS surface embedding.

Casting was successful in embedding sensors with a good bond, but this process requires the embedding material to be molten and its *careful handling*, so it would only be possible in cases where the metal does not have a melting point above 800°C, in order not to damage the optical fibre. Another constraint is the pre-preparation of the specimen prior to the use of this technique which is not possible in all applications.

Both laser cladding and laser AM techniques have successfully been used to embed FOS and FBG-based fiber optic sensors into metallic structures with a low or high melting point. The work done has shown that it is possible to embed Cu and Ni coated FOS with overall diameters greater than 300µm with low losses, and yet still enabling satisfactory strain and temperature measurement results. In the research carried out, both Ni and Cu coated FBG-based fibre optic sensors were embedded successfully and shown to give a similar mechanical and thermal response to those non-embedded sensors and give good cross-comparison with the response of the conventional gauge sensor used for that purpose.

The potential of both manual and automatic TIG welding, as effective production techniques for the metal-embedding of FOS, has been successfully demonstrated for both nickel-and copper-coated FBGs. With both techniques and the coating materials considered, the sensitivity of the embedded FBGs is linear with temperature and strain and the sensors and fibre withstand the coating process. The Ni re-coated FBG sensor, embedded using the automatic TIG process, shows the best performance since the spectrum appearance before and after embedding remains unchanged and the original sensitivity remains constant with strain and temperature and the cross-section metallography undertaken shows no damage to the coating. Cu re-coated FBG sensors show more damage in the metallography results reported, especially in the case of the use of the manual TIG technique. The cross-section metallography results, in the latter case have shown how the coating is severely damaged with the use of this technique. This effect is also observed in the spectral analysis of this sensor after it has been embedded. This damage translates to a poorer performance of the sensor, as temperature and strain sensitivities are altered when compared with the original sensitivities of the coated sensors before embedding. It can therefore be concluded that Ni re-coated FBGs withstand the process better than Cu re-coated FBGs. Overall, although both techniques have been successful, the manual TIG process is more hostile to the sensor than the automatic TIG approach, there being a trade-off between the cost of the technique (lower for manual TIG welding) and the performance of the sensors (better for automatic TIG welding). Thus, with TIG welding being a widely available technique, inexpensive when compared to other high-power laser-based FOS metal embedding techniques,

Metal coating and embedding fibre optical sensors for industrial applications.

Chapter 4: Sensor embedding process and characterization.

the results presented are important in choosing the best methods to use to ensure the widespread of the use of embedded FOS in metals for a diverse range of sensing applications.

The results are therefore encouraging for the use of sensors of this type being incorporated to create metallic *smart structures* given the similarity of the performance of the sensors to those used in the conventional way (i.e. not metal embedded) and through the significant improvement to the durability of the sensors seen through the use of this technique. FBGs can be written into fibres which sustain high temperatures so there is considerable potential for further increasing the operational temperature with the use of suitable materials.

Chapter 5. Experimental validation of FOSs embedded into metallic components

In this chapter, the metallic coated and embedded FOSs (Fibre Optic Sensor), developed in the previous chapters, were validated by monitoring the antifriction material of bearings on ships. This work has been developed under the framework of the NEXT-BEARINGS project, which aims to develop a monitoring system, based on FOS, for monitoring the bearing operation and antifriction material degradation, to prevent maintenance actions and, alarm and prevent if unexpected events are detected.

The validation was carried out using two different test-benches adapted to meet different technical aims. On one hand, the response of the embedded FOS front to the antifriction material degradation (e.g. defects, cracks, flakes, erosion, etc) was analysed, and a mechanical fatigue machine was especially designed and developed to test steel specimens with 3-20mm coating thickness of antifriction material coating, simulating an antifriction bearing section. It is also able to generate accelerated deterioration in the antifriction material which is monitored by the embedded FOS with data being analysed for material characterisation. In this case, only FBGs were embedded in the antifriction material coating layer of the specimen. On the other hand, to validate the embedded FOS response to the bearing condition monitoring, a test-bench to test antifriction bearing in a real vessel was used. In this case, FBGs and Rayleigh distributed FOS were embedded in the antifriction material coating layer of the steel bearing.

In this chapter, each validation made using each specific test-bench, is presented, and analysed in detail.

5.1 Introduction

An antifriction bearing is a component consisting of one or two concentric rings, on which the shaft of a machine is supported and rotates. Its function is to support rotating components, such as shafts or half shafts that are part of mechanical systems, in their correct position and transfer axial and radial loads to the supporting structure. Their role is to reduce wear between the shaft and other parts with a low coefficient of frictional wear that support high loads and can reach high speeds by sliding, separated from a lubricant film, without the aid of balls or bearings. They are used extensively in blowers, electric motors, compression ignition engines, turbines, steam engines, etc. The work presented here was carried out for monitoring antifriction bearings from the naval sector, but the developments could be further expanded to other sectors with similar issues and/or components. Figure 5.1.a shows the bearing housing and Figure 5.2.b shows the specific antifriction bearings on which, the work presented in this chapter, was developed.

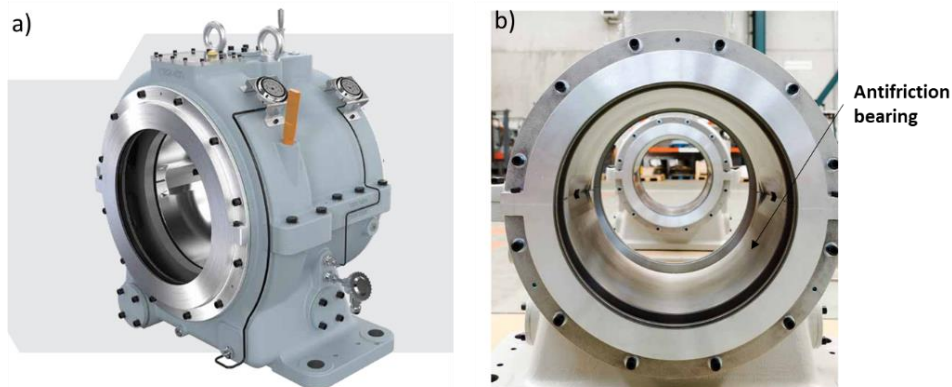


Figure 5.1: Typical hydrodynamic bearing for marine sector. (a) Bearing housing and (b) detail of the antifriction bearing located in the inner part of the bearing housing [3].

Figure 5.2 shows the bearing house (a) and antifriction bearing shells (b) and (c) on a ship shaft (d) and (e).

As shown in the Figure 5.2, an antifriction bearing usually consists of a metal base material (e.g. crude steel, steel or bronze) coated with an antifriction material layer, with around 3-20mm of thickness, of a white material alloy (e.g. Sn, Pb). The antifriction material could be deposited on the base-material bearing by different techniques, such as centrifugal casting, welding, thermal spraying or casting by gravity; depending on the bearing size and material (base-antifriction) composition.

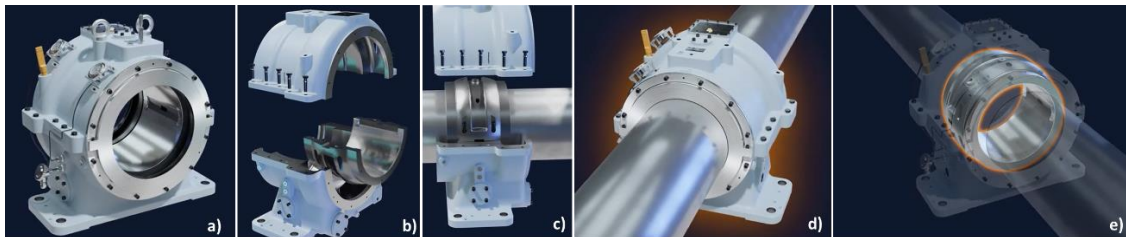


Figure 5.2: a) Bearing housing, b) and c) bearing shell, d) bearing on the shaft, e) antifriction bearing appearance on the shaft [3].

These bearing components, normally, have a limited life because they work under harsh operation conditions (loads, temperatures, lubricant, friction, etc.). The main factors which affect the lifetime of an antifriction bearing are as follows [108], [109]:

1. The operation conditions: loads, speed and temperature.
2. The quality of the bearing lubrication: oil quality, oil quantity and, specially, uncontaminated oil.
3. Assurance of a good bearing installation: no misalignments, distortions or damages.
4. No manufacturing defects.

The most typical defects that appear in the antifriction bearings during their normal operations are shown in Figure 5.3: wear, pitting, erosion, cracks and flakes. These defects could cause the bearing failure and consequently the entire machine or element failure (in motor, turbine, ship, etc.).

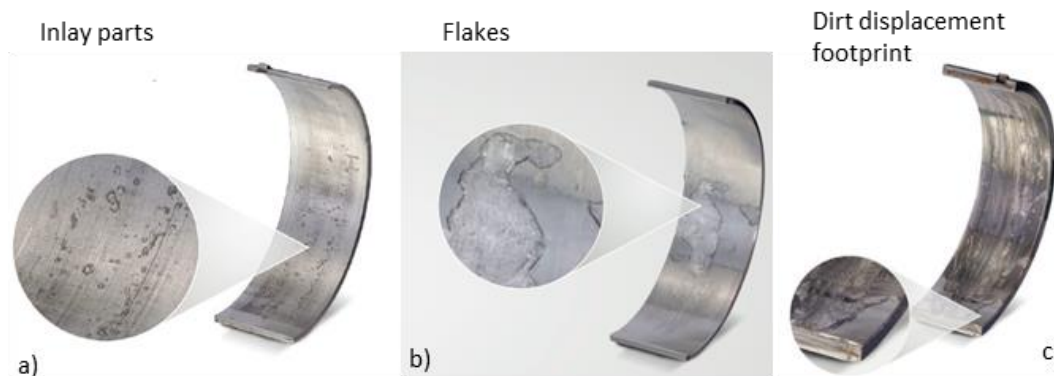


Figure 5.3: Some of the typical antifriction bearings defects due to particles: (a) inlay steel parts due to contamination of oil, (b) flakes due to wear and (c) tear [110].

Moreover, antifriction bearings components are usually installed in locations that are either remote or difficult to access, making their in-situ inspection and maintenance difficult or impossible. However, failures in bearings can result in irreversible damage, continuous operation with an undetected bearing failure may cause excessive heating, possibly damaging the shaft and bearing housing.

The conventional approach for antifriction bearings diagnosis is based on visual inspection, ultrasound and penetrating fluids inspections during the maintenance shutdowns and bearings are usually required to be dismantled. The process is time-consuming and involves a high cost which is not recommended. Under normal maintenance checks, only the parts of the bearing that are visible are inspected, as well as the alignment of the bearing, with respect to the shaft and the bearing house. Hence, it is often not possible to fully know or analyse the condition of the antifriction material, to detect and repair defects and calculate its remained service life. New monitoring techniques, such as vibrations or acoustic emissions and lubricant analysis were studied and introduced for bearings diagnosis [111] including fibre optic sensors, for detection or prediction of failures in bearings [112]–[114]. The most relevant development based on FOS is the “SKF Load Sensing Bearings – for pumps and compressors” [109], [115] monitoring system, based on FBGs, to monitor vibration, load, speed and temperature to determine the condition monitoring of rolling bearings.

In above mentioned studies, glued FBGs or commercial sensors are integrated in the bearing house or external part of the bearing to monitor their vibration and predict maintenance actions required. But no system is able to directly monitor the state of the antifriction material which usually deteriorates first and is the origin of the other failures.

In this chapter, a monitoring system based on FOS was developed and embedded in the antifriction bearing material to monitor, in real-time, the antifriction material status and the bearing operation and, additionally to be able to predict maintenance actions required to prevent catastrophic failures. As a result a Digital-Twin can be created through the establishment of a behaviour model, which leads to the NEXT-BEARINGS project, which is beyond the scope of this thesis. Taking into account these two purposes, the validation was made by two different test-benches as described above.

5.2 Validation of the FOS monitoring system for antifriction material degradation

The service life of antifriction bearings is difficult to estimate using standard fatigue testing carried out on a specific test-bench able to simulate the bearing operation. In this type of test, the specimens are subjected to tensile-compression cycles. However, the dynamic stress exerted on an antifriction bearing is characterized by a pulsating compression stress on the sliding surface to simulate the rotating shaft effect during operation. This does not involve metal

contact, but the stress is transmitted through the lubricant film. Therefore, the antifriction bearing is mainly subjected to fatigue loads, which cause coating flakes, cracks, wear, etc. For this reason, it is necessary to design test benches where the operating conditions are simulated in order to be able to know the service behaviour of the bearing. For the antifriction material degradation study, an ad-hoc test-bench was designed. The design of the test-bench was not based on any reference standards, since it does not exist, rather it was based on the experience of the manufacturer of bearings involved in this work and in the conditions of real service.

In the prototype test bench developed, the tests will be carried out under conditions as close as possible to those encountered in real operation. The small-scale specimen would be evaluated using a non-destructive testing (NDT) method to correlate recorded signals with the deterioration of the specimen. The test bench applies a high number of operating cycles on the specimen tested to simulate the antifriction coating behaviour e.g. forming flakes, cracks, wear and tear as shown in Figure 5.3, along with the output signals of the embedded FOS. The key components of the test-bench prototype are shown in Figure 5.4.a, which include a fatigue machine where the specimen was tested as shown in Figure 5.4.b; a hydraulic module was used to lubricate the specimen; a pressure pump to apply different levels of load on the specimen and a control cabinet to configure the operation parameters (e.g. rotational speed) and visualize the signals generated from commercial sensors (such as oil and motor temperature, pressure and rotational speed).

The booth was filled with a specific lubricant oil, on which an antifriction coated test specimen was mounted. The test specimen simulates the sliding surface of the antifriction bearing (section). For each test, system-specific parameters were monitored to control working conditions (motor torque, engine temperature, pressure exerted on the specimen, lubricant temperature...) and measures derived from the test (deformation and temperature supported by the antifriction coating) to correlate them with the test effect on the specimen.

A rotation shaft is located inside the booth of the bench, in which a support with 3 pins is mounted to simulate the shaft of a vessel. The 3 pins exert the pulsating load supported by the bearings, on the test specimen and, rotate emulating the rotating movement of the shaft. The vertical force (load on the test specimen) was generated using a toroidal-shaped hydraulic cylinder, activated by a manual pressure pump. The shaft on which the pins WERE mounted is operated by an electric servo motor which provides the rotational motion. Figure 5.5.a shows the location of the antifriction specimen and the hydraulic pins which were responsible for generating the pressure and friction to the specimen, through the lubricant oil. Figure 5.5.b shows an antifriction specimen, mounted on top of the booth bench. The specimen consists in a steel "donut" with the antifriction (tin alloy) material coating of a 5mm of thickness, in one of its surfaces. The antifriction material coating layer was applied using laser deposition by Wärtsilla (project partner).

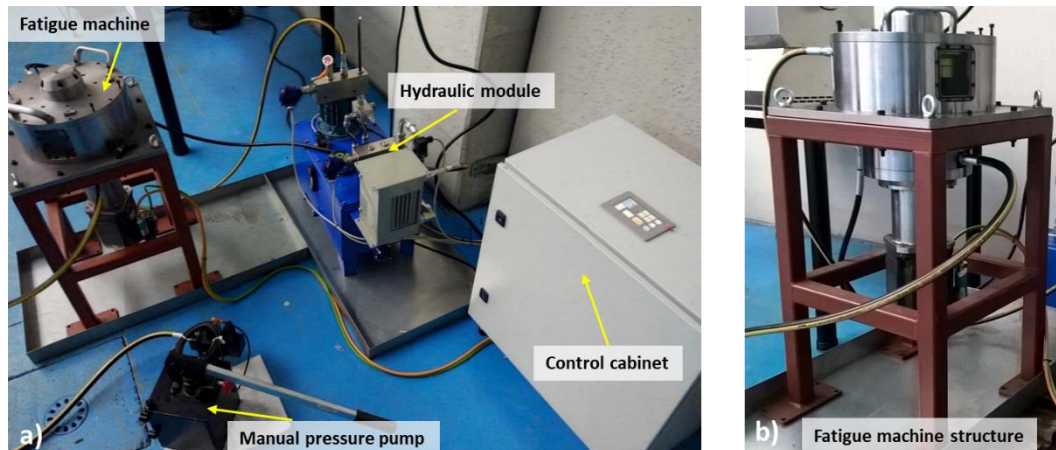


Figure 5.4: (a) Components of the fatigue prototype test bench. (b): Detail of the fatigue machine structure.

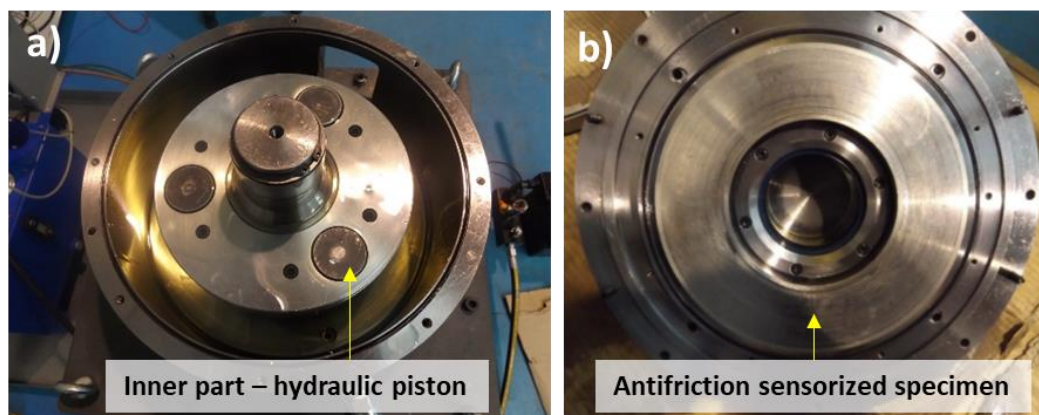


Figure 5.5: (a): Detail of the pistons inside the fatigue machine to apply the pressure on the specimen through the lubricant oil. (b): antifriction specimen where the FOS was embedded.

The test-bench allows the application of accurately controlled pressures on the specimen surface, using the manual pump as well as the possibility of monitoring its value. Also, the test-bench has some PT100 sensors to control the oil immersion booth temperature, oil output temperature and motor temperature. Furthermore, it is possible to select the rotating operation speed. The data from all these parameters was recorded to allow comparison with the FOS output.

5.2.1 Sensorised antifriction specimens fatigue test

The specimen tested and discussed in this section was instrumented with two Ni and two Cu coated FBG sensors using welding techniques as presented in Chapter 4.

Figure 5.6 shows the procedure to embed the metallic coated FBGs in the antifriction material specimen. Figure 5.6.a shows the metallic coated fibre located in a groove (1x1mm) made on the specimen antifriction material coating layer. To prevent the misalignment of the fibre during the embedding process, it was fixed to the groove using tin spot welding. The coated fibre was welded using an automatic TIG technique, adding the same antifriction tin alloy material of the coating layer. Figure 5.6.b shows the four metallic coated fibres embedded in the four grooves. Three of them had embedded FBGs and the fourth a Ni coated fibre. Figure 5.6.c shows the surface of the specimen machined to obtain a homogenous and good quality surface for testing. During the embedding process a Cu coated FBG was broken and during the post-processing, a Ni coated FBG was also damaged. Finally, a Cu coated FBGs survived the entire process. This FBG was re-coated with Cu and it had 550 μ m of total diameter (212 μ m of Cu thickness).

On the surface of the specimen there are four holes not filled during the welding process to protect the outlet of the fibre. The holes are at the end of the groove, where the fibre is located and allows smooth passage of the fibre away from the specimen.

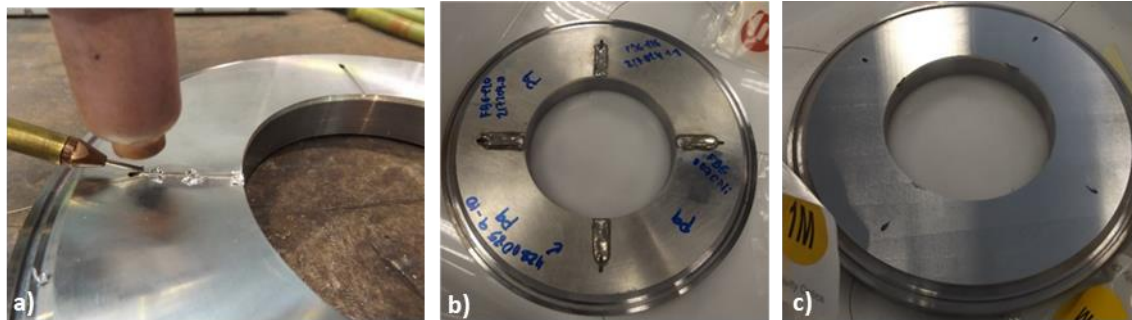


Figure 5.6: Procedure to embed the metallic coated FBGs in the antifriction material specimens. Left: Detail of the metallic coated FBG located in the antifriction material groove and fixed by two tin weld spots points. Centre: Appearance of the specimen after having embedding the FBGs by automatic TIG welding. Right: Appearance of the specimen, with the embedded FBGs, after being machined to unify the specimen antifriction material surface.

Figure 5.7 shows the sensorised specimen assembly procedure. Figure 5.7.a shows the specimen with the FBGs embedded. Figure 5.7.b shows the step where the sensorised specimen assembled in the fatigue test-machine top and the FOS connection exit. Figure 5.7.c shows the final appearance of the sensorised specimen assembled on the test-bench.



Figure 5.7 (a): Specimen with the FBGs embedded. (b): Detail of the specimen assembly on the test-bench machine top. (c): the sensorised specimen assembled.

The fatigue tests performed with this type of sensorised specimens include subjecting the specimen to mechanical fatigue tests using a combination of different pressures and different rotation speeds of the pins, causing friction against the antifriction specimen surface. The objective of these tests was to generate the antifriction coating layer degradation, to analyse the response of the embedded FBG sensor and to generate a database to be used to develop the prediction model, with which to estimate the state of the antifriction material and the process parameters. During each fatigue test carried out, the following data was recorded: FBGs response, lubrication oil temperature, motor temperature, pressure applied, pin rotation speed and motor torque. The FBGs response was then correlated with the other process parameters.

The mechanical fatigue tests were carried out by applying rotational speed between 33-667 rpm and pressures between 5-74 bar, for a total of 31 mechanical tests of total duration 5500h and applying a total of 143 million cycles over the same sensorised specimen. Table 5.1 shows the parameters and the time duration of each test carried out.

	Pressure (bar)	Rotary speed (rpm)	Time (h)		Pressure (bar)	Rotary speed (rpm)	Time (h)
Test 1	7 - 17	667	30	Test 17	14 - 48	167 - 500	700
Test 2	5 - 20	667	95	Test 18	36 - 49	167 - 667	1050
Test 3	21	667	100	Test 19	8 - 47	83	90
Test 4	21	667	75	Test 20	8 - 57	167	90
Test 5	5 - 20	667	70	Test 21	8 - 34	667	30
Test 6	21	667	100	Test 22	8 - 25	667	30
Test 7	21	667	100	Test 23	0	167 - 667	25
Test 8	21	667	100	Test 24	12 - 25	667	30
Test 9	7 - 22	667	95	Test 25	9 - 50	167 - 667	220
Test 10	7 - 22	667	115	Test 26	9 - 50	167 - 500	260
Test 11	5 - 22	667	95	Test 27	9 - 50	167 - 667	220
Test 12	7 - 22	667	100	Test 28	25 - 74	33 - 667	420
Test 13	22	33 - 667	240	Test 29	9 - 50	83 - 667	150
Test 14	7 - 36	667	210	Test 30	9 - 50	83 - 667	25
Test 15	34 - 42	667	250	Test 31	9 - 55	83 - 667	250
Test 16	35 - 40	667	95				

Table 5.1: Summary of the mechanical tests carried out and the parameters applied in each one.

Figure 5.8 shows the wavelength variation of the Cu embedded FBGs during the tests: test 1, test 14 and test 26. The sign response of the FBGs is in comparison with some of the parameters monitored and applied for each test (pressure, rotational speed and oil temperature). It was observed in all the tests that the embedded FBGs varies with changing oil temperature, rotational speed and applied pressure on the antifricition specimen. This is due to the cross-sensitivity of the grating itself. The *sinusoidal shape* of the FBG sensor signal is due to the oil temperature changes during the test. It changes between 50-55°C. During all tests conducted, the embedded FBGs showed a response with a good signal-to-noise ratio.

In addition to the relatively rapid observed temperature fluctuation referred to above (in Figure 5.8) there is a significantly higher frequency component embedded in the signal that cannot be resolved over the timescale used in Figure 5.8. Therefore, Figure 5.9 represents a zoomed-in version of Figure 5.8 (test 14) over the entire interval of 1 second time frame, around the time of 167 hours (highlighted in Figure 5.8), when it was subjected to 37 bars of pressure and 667 rpm. The FBGs signal shows some equi-spaced peaks, which are a result of the pins' effect each time they pass through the sensorized specimen zone just above the sensor. This is because the pressure at this zone changes momentarily due to the pin's pressure effect on the specimen. One of the peaks produces a higher pressure on the FBGs than the others. This could be due to differences in thickness between them. From FBG signal is possible to determine the rotational speed because there are 11 peaks in 1s, which means that the speed is 667rpm. The peak amplitude depends on the applied pressure. For higher pressures the wavelength amplitude is higher.

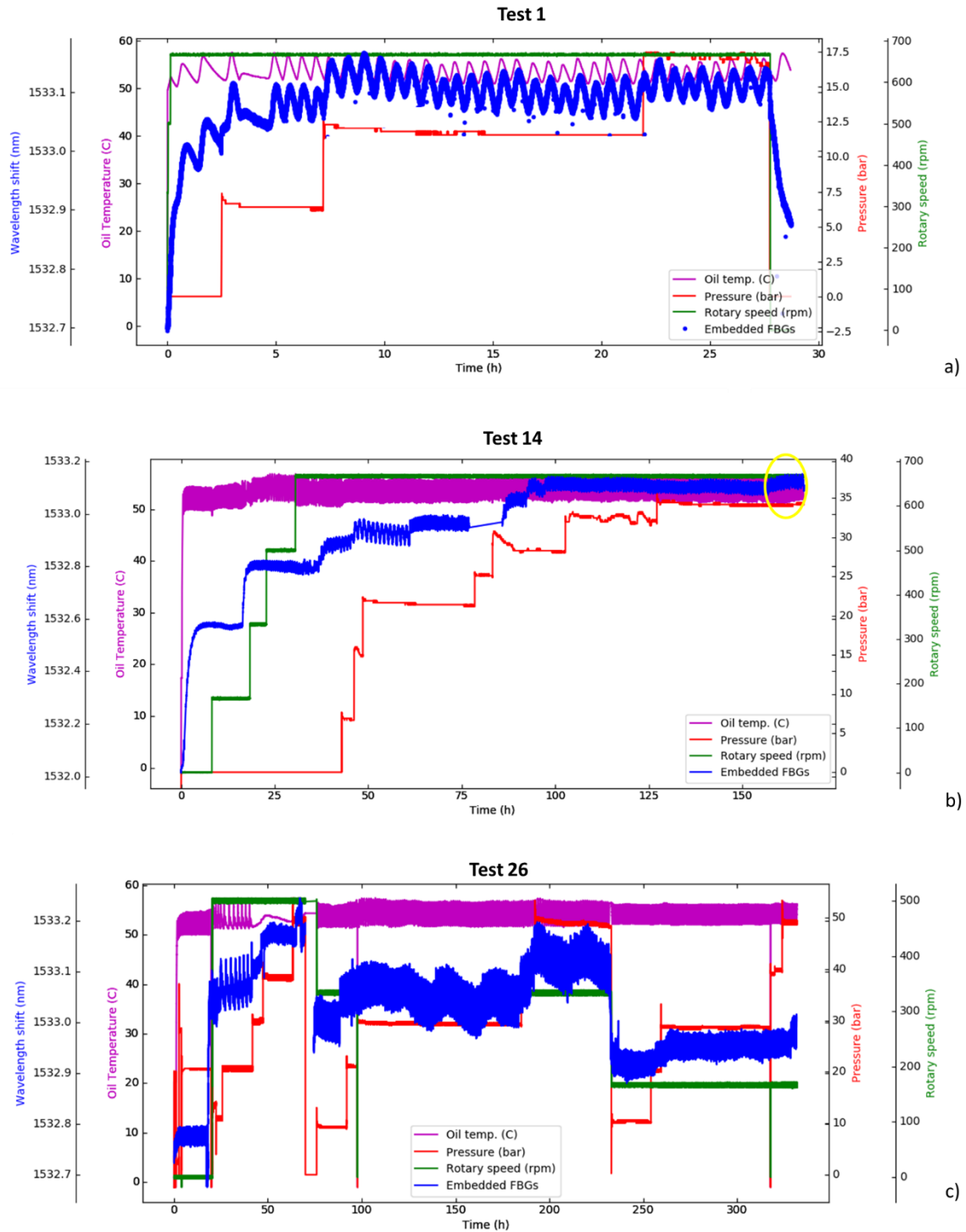


Figure 5.8: Response of the Cu coated FBGs embedded in the antifriction coated specimen during some of the fatigue tests done. a) test 1, b) Test 14, c) Test 26.

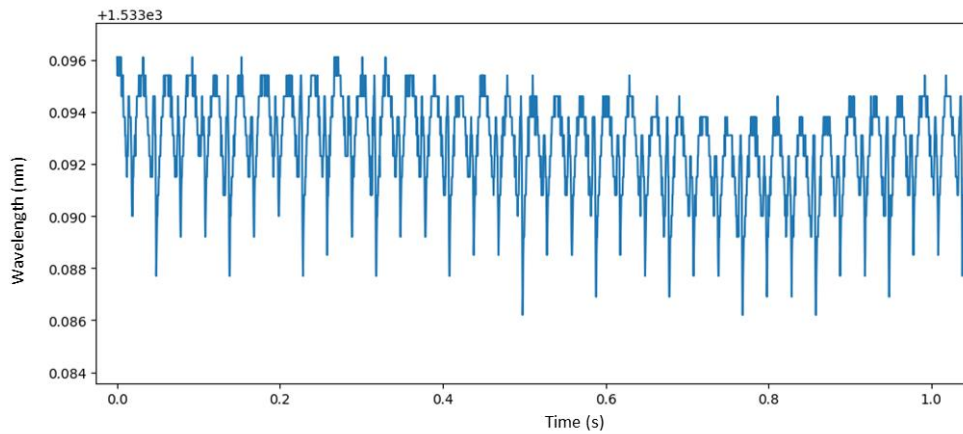


Figure 5.9: Detail of the embedded FBG response for 1s of time at 667rpm and 35bar of pressure.

It is also possible to extract other information, such as the rotational speed of the fatigue machine, from the FBG signal using a Fast Fourier Transform (FFT). Figure 5.10 shows frequency peaks corresponding to rotation speeds of 667rpm (Figure 5.10.a), 167rpm and 83rpm (Figure 5.10.b and Figure 5.10.c) respectively based upon the FFT data analysis. They correspond to the principal frequencies of 33Hz, 8.3Hz and 4.16Hz which are a multiple of the rotational speed and are not influenced by the applied pressure.

In summary, the embedded FBG response does reflect variations in the oil temperature, pressure and rotational speed. It is possible to use this approach, coupled with other channels of information, to obtain real-time information of the operational condition of bearings that the specimen simulates.

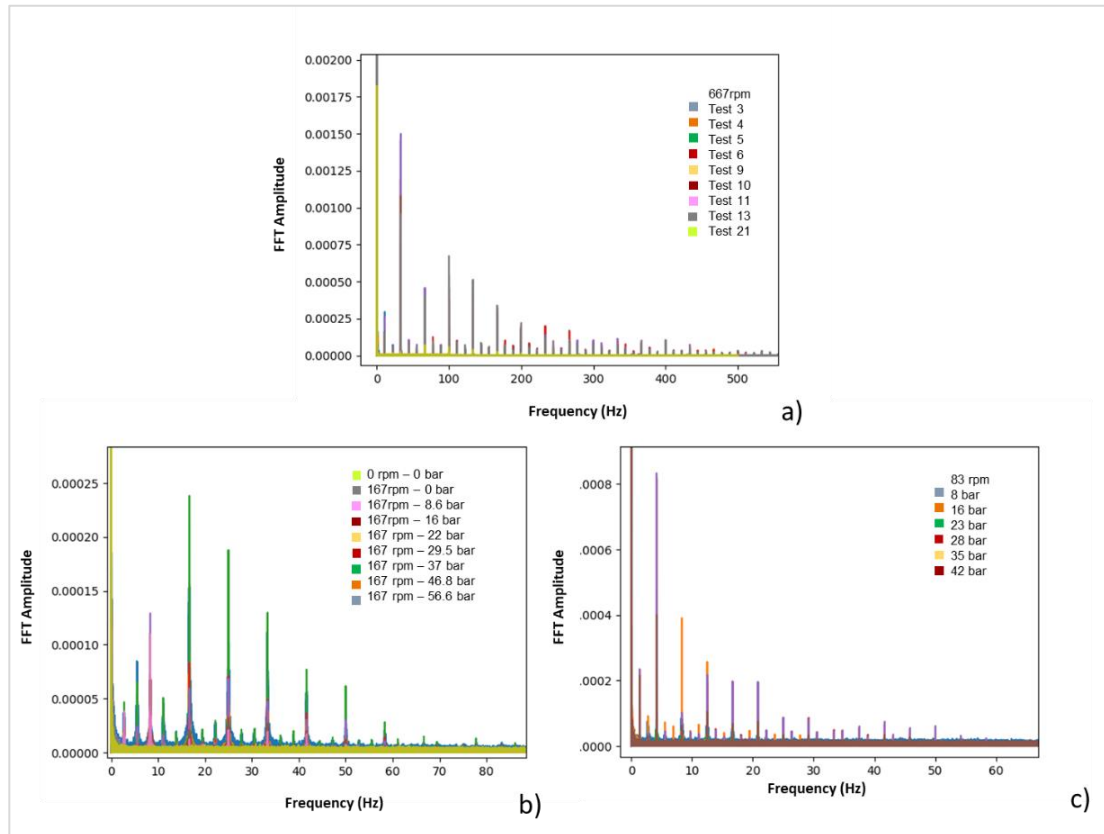


Figure 5.10: FFT of the embedded FBGs signal for some of the rotational speeds applied in the Tests done. a) FFT comparative for 9 different tests done at 667rpm. b) comparison for the Test 20, made at 167 rpm applying different pressures. c) FFT made for Test 19, where the rotational speed was 83 rpm applying different pressures.

Following 20 tests (3800h) no change was observed in the FBG sensor signal. This is indicative of no degradation in the antifriction material. To verify this, an inspection on the antifriction material of the sensorised specimen was made using both visual inspection as well as using penetrating liquids and eddy-current techniques. Figure 5.11.a shows the appearance of the sensorised antifriction material specimen before its test using the mechanical fatigue machine. Figure 5.11.b shows the appearance of the sensorised antifriction material specimen after 3800h of fatigue tests. Some wear was observed in the area where the pins slide, but nothing significant, being only superficial damage.

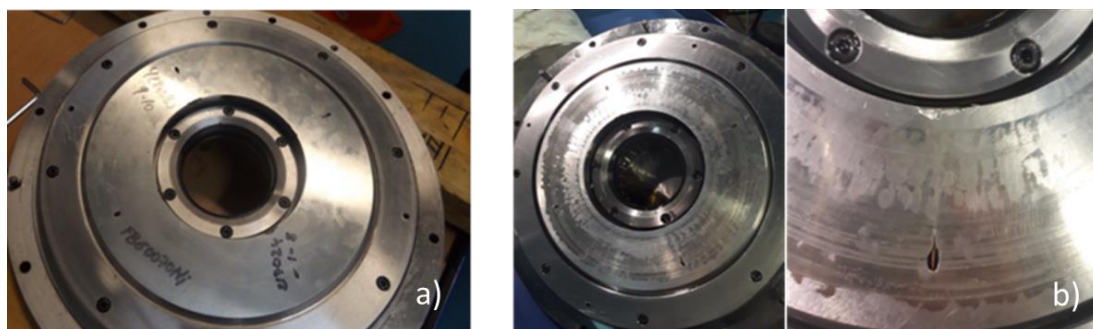


Figure 5.11: a) Appearance of the sensorised specimen before to be tested. b) Appearance of the sensorised specimen after 20 fatigue tests.

Figure 5.12 shows the results obtained using the penetrating liquids technique analysis. The liquids do not show any significant defects, just some light scratches along the central part of the specimen, due to the effect of the pins. The holes through which the fibre optic sensor cables

are pulled out were deliberately left uncovered to protect the optical fibre from the welding process.

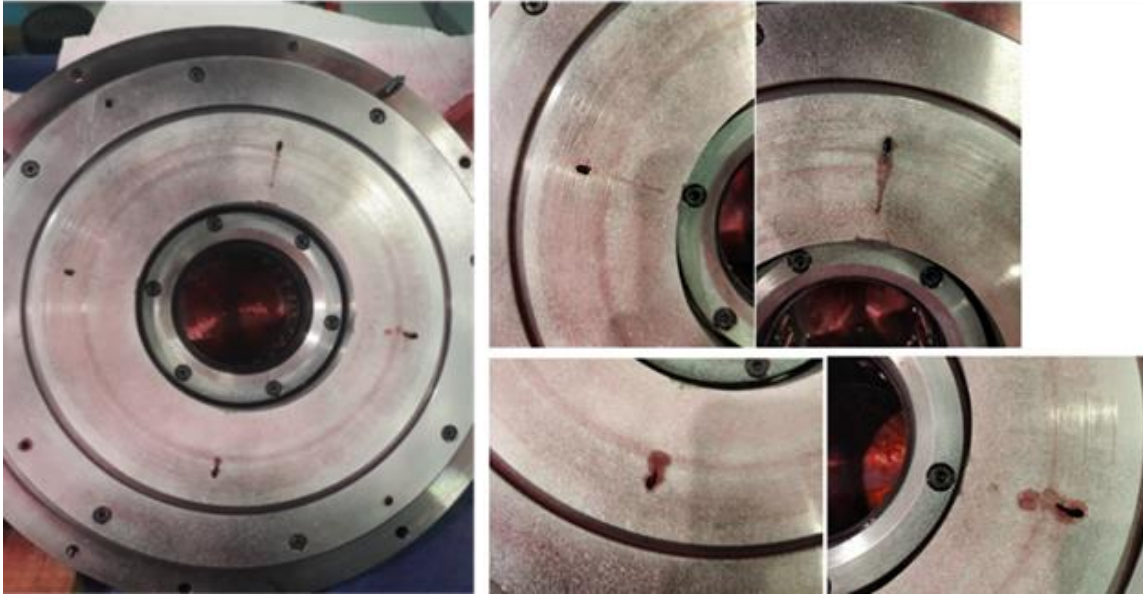


Figure 5.12: Appearance of the sensorised antifriction material specimen after 20 mechanical fatigue tests, inspected by penetrating liquids technique.

Finally, a wear measurement of the specimen surface, using an eddy current technique, was carried out in different areas of the specimen to find out how much of the antifriction material layer had worn away. Master samples of antifriction material coating between 2.2mm - 3mm of coating thickness were prepared for the calibration of the eddy-current equipment, as shown in Figure 5.13.a. The equipment was calibrated against these samples and the surface of the tested specimen was analysed, as Figure 5.13.b shows. The measured wear on the entire specimen was <math><0.1\text{mm}</math>, so it was determined that the specimen was in good condition, with no defects, and that fatigue testing could continue.



Figure 5.13: (a): Eddy current equipment and antifriction material samples with different thickness to calibrate the equipment. (b): Inspection of the sensorised antifriction material specimen by eddy current technique.

The specimen was then re-assembled in the fatigue machine and the tests continued by applying a higher pressure and using a lower rotational speed, with the aim of accelerating the degradation process of the specimen. After nine further tests, there was no observable change in the embedded FBG sensor signal which confirms that no degradation of the antifriction material was achieved.

Following test 29, a re-inspection of the status of the specimen was undertaken. As the specimen showed no further defects or any wear and tear, some artificial defects were deliberately created inside the material in order to 'see' the response from the embedded FBGs. Figure 5.14.a shows the appearance of the sensorised specimen with some defects: two cracks and one wear of around 30mm of length made in the vicinity of where the FBG sensor was embedded. Figure 5.14.b shows the appearance of the specimen after the test 31.

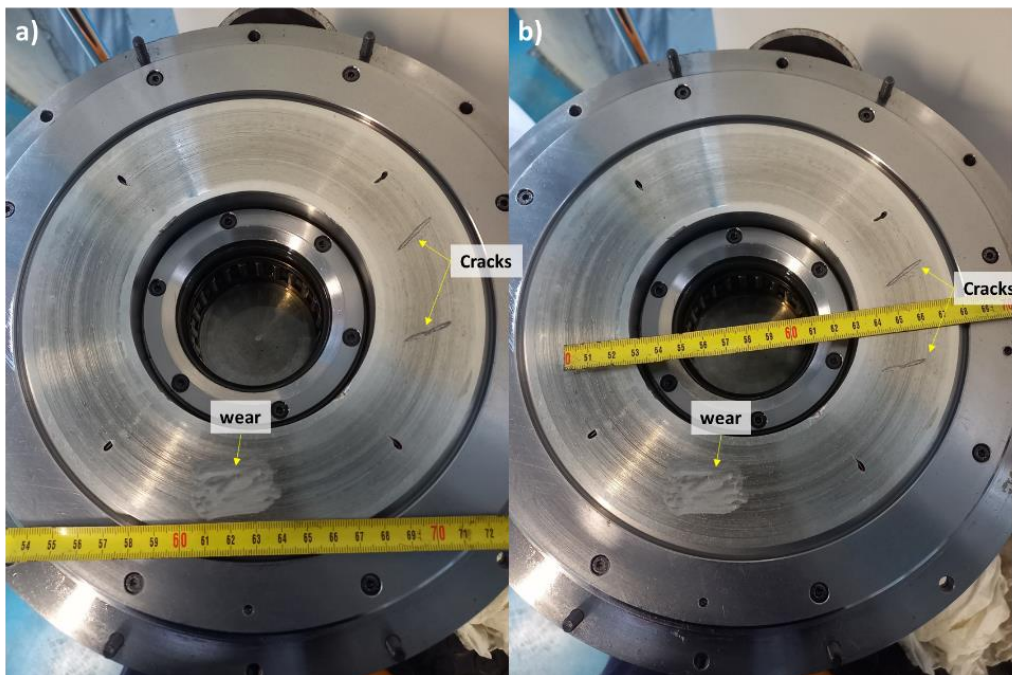


Figure 5.14: (a): Appearance of the sensorised antifriction specimen after 29 tests and detail of the artificial defects made: wear and two cracks. (b): Appearance of the specimen after the test 31.

Figure 5.15 shows the sensor response after the mechanical test 31 with the artificially induced defects on the sensorised specimen. The detailed analysis in Figure 5.16 shows that it is possible to detect some irregularities (noise) in the FBG signal and some double peaks when the pins passed through the embedded FBGs. However, it was difficult to obtain a clear frequency response due to the presence of the defects.

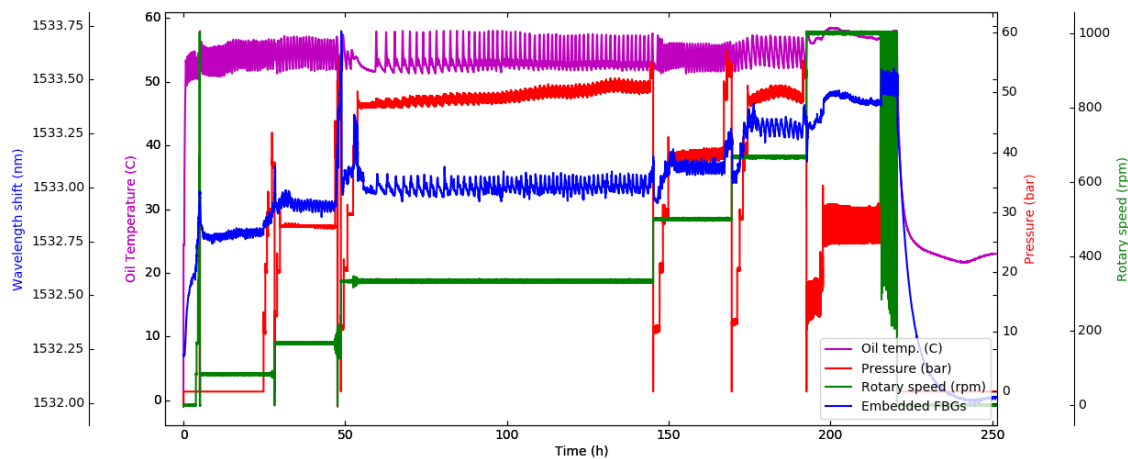


Figure 5.15: Response of the Cu coated FBGs embedded in the antifriction coated specimen during the fatigue tests 31, carried out after the defects made on the specimen.

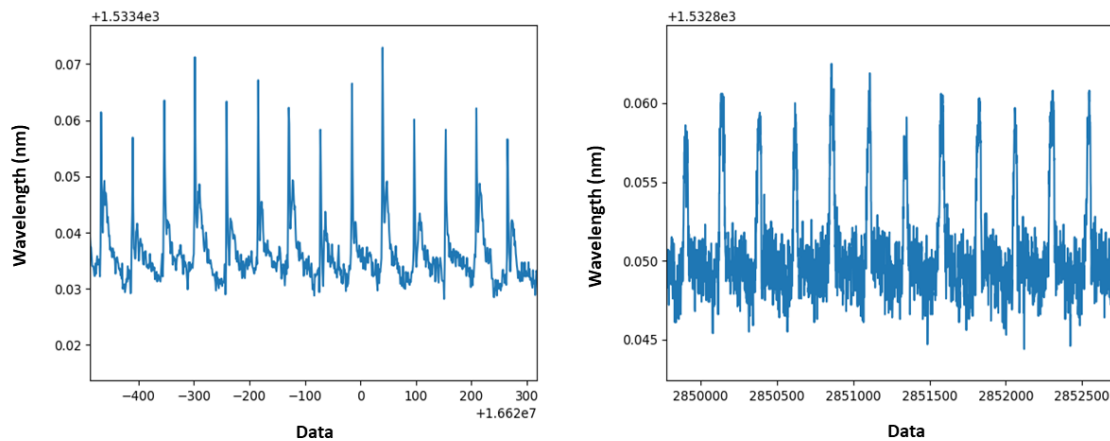


Figure 5.16: Detail of the embedded FBGs response for two different rotational speed and pressures applied on the sensorised specimen during the test 31.

Based on results obtained, it was concluded the fatigue machine cannot generate damage to the anti-friction material of the sensorised specimen, although these tests do serve the useful purpose to train the response of the embedded FBG sensor for potential modelling of its behaviour in operation and predict the working conditions of the bearing. It was demonstrated that the embedded FBGs in the antifriction material produce reliable signals for more than 5500h under fatigue and respond to the change in temperature, pressure and rotational speed. Finally, the embedded FBGs change its response in presence of defects which was one of the principal aims of the development.

5.3 Validation of the FOS monitoring system for antifriction bearing operation

Further to the above experimental simulation tests, a (real) antifriction bearing was sensorised by FOS and tested in a test-bench under real operation conditions. To monitor the antifriction bearing, two arrays of three FBGs together with two distributed Rayleigh-scattering-based FOSs, monitored using an ODISI interrogator (LUNA), were used.

Initially the FOS location and distribution in the antifriction bearing were determined. Figure 5.17.a shows the antifriction bearing with 5mm of coating thickness to be sensorised. Figure 5.17.b shows a schematic diagram showing the location of the location of two grooves, of 1.5x1.5mm and 280mm of length, where the FOSs are to be embedded. For each half shell of the bearing, one is for the FBGs array and the other is for the distributed FOS. As the antifriction bearing is symmetric, two holes at each bearing extreme were made for each groove, in order to have two connection fibres for each embedded FOS, to be connected by any of the two exits, just in case one of the exists was damaged during the assembly process. Furthermore, in the case of the Rayleigh distributed FOS, the second exit was used to splice the coreless fibre, as this part was not Ni coated and therefore it was not possible to embed it.

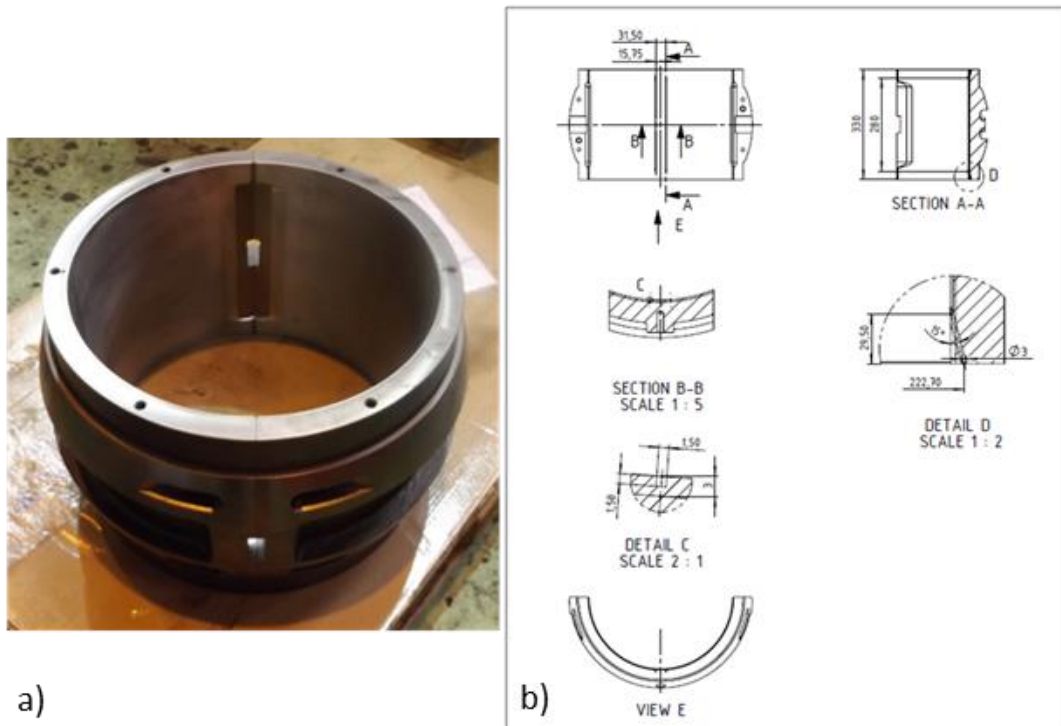


Figure 5.17: (a) Antifriction coated bearing to be sensorised. (b): Machining drawing, for the integration of FBG and distributed fibre optic sensors.

Then, the FBGs arrays and distributed FOS were designed and manufactured. Figure 5.18 shows the axial layout of the FBG arrays and distributed FOS that would be embedded in the antifriction coating material of the bearing. Both optical fibres, FBG array and distributed FOS, would have the same metallic coating. The central part, which was embedded in the antifriction layer of the bearing has a total diameter of 800 μ m, which corresponds to a metallic coating of 338 μ m thickness, in order to assure the protection of the optical fibre during the TIG embedding process. The rest of the optical fibre had a total diameter around 400 μ m (138 μ m of metallic coating thickness). The embedding technique was manual TIG welding as the embedding was performed by the operators of the partner company of the NEXT-BEARINGS project. The metallic coating material applied in these FOS was Ni, because it was the coating material with which the best results were achieved in the embedding tests by manual TIG welding, explained in Chapter 4.

For the FBGs arrays, the FBGs location was also defined, one of the FBGs was located in the centre of the bearing shell and the other at 20mm from the borders of the bearing.

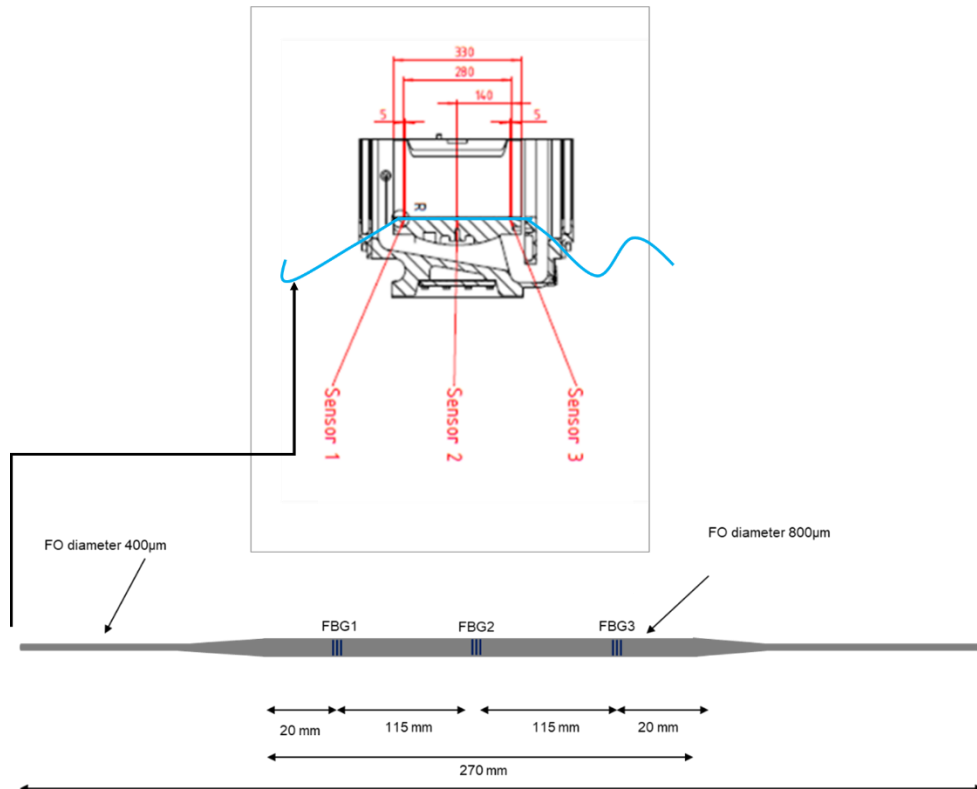


Figure 5.18: Design of the metallic re-coated FOS to be embedded in the antifriction material coating of the bearing.

After the bearing was machined, the sensors were manufactured and integrated into the bearing. To do this, the sensors were placed in the grooves, the FBG arrays in one of the grooves (from each half shell) and the distributed sensors in the other parallel to it, before being embedded by manual TIG welding using the same adding material as the antifriction material (tin alloy). Finally, the weld seams applied to embed the sensors were machined to obtain an uniform antifriction coating surface throughout the bearing. All embedded sensors survived the embedding process without any damage. Figure 5.19 shows photographs from each step done during the embedding process and the final appearance of the antifriction bearing with the FOS embedded. Figure 5.19.a shows one of the antifriction bearing shells with the machined grooves ready to be sensorised. Figure 5.19.b shows one of the grooves with a Ni metallic coated distributed FOS located in the groove to be embedded. Figure 5.19.c shows the distributed FOS embedded and FBGs array located and the process of embedding being initiated by manual TIG welding. Figure 5.19.d shows the manual TIG welding embedding process of one of the metallic coated FBGs array. Finally, Figure 5.19.e shows the final appearance of the two sensorised half antifriction bearing shells after the manual TIG embedding process.

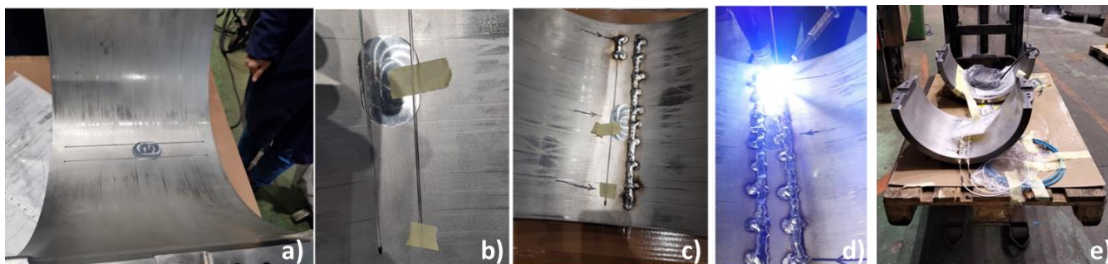


Figure 5.19: Embedding FOS procedure and final antifriction bearing appearance. a) Antifriction bearing shell with the machined grooves, b) detail of the groove with one Ni metallic coated distributed FOS located in the groove, c) distributed FOS embedded and FBGs array located and started to be embedded by manual TIG welding, d) image during the manual TIG welding embedding process of one of the metallic coated FBGs array, e) two half shells after the manual TIG embedding process.

All the Ni-coated FOSs (two FBG arrays and two distributed FOSs) survived the manual TIG welding process, exhibiting good output signal throughout the process. Figure 5.20.a shows the appearance of the two sensorised antifriction bearing shells after the machining of the surface. Figure 5.20.b shows the optical fibres connection exit from the sensorised bearing.

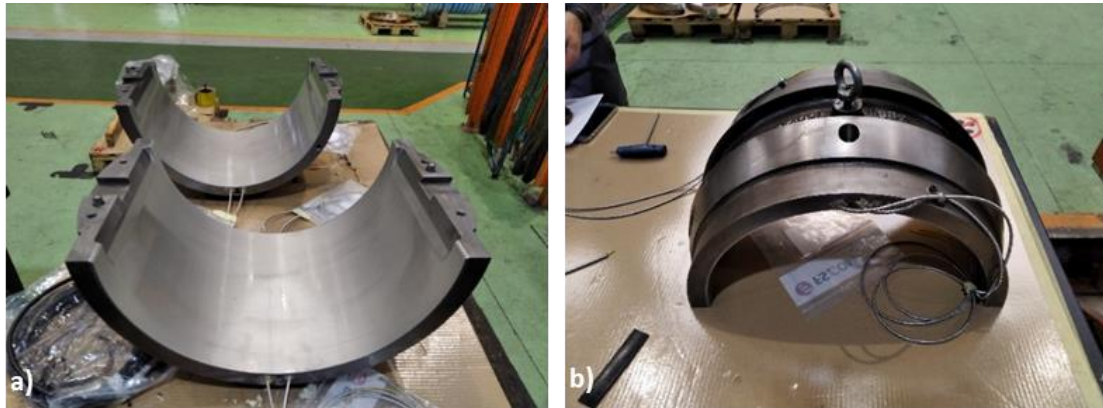


Figure 5.20: (a): Sensorised antifriction bearing shells appearance after the surface machined. (b): FOS exit.

Finally, the sensorised antifriction bearing was installed in the test-bench, as shown in Figure 5.21, for testing. The sensorised antifriction bearing had one array of three equi-spaced FBGs located on the central zone of each bearing shell, three equi-spaced FBGs in the central area of the half bottom of the bearing, and other three equi-spaced FBGs in the central area of the upper half of the bearing. The distributed Rayleigh FOS were parallel to the FBGs, offset by a few cm. During the assembly of the sensorised bearing in the test-bench, the Rayleigh distributed FOS extremity, from the coreless fibre (end section of fibre sensor) had to be bent with a small radius due to the very narrow access area. This resulted in the Rayleigh FOS signal being not fully readable either with noise or no signal for some sections of the fibres.

On this test-bench it is possible to simulate the real operation conditions of a bearing in service and even apply real limit conditions, in order to analyse its response under potential extreme circumstances.



Figure 5.21: Final appearance of the FOS sensorised antifriction bearing installed in the test-bench.

A total of eleven tests were performed in the test-bench and a summary of the conditions applied in each test is shown in Table 5.2.

	Pressure (bar)	Rotary speed (rpm)	Number of repetitions
Test 1	170	250 - 50	1
Test 2	250 - 80	250 - 50	1
Test 3	250	250	1
	250 - 80	50	1
Test 4	250	250 - 25	1
Test 5	250	250 - 25	1
Test 6	250 - 80	250 - 150	3
Test 7	250 - 80	250 - 150	1
		100 - 50	3
Test 8	210 - 80	250 - 25	1
Test 9	210 - 80	250 - 25	1
Test 10	210 - 80	250 - 25	1
Test 11	210 - 80	250 - 25	1

Table 5.2: Summary of the tests made in the test-bench.

Figure 5.22 shows the final appearance of the two shells of the sensorised bearing after the eleven tests made in the test-bench. Also, it shows the detail of the FBGs location. The antifriction coating does not show any noticeable defect or wear on its surface, only some minor and normal scratches in the lower shell (Figure 5.22.a), while the upper part does not show any defect or mark (Figure 5.22.b).

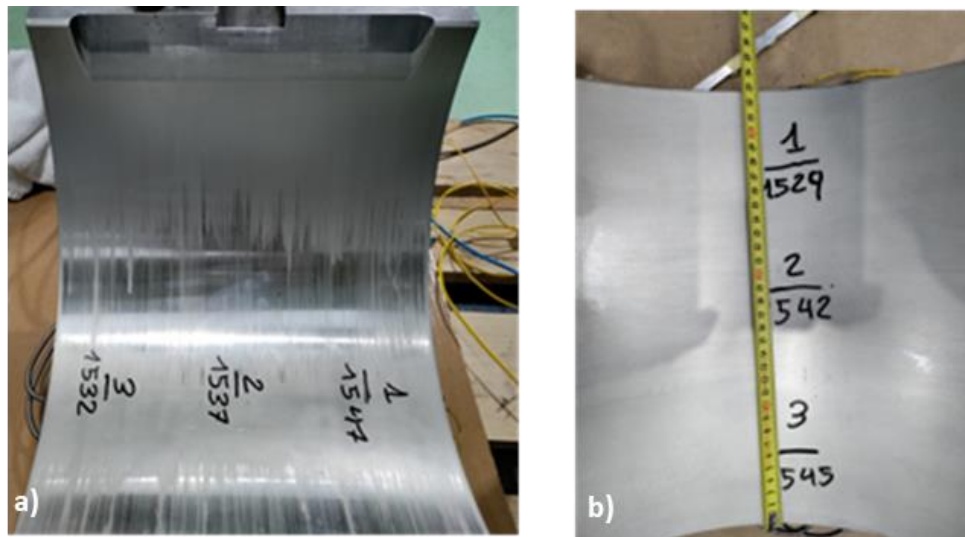


Figure 5.22: Appearance of the two half shells of the sensorised bearing after the eleven tests made. (a): below part. (b): above part.

5.3.1 Results from the embedded FBGs

Figure 5.23 shows the results from a randomly selected set of tests (test 2, test 6, test 7 and test 11) carried out in the test-bench. Figure 5.24 shows the response of the FBGs embedded in the two half-shells of the antifriction material bearing, plotted in dark blue from the lower part and

Metal coating and embedding fibre optical sensors for industrial applications.

Chapter 5. Experimental validation of FOSs embedded into metallic components.

light blue from the upper part of the bearing. The layout of 3 the FBGs within one fibre is similar to that shown in Figure 5.18.

In addition, lubricating oil temperature and rotational speed are represented in magenta and red, respectively.

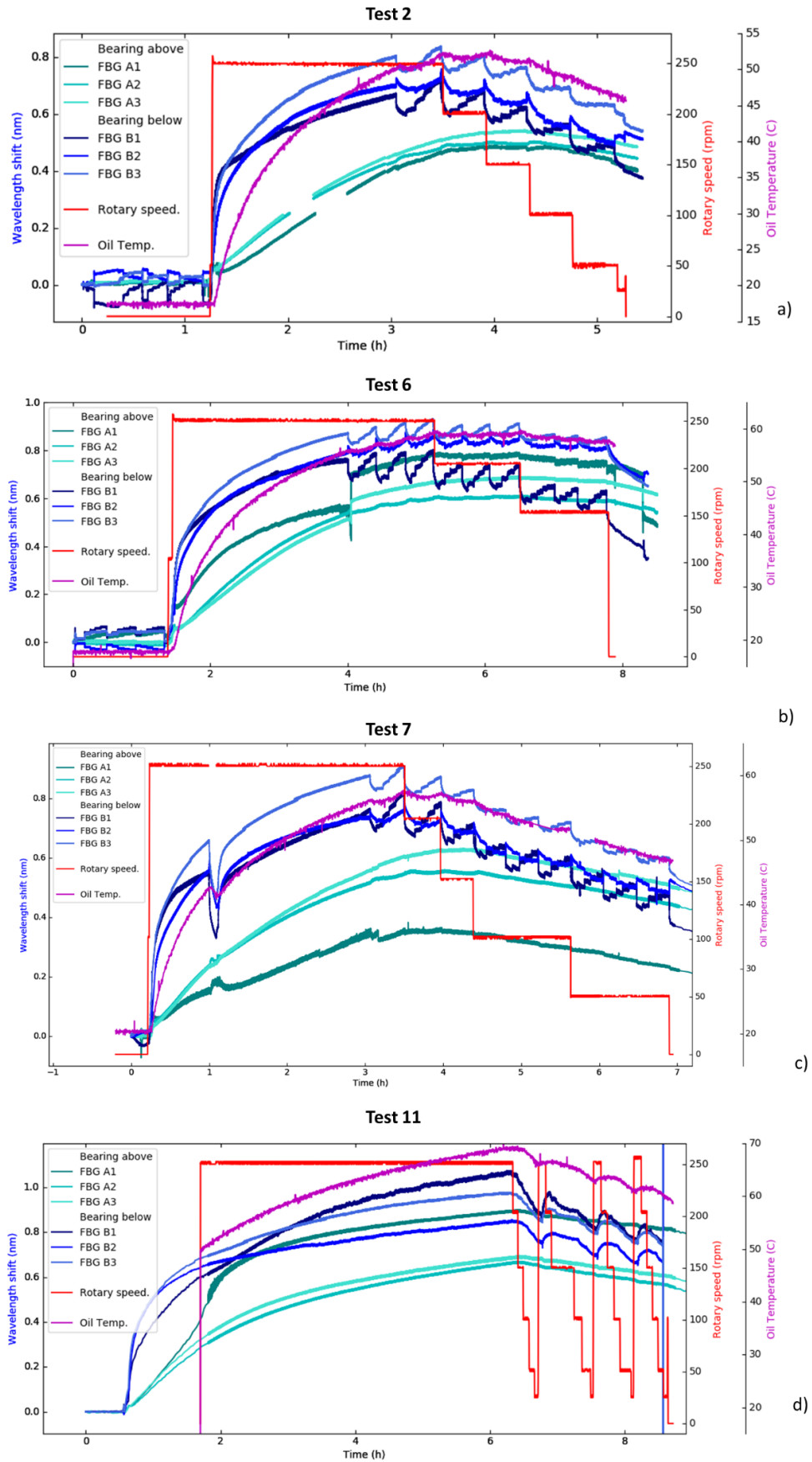


Figure 5.23: Response of the Ni re-coated FBGs embedded in the antifriction bearing during some of the tests carried out in the test-bench. a) test 2, b) test 6, c) test 7, d) test 11.

Figure 5.23.a corresponds to the test 2 where first three static pressure ramps were applied in static mode (without any rotational speed applied), to analyse the FBGs sensitivity and response. Three repetitions of pressures between 80bar to 250bar in steps of 40bars were applied. Then, the bearing rotation was turned on, the oil was heated, a rotational speed of 250rpm (on the shaft) and a pressure of 80bar (on the bottom of the bearing) were also applied. When the oil temperature was around 50°C, the minimum operation temperature for the lubricant oil, the pressure was increased in steps of 40bar up to 250bar. Then, the rotational speed was changed to 200rpm and the pressure was varied from 250 to 80 bar in steps of 40bar. This was repeated for each rotational speed applied. Figure 5.23.b and Figure 5.23.c shows the results obtained from tests 6 and 7, which were similar to test 2 but include more repetitions for each combination of rotational speed and pressure applied in order to analyse the FBGs repeatability. Finally, Figure 5.23.d show the results from the final test, test 11. In this case, the pressure was maintained constant, while the rotational speed was changed from 25rpm to 250rpm (for each pressure applied).

The pressure variation data was saved manually and measured using the conventional strain gauges glued on the outside and underside of the bearing structure. In the signal of the FBGs embedded in the lower part of the bearing, some step-shaped changes in sensor response were observed as shown in Figure 5.24. These step-changes are due to the pressure variations applied from 80 to 250 bar.

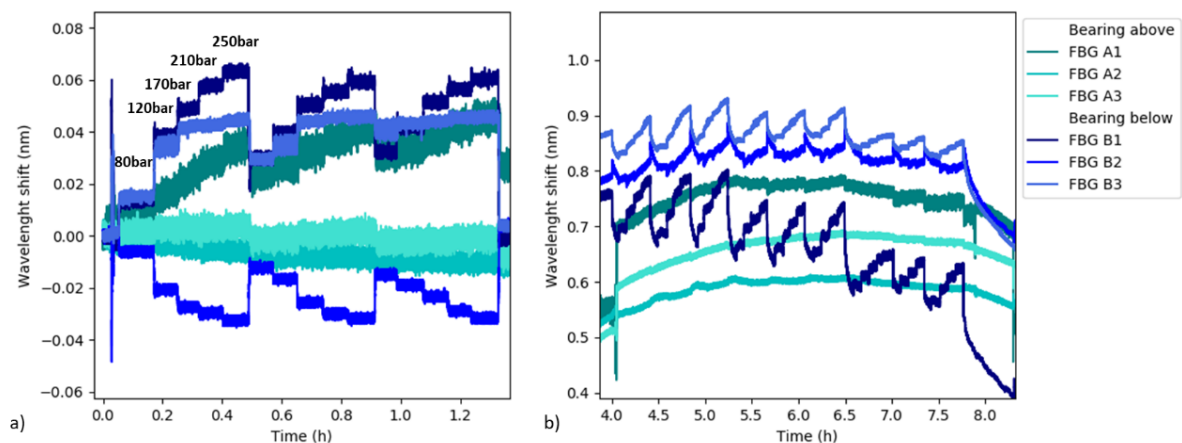


Figure 5.24: Detail of the embedded FBGs response for the test 6, front to: (a): pressure variations in static (no rotational speed applied), and (b): rotational speed and pressure variations.

Figure 5.25.a shows the response of the conventional strain gauges glued on the outer bearing structure for test 2. Figure 5.25.b shows the detail of the conventional strain gauges during the static pressure variation test. In general, they show a noisy signal, due to the vibrations during the bearing operation and a low sensitivity to the pressure variations. Only the conventional strain gauge 3 shows a higher sensitivity during the static pressure variations.

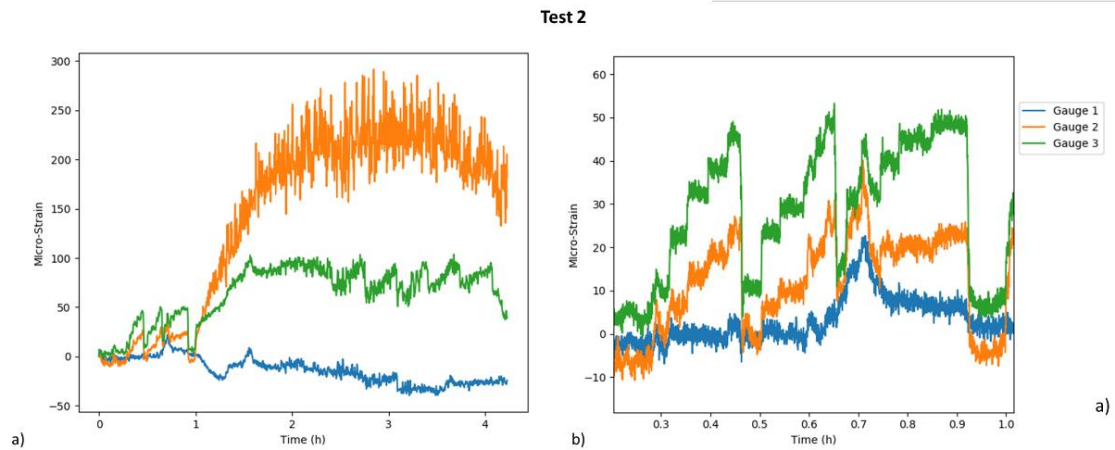


Figure 5.25: (a): Conventional strain gauges response for the test 2. (b): Detail for the static pressure variation.

From the data of Figure 5.24 and Figure 5.25 it is concluded that all the embedded FBGs have exhibited a stable signal response along all the tests done, both FBGs arrays are sensitive to temperature variations. In addition, the FBGs embedded in the below part of the bearing are more sensitive to pressure variations. This was expected as the pressure was applied directly lower this area. FFT were performed for each embedded FBGs in order to determine the rotational speed. Figure 5.26 shows a representative sample of some FFT responses for the embedded FBGs. Figure 5.26.a shows a FFT response comparison for 3 FBGs embedded in the lower half shell of the bearing during test 6, applying 250bar of pressure and 250rpm of rotational speed. All the embedded FBGs have the same frequency peaks at 250rpm (3.12Hz). In addition, despite the fact that the sensors embedded in the above half shell bearing have shown to be less sensitive to pressure variations, they are sensitive to rotational speed variations. Figure 5.26.b shows a comparison of the FFT response of FBG1 embedded above, applying 250bar and three different speeds (250rpm, 200rpm and 150rpm), during test 2. Each FFT made for each rotational speed, shows a principal frequency peak equi-spaced between them, characteristics of each applied rotational speed: around 1.8Hz for 150rpm, 2.5Hz for 200rpm and around 3.1Hz for 250rpm, the same frequency as that obtained for the embedded sensors of the lower section for 250rpm (Figure 5.26.a). Finally, a characteristic frequency dependency with the applied pressure was studied. For this, a comparison of FFT for 250rpm and pressures from 80 to 250bars was made for one of the embedded FBGs, FBG2 embedded in the lower part of the bearing. Figure 5.26.c shows this FFT comparison, all the FFTs, independently of the pressure applied, showed the same frequency peaks.

In conclusion, all the embedded FBGs are able to detect variations in the applied rotational speed. The characteristic frequencies obtained from the FFT are the same for all the embedded FBGs and independents of the applied pressure. Therefore, it is possible to determine the operation rotational speed by making a FFT for any of the embedded FBGs. Also, is possible to determine the operation temperature from all the embedded FBGs (below or above). However, in the case of the applied pressure, it is better to record the information from the FBGs embedded in the lower part of the bearing, where the pressure is directly applied and the pressure signal is stronger.

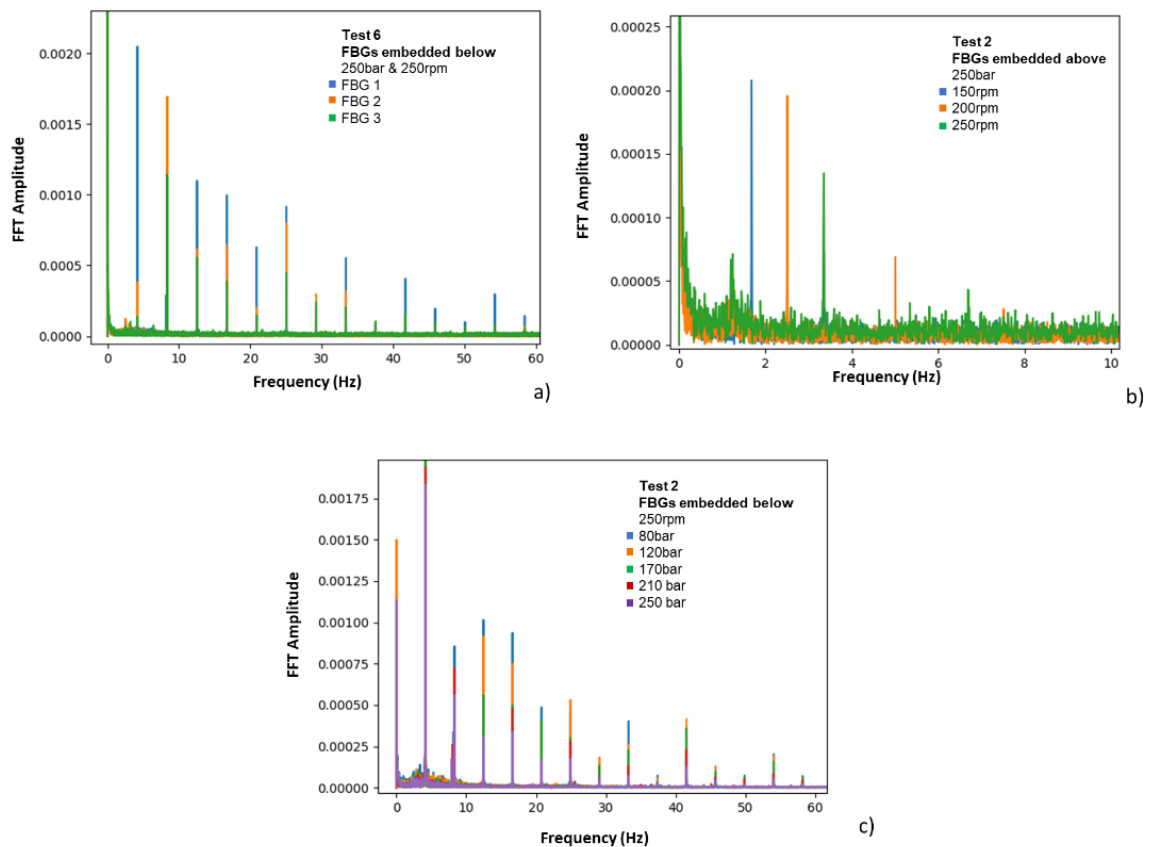


Figure 5.26: FFT response for some of the embedded FBGs. a) FFT response for the FBGs embedded in the below half shell bearing. Test 6 applying 250rpm and 250bar. b) FFT response for the FBG 1 embedded in the above half shell bearing, during the test 2 applying 250bar and different pressures (150rpm, 200rpm and 250rpm). c) FFT response for the FBGs embedded in the below half shell bearing during the test 2 applying 250rpm and several pressures between 250bar to 80 bar.

5.4 Summary

In this chapter results have been presented for Ni and Cu metallic coated FBG and distributed FOS were embedded in an antifriction metallic material and validated experimentally both in laboratory and on test-benches. Their response under different operation conditions was analysed in face of antifriction coating degradation.

FBGs were embedded in antifriction material specimens to monitor their degradation using a fatigue machine, specifically designed and developed to apply mechanical fatigue and thus accelerating the antifriction material degradation and to characterise and analyse the response of the FBGs under this degradation. This machine was able to apply friction on the antifriction material specimen coating at different pressures and rotational speeds, applying a lubricant oil film between the pins and the specimen surface.

Three of the Cu and Ni coated FBGs manufactured, were embedded in the specific antifriction coated specimens using the automatic TIG technique. Although, in the end only one of them could be tested in the fatigue machine because of the problems encountered during the sensorised specimen assembly. The embedded FBGs were tested for more than 5500h obtaining a stable response against all externally applied conditions tested. From the embedded FBGs it was possible to determine the pressure, rotational speed and temperature of operation. After more than 5200h of fatigue tests, the specimen did not show any significant sign of wear or

Metal coating and embedding fibre optical sensors for industrial applications.

Chapter 5. Experimental validation of FOSs embedded into metallic components.

defects in the antifriction coating layer. Subsequently, it was necessary to impose artificial damage on the surface of the antifriction coating layer to analyse the embedded FBGs response. It was observed that some changes in the FBGs response are related directly to the defects introduced.

The metallic coated FOS were also embedded in a commercial/real antifriction bearing and tested in a test-bench under real operation conditions. In this case, FBGs and Rayleigh distributed FOS were embedded in the antifriction material coating layer of the steel bearing, but unfortunately the distributed FOS was partially damaged.

In this validation, all the embedded FOS were able to monitor the temperature variations. In addition, the embedded FBGs were able to monitor the rotational speed and in particular, the FBGs embedded in the lower part of the bearing were also able to monitor the pressure variations.

In general, in this chapter the metallic coated FOS developed in the previous chapters were embedded and tested successfully in a metallic component using two different welding techniques. They were also under real operation conditions, obtaining a stable response from long-term tests. The embedded FOS has shown its response to the whole operation conditions, with changes in temperature, pressure and rotational speed. Finally, it was also demonstrated that the embedded FOSs have the potential for efficiently detecting damage or defects in real time, thus to inform required preventive actions.

Chapter 6. Metal coated FOSs for monitoring Concentrated Solar Power Plants (CSP).

In this chapter, the metallic coated Fibre Optic Sensors (FOS) were designed to monitor new concrete storage solutions for Concentrated Solar Power plants (CSP), under the framework of the NEWSOL (New StOrage Latent and sensible concept for a highly efficient CSP Plants) European project [2]. The NEWSOL project has developed a new strategy for high efficient thermal energy harvesting in CSP systems by combining novel functional and advanced materials into a dual solid/liquid media. It consists of two new Hybrid and Thermal Energy Storage system architectures: a novel thermocline tank concept for new CSP plants and an advanced concrete module for retrofitting existing CSP plants. The most promising materials to be developed include: 1) Two sensitive heat storage concretes with high thermal stability, high specific heat storage capacity and enhanced thermal conductivity; 2) Novel heat transfer fluids (molten salts), which also act as sensitive heat storage liquid materials, that allow higher operating temperatures than thermal oil fluid with improved heat capacities; 3) Low cost rock filler materials (e.g. waste) to enhance sensitive heat storage capacity at the expense of less use of molten salts; 4) enhanced storage sustainability through minimisation of heat storage losses using two novel insulation cover materials solutions. Furthermore, to obtain information about these novel materials behaviour, a novel and integrated monitoring system based on FOS (FBGs and distributed) has been developed to monitor the thermocline and module operation, as well as their Structural Health Monitoring (SHM).

This chapter includes the development, integration and validation of the monitoring system based on FOS, through the process of FOS laboratory characterization, mid-scale validation and full-scale design and integration.

6.1 Introduction

NEWSOL's main objective is to implement an innovative thermal energy storage design based on the combination of new functional and advanced materials, such as solid (concrete and filler), liquid (salts) sensitive heat storage media, latent heat storage media (e.g. PCMs (Phase Change Materials)) and heat insulating materials. All these components can be used to build two innovative system architectures: a single concrete thermocline molten salt tank and a concrete module. In addition, in order to assess their degradation and performance, including stability, thermal performance, yield and conversion efficiency, it is essential for NEWSOL to rely on advanced monitoring technologies (up to 550°C) for both architectures. The deployment of novel molten salts and the high operating temperatures imply working in harsh environments (high temperatures up to 550°C and corrosive environment) that many technologies do not withstand. Therefore, monitoring systems for Thermal Energy Storage (TES) have traditionally relied upon a few thermocouples located in specific positions, a monitoring technology which is limited and does not offer enough information to assess the structural degradation and concrete performance. FOSs are a promising alternative, in particular Fibre Bragg Gratings (FBG) and Brillouin distributed sensors (BDS), which are the technologies selected for NEWSOL. Their electro-magnetic immunity, light weight, small size, multiplexing possibilities and capability of operating in harsh environments (near 1000°C) make them well suited for NEWSOL's particular application. Furthermore, they offer quasi-distributed (by FBG) and fully distributed (by BDS) measurements, reducing blind spots and allowing continuous health monitoring of the structure. Thus, in NEWSOL a monitoring system based on strain and temperature FOS was developed, integrated and validated to monitor, on the novel thermocline and storage module, their operation and durability. In this chapter the FOS monitoring system, based on FBGs will be explained, with a particular focus on the design, development, integration and validation of the FBGs based monitoring system from lab-scale to full-scale (prototype).

The most widely employed conventional transducers for SHM include thermocouples for temperature monitoring, strain gauges for strain monitoring and embedded or surface-bonded piezoelectric sensors for vibrations or acoustic emission (AE). However, these technologies possess serious drawbacks for monitoring large structures at high temperature or corrosive environments (molten-salts exposition). Thermocouples and strain gauges are hard to multiplex and are subject to electric and magnetic disturbances. In the case of piezoelectric sensors, they lose the piezoelectric effect above the Curie temperature (300°C) and exhibit degradation due to repeated thermal cycling. Furthermore, they do not offer very good multiplexing capacities, and resistance to corrosion. For all these reasons, fibre optic sensors were selected to be integrated in the NEWSOL structures, due to their technical advantages as discussed extensively in this thesis.

However, fibre optic sensors are elements characterised by small size but are fragile. Direct installation of these devices during the building process could break the fibre optic sensors, and/or affect their durability and/or their response. To avoid this, some protective encapsulations have been developed [116], [117] to ensure both the protection of the fibre sensor(s) and their correct measurement. There are two principal ways to integrate the sensor into a structure: gluing to the surface or embedding into the structure. The latter was the approach used in this project.

The design of the NEWSOL concrete prototypes is shown in Figure 6.1. Figure 6.1.a shows the drawing of the thermocline tank prototype and Figure 6.1.b of the energy storage module prototype. The FOSs have been embedded in different concrete layers of the module and thermocline tank, as well as, in the molten salts (located inside the thermocline tank). The embedded sensors into the structural materials give smartness to the structures and allow the monitoring of critical points (in real-time) which the other conventional sensors cannot provide. The sensors were embedded during the building process of the NEWSOL prototypes.

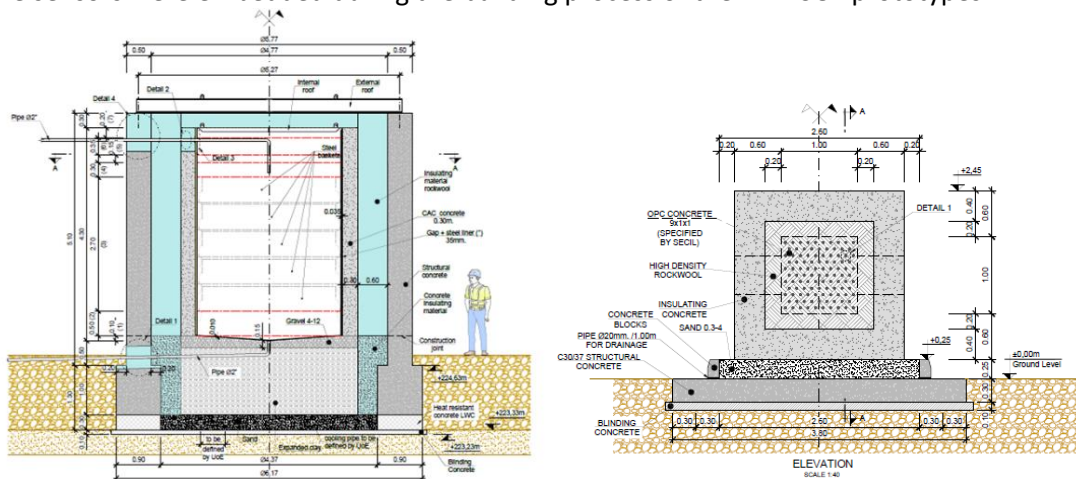


Figure 6.1: NEWSOL concrete prototypes final design. a) Thermocline tank, b) energy storage module.

Due to the delay caused by covid, there is little information extracted from the installed Brillouin distributed sensors so this chapter focuses only on the development carried out for the construction of a strain and temperature monitoring system based on FBGs, in order to integrate them in the NEWSOL project prototypes.

6.2 FOS coating and packaging development

As highlighted above, it is important to develop an FOS that can not only withstand high temperatures but also a corrosive environment. In this project, metallic coated and encapsulated FOS were developed and embedded both in the concrete and in the molten salts to monitor temperature and strain of the structures/materials.

The metallic coating was based on Ni, following the manufacturing process explained in Chapter three, both for FBGs and for distributed sensors. While the packaging sensors were based on encapsulating coated Ni or commercial polyimide coated FBGs in a stainless-steel capillary tube of 3.2mm of external diameter and 2.7mm of internal diameter.

6.3 Validation on a laboratory scale

The objective in this part of the investigation was to build samples to characterize the embedded sensors when they are subject to conditions similar to those required at the final stage of NEWSOL. The manufactured samples with embedded strain and temperature FBGs were subjected to temperature cycling once cured. The strain FBGs with a diameter of around 500-600 μm were coated with Ni. They were encapsulated from the connector extreme to a few centimetres before the FBGs position to protect them during integration and subsequent testing. The temperature FBG sensors were, also, coated with Ni (with a diameter of around 500-600 μm) as well as being encapsulated in a 316L stainless steel with an external diameter of 3.2mm, which makes it strain-free.

Two concrete specimens (mini-modules, Figure 6.2) were developed in order to investigate the sensor response e.g. to temperature, strain but also to assess their capability of withstanding the harsh environment encountered during curing. These mini-modules, were also used to analyse the performance of the novel concretes developed for the final NEWSOL prototypes. This chapter includes only the results from one representative mini-module, designed as mini-module 1. Figure 6.2 shows the design of the mini-module 1 manufactured in a laboratory scale, made using some of the novel concretes developed for the thermozone and module as final prototypes.

The specimen was made up of two different components, the core and the insulating layer. Each one of them was formed by a different type of concrete. The first was made with high thermal performance concrete (core) and the other with foam concrete (insulating concrete). The dimension of the core is 150x200x300mm, and the insulating layer 300x300x300mm, which surrounds the core. Moreover, 4 steel tubes (400mm long and 33mm diameter) were embedded along the core, simulating the pipes employed to propagate the heat of the fluid through the structure.

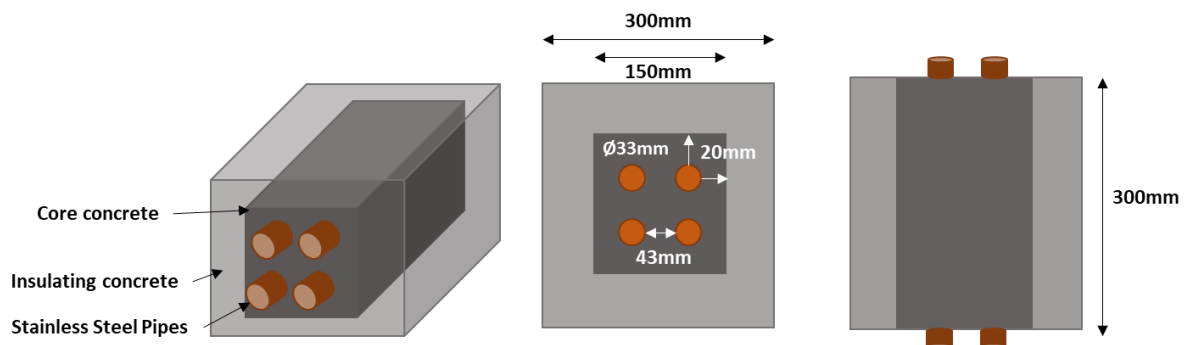


Figure 6.2: Design of the mini-modules developed at laboratory scale.

In this study, the most relevant information is provided by monitoring the behaviour of the high thermal performance concrete, and according to this, most of the embedded sensors are in the core of the specimen, as shown in Figure 6.3. The location of sensors was selected to maximize the relevance of the measured data when the thermal cycles were performed. The purpose of the selected points was to monitor the temperature profile of the concrete and also, the temperature changes at the interface between the different layers. In total 14 different locations were monitored, with 10 points for the core and 4 for the insulating.

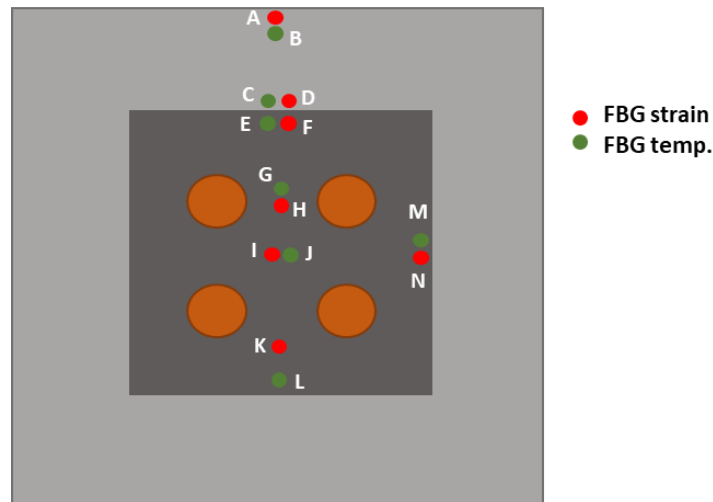


Figure 6.3: FBGs location for the mini-module 1.

To monitor the mini-module 1 specimen, different configurations of FBGs were employed. The strain Ni coated FBGs were directly embedded in contact with the concrete, while the temperature FBGs were encapsulated in a SS316L capillary tube. Strain sensors depend on both temperature and strain, therefore the temperature references are required to compensate the temperature effect. Therefore, some monitoring locations of the specimen have sensor arrays formed by 2 or 3 FBGs equally spaced on the same fibre, while the others only have one FBG, such as that in the centre of the long axis of the core. The total number of embedded sensors was 22 at 14 different locations of the specimen, 11 of these sensors were employed to monitor temperature and the other 11 to monitor strain. The temperature sensors have a double purpose, to determine the temperature of the concrete, and to eliminate the temperature variations that the strain sensors suffer, allowing the strain calculation. This is the reason why the locations are in pairs which are located in close proximity.

The mini-module 1 was manufactured in two steps: first the core was cast together with the tubes and its corresponding sensors, and after 24 hours curing, the insulating layer of foam and the remaining sensors were added. During the casting, the sensor at position F was found to be broken, and thus the final number of monitoring sensors was 21. Figure 6.4 shows the manufacturing process. First, the core concrete layer mould and the FBGs were located at their defined positions (Figure 6.4.a), then, the high thermal performance core concrete was poured to fill the formwork and embed the FBGs (Figure 6.4,b). One day later, the core concrete formwork was removed and a new mould was added to pour the insulating concrete (Figure 6.4.c), the FBGs defined for this layer were located (Figure 6.4.d) and finally, the insulating concrete was poured (Figure 6.4.e). The completed mini-module specimen is shown in Figure 6.4.f.

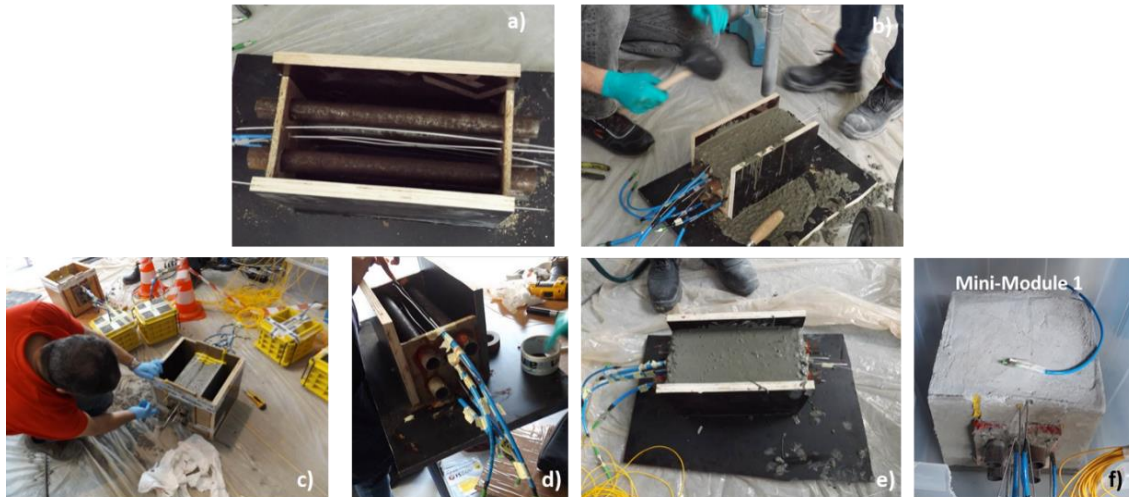


Figure 6.4: Mini-module sample manufacturing process. a) preparation of the core formwork and placement of the core FBGs, b) core concrete filled, c) insulating concrete formwork preparation, d) integration of the FBGs located in the insulating concrete, e) insulated concrete filled, f) final appearance of the mini-module concrete sample with the embedded FBGs.

The above concrete curing process, which takes 28 days, was monitored by recording the data from all the strain FBGs embedded and some of the temperature sensors. Figure 6.5 shows the measured temporal response from, the strain and temperature FBG sensors, during the first 28 days after the insulating concrete layer of the specimen had been cast. During the few hours after the concrete was poured into the mould, the FBGs detect relatively large variations in strain and temperature due to the concrete hydration and hardening. The temperature evolution was not completely monitored, it started after some hours when the temperature was already decreasing slowly to reach ambient (room) temperature. Figure 6.5.b shows the response of some sensors embedded in the insulating layer in wavelength values and Figure 6.5.c shows the temporal response of these FBGs for strain and temperature having removed the temperature dependence from the strain sensors signal. Regarding the strain sensors, it was observed that the strain FBGs at position A suffers more strain variation than the other at position D, which is close to the border of the two different layers. A sensor is embedded at the centre of the surface of the piece. In both cases, the greater strain variation was registered over the first 10 days.

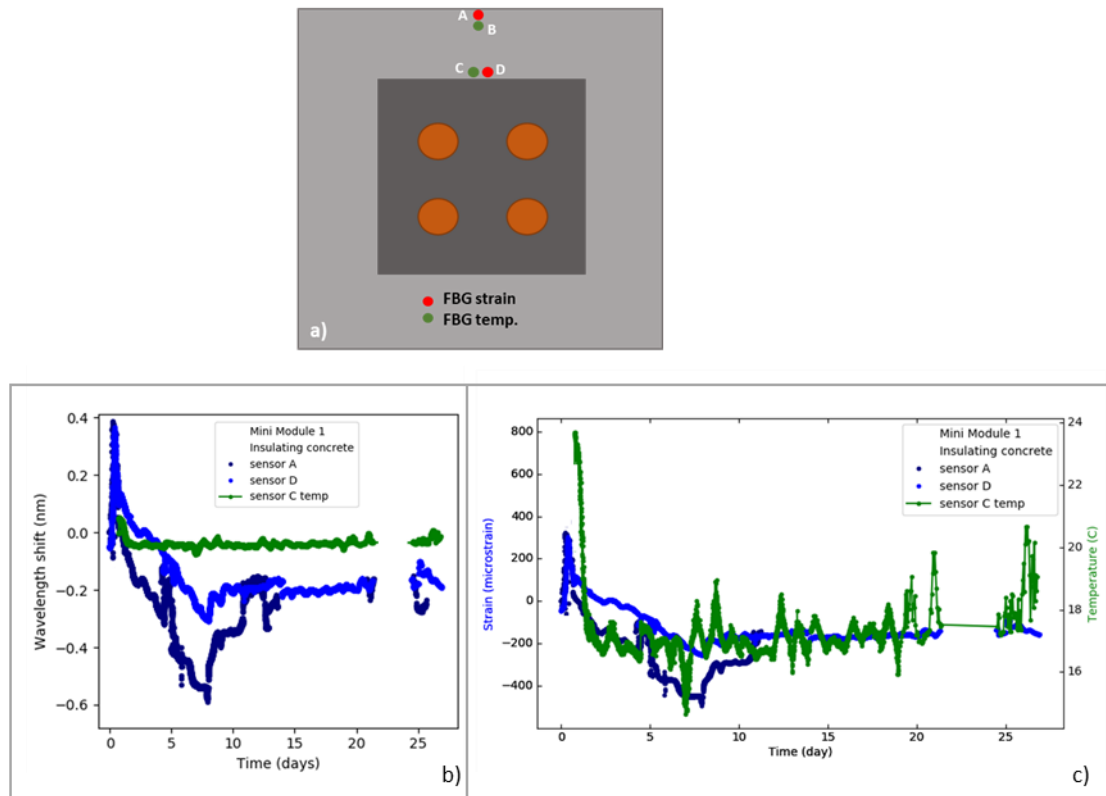


Figure 6.5: a) FBGs location in the insulating concrete layer. b) Response of the A, C and D FBGs embedded in the insulating layer, in wavelength shift values during the 28 days after filling the insulating layer. c) Response of these strain and temperature FBG sensors in strain and temperature values after decoupling temperature from strain.

Figure 6.6 and Figure 6.7, show the data obtained from temperature and strain sensors embedded in the core concrete layer of the specimen, over the first 28 days. The data is with the temperature component removed from the embedded strain sensors. During the first hours, when the concrete is settling, the temperature and the strain change more quickly, showing a variation around 6-9°C during the hydration of the core concrete. After the exothermic process (highlighted in figures) is completed, the temperature of the concrete returns to room temperature. After 24 hours, there is another temperature peak captured by the sensors. This is due to the manufacturing of the insulating layer, which was built 24h later around the core. The increase was around 10°C, which means that the exothermic reaction for the insulating concrete during the hydration process is higher than that for the core concrete. The FBGs embedded in the core concrete detects both the exothermic reaction and hardening of the insulating concrete. Due to the limited availability of interrogators, it was only possible to register the temperature of two temperature FBGs during the 28 days.

To have a better resolution of the temperature gradient, some of the temperature FBG sensors were multiplexed, e.g. the G and L sensors. They have two and three FBG sensors, respectively, multiplexed in the same fibre forming two array sensors, longitudinally to the module and pipes. In Figure 6.6, it is noticeable that the temperature measured by one sensor of each array differs from the others by around 3°C, this is because they are located along the longitudinal axis of the core, and the sensor close to the surface of the concrete is influenced more by the room temperature. This means that the temperature and consequently the strain around this *small* specimen is not homogeneous, which could possibly cause cracks or failures in service. The lower frequency wave-shape fluctuations recorded for the first 48 hours are due to the temperature variation between day and night.

The response of the H strain FBG sensor is showed in Figure 6.7.b. Due to the interrogator channels availability it was only possible to register this sensor response during the 28 days of

hardening process, which is corresponding with the G temperature FBG sensor. The H1 and H2 strain response during the hardening process varies around $100\mu\epsilon$, but while H1 FBGs varies in negative (contracts), H2 FBGs varies in positive (expanded).

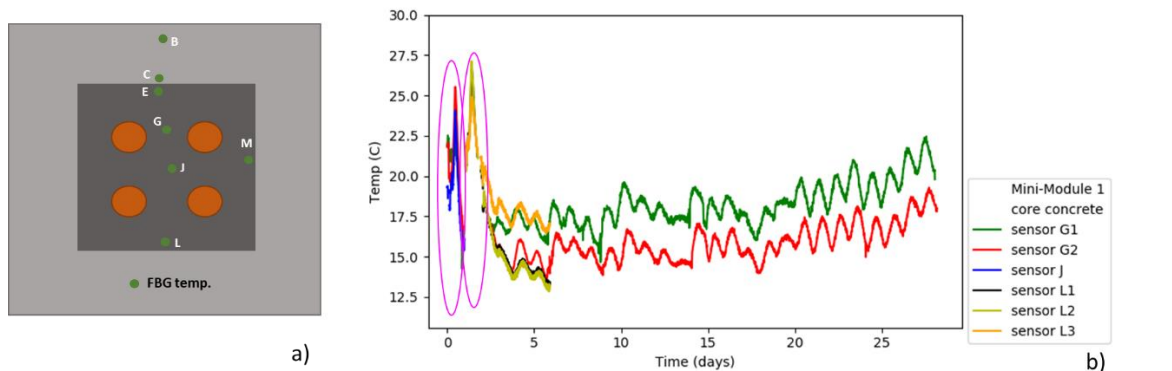


Figure 6.6: a) Temperature FBGs location. b) Response from the temperature FBG sensors embedded in the core concrete of the specimen along the 28 days.

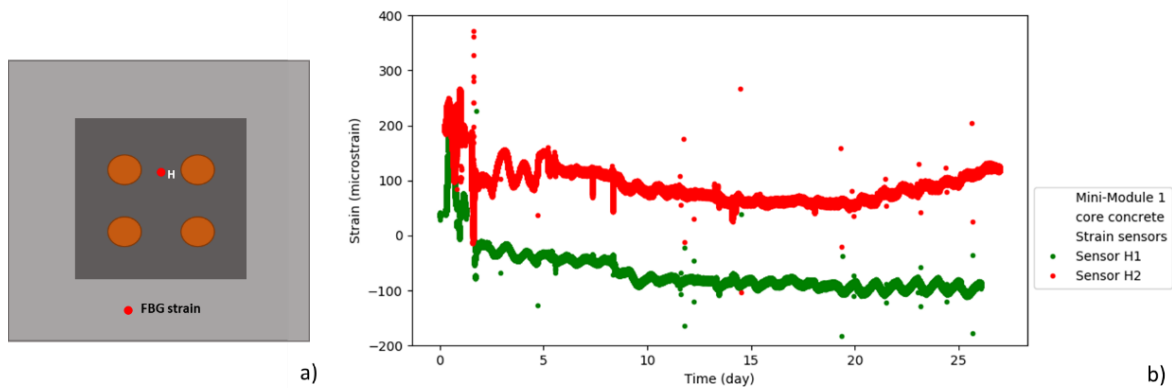


Figure 6.7: Strain H FBGs location. b) Response from the strain H FBG sensors embedded in the core concrete of the mini-module specimen, for the 28 days after the core concrete filled.

After the mini-module was fully cured, some heating cycles were carried out. The cycle commenced with a slow heating cycle from room temperature to 700°C to 'dehydrate' the concrete and avoid the collapse of the piece during the following fatigue cycle tests. Taking advantage of the metal tubes embedded in the core, the specimen was heated by the Joule effect by connecting both ends of a tube to a current source. Figure 6.8.a shows the set-up used to make these tests and Figure 6.8.b and c show the detail of the electrical connection through the right bottom pipe of the mini-module. To avoid thermal losses, during the heating process, the mini-module specimen was wrapped with rockwool.

This approach was chosen to simulate real applications. For example, the energy storage module will be heated by the pipes, through which the molten salts will pass and, in the case of the thermocline tank, it will be heated by conduction by heat transfer from the molten salts stored inside it.

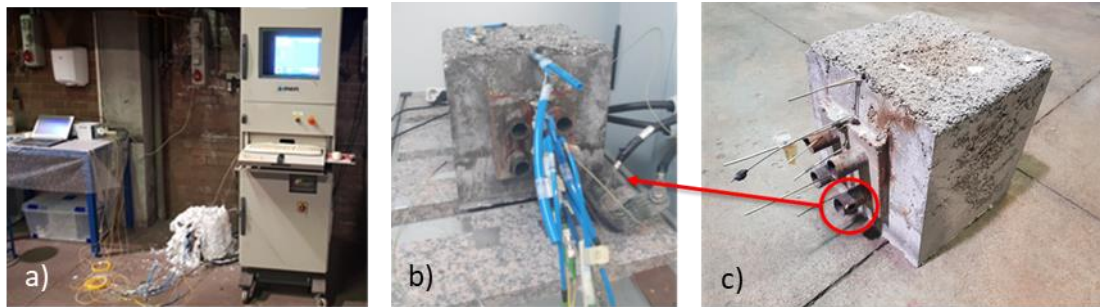


Figure 6.8: Experimental set-up for heating the mini-module: a) Machine to apply the heat through Joule's effect connected to the mini-module specimen. b) mini-module connected to the electrical connection cable through the steel pipe. c) mini-module connected to the electrical connection cable through the steel pipe, with a red circle highlighting the connection point.

The first heating cycle was very slow due to the water that could be remaining inside the specimen (dehydration), and it had to be gradually evaporated to avoid the possibility that cracks could appear or even the collapse of the sample. Moreover, a slow heating cycle ensured that the shrinkage of the concrete would be minimized. The following thermal heating procedure was applied to the specimen: increasing from 20°C to 80°C in 12 hours; maintaining constant for 6 hours, raising to 110°C over another 6 hours; raising to 290°C in 12 hours; keeping stable for 6 hours and finally 12 more hours to reach the desired temperature of 500°C. After this, the temperature was progressively increased up to reach near 700°C at which point the process was stopped. Due to limitations on the programming of the machine employed to heat the tube, the total time needed to finish this first heating cycle was 170h. The temperature control of the heating cycles was achieved using thermocouples located inside the heated tube and connected to the controlling machine.

Figure 6.9 shows the response of the temperature and strain FBG embedded in the mini-module specimen during the first heating cycle to dehydrate the concrete material. The embedded FBGs were not annealed before they were embedded, and therefore this first heating process was also used as annealing for them. Figure 6.9.b shows the response in wavelength variation for the temperature FBGs embedded in the mini-module. The wavelength variation is higher for the FBGs located in the centre of the module and lower for the FBGs located in the insulating layer, which means that in the middle of the module higher temperatures are reached and the insulating layer works well to prevent the heat from escaping to the outside.

The strain FBGs output variation with time is shown in Figure 6.9.c. The sensors with a higher wavelength variation were also the sensors located in the centre of the core concrete, while the FBG sensors A and D, located in the insulating layer show a negative variation, which could be related with the growth, during the heating cycle, of a small crack detected in the top face of the insulating concrete located close to the FBGs location.

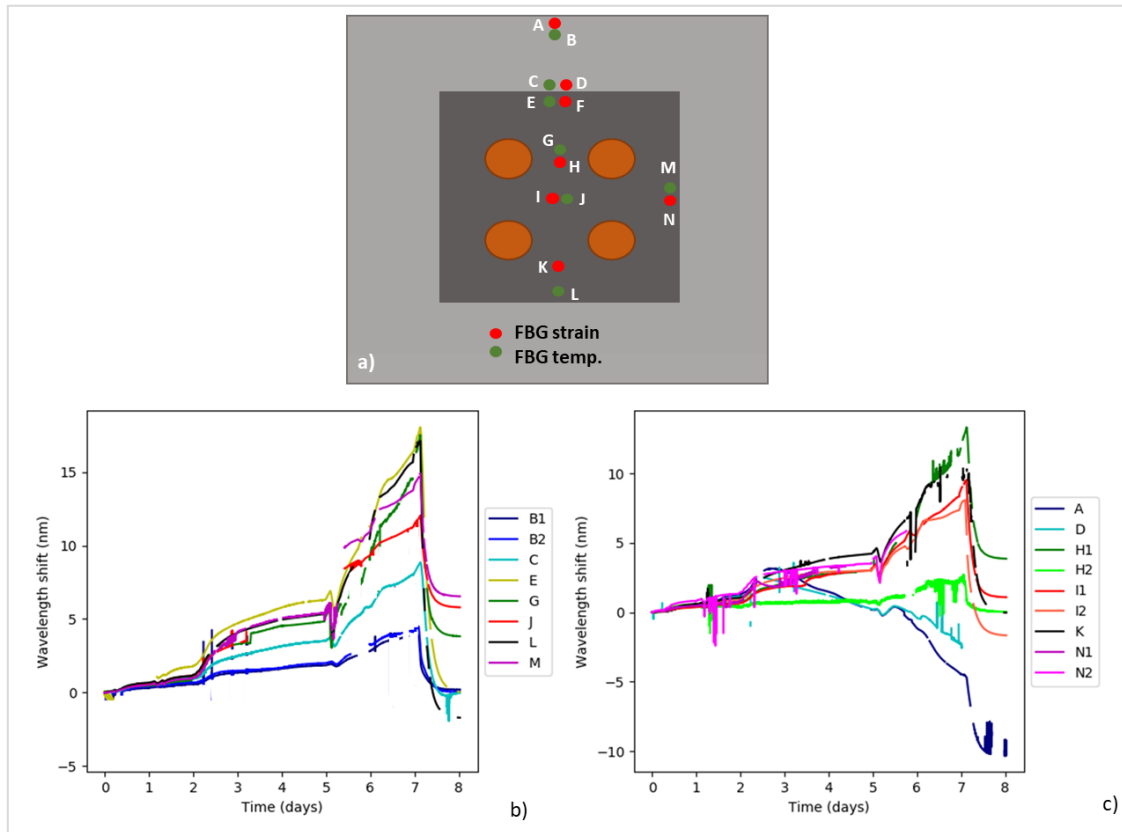


Figure 6.9: a) FBGs location for the mini-module 1. b) FBG response during first heating for temperature sensors, c) FBG response during first heating for strain sensors.

After the dehydration process was completed, some thermal fatigue tests were undertaken. It includes three different stages, represented in Figure 6.10, all of which sets a maximum temperature of 500°C (on the pipes) to simulate the real operation conditions on the module (prototype), where the molten salts pass at this temperature through the pipes. The molten salts worked in a temperature regimen between 200-500°C. The aim of these tests was to study the novel concrete module operation and durability, under accelerated lifetime testing, simulating the day/night heating/cooling operation regime of a Concentrated Solar Power (CSP) plant. For this reason, the mini-module was tested at the maximum temperature of operation.

The three temperature cycling stages were as follows:

- At the first stage the heated steel pipe of the mini-module (right-down Figure 6.8.c) was heated from 20°C to 500°C and then cooled from 500°C to 290°C. At this point, five consecutive cycles of heating and cooling are scheduled from 290°C to 500°C. The heating time required to reach 500°C was between 5-6 hours. After 5 cycles, the module was cooled down to room temperature.
- The second stage involved one cycle from 20°C to 500°C and then return to room temperature. And after this, the module was continuously cycled from 290°C to 500°C during 10 days. Finally, the module was returned again to room temperature.
- The third and final stage, involves three cycles from 100°C temperature to 500°C in steps of 120°C.

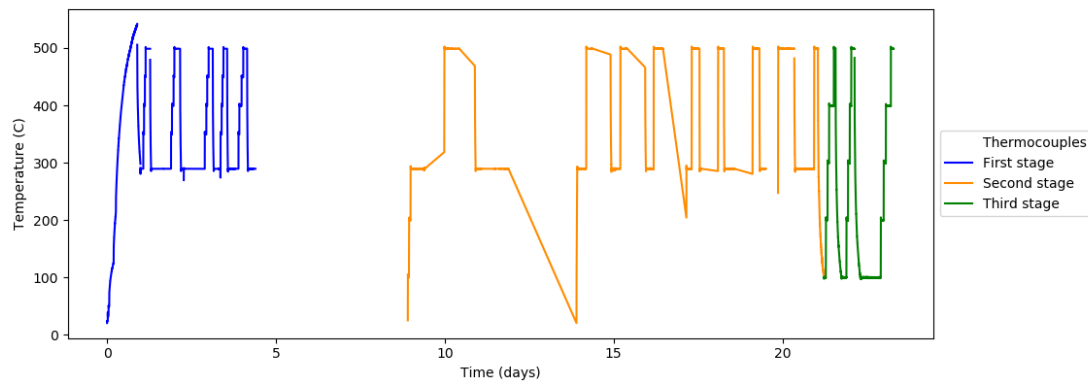


Figure 6.10: Diagram representing the three different stages applied to carried out the heating test of the mini-module.

The temperature applied by the current source to heat the tube, was monitored by a thermocouple located inside it. In addition, three other thermocouples were installed to monitor the temperature on the other points. Figure 6.11 shows the location of the thermocouples. A total of four thermocouples (T1,T2,T3 and T4) were located in the mini-module specimen. Two on the heated pipe, one inside and the second welded to the beginning of the tube. The third and fourth thermocouple were located inside the upper tubes of the specimen.

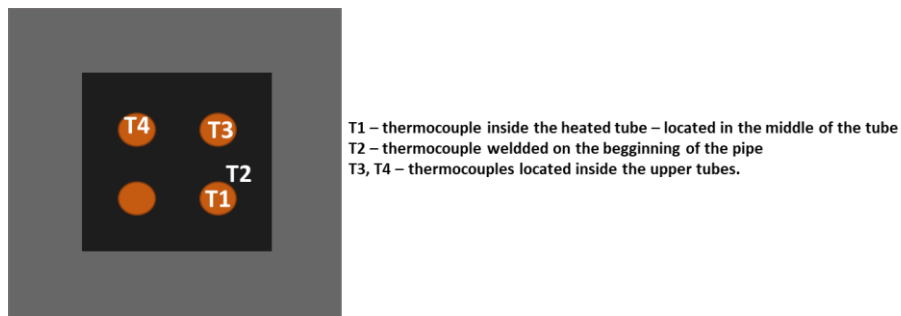


Figure 6.11: Thermocouple distribution for the mini-module heating test.

Figure 6.12 shows the temporal response of the thermocouples for all the heating cycles carried out. The thermocouples signal was recorded using the heating machine, because it needs the thermocouple to control the temperature and switch the current source on or off. Therefore, the machine was only active when the current is applied (when heat is required), for this reason, the thermocouples signal is only visible when the machine was applying heat. In the thermocouples signal showed that the temperature measured in the middle of the pipe heated, is higher, more than double, than those measured in the rest of the tubes monitored. The core concrete shows a better thermal conductivity than the traditional concretes.

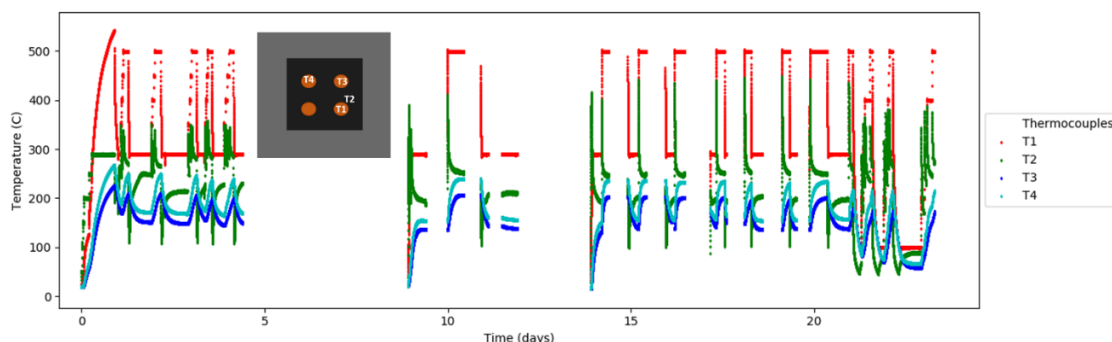


Figure 6.12: Thermocouples response during the thermal cycles.

Figure 6.13.a shows the location representation of the thermocouples and temperature FBGs located in the mini-module. Figure 6.13.b shows the response of the temperature FBGs during the thermal cycles. The temperature profiles measured with the temperature FBGs show the same temperature variation trend as that applied to the specimen. The maximum temperature reached is around 420°C, 120°C lower than the value measured by the thermocouple T1 (540°C), as Figure 6.13.c shows. This can be attributed to the heat absorbed by the concrete, where the FBGs are embedded.

The difference in temperatures measured by sensors is an important feature of these measurements. As expected, the L sensor which is closer to the heating tube shows the highest value of around 400°C. The E and M sensors, located in the borders of the concrete measured a similar temperature. Those embedded into the insulating layer show temperatures between 100-200°C, when their location is further away from the heating tube, confirming the concrete works properly as an insulated layer.

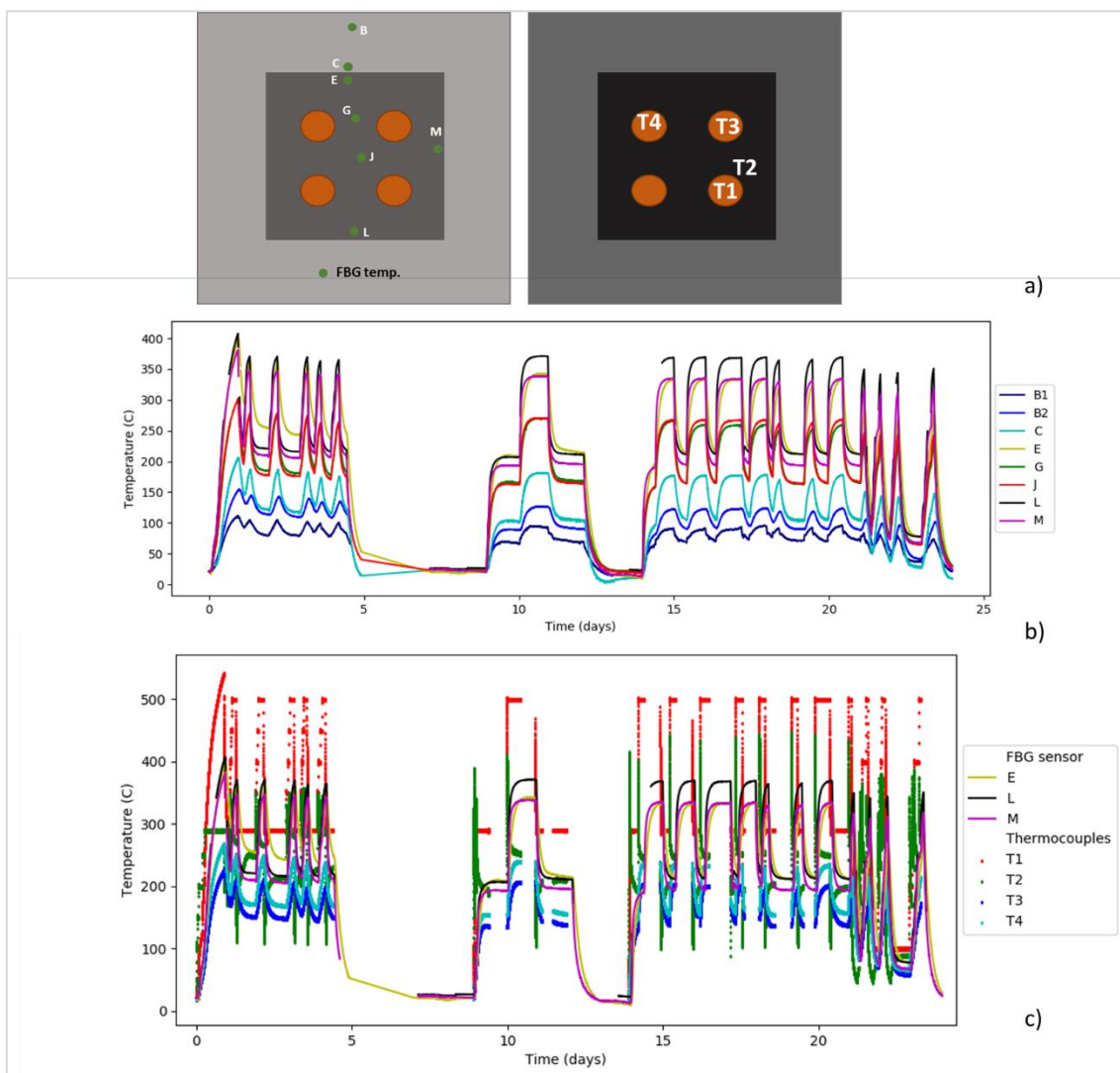


Figure 6.13: a) Temperature FBG and thermocouple sensors location b) Temperature FBGs response during the thermal fatigue tests. c) Comparison between E, L and M temperature FBGs and the thermocouples.

Figure 6.14.a shows the location of the strain sensors, Figure 6.14.b shows the wavelength variation of the strain FBGs with time and, Figure 6.14.c illustrates the time response of the sensors in strain values after compensating for temperature variation. The H2 FBG sensor barely detects any strain, which could be attributed to a poor embedding or a defect (pore) in that

area. On the other hand, the H1 sensor exhibits a higher strain variation, it suffered a jump in the signal after the first heating, which could also be consistent with a defect in that area. Sensors I1, I2 and K show a similar response, which is consistent with their similar location in the mini-module. Finally, sensor A, located in the insulating layer, shows a lower strain variation, than the sensors in the core because of the different composition of each material.

The strain 'peaks' observed at the end of each heating or cooling ramp are attributed to a minimal mismatch in response time between each pair of decoupled sensors and a slight temperature difference between them at that particular moment.

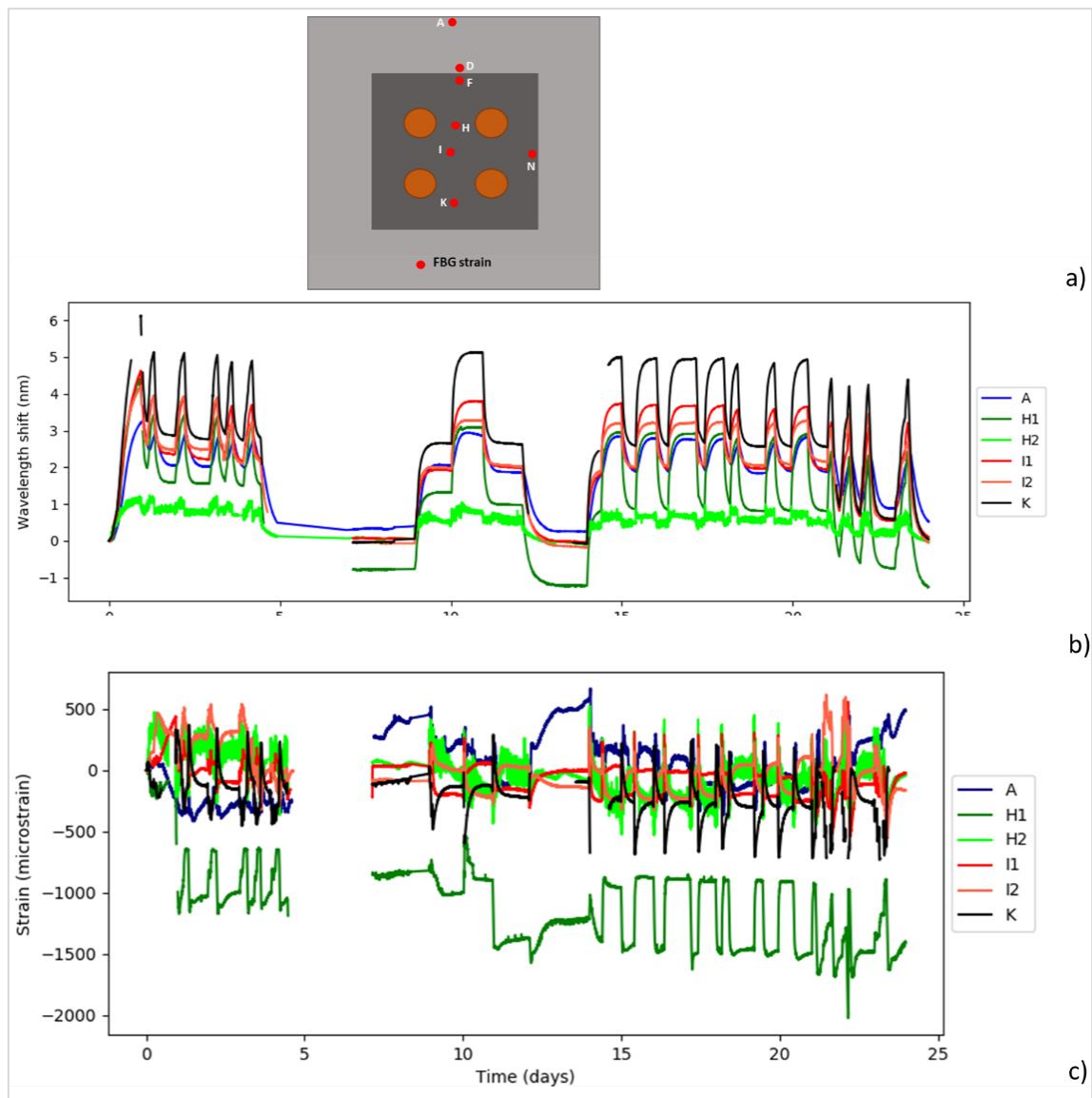


Figure 6.14: a) Strain FBGs location, b) Response of the strain embedded FBGs during the thermal cycles in wavelength variation. b) Response of the strain embedded FBGs during the thermal cycles in strain.

The test was finished following completion of 18 thermal cycles. Figure 6.15 shows the final appearance of the specimen which had been thermally tested. The insulating concrete was broken and was easily separated from the core concrete. It seems the insulating concrete was never well bonded with the core concrete, because the surface of the core concrete has a smooth surface. Meanwhile, the core concrete shows a good appearance without major cracks and with only minor cracks in the surface of the core concrete.



Figure 6.15: Pictures of the Mini-Module 1 after the thermal cycles test.

6.4 Validation on a medium scale

Following the above investigation, it was decided to manufacture prototypes of a medium scale both to analyse the scalability of the demonstrator designs and the behaviour of novel concrete in large quantities and volumes, and to optimise the FOS's integration at each defined location. In this investigation, the mid-scale prototypes were thermally tested and monitored to obtain the behaviour of the novel concrete with longer dimension than those tested in section 6.3.

Figure 6.16 show the design (a) and final appearance (b) of the mid-scale module manufactured tested in this part and, Figure 6.17 show the mid-scale tank design (a) and its final appearance (b).

As shown in Figure 6.16.a, the core of the mid-scale module was made of a high performance concrete with a total of 14 stainless steel tubes embedded. An external insulating concrete longer was added to retain the heat of the pipes inside the core concrete, designed to keep the molten salts above their solidification temperature. The overall dimension is 800x800x1200mm (high x width x length) and the core concrete is of 400x400x1200 mm with 200 mm extra in each dimension for an insulation layer.

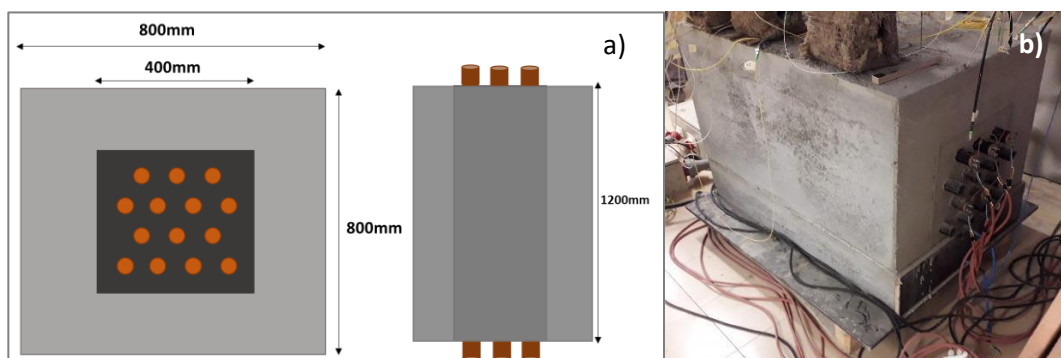


Figure 6.16: a) Mid-scale module design, b) final appearance of the mid-scale module.

The mid-scale thermocline tank was designed to evaluate the heat performance of the novel concrete. It requires the assessment of its warming-up during the concrete hydration phase and the duration curing and hardening in a safe and efficient way. The outcome will help to define the final thermocline tank design where the volume would be much larger. As shown in Figure 6.17.a, the mid-scale tank was a concrete structure of 1000x500x300mm (high x length x width) with a steel liner of a few centimetres thick, through which the concrete is heated, simulating a section of the final prototype, where the molten salts will be contained in a steel liner which will be separated a few centimetres from the high performance concrete layer.

The high performance concrete materials for the core module and for the first concrete layer of the thermocline are different, and manufactured by different NEWSOL partners.

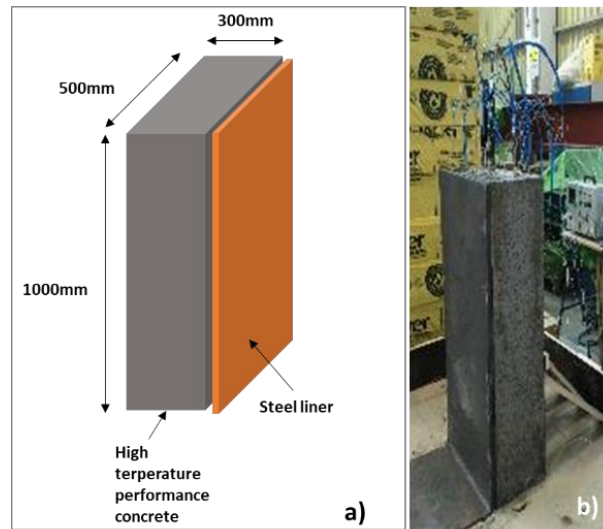


Figure 6.17: a) Mid-scale first concrete layer tank section design, b) final appearance of the mid-scale first concrete layer tank section.

6.4.1 Manufacturing and validation of the mid-scale module

The mid-scale module was manufactured by a partner in three steps and the complete construction took several months. First, the insulating concrete base was made. Secondly, the core concrete with the embedded steel pipes were made and finally the insulating concrete layer manufacturing was completed. To improve the bond between the steel pipes and the core concrete, spiral-shaped marks were etched in the surface of the embedded pipes. The manufacturing process took almost six months because it had to wait at least one month between each manufacturing stop, which is the time taken for the concrete curing in order to assure the mechanical resistance of each manufactured layer, before adding the next layer. Each described phase, in turn, took several days, for the moulds to be designed, cut, assembled with sensors integrated. Finally, the concrete was mixed and poured into the moulds and in sequence.

A total of 30 FBGs (22 for temperature and 8 for strain measurements) and 16 thermocouples were integrated in the mid-scale module. Figure 6.18 shows the FBG and thermocouples locations in the mid-scale module:

- 10 temperature FBGs and 4 thermocouples in the insulating concrete.
- 12 temperature FBGs and 12 thermocouples in the core and pipes.
- 3 strain FBGs in the pipes.
- 5 strain FBGs in the core concrete.

Figure 6.19 shows in detail the exact locations of FBG and thermocouples through six dissections of the module. The strain FBGs were not embedded in the insulating concrete layer as the focus of this mid-scale test was on the core concrete performance, for the insulating concrete, only temperature monitoring was required.

The temperature FBG sensors were formed using polyimide coated FBGs encapsulated in 316L stainless steel capillary tubes and the strain FBG sensors were coated with Ni forming up to 550µm of diameter. In this case, the polyimide coated FBGs were selected for the temperature sensors because there was no time for manufacturing 22 arrays of Ni coated FBGs, and

furthermore, in the laboratory test (previous section), no temperatures above 350°C were detected, which is within the operating range of polyimide coated fibres.

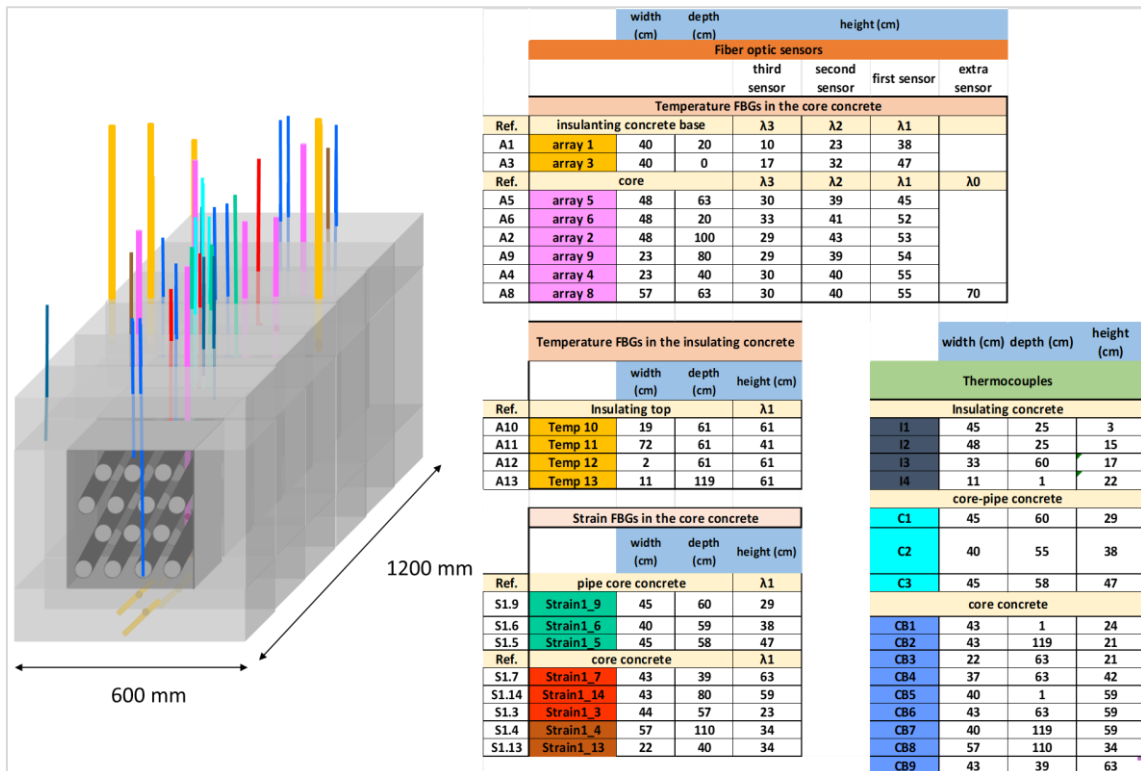


Figure 6.18: FBG and thermocouples sensors distribution in the Mid-scale Module prototype.

The distribution of the sensors was arranged in order to provide an evaluation of the essential constituents of the system, insulation concrete, storage concrete (core) and piping.

The thermocouples placed in the insulation concrete were designated “I”, in the storage concrete (core) “CB” and those placed next to the piping “C”. FBG temperature sensors were labelled “A” and strain sensors “S” as shown in the tables in Figure 6.18. Each temperature sensor array embedded in the insulating concrete base and in the core concrete layer included three FBG sensors, except array 8 (A8) which has four sensors. They are positioned at different heights to obtain a spatial temperature distribution. On the top of the insulating concrete layer, there was only one FBG per fiber. The same was for the strain sensors.

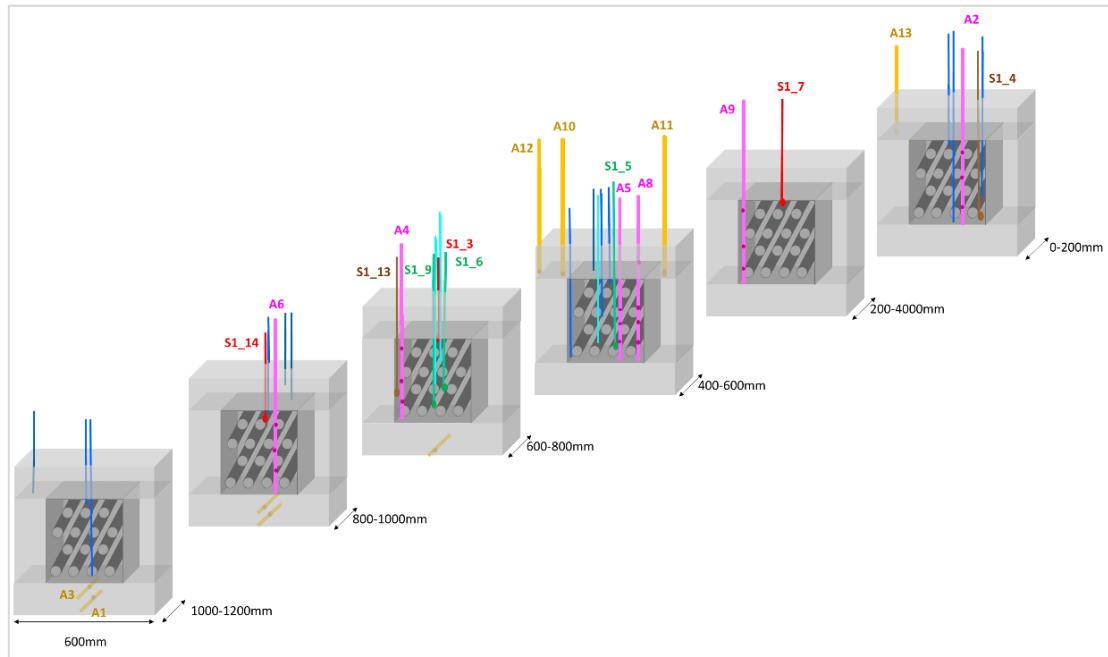


Figure 6.19: FBG and thermocouples sensors position in the prototype along the mid-scale module prototype. Only FBGs reference is included.

Figure 6.20 shows the time resolved variation from temperature FBG sensors due to the core concrete and insulating concrete manufacturing. The first heating peak of the graphs was because of the exothermic reaction during the first hour of the concrete hardening. The second peak is because of the exothermic reaction of the insulating concrete manufacturing step. Figure 6.20.a shows the layout of the FBG temperature sensors embedded in the core concrete layers. The time response of the sensors located at heights of around 300mm, 400mm and 550mm are shown respectively in Figure 6.20.b, Figure 6.20.c and Figure 6.20.d. The data shows that the temperature reached at different heights is similar, although in the middle height it is a little higher. This means that the hydration of the core is homogeneous along the core concrete layer. In addition, it is observed that the core concrete exothermic reaction reached is smaller than that for the insulating concrete. As expected, the temperature closer to the insulating layer is higher than the locations further away.

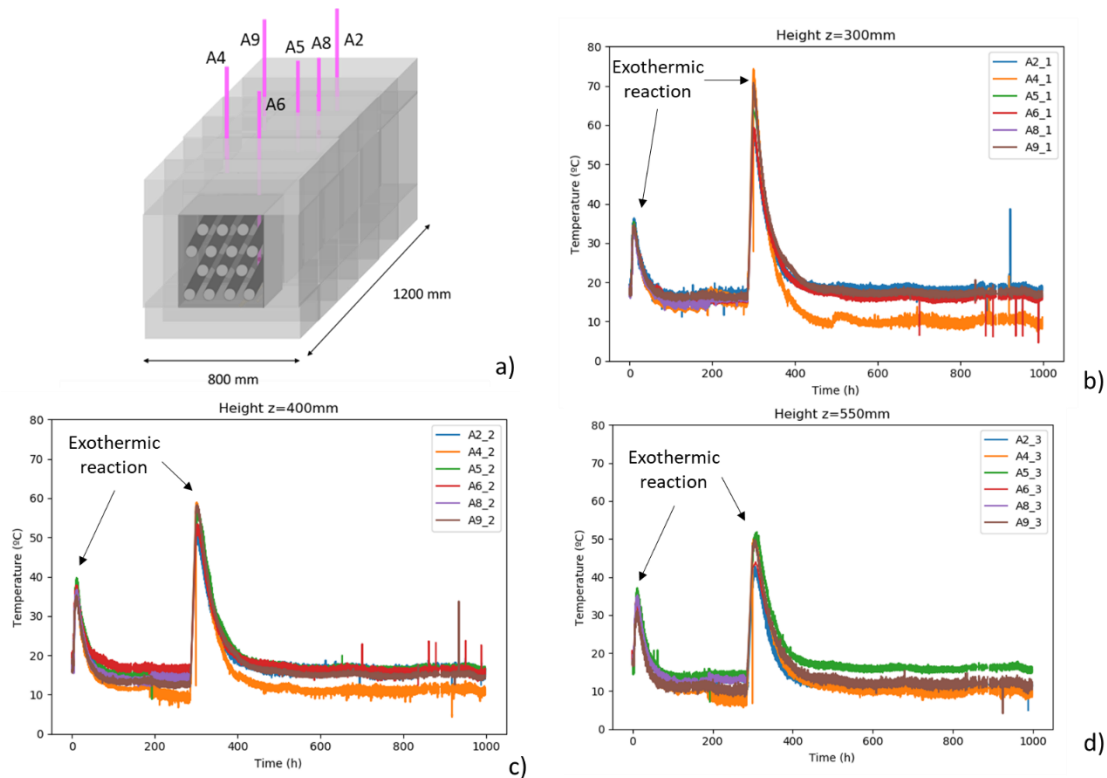


Figure 6.20: a) Mid-scale module representation with the temperature FBGs embedded in the core layer. Graphs representing the temperature FBG sensors response during the core and insulating layers hardening and curing process: b) comparison for the temperature FBGs embedded at 300mm of height, c) comparison for the temperature FBGs embedded at 400mm of height, d) comparison for the temperature FBGs embedded at 550mm of height.

Figure 6.21 shows the temperature response from the sensors embedded in the insulating (lateral and top) layer. The A13 sensor was broken during the manufacturing process. A10 and A11 show a similar response but higher than that from A8 as the latter were located nearer to surface of the insulating concrete layer.

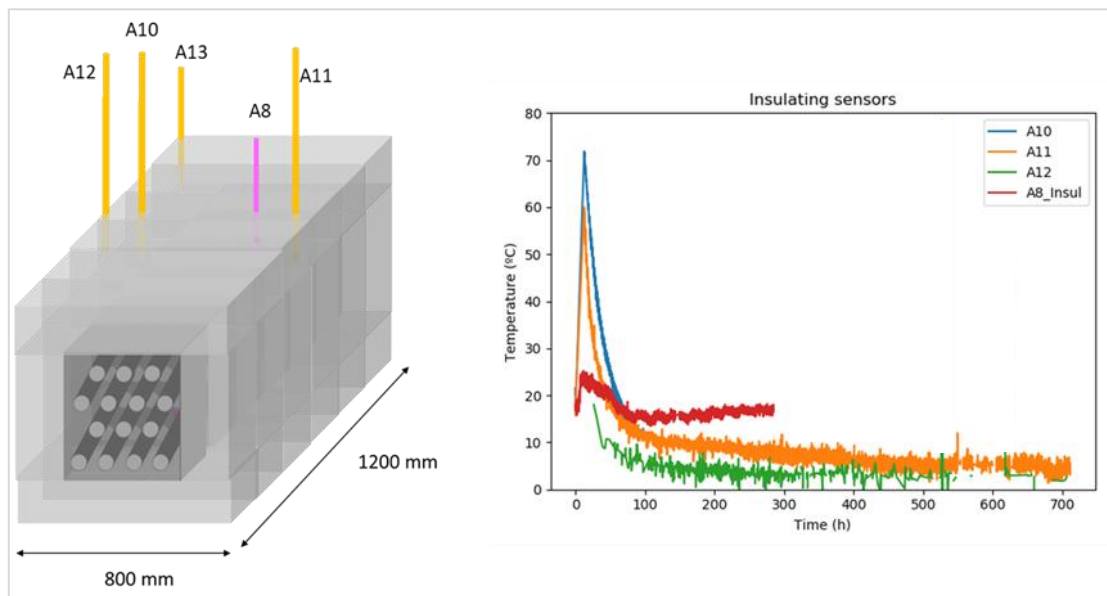


Figure 6.21: Representation of the FBG sensors for the insulating (top) concrete and their response after the third step manufacturing: insulating layers hardening and curing process.

Figure 6.22 shows a comparison between temperature and strain responses from some of the sensors embedded in the core concrete layer.

The strain was monitored by a total of five embedded FBGs: strain1_5 and strain1_9 located between the pipes and the core concrete at different locations, and strain1_4, strain1_13 and strain1_14 located at different locations inside the core concrete layer. To calculate the strain values for each strain FBGs, the temperature signal was subtracted using as reference the nearest temperature FBGs to each strain FBGs monitored. Figure 6.22 from b to d shows the time response of each of the strain FBGs monitored and directly compared with the proximal temperature FBGs, during the hardening and curing of the mid-scale module manufacturing. A higher compression strain was detected by the sensor 1_4, at the lower end of the module.

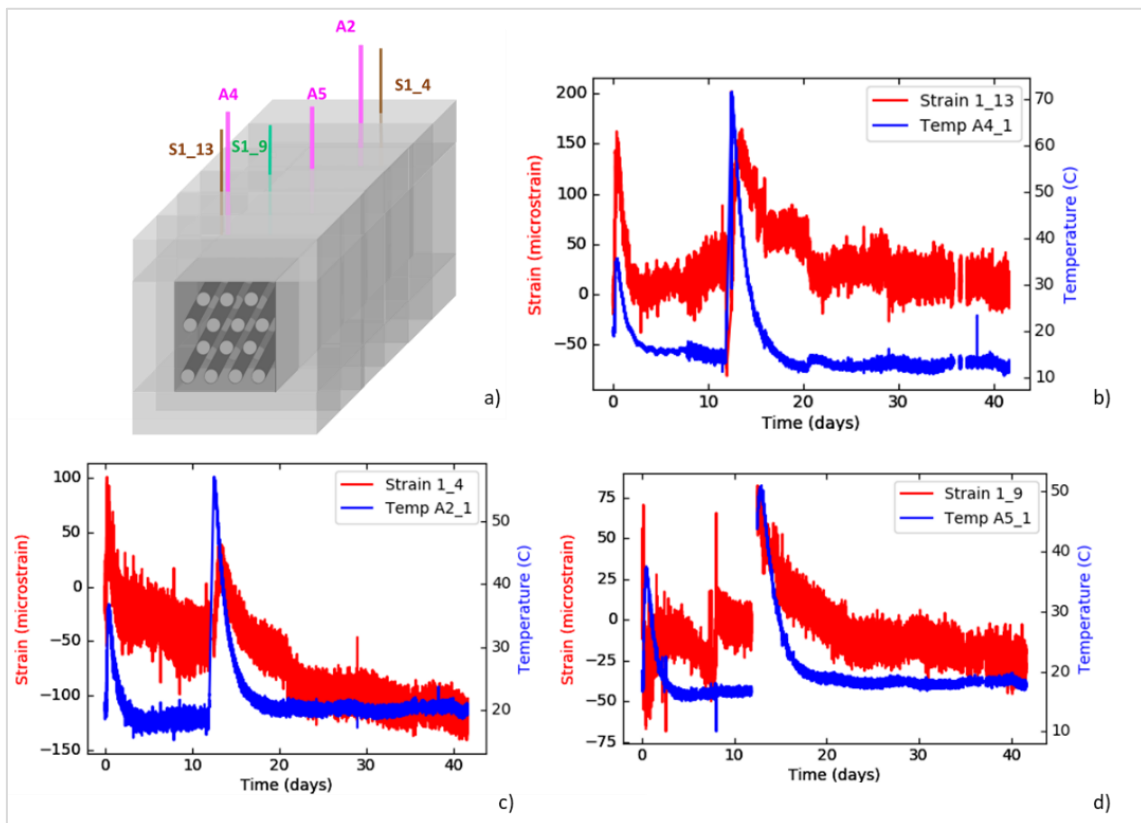


Figure 6.22: a) Mid-scale module representation with the strain FBGs embedded in the core layer. Graphs representing the response of some strain FBG sensors vs. temperature FBGs embedded in the core concrete layer during the core and insulating layers hardening and curing process: a) design of the strain FBGs embedded in the core concrete, b) comparison between the FBG strain1_13 and the temperature FBGs A4_1, c) comparison between the FBG strain1_4 and the temperature FBGs A2_1, d) comparison between the FBG strain1_9 and the temperature FBGs A5_1.

After the curing process, the mid-scale module was thermally tested at the facilities of a NEWSOL partner (SECIL). For safe operation, it was agreed to divide the tests into three stages to minimize the risk of crack formation. Instead of using molten salts, electrical resistances were used to heat the system—coupled with a methodology applied to minimise impacts caused by sudden temperature rises.

The 3-stage heating process is shown in Figure 6.23. The aim was to dehydrate the concrete mid-scale module with data obtained for optimisation of the final prototype, which required heating to 500°C for a complete dehydration of the material. Figure 6.23 shows the 3-stage heating platform. The first was to heat the mid-scale prototype up to 150°C (in the resistances) very slowly. Then, it was cooled down to room temperature. The second phase includes heating up to 190°C, stopping the heating to assess the thermal storage power of the module for some

hours and then heating the module up to 290°C. Finally, the third phase includes heating from 200°C to 500°C in steps of 100°C, allowing a few hours of cooling down between heating steps. The module was heated during the working hours and it was cooled during the rest of the day (from 6pm to 8am).

The FBGs temperature signal was recorded for the second and third heating phases. It was not possible to monitor the first because of problems that occurred with the interrogator connection.

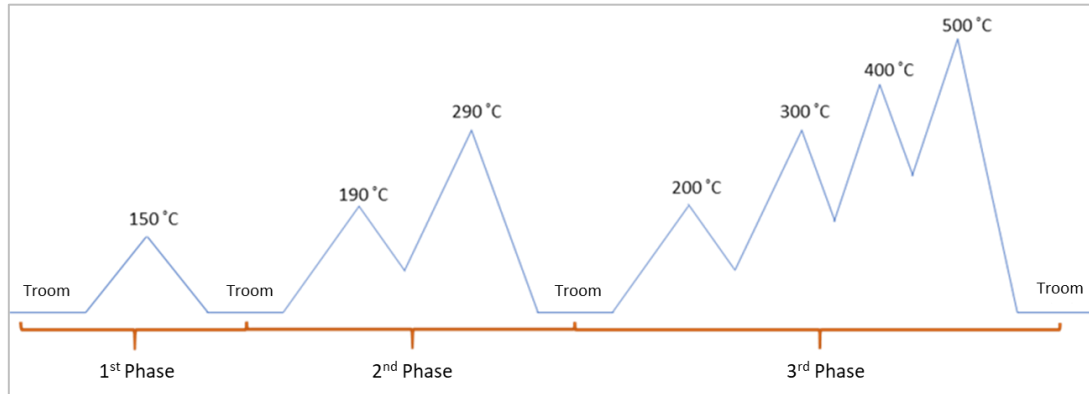


Figure 6.23: Schematic of the heating process stages.

Figure 6.24 shows the response of the temperature FBG sensors embedded in the insulating concrete layer during the heating tests monitored (2nd and 3rd phases). There is a big temperature difference between the temperature array A1 and the others, because it was located closer to the core concrete layer. FBGs A1_3 reach the higher temperature because they were located in the middle of the module. This means that this insulating concrete exhibits excellent thermal insulating behaviour.

The FBGs located in the insulating concrete layer but further away from the core detect lower temperatures. For example, the insulating concrete surface temperature, at the maximum heating cycle, was measured to be 100°C lower than that at the core.

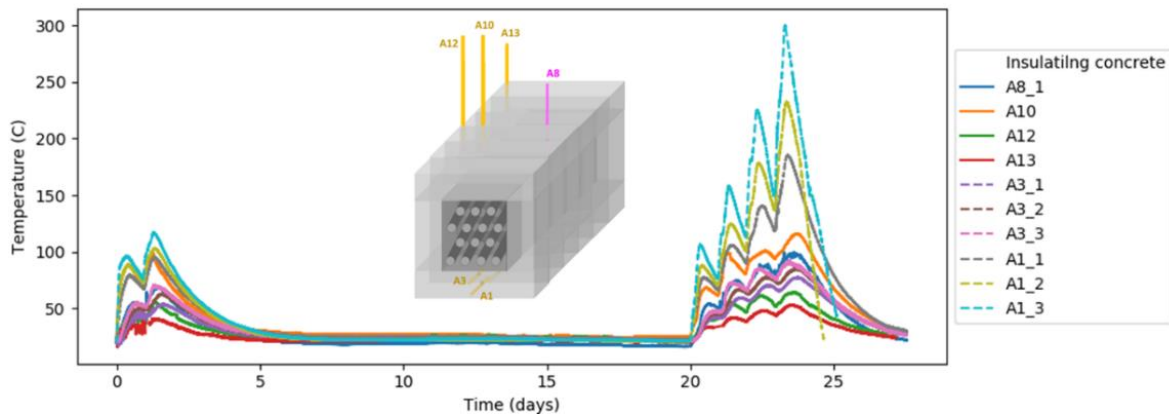


Figure 6.24: Temperature response for the temperature FBGs located in the insulating layer (top and bottom) for 2nd and 3rd heating phases.

Figure 6.25 shows the temperature variations recorded by the temperature FBGs embedded in the core concrete. The signal of these FBGs located at different heights, with reference to the bottom of the insulating layer, is shown respectively in Figure 6.25.a at 45-55cm, Figure 6.25.b 39-43cm and, Figure 6.25.c 29-33cm.

FBG A5 was placed next to a pipe so its temperature was always higher than the rest of the FBGs located at the same height. The thermocouples close to this point has the same temperature response. The higher temperatures were detected in the central part of the core concrete module, where the AX_2 was located, compared to the upper part (AX_1).

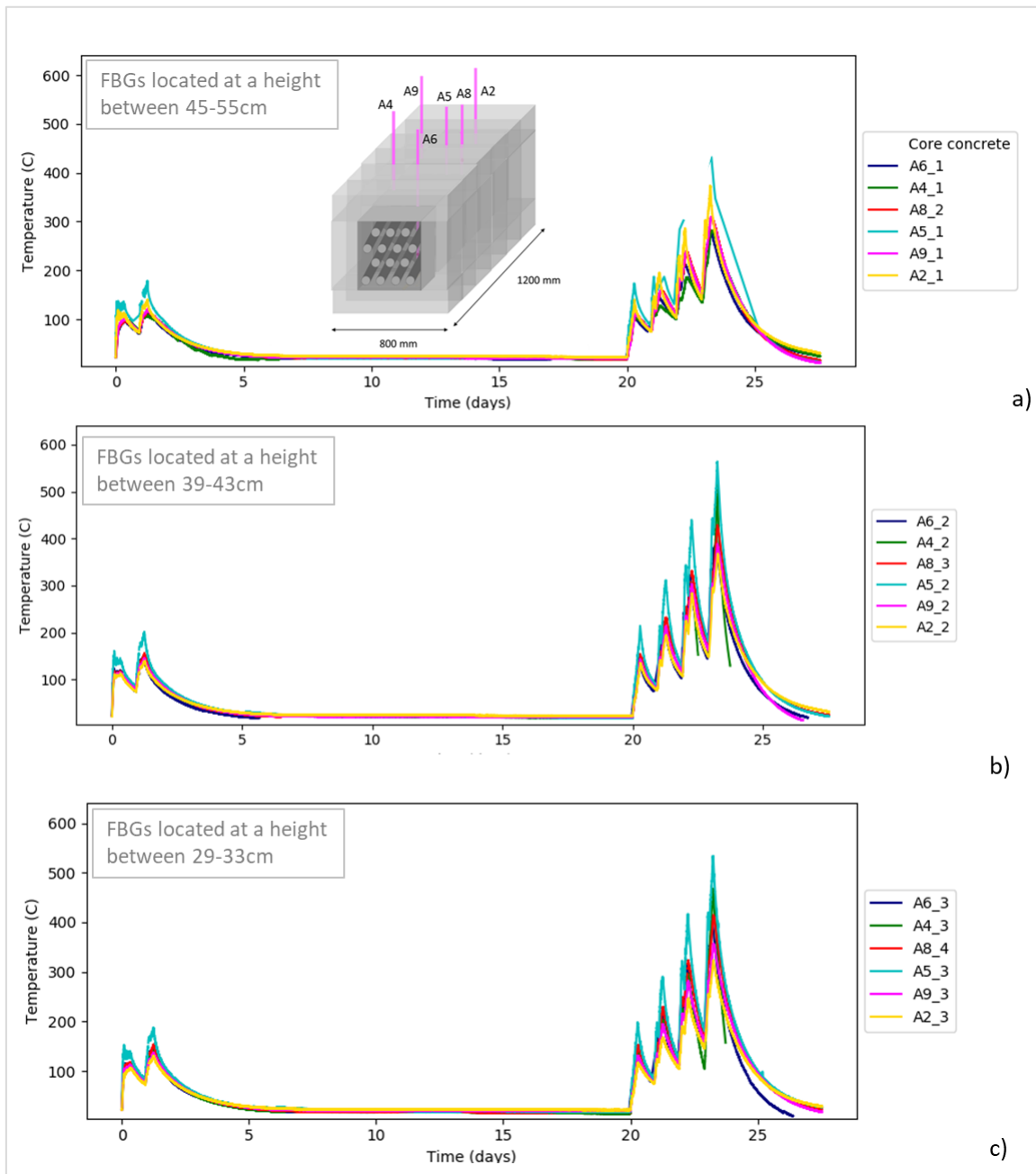


Figure 6.25: Temperature response for the temperature FBGs located in the core concrete. a) Represents the response for the FBGs located at a height between 45-55cm, b) represents the response for the FBGs located at a height between 39-43cm and c) represents the response for the FBGs located at a height between 29-33cm.

Figure 6.26 shows the response of the strain sensors in wavelength variation (a) and strain variation (b) for the FBGs embedded in the core concrete material. The sensors S1.5 and S1.9 were located between a pipe and the concrete. The strain FBG S1.5 shows a jump in the signal which is suspected to be due to the debonding between the concrete and the pipe or a defect in the fibre or concrete. Therefore, it is possible to that an error could be made in the calculation of the strain values because the thermal coefficient has changed from its original value. All the strain sensors show a compression variation when the concrete is heated, which could be because of the effect of the expansion of the steel pipes on the concrete. Also, S1.9 located attached to a pipe shows a strain behaviour different from the others embedded directly on the core concrete.

Similarly to the mini-module, we observe strain 'peaks' following the completion of each heating or cooling ramp. However, it has proven challenging to refine these results due to a minimal mismatch between the response times of each pair of decoupled sensors and a slight temperature difference between them at that moment.

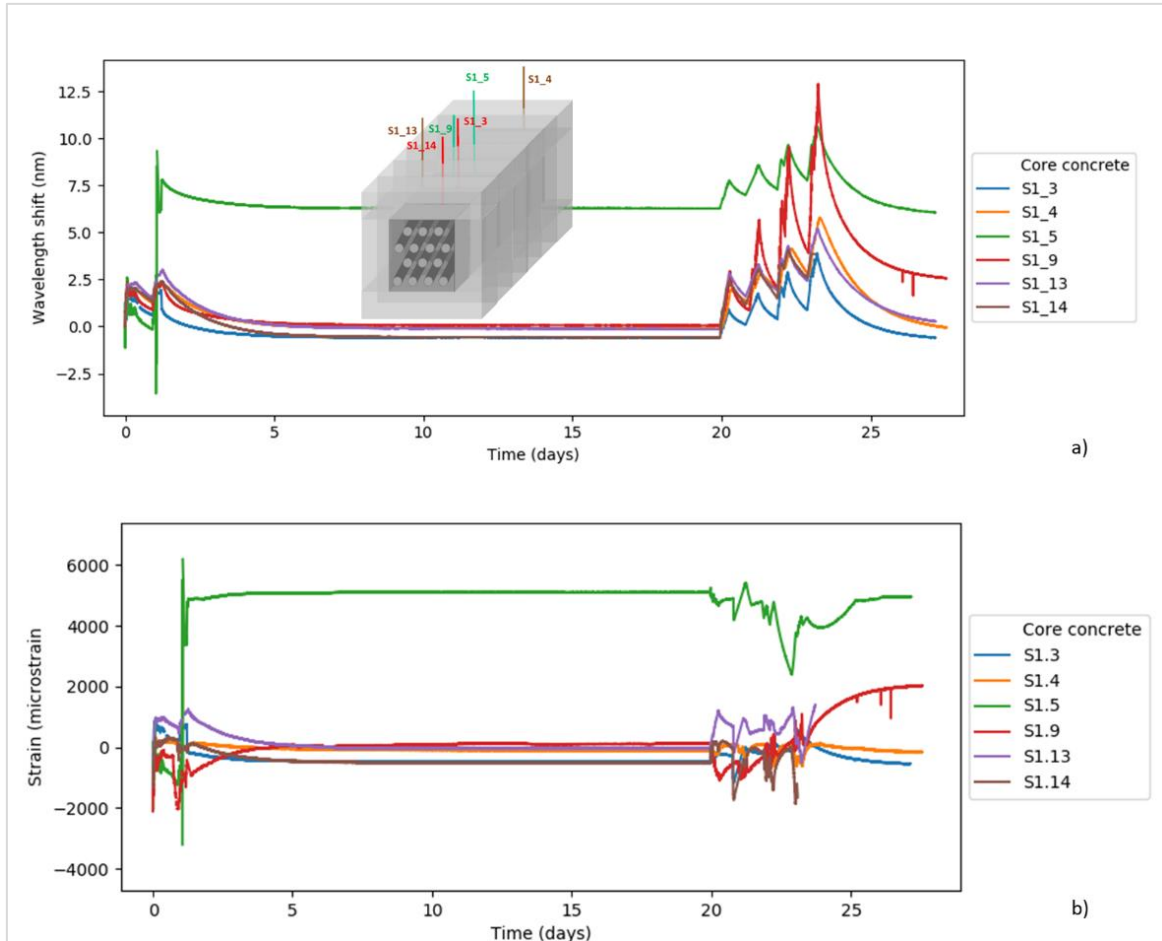


Figure 6.26: Response of the strain FBGs embedded in the core concrete material.

6.4.2 Manufacturing and validation of the mid-scale thermocline tank

A mid-scale analysis was carried out for a section of the prototype tank, with the main objective of studying the thermal performance of the new concrete developed, to ensure the safe operation of the final prototype tank. The mid-scale tank section was manufactured with dimensions 1000 x 500 x 300mm (high x length x width) and with a steel plate assembled to one side of the mid-scale tank and a few cm of gap between them. The structure is shown in Figure 6.17. The tank was heated using thermal blankets located over the steel plate. The entire specimen was covered by rockwool insulation to minimise thermal losses.

The construction of the mid-scale tank was carried out by Acciona (NEWSOI partner). It had three main aims: i) to demonstrate the suitability of the up-scaled concrete mix, ii) to simulate the high thermal operating conditions and to evaluate the thermal performance at large scale with all of the prototype layers and iii) this test will also allow the optimum location of the sensors to be identified in order to achieve an effective monitoring of the thermocline tank, and to validate the FOS sensors data. The aim was to evaluate how heat flows through the concrete and determine the temperature profile that will arrive at the external boundary of the concrete structure. Focusing on this aim, the evolution of heat flow was recorded across all the layers

from the steel plate. For that purpose, the concrete layer was integrated with fibre optic sensors and conventional thermocouples (from an other NEWSOL partner, CSIC), which are record temperature and strain. FBGs were embedded at different locations and depths of the concrete to measure both temperature and strain variations. Seven different fibre sensor arrays were embedded, each one of them formed by 3 FBGs. Accordingly, a total of 21 polyimide coated FBGs were employed to monitor the temperature variations inside the concrete sample. The temperature sensors were embedded using 316 stainless steel capillaries. Furthermore, five more FBGs, coated with Ni up to 600µm of total diameter, were embedded to monitor the strain of the concrete.

The concrete specimen was manufactured in one day. Initially, the thermocouples and FBGs were located at the defined positions, fixing them to the framework and the concrete mix was subsequently poured. Figure 6.27 shows the position of the FBGs and their distribution on the concrete specimen.

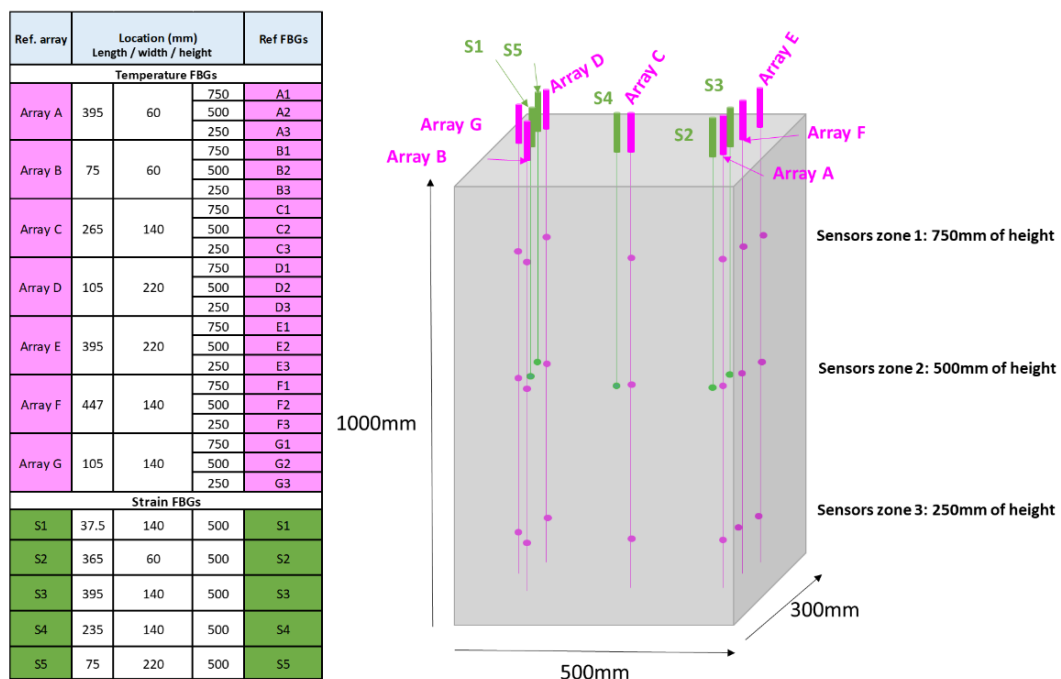


Figure 6.27: Table with the locations of the FBGs embedded and design of the mid-scale tank section.

As in the case of the previous concrete specimens manufactured, the hydration and hardening concrete process were monitored by the strain and temperature embedded FBGs. Figure 6.28 shows the response of the embedded temperature FBGs during the first few days of the concrete curing. Each graph shows the temperature FBGs located at different heights Figure 6.28.a refers to the FBGs located at 250mm of height, Figure 6.28.b at 500mm, and Figure 6.28.c 750 mm.

The temperature obtained from the temperature FBG sensors is very similar along the locations monitored, varying from 80-110°C. It was observed that the temperature at the center of the mid-scale tank (500mm in height) was higher than elsewhere. The temperature values obtained using the FBGs were in good agreement with the data obtained using the thermocouples. It was notified that this concrete has a high exothermic reaction during the hydration process, which has to be taken into consideration for the optimisation of the thermocline tank demonstrator.

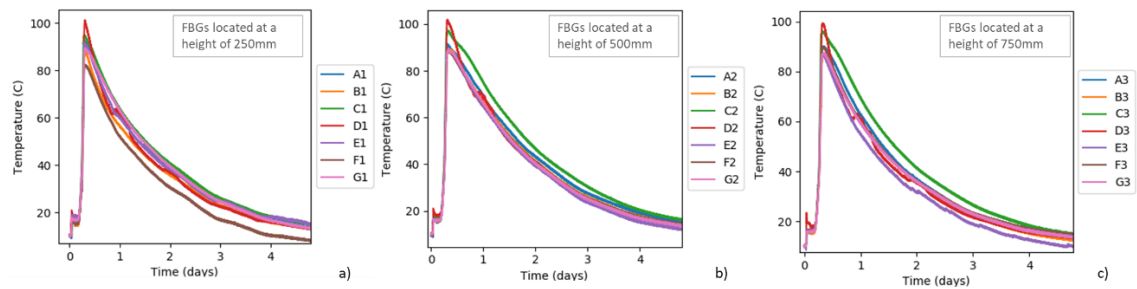


Figure 6.28: Temperature FBG sensors response during the hydration and the first hours of hardening process for the FBGs located at: a) 250mm of height, b) 500mm of height, c) 750 mm of height.

Figure 6.29 shows the strain response of the Ni coated embedded FBGs during the curing process in terms of wavelength variation (a) and in strain values (b, after temperature decoupling). The S2 strain sensor was the sensor which suffers a higher contraction because it was close to one surface of the mini-tank, and in contrast, the S4 strain sensor suffers a higher expansion during the hydration phase and a smaller contraction at the end of the hardening process, because it was contained in the middle of the tank.

Between day 5 and day 15, there was no recorded signal due to a connection failure. The interrogator was accidentally disconnected from the power source.

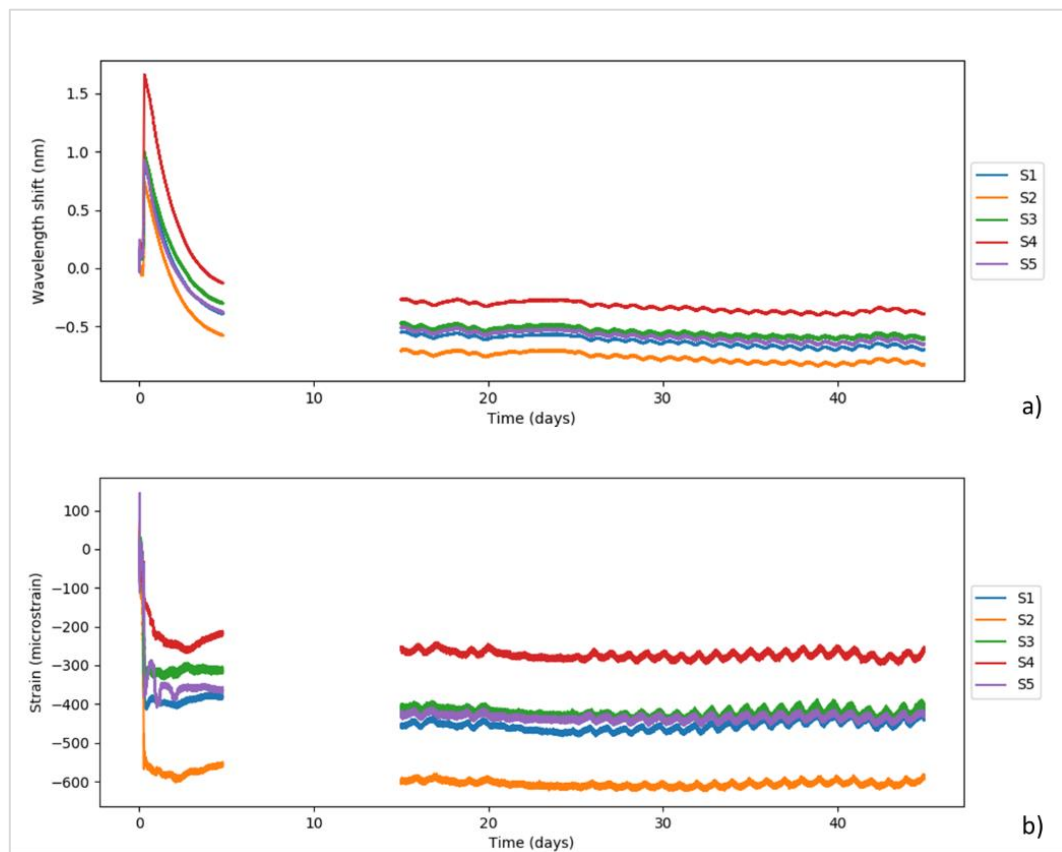


Figure 6.29: Strain FBG sensors response during the whole curing concrete process. a) Raw data in wavelength variation. d) response in strain values after temperature decoupling.

After a few months from the manufacturing of the mid-scale tank section, it was thermally tested. For this, two thermal blankets were located on the steel plate surface to heat it, simulating the heat of the molten salts. First, a heating cycle for dehydrating the concrete was carried out. The concrete tank section was heated through the thermal blankets, from room

temperature to 500°C, in four steps (120°C, 290°C, 350°C and 500°C) with a duration of 24h for each step. It was not possible to monitor the first heating cycle using the embedded FBGs because of a problem that occurred with the polymeric connectors of the sensors which were damaged outside the concrete piece. Subsequent, reconnection enabled reactivation of most of the temperature sensors, except array E and FBG F2. Strain sensors have also been affected by the connection failure, but S4, located at the centre of the tank specimen survived.

After the first heating to dehydrate the concrete, a thermal fatigue test was carried out. Figure 6.30.a shows a thermal cycle applied by turning on and off of thermal blankets to simulate the charge and discharge processes during the final thermocline tank prototype operation. Figure 6.30.b shows the thermal cycle applied to the mid-scale tank section, according with the simulation process. The temperature was maintained for 4 hours so as to achieve one daily cycle. The first heating up to the maximum temperature (500°C) was made in order to achieve 300°C in the air gap. After that, the cycles were programmed to occur between 200 to 500°C simulating the operating conditions of the tank. The availability of the workshop for doing the fatigue test was 5 days, so the number of repetitive cycles was limited to 3.

The steel plate and thermal blankets were located on the side of temperature arrays D and E.

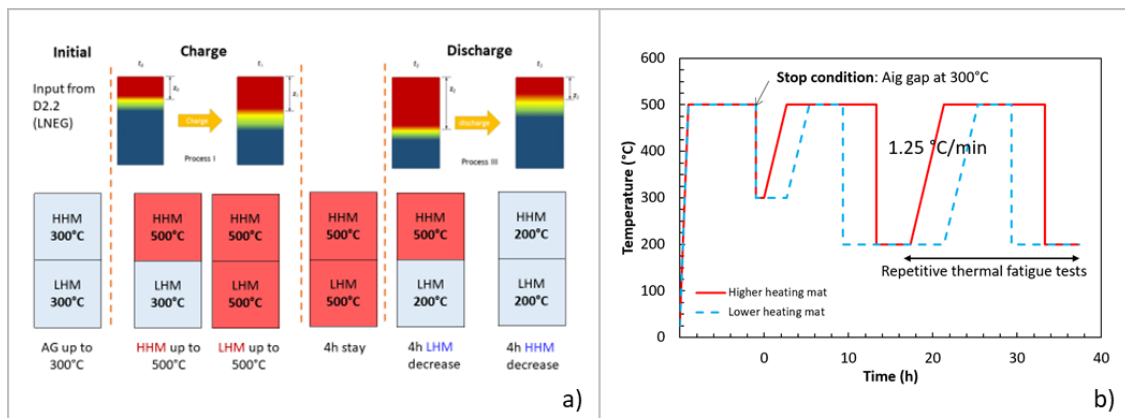


Figure 6.30: a) Charge and discharge processes and program of the heating source and b) thermal cycle applied.

The following figures represent a comparison for the temperature FBGs during the thermal tests. Figure 6.31 shows the comparison of the FBGs located at the same height and Figure 6.32 shows the comparison between the FBGs located at a similar location (X,Y) of the mid-scale tank.

Figure 6.31.a shows the temporal response of the temperature FBGs located at 750mm of height (close to the top of the tank), Figure 6.31.b shows the response of the temperature FBGs located at 500mm height from the bare and, Figure 6.31.c shows the response of the temperature FBGs located at 250mm of height (close to the bottom of the tank). Figure 6.31 clearly shows that the sensors at the higher position reach a higher temperature than the others, as expected, because of the thermal transfer. It is also because the thermal blanket located in the upper half of the mid-scale tank was heating continuously, while the one located in the lower half, was turned on and off to simulate the discharge and charge operation. The temperature gradient for the three FBGs of the same array was observed to be between 30-50°C, depending on the sensor location relative to the heat source.

In addition, it was also observed that despite the fact that 500°C was applied on the steel plate, due to the gap, a maximum of only 300°C was detected in the most proximal zone of the mid-scale tank.

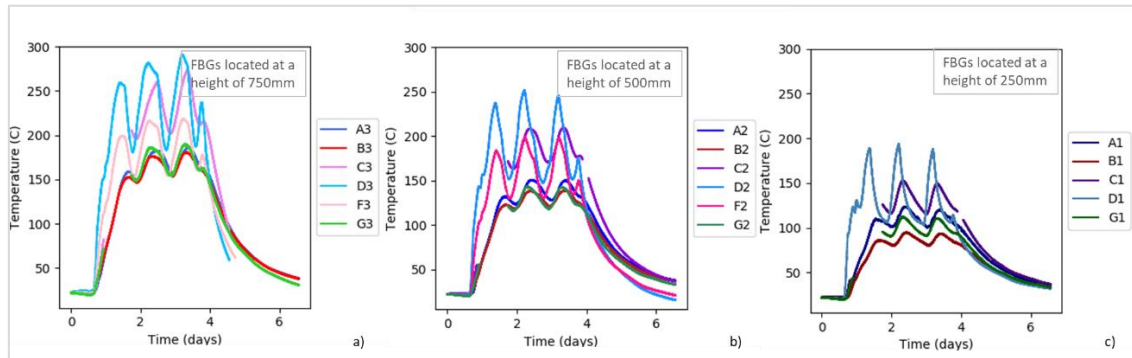


Figure 6.31: Detail of the temperature measured by the temperature FBGs at different heights: a) comparison for the FBGs located at 750mm of height; b) comparison for the FBGs located at 500mm of height; c) comparison for the FBGs located at 250mm of height.

Figure 6.32 represents another way to compare the temperature FBGs response. This method involves a study of the thermal gradients obtained along a section of the mid-scale tank. Figure 6.32.a shows a comparison for the FBGs B,D and G located in the left section of the mid-scale tank, Figure 6.32.b shows a comparison for the FBGs C located in the central part of the mid-scale tank, Figure 6.32.c shows a comparison for the FBGs A and F located in the right section of the mid-scale tank.

For the FBGs located in the right part of the concrete tank (seeing the tank from the cold side), it is noticeable that the F sensors reached higher temperatures, but also faster than the A ones due to their proximity to the heating source. The temperature reached has similar to that from arrays G and B located in the left part of the tank, although array D recorded a higher temperature because it was located closer to the heating source. The temperatures registered in the central part of the tank, by array C, are relative higher than those from left and right parts of the tank but at the same relative position. This means that the concrete concentrates the temperature in the central part.

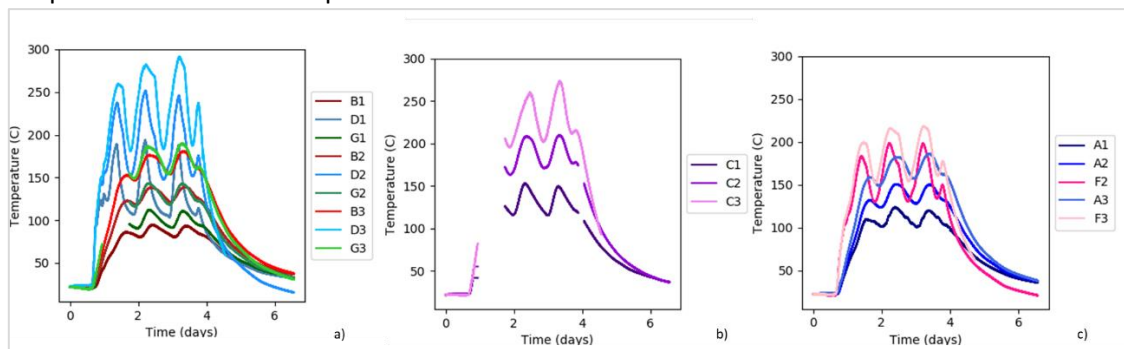


Figure 6.32: Detail of the temperature measured by the temperature FBGs at different locations: a) comparison for the FBGs located in the left section of the mid-scale tank, FBG sensors B,D and G; b) comparison for the FBGs located in the central part of the mid-scale tank, FBG sensors C; c) comparison for the FBGs located in the right section of the mid-scale tank, sensors A and F.

Using the temperature data recorded with the FBG sensors at different locations and heights of the mid-scale tank, some interpolations of the data were calculated, obtaining images of the temperature distribution in all the concrete specimen. Figure 6.33 represents the interpolated temperature in two different layers of the mini tank at a specific time of the thermal cycle. The black points of the images represent the location of the FBG sensors embedded into the mid-scale tank. Figure 6.33.a was obtained using the data of sensors in positions B, G, and D, meanwhile, Figure 6.33.b was generated with the temperature data from sensors G, C and F.

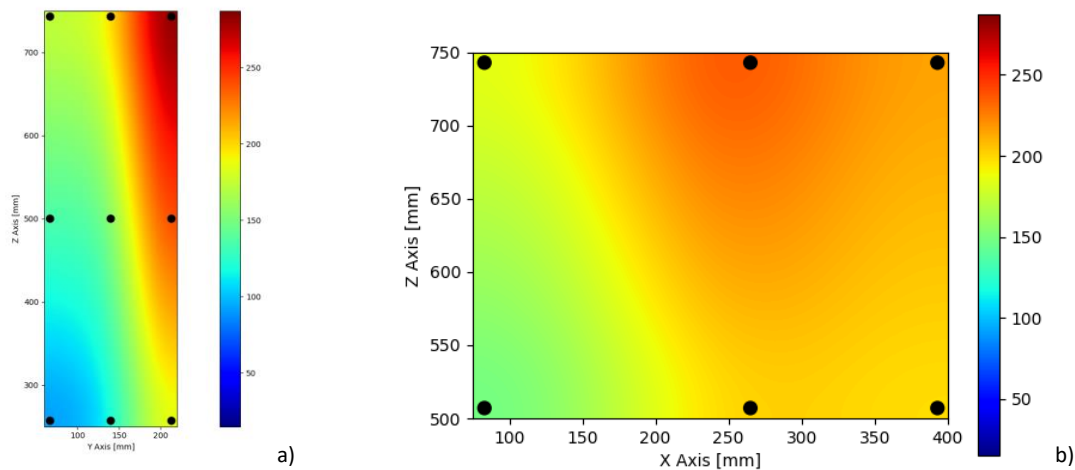


Figure 6.33: Representation of the temperature distribution in the concrete layers through the interpolation of the measured data. a) representation of the temperature gradient for the left side, sensors D, G and B. b) representation of the gradient temperature along the central part of the concrete, sensors G, C and F.

Finally, Figure 6.34 shows the comparison between the temperature FBGs C2, and the strain S4 FBG during the thermal test. S4 sensor shows a positive strain variation, which means that the FBG detected an expansion, due to the concrete dilatation. In this case the concrete expanded.

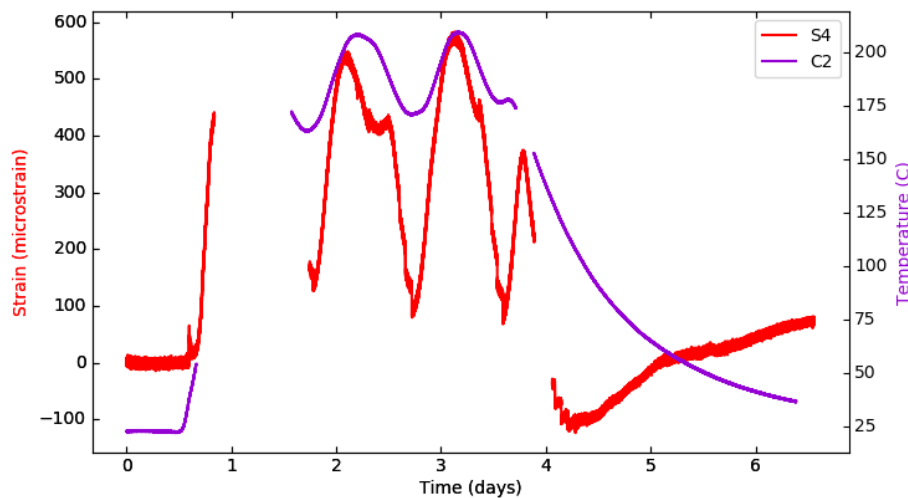


Figure 6.34: Comparison for the strain FBGs S4 and temperature C2 FBGs.

6.5 NEWSOL prototype design and integration

The study of medium-scale demonstrators has made it possible to design the manufacturing procedure for the final NEWSOL module and thermocline tank demonstrators. FOS integration is considered as an integral part of the manufacturing process to allow the critical points of the whole demonstrator being closely monitored.

To monitor the *Thermocline Tank* (TT) demo operation, a FOS network was designed, manufactured and integrated (by AIMEN) into different layers of the TT. This network was composed of FOSs (FBGs) and distributed FOS (Brillouin, BOTDR and BOTDA) to validate both technologies and compare them for selection to be integrated in the future installations of TT.

The FBGs network is composed of a total of 180 FBG sensors and, the distributed network is composed of 32 optical fibres. Table 6.1 shows the FOS distribution on the TT layers¹.

		TANK											
		Molten salts		Air GAP		CAC concrete		Rock wool		Structural concrete		Foundations	
		Fiber	Sensors	Fiber	Sensors	Fiber	Sensors	Fiber	Sensors	Fibre	Sensors	Fibre	Sensors
FBG sensors (punctual sensors)	Temperature	32	96	6	18	10	30	8	24	-	-	4	12
	Strain	-	-	-	-	10	30	-	-	-	-	-	-
Distributed sensors	Temp.	7	N/A	6	N/A	8	N/A	8	N/A	-	-	1	N/A
	Strain	-	-	-	-	8	N/A	-	-	-	-	-	-

Table 6.1: Distribution of FOS sensors in the TT.

For each layer of the TT a different FOS design was prepared, in response to the request from designers and operators partners. For example, for the CAC (Calcium Aluminate Cement) concrete layer, each optical fibre was inscribed with 3 FBGs, separated 50cm apart, and the total length of the fibre (array) was around 7m. Each distributed FOS designed to be installed in the CAC layer was around 15m.

The strain FOSs (FBG and distributed) were coated with Ni up to a total thickness of 550µm. The temperature sensors (FBGs coated with polyimide and distributed) were encapsulated in a 316L stainless steel capillary tube of 3.17mm external diameter.

Figure 6.35 shows the distribution of FOSs at different layers of the TT. Figure 6.35.a shows the FOS distribution to monitor the temperature of the molten salts (inside the tank), Figure 6.35.b shows the FOS distribution to monitor the temperature on the air gap, between the molten salts and the concrete, Figure 6.35.c shows the design of the FOS distribution to monitor temperature and strain in the high performance concrete (CAC concrete) layer, Figure 6.35.d shows the design of the FOS distribution to monitor the temperature on the rockwool layer and, Figure 6.35.e shows the design of the FOS distribution to monitor temperature on the foundations layer. The aim of the FOS monitoring system is to monitor the temperature and strain gradient of the TT demo during the construction and its validation, simulating the real operation of the tank.

¹ layers are refer to: layer 1 = high thermal performance concrete (CAC concrete), layer 2 = rock wool, layer 3 = structural concrete, layer 4 = foundations, layer 5 = molten salts and baskets.

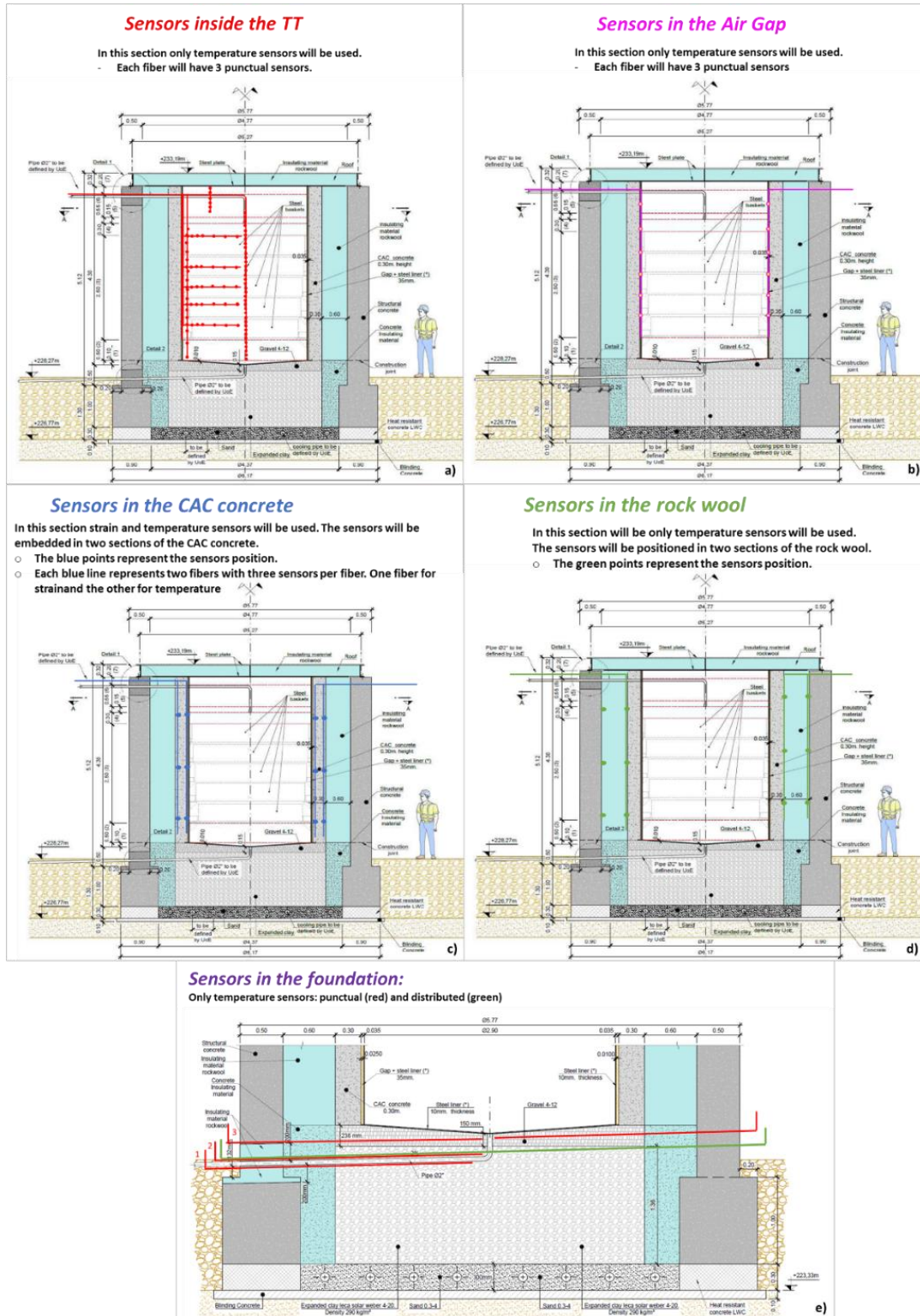


Figure 6.35: Design of the FOS distribution in the different layers of the TT tank. a) Design of the FOS distribution to monitor the temperature of the molten salts (inside the tank), b) design of the FOS distribution to monitor the temperature on the air gap, between the molten salts and the concrete, c) design of the FOS distribution to monitor the temperature and the strain in the high performance concrete, d) Design of the FOS distribution to monitor the temperature on the rockwool layer, e) Design of the FOS distribution to monitor the temperature on the foundations layer.

The manufacturing of the TT was undertaken in different steps and its construction took more than 1 year. The foundations layer was first manufactured, followed by the high thermal performance concrete layer (CAC) and the rockwool layer. After the completion of the structural concrete layer, all the components were placed inside the tank before placing the cover on the top of the tank.

At each layer, the required FOSs were integrated, before the concrete was poured or during the integration of rockwool and (inside) components. Each FOS integration took 2-3 days. Figure 6.36 shows the FOS installation in the CAC concrete layer. The FOS sensors were located in the walls of the formwork before pouring CAC.



Figure 6.36: TT demo CAC formwork and FOS integration before pouring the CAC.

The CAC concrete was poured in four times, originally three. Each time it was poured to reach around 1.5m, but the third pouring was of 1m and the whole process was completed following a 4th pour time. After the FOS integration, the FBG sensors were connected to the interrogator and the response of these sensors during the pouring, hardening and curing of the CAC was recorded. The FBG sensors were embedded on both sides of the CAC layer at a height of 0.75m, 1.25m, 1.75m, 2.25m, 2.75m and 3.32m as shown in Figure 6.37. The TT has a spherical geometry, in which four outlets were designed to take-out the connections of the FOS sensors, one for each tank *quarter*, equidistant from each other. For the FOS integrated in the CAC concrete layer, two opposite exits, S1 and S3, were used as depicted in Figure 6.37.

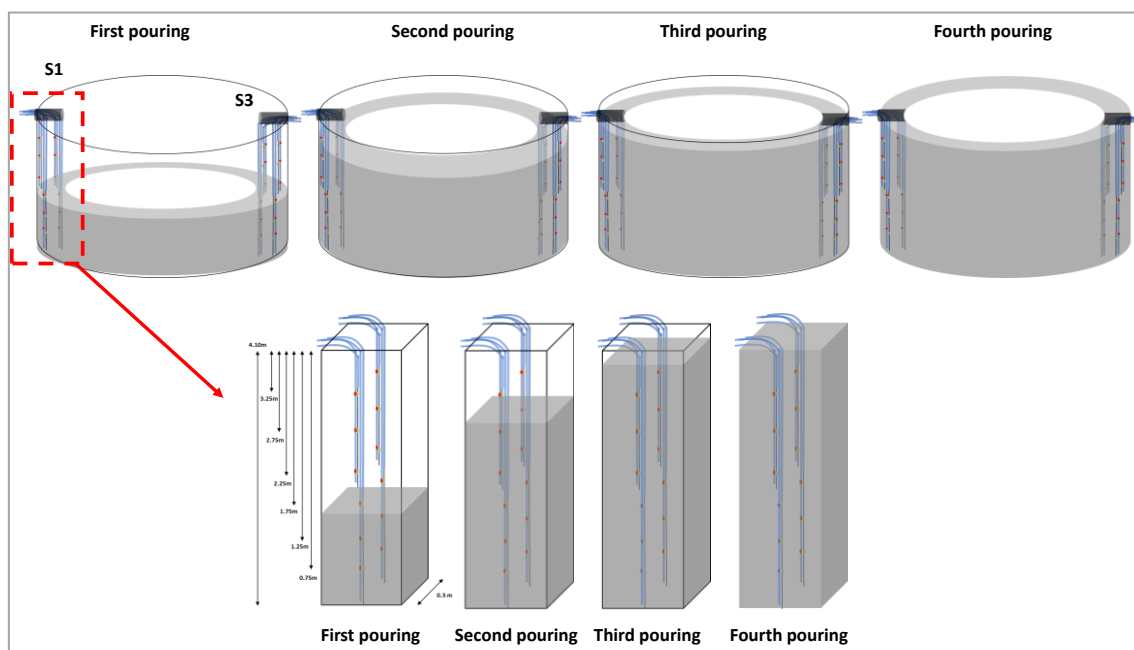


Figure 6.37: Representation of the CAC pouring and FBG sensors embedding.

Figure 6.38 shows the temperature recorded using the FBG sensors during the CAC pouring, hardening and curing². Figure 6.38.a shows the response of the temperature FBGs located on the internal side of the CAC close to exit S3 and the air gap. Figure 6.38.b shows the response of the temperature FBGs located on the other internal side close to exit S1 and the air gap. Figure 6.38.c shows the response of the FBGs located on the external side of CAC, close to exit S3, and the rockwool layer. Figure 6.38.d shows the response of the FBGs located on the external side of CAC, close to exit S1 and the rockwool layer.

It was not possible to monitor for some days including the second pouring, because there was a technical problem with the interrogator and the other construction works around the tank.

As illustrated in Figure 6.38, each pouring process induces a heat peak because of the exothermic reaction of the concrete during the hydration process. The temperature registered for each pouring was similar and the maximum temperature detected during the hardening of the CAC concrete was around 120°C. This temperature is similar to that reached in the mid-scale tank, although in this case it was slightly higher because of the hot weather and the larger CAC mass. The measured temperature is homogeneous through the whole CAC layer.

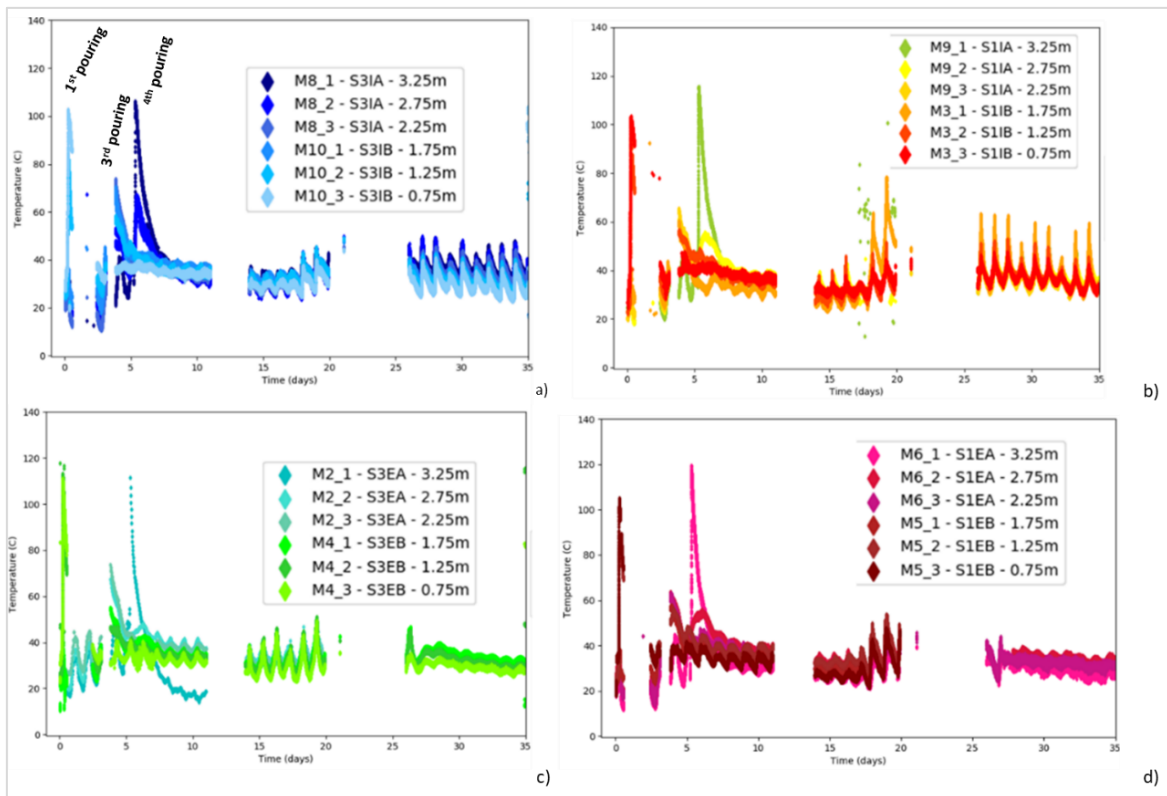


Figure 6.38: Response of the temperature FBG sensors embedded in the CAC layer, after the first CAC pouring. a) shows the response of the temperature FBGs placed in the side of the TT exit S3, at the internal side of the CAC, close to the air gap. b) shows the response of the temperature FBGs located in the side of the TT exit S1, at the internal side of the CAC, close to the air gap. c) shows the response of the FBGs located in the side of the TT exit S3, at the external side of the CAC, close to the rockwool layer. d) shows the response of the FBGs located in the side of the TT exit S1, at the external side of the CAC, close to the rockwool layer.

Figure 6.39 shows the time response of the strain FBG sensors embedded in the CAC concrete for the curing process. The strain recorded at the end of the curing process was seen to be similar

² The references of the sensors showed in the graphs means: MX = reference for the temperature FBG sensor. S1XX or S3XX means the side of the TT demo which the FOS were embedded. XX = IX ó EX, I means internal side of the CAC layer and E means external side of the CAC layer. XX = XA or XB, A means Above (sensors at 3.25m, 2.75m, 2.25m); B means Below (sensors located at 0.75m, 1.25m, 1.75m).

to that for the mid-scale tank tested in the previous section. There are some anomalies, such as a much larger strain obtained from the FBG sensor embedded at 0.75m height in the SIEB position. This could be caused by the poor quality in the sensor integration in the CAC. The strain FBG embedded at 1.75m S3IB shows a higher strain than the rest because it was embedded between two pouring stages and at this point the CAC shows some defects.

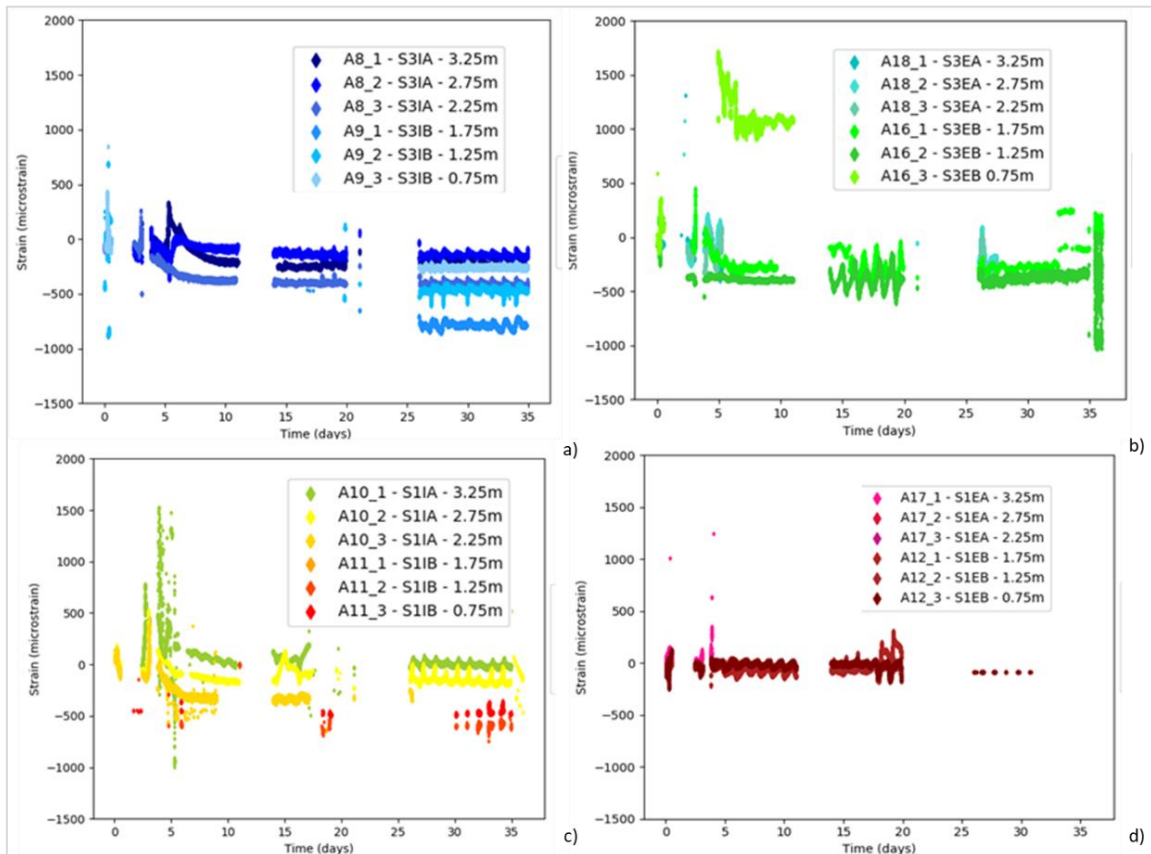


Figure 6.39: Response of the strain FBG sensors embedded in the CAC layer, after the first CAC pouring. a) shows the response of the strain FBGs placed in the side of the TT exit S3, at the internal side of the CAC, close to the air gap. b) shows the response of the strain FBGs located in the side of the TT exit S1, at the internal side of the CAC, close to the air gap. c) shows the response of the FBGs located in the side of the TT exit S3, at the external side of the CAC, close to the rockwool layer. d) shows the response of the FBGs located in the side of the TT exit S1, at the external side of the CAC, close to the rockwool layer.

6.6 Summary

In this chapter a new application for the Ni coated FOS was developed and validated. The Ni coated FOS were successfully embedded to monitor the thermal performance of novel high performance concretes, for Concentrated Solar Power plants. The FOS monitoring system was designed, developed and validated on different scales, from lab to real operation, with good and consistent results having been obtained.

On laboratory and middle scales the embedded FBGs were subjected to thermal tests up to more than 700°C, for which other sensors, including commercial FBGs, have not been able to withstand for a long test period. Finally, FBG and distributed FOSs were manufactured and integrated in the TT demo successfully, and the CAC pouring process was monitored. To have a complete knowledge about the technologies and the potential for this kind of industrial installations, a complete validation phase must be done to draw clear conclusions. So far FOS monitoring system has shown great potential for the condition monitoring of the Solar Power Plants components.

Chapter 7. Conclusions and future work

7.1 Conclusions of the work carried out

The extensive work carried out in this thesis opens up the real possibility of integrating optical fibre sensors into industrial applications subjected to harsh environments. Considering the specific requirements of each application, optical fibre sensors, including point technologies like FBGs and distributed technologies like Brillouin or Rayleigh, can be adapted.

This thesis addressed the development of a monitoring system based on optical fibre sensors for two entirely different use cases within the framework of the NEXT-BEARINGS and NEWSOL projects. A procedure was developed to coat optical fibre sensors, primarily FBGs but also distributed sensors, with metal. This procedure involved a combination of gold sputtering and electroplating deposition of Ni or Cu for FBG sensors, and only electroplating deposition for distributed sensors. It yielded a flexible and modular process that allows for uniform coating of meters (up to tens of meters) of optical fibre with layer thicknesses ranging from 20 μ m to 700 μ m (or even more).

The Ni coated sensors developed can withstand exposure to temperatures of up to 1000°C for short periods and resist temperatures between 700°C and 800°C for extended durations. These sensors can also monitor strain in environments up to 650°C, where they were tested for over 20 days.

Once coated with metal, these sensors were shown to withstand embedding processes using various techniques, including casting and TIG or laser cladding. Successful embedding was achieved in tin-based alloys and Ni-Cr (Inconel) alloys using these embedding techniques. The minimum thickness of metallic coating layer required to support embedding was around 140 μ m, depending on the embedding technique, strategy, and the material's melting point in which they were embedded.

To verify the research, the metallic coated and embedded FBGs were validated under operational conditions for each use-case.

In the case of the NEXT-BEARINGS project, Ni and Cu-coated FBGs were embedded in antifriction specimens using automatic TIG welding. These sensors were fatigue tested for over 5500 hours, with varying pressures (up to 74 bar), rotary friction speed (up to 667rpm), and temperatures (50-55°C), simulating accelerated degradation of the antifriction material. The embedded FBGs demonstrated a stable and sensible signal to variations in speed, temperature, and pressure. They also responded to defects introduced into the antifriction coating layer.

In a separate experiment, two different arrays of 3 Ni coated FBGs, were embedded in the top and the bottom of an antifriction bearing and tested under real operational conditions, including temperature (~50°C), pressure (up to 250bar), and rotational speed variations (up to 250rpm). All the embedded sensors were sensible to temperature and rotary speed variations, while the sensors at the bottom of the bearing could also monitor pressure changes.

In summary, for NEXT-BEARINGS use-case, the monitoring system based on embedded Ni coated FOS responded to all operational conditions and had the potential to detect damages or defects, facilitating preventive actions.

In the validation carried out under the NEWSOL project, second use-case, Ni-coated FBGs were designed, developed, and validated at the laboratory, mid-scale, and full-scale levels to monitor new concrete storage solutions for Concentrated Solar Power (CSP) plants. The Ni coated FBGs were directly embedded in the concrete structures during the concrete pouring, enabling not

Metal coating and embedding fibre optical sensors for industrial applications.

Chapter 7: Conclusions and future work.

only the monitoring of their subsequent operation but also the structure manufacturing process, as well as the concrete curing process. Across all three scale validations, the embedded FBGs were capable of tracking the applied thermal cycle (up to 500-700°C), monitoring strain and temperature, and even detecting some defects that emerged. This highlights the potential of the FOS monitoring system for the condition monitoring of solar power plant components.

7.2 Future work

The future work will be oriented in this direction:

- Complete the validation for the NEWSOL thermocline tank to know the FOS performance in real scale.
- Study the response and durability of different bi-metallic coating behaviour under high temperatures exposition.
- Study new coating techniques, for example plasma coating or thermal spray coating.
- Develop a comprehensive model to know the behaviour and relations between the metallic coated FOS when they are embedded.
- Embed metallic coated in metals with higher melting points by TIG and Laser procedures to introduce them in other applications for condition monitoring or process monitoring, such as monitoring metallurgical furnace components degradation or thermoconforming processes.
- Try to licence the knowhow or IP generated from research to FOS developers or potential users for wider industrial acceptance.
- Test the metallic coated FOS under harsher conditions to further explore their real potential.

7.3 References

- [1] Wartsilla, 'Wärtsilla NEXT-BEARINGS project'. [Online]. Available: <https://www.wartsila.com/esp/about/proyectos-cofinanciados/next-bearings>.
- [2] N. E. W. O. L. project, 'NEWSOL project'. [Online]. Available: <http://www.newsol.uevora.pt/>.
- [3] Wartsilla, 'Wärtsilla seals and bearings'. [Online]. Available: <https://www.wartsila.com/marine/build/seals-and-bearings/wartsila-intermediate-shaft-bearings>.
- [4] B. Aissa, E. I. Haddad, R. V. Kruzelecky, and W. R. Jamroz, *Fibre Bragg Gratings in Harsh and Space Environments*. London: Institution of Engineering and Technology, 2019.
- [5] M. M. Werneck, R. C. S. B. Allil, B. A. Ribeiro, and F. V. B. Nazaré, 'A Guide to Fiber Bragg Grating Sensors', in *Current Trends in Short- and Long-period Fiber Gratings*, IntechOpen, 2013.
- [6] D. C. J. K. O. Hill, Y. Fujii and B. S. Kawasaki, 'Photosensitivity in optical fiber waveguides: Application to reflection filter fabrication', *Applied Physics Letters*, vol. 32, pp. 647–649, 1978.
- [7] B. S. Kawasaki, K. O. Hill, D. C. Johnson, and Y. Fujii, 'Narrow-band Bragg reflectors in optical fibers', *Opt Lett*, vol. 3, pp. 66–68, 1978.
- [8] E. Hecht, *Optics*. Reading: Addison-Wesley, 2002.
- [9] Y. Tu, L. Ye, S.-P. Zhou, and S.-T. Tu, 'An Improved Metal-Packaged Strain Sensor Based on A Regenerated Fiber Bragg Grating in Hydrogen-Loaded Boron–Germanium Co-Doped Photosensitive Fiber for High-Temperature Applications', *Sensors*, vol. 17, no. 3, p. 431, 2017.
- [10] M. Cavillon *et al.*, 'Overview of high temperature fibre Bragg gratings and potential improvement using highly doped aluminosilicate glass optical fibres', *Journal of Physics: Photonics*, vol. 1, no. 4, 2019.
- [11] R. Sante, 'Fibre Optic Sensors for Structural Health Monitoring of Aircraft Composite Structures: Recent Advances and Applications', *Sensors*, vol. 15, no. 8, pp. 18666–18713, 2015.
- [12] A. Güemes, M. Frovel, A. Fernandez-López, J. M. Pintado, J. Garcia-Ramirez, and E. Reyes, 'Experimental validation of a fiber-optic based SHM system', in *7th Asia-Pacific Workshop on Structural Health Monitoring, Hong-Kong SAR*, 2018.
- [13] S. Semjonov, 'Hermetically coated specialty optical fibers', in *Proceedings of SPIE - The International Society for Optical Engineering*, 2010.
- [14] A. Mendez and T. F. Morse, *Specialty optical fibers handbook*, Elsevier. 2011.
- [15] X. C. Li, F. Prinz, and J. Seim, 'Thermal behavior of a metal embedded fiber Bragg grating sensor', *Smart Mater Struct*, vol. 10, no. 4, pp. 575–579, 2001.

- [16] X. Li and F. Prinz, 'Embedding of Fiber Optic Sensors in Layered Manufacturing', in *International Solid Freeform Fabrication Symposium*, 2000.
- [17] X. Ke and W. Xu, 'Continuous fabrication of metal-coated optical fiber for distributed sensing', in *IEEE Photonics Conference (IPC)*, 2017.
- [18] E. Miliutina *et al.*, 'Fast and All-Optical Hydrogen Sensor Based on Gold-Coated Optical Fiber Functionalized with Metal-Organic Framework Layer', *ACS Sens*, vol. 4, no. 12, pp. 3133–3140, 2019.
- [19] H. Alemohammad, E. Toyserkani, and C. P. Paul, 'Fabrication of smart cutting tools with embedded optical fiber sensors using combined laser solid freeform fabrication and moulding techniques', *Opt Lasers Eng*, vol. 45, no. 10, pp. 1010–1017, 2007.
- [20] X. Zhang, H. Alemohammad, and E. Toyser, 'Sensitivity alteration of fiber Bragg grating sensors with additive micro-scale bi-material coatings', *Meas Sci Technol*, vol. 24, no. 2, 2013.
- [21] S.-T. Shiue, C.-H. Yang, R.-S. Chu, and T.-J. Yang, 'Effect of the coating thickness and roughness on the mechanical strength and thermally induced stress voids in nickel-coated optical fibers prepared by electroless plating method', *Thin Solid Films*, vol. 485, no. 1–2, pp. 169–175, 2005.
- [22] R. F. Wright, J. Egbu, P. Lu, Buric Michael, M. Ziomek-Moroz, and P. R. Ohodnicki Jr, 'Electrolessly Coated Optical Fibers for Distributed Corrosion Monitoring', in *Corrosion*, Nashville, TN, Mar. 2019.
- [23] Z. J. Setmire, J. J. Zayhowski, and J. Wilson, 'Metalized double-clad optical fiber', US 10073218B2, 2016
- [24] R. R. Jakka, 'Advanced process to embed optical fiber sensors into casting', MISSOURI UNIVERSITY OF SCIENCE AND TECHNOLOGY, 2018.
- [25] S. Sandlin, T. Kinnunen, J. Rämö, and M. Sillanpää, 'A simple method for metal re-coating of optical fibre Bragg gratings', *Surf Coat Technol*, vol. 201, no. 6, pp. 3061–3065, 2006.
- [26] X. Zheng, W. Hu, N. Zhang, and M. Gao, 'Optical corrosion sensor based on fiber Bragg grating electroplated with Fe-C film', *Optical engineering*, vol. 53, no. 7, 2014.
- [27] R. -s Shen *et al.*, 'Electroless Nickel Plating and Electroplating on FBG Temperature Sensor', *Chem Res Chin Univ*, vol. 24, no. 5, pp. 635–639, 2008.
- [28] X. M. Li, W. Chen, Z. Q. Huang, S. Huang, and K. D. Bennett, 'Fiber optic corrosion sensor fabricated by electrochemical method', in *5th Annual International Symposium on Smart Structures and Materials*, San Diego, 1998.
- [29] W. Hu, H. Cai, M. Yang, X. Tong, C. Zhou, and W. Chen, 'Fe–C-coated fibre Bragg grating sensor for steel corrosion monitoring', *Corros Sci*, vol. 53, no. 5, pp. 1933–1938, 2011.
- [30] Y. Li, Y. Feng, X. Peng, and H. Zhang, 'Simultaneous measurement of the temperature and force using a steel cantilever soldered with a partially nickel coated in-fibre Bragg grating', *Opt Commun*, vol. 285, no. 21–22, pp. 4275–4279, 2012.

- [31] Y.-L. Chou, C.-W. Wu, R.-T. Jhang, and C.-C. Chiang, 'A novel optical fiber temperature sensor with polymer-metal alternating structure', *Opt Laser Technol*, vol. 115, pp. 186–192, 2019.
- [32] Y. Tu, Y.-H. Qi, and S.-T. Tu, 'Fabrication and thermal characteristics of multilayer metal-coated regenerated grating sensors for high-temperature sensing', *Smart Mater Struct*, vol. 22, no. 7, 2013.
- [33] Y. Li, H. Zhang, Y. Feng, and G. Peng, 'A plating method for metal coating of fiber Bragg grating', *Chinese Optics Letters*, vol. 7, no. 2, pp. 115–117, 2019.
- [34] J.-F. Xie, H. Zhang, Z. Zhu, J.-N. Xu, R.-H. Hu, and L.-F. Song, 'A study of the temperature sensitivity of fiber Bragg gratings after metallization', *Smart Mater Struct*, vol. 16, no. 5, p. 1837, 2007.
- [35] J. He, L. Ding, J. Cai, W. Zhu, and J. Dai, 'A novel high temperature resistant Mo-Cu functional gradient coating for optic fiber Bragg grating', *Results Phys*, vol. 14, 2019.
- [36] Y.-L. Wang, Y. Tu, and S.-T. Tu, 'Development of Highly-Sensitive and Reliable Fiber Bragg Grating Temperature Sensors With Gradient Metallic Coatings for Cryogenic Temperature Applications', *IEEE Sens J*, vol. 21, no. 4, pp. 4652–4663, 2021.
- [37] H. CABLE, 'Metal-coated optical fiber and its manufacture', JPH10300997A, 1998
- [38] M. MIYAMOTO, 'Method and apparatus for fabrication of metal-coated optical fiber', EP2969255B1, 2019
- [39] M. MIYAMOTO and C. Sakura-shi, 'Method for fabrication of metal-coated optical fiber', EP3194346B1, 2016
- [40] M. S. Chen, 'Metalization of non-hermetic optical fibers', US 6251252 E1, 2001
- [41] M. J. Lives and T. W. L'angel, 'Method of metallization of an optical waveguide', US6753034B2, 2004
- [42] J. Grunwald, 'Metallization of optical fibers', US 2003/0173226 A1, 2003
- [43] V. Ramadas, M. F. Azman, and S. A. Ibrahim, 'Numerical analysis of metal-layer in optical fiber clad', in *AIP Conference Proceedings*, 2020.
- [44] P. Cherpak, R. Shaidullin, and O. Ryabushkin, 'Dependence of optical attenuation on radiation wavelength and waveguide geometry in copper-coated optical fibers', in *The European Physical Journal Conferences*, 2020.
- [45] V. V Voloshin *et al.*, 'Effect of metal coating on the optical losses in heated optical fibers', *Technical Physics Letters*, vol. 35, no. 4, pp. 365–367, 2016.
- [46] I. Laarossi, M. Á. Quintela-Incera, and J. M. López-Higuera, 'Comparative Experimental Study of a High-Temperature Raman-Based Distributed Optical Fiber Sensor with Different Special Fibers', *Sensors*, vol. 19, no. 3, p. 574, 2019.
- [47] C. Lupi *et al.*, 'Critical Issues of Double-Metal Layer Coating on FBG for Applications at High Temperatures', *Sensors*, vol. 19, no. 18, p. 3824, 2019.

- [48] N. Saheb and S. Mekid, 'Fiber-Embedded Metallic Materials: From Sensing towards Nervous Behavior', *Materials*, vol. 8, no. 11, pp. 7938–7961, 2015.
- [49] C. Lee, H. F. Taylor, A. M. Markus, and E. Udd, 'Optical-fiber Fabry–Perot embedded sensor', *Opt Lett*, vol. 14, no. 21, pp. 1225–1227, 1989.
- [50] C. E. Lee, W. N. Gibler, R. A. Atkins, J. J. Alcoz, and H. F. Taylor, 'Metal-embedded fiber-optic Fabry–Perot sensors', *Opt Lett*, vol. 16, no. 24, pp. 1990–1992, 1991.
- [51] C. E. Lee, J. J. Alcoz, W. N. Gibler, R. A. Attins, and H. F. Taylor, 'Method for embedding optical fibers and optical fiber sensors in metal parts and structures', *Fiber Optic Smart Structures and Skins*, vol. IV, 1588, pp. 110–116, 1991.
- [52] K. Weraneck *et al.*, 'Strain Measurement in Aluminium Alloy during the Solidification Process Using Embedded Fibre Bragg Gratings', *Sensors*, vol. 16, no. 11, p. 1853, 2016.
- [53] M. Lindner *et al.*, 'Fiber Bragg Sensors Embedded in Cast Aluminum Parts: Axial Strain and Temperature Response', *Sensors*, vol. 21, no. 5, p. 1680, 2021.
- [54] Y. Zhuang, 'Embedded fiber optic sensors for temperature monitoring of continuous casting mold', MISSOURI UNIVERSITY OF SCIENCE AND TECHNOLOGY, MISSOURI, 2018.
- [55] Y. Zhang, L. Zhu, F. Luo, M. Dong, X. Ding, and W. He, 'Fabrication and characterization of metal-packaged fiber Bragg grating sensor by one-step ultrasonic welding', *Optical Engineering*, vol. 55, no. 067103, 2016.
- [56] Y.-L. Wang, Y. Tu, and S.-T. Tu, 'A Study of Tensile and Fatigue Loading Effects on the Performance of Metal-Packaged FBG Strain Sensor Developed for Cryogenic Applications', *IEEE Sens J*, vol. 22, no. 12, pp. 11763–11774, 2022.
- [57] S. E. Baldini, D. J. Tubbs, and W. A. Stange, 'Embedding fiber optic sensors in titanium matrix composites', in *SPIE Microelectronic Interconnect and Integrated Processing Symposium*, San José, United States, 1990.
- [58] D. Yi, S. Costil, P. Pfeiffer, and B. Serio, 'Optical fiber embedding in thermal spray coating promises new smart materials design able to operate under harsh environment', in *Proceedings of SPIE - The International Society for Optical Engineering*, 2014.
- [59] Y. Huang, X. Liang, S. A. Galedar, and F. Azarmi, 'Integrated Fiber Optic Sensing System for Pipeline Corrosion Monitoring', in *Pipelines 2015*, Baltimore Maryland, United States, 2015, pp. 1667–1676.
- [60] X. Liang, 'IN-LINE FIBER OPTIC SENSING SYSTEM FOR PIPELINE CORROSION DETECTION', University North Dakota, Fargo, 2015.
- [61] F. Deng, Y. Huang, F. Azarmi, and Y. Wang, 'Pitted Corrosion Detection of Thermal Sprayed Metallic Coatings Using Fiber Bragg Grating Sensors', *Coatings*, vol. 7, no. 3, p. 35, 2017.
- [62] F. Deng, Y. Huang, and F. Azarmi, 'Corrosion Behavior Evaluation of Coated Steel Using Fiber Bragg Grating Sensors', *Coatings*, vol. 9, no. 1, p. 55, 2019.
- [63] S. Sandlin, A. Hokkanen, and T. Varis, 'Coating integrated optical fibres for monitoring of boiler heat transfer surfaces', *Energy Maaterials*, vol. 2, no. 2, pp. 122–128, 2007.

- [64] X. Lu, P. J. Thomas, Y. Zhang, H. Liao, S. Gomes, and J. O. Hellevang, 'Characterization of Optical Fibers Directly Embedded on Metal Using a Particle Spray-Based Method', *IEEE Sensors*, vol. 20, no. 12, pp. 6414–6421, 2020.
- [65] S. Sandlin and A. Hokkanen, 'Embedding optical fibers in metal alloys', *IEEE Instrum Meas Mag*, vol. 6, no. 2, pp. 31–36, 2003.
- [66] T.W.I., 'TWI Global'. [Online]. Available: <https://www.twi-global.com/media-and-events/insights/vacuum-furnace-brazing>.
- [67] J. Mathew *et al.*, 'Integrating Fiber Fabry-Perot Cavity Sensor Into 3-D Printed Metal Components for Extreme High-Temperature Monitoring Applications', *IEEE Sens J*, vol. 17, no. 13, pp. 4107–4114, 2017.
- [68] S. Sandlin, T. Kosonen, A. Hokkanen, and L. Heikinheimo, 'Use of brazing technique for manufacturing of high temperature fibre optical temperature and displacement transducer', *Materials Science and Technology*, vol. 23, no. 10, pp. 1249–1255, 2007.
- [69]. Y Chen Z. Zhu and Y. Zhang, 'The temperature sensitivity of fiber bragg gratings embedded in an Al 6061 matrix by ultrasonic welding', *J Intell Mater Syst Struct*, vol. 28, no. 11, pp. 2173–2179, 2011.
- [70] Y. Li, W. Liu, Y. Feng, and H. Zhang, 'Ultrasonic embedding of nickel-coated fiber Bragg grating in aluminum and associated sensing characteristics', *Optical Fiber Technology*, vol. 18, no. 1, pp. 7–13, 2012.
- [71] S. K. Chilelli, J. J. Schomer, and M. J. Dapino, 'Detection of Crack Initiation and Growth Using Fiber Bragg Grating Sensors Embedded into Metal Structures through Ultrasonic Additive Manufacturing', *Sensors*, vol. 19, no. 22, p. 4917, 2019.
- [72] A. Hehr *et al.*, 'Integrating Fiber Optic Strain Sensors into Metal Using Ultrasonic Additive Manufacturing', *The Journal of The Minerals, Metals & Materials Society (TMS) - JOM*, vol. 70, pp. 315–320, 2018.
- [73] A. Hehr, M. Norfolk, D. Kominsky, A. Boulanger, M. Davis, and P. Boulware, 'Smart Build-Plate for Metal Additive Manufacturing Processes', *Sensors*, vol. 20, no. 2, p. 360, 2020.
- [74] C. M. Petrie, N. Sridharan, M. Subramanian, A. Hehr, M. Norfolk, and J. Sheridan, 'Embedded metallized optical fibers for high temperature applications', *Smart Mater Struct*, vol. 28, no. 5, 2019.
- [75] A. Hehr, M. Norfolk, J. Sheridan, and M. Davis, 'Spatial Strain Sensing Using Embedded Fiber Optics', *The Journal of The Minerals, Metals & Materials Society (TMS) - JOM*, vol. 71, pp. 1528–1534, 2019.
- [76]. Y Liu D. C. Sweeney A. M. Schrell and C. M. Petrie, 'Metal-embedded fiber optic sensor packaging and signal demodulation scheme towards high-frequency dynamic measurements in harsh environments', *Sens Actuators A Phys*, vol. 132, no. 112075, 2020.
- [77] H. C. Hyer, D. C. Sweeney, and C. M. Petrie, 'Functional fiber-optic sensors embedded in stainless steel components using ultrasonic additive manufacturing for distributed temperature and strain measurements', *Addit Manuf*, vol. 52, p. 102681, 2022.

- [78] C. Y. Kong and R. Soar, 'Method for embedding optical fibers in an aluminum matrix by ultrasonic consolidation', *Appl Opt*, vol. 44, no. 30, pp. 6325–6333, 2005.
- [79] Fabrisonic, 'Fabrisonic'. [Online]. Available: <https://fabrisonic.com/>.
- [80] M. NORFOLK, D. BARTHOLOMEW, and C. SIDLOSKY, 'WELD ASSEMBLY FOR ULTRASONIC ADDITIVE MANUFACTURING APPLICATIONS', US9446475B2, 2016
- [81] X. Li, J. Johnson, J. Groza, and F. Prinz, 'Processing and microstructures of fiber Bragg grating sensors embedded in stainless steel', *Metallurgical and Materials Transactions A*, vol. 33, no. 9, pp. 3019–3024, 2002.
- [82] X. Li, W. Tang, and A. Golnas, 'Embedding and characterization of fiber-optic and thin-film sensors in metallic structures', *Sensor Review*, vol. 24, no. 4, pp. 370–377, 2004.
- [83] A. S. Hamidreza, 'Development of Optical Fiber-Based Sensing Devices Using Laser Microfabrication Methods', University of Waterloo, 2010.
- [84] H. Alemohammad and E. Toyserkani, 'Metal Embedded Optical Fiber Sensors: Laser-Based Layered Manufacturing Procedures', *J Manuf Sci Eng*, vol. 133, no. 3, p. 31015, 2011.
- [85] R. R. J. Maier *et al.*, 'Optical fibre sensing in metals by embedment in 3D printed metallic structures', in *23rd International Conference on Optical Fibre Sensors*, Santander, Spain, 2014.
- [86] O. project, 'Cordis Europe'. [Online]. Available: <https://cordis.europa.eu/project/id/310279>.
- [87] D. Havermann, 'Study on fibre optic sensors embedded into metallic structures by selective laser melting', Heriot-Watt University, Edimburg, 2015.
- [88] D. Havermann, J. Mathew, W. N. Macpherson, and D. P. Hand, 'Measuring residual stresses in metallic components manufactured with fibre Bragg gratings embedded by selective laser melting', in *24th International Conference on Optical Fibre Sensors*, Curitiba, Brasil, 2015.
- [89] D. Havermann, J. Mathew, W. N. MacPherson, R. R. J. Maier, and D. P. Hand, 'Temperature and Strain Measurements With Fiber Bragg Gratings Embedded in Stainless Steel 316', *Journal of Lightwave Technology*, vol. 33, no. 12, pp. 2474–2479, 2014.
- [90] P. Stoll, J. Mathew, A. Spierings, T. Bauer, R. Maier, and K. Wegener, 'Embedding fibre optical sensors into SLM parts', in *27th Solid Freeform Fabrication Symposium*, Austin, TX, USA, 2016.
- [91] J. Mathew, W. N. Macpherson, D. P. Hand, and R. R. J. Maier, 'Stainless steel component with compressed fiber Bragg grating for high temperature sensing applications', in *Sixth European Workshop on Optical Fibre Sensors (EWOFs'2016)*, Limerick, Ireland, 2016.
- [92] R. Zou *et al.*, 'A Digital Twin Approach to Study Additive Manufacturing Processing Using Embedded Optical Fiber Sensors and Numerical Modeling', *Journal of Lightwave Technology*, vol. 38, no. 22, pp. 6402–6411, 2020.

- [93] E. Seo *et al.*, 'Laser powder bed fusion for AI assisted digital metal components', *Virtual Phys Prototyp*, vol. 17, no. 4, pp. 156–169, 2022.
- [94] M.-F. project, 'Multi-Fun'. [Online]. Available: <https://www.multi-fun.eu/>.
- [95] Pipe Bernstein, 'Evaluación de revestimientos metálicos y no metálicos resistentes a la corrosión en aguas del lago de Maracaibo', Maracaibo, Venezuela, 2013.
- [96] N. Pinto, P. Carrión, and J. Quiñones, 'Electroless deposition of nickel on electrospun fibers of 2-acrylamido-2-methyl-1-propanesulfonic acid doped polyaniline', *Materials Science and Engineering: A*, vol. 366, no. 1, pp. 1–5, 2004.
- [97] T. Grandal, E. Piñeiro, and F. Rodriguez, 'Metallic coating techniques for fiber Bragg grating sensors', in *8th Iberoamerican Optics Meeting and 11th Latin American Meeting on Optics, Lasers, and Applications*, O Porto, 2013.
- [98] I.N.P.H.O.T.E.C.H., 'Inphotech'. [Online]. Available: <https://inphotech.com/>.
- [99] E.N.G.I.O.N.I.C., 'ENGIONIC'. [Online]. Available: <https://engionic.de/en/home>.
- [100] M. M. Waite, S. I. Shah, and D. A. Glocker, 'Society of vacuum coaters'. [Online]. Available: https://www.svc.org/DigitalLibrary/documents/2010_Spring_MMWaite_SIS Shah_DAGlocker_p42-50.pdf.
- [101] A. I. Científica, 'Aname Instrumentación Científica'. [Online]. Available: <https://microscopiaelectronica.com/index.php/equipos-microscopia-electronica/recubridores/recubridorsputteringbajocoste>.
- [102] I. Fiber, 'IVG Fiber'. [Online]. Available: http://www.ivgfiber.com/metallized_fiber.htm.
- [103] H.B.M.-Fibersensing, 'HBM-Fibersensing'. [Online]. Available: https://www.hbm.com/en/4604/fs22-industrial-braggmeter-optical-interrogator/?product_type_no=Optical%20Interrogator%20FS22:%20Static%20and%20Dynamic%20Measurement.
- [104] M. Optics, 'Micron Optics'. [Online]. Available: http://www.micronoptics.ru/sensing_instruments.html.
- [105]. N J Alberto de Oliveira . I. Abe and H. J. Kalinowski, 'Fibre Bragg Gratings, towards a Better Thermal Stability at High Temperatures', *Phys Procedia*, vol. 62, 2015.
- [106] A. ROSE, R. J. ESPEJO, and R. M. CRAIG, 'Annealed fiber: properties and applications', in *Conference Proceedings. LEOS'98. 11th Annual Meeting. IEEE Lasers and Electro-Optics Society 1998 Annual Meeting*, 1998.
- [107] Y. Li, M. Yang, D. N. Wang, J. Lu, T. Sun, and K. T. V Grattan, 'Fiber Bragg gratings with enhanced thermal stability by residual stress relaxation', *Opt. Express*, vol. 17, no. 22, pp. 19785–19790, 2009.
- [108] A. Luiz Octavio Amaral, 'Chapter 12 - Antifriction Bearings', in *Machinery Failure Analysis Handbook*, Gulf Publishing Company, 2006, pp. 143–172.

- [109] S.K.F., 'SKF - Bearing damage and failure analysis'. [Online]. Available: https://www.skf.com/binaries/pub12/Images/0901d1968064c148-Bearing-failures—14219_2-EN_tcm_12-297619.pdf.
- [110] M. S.- Motorservice, 'MS-Motorservice - Daños en cojinetes de fricción'. [Online]. Available: https://cdn2.ms-motorservice.com/fileadmin/media/MAM/PDF_Assets/Da%C3%B1os-en-cojinetes-de-fricci%C3%B3n_870264.pdf.
- [111] S. Zeashan, S. Ali, and P. P. M, 'Antifriction Bearing Diagnostics in a Manufacturing Industry – A Case Study', *Journal of Mechanical Engineering and Automation*, vol. 6, pp. 58 – 62, 2016.
- [112] M. Mieloszyk, K. Majewska, G. Zywica, and T. Z. Kaczmarczyk, 'Fibre Bragg grating sensors as a measurement tool for an organic Rankine cycle micro-turbogenerator', *Measurement*, vol. 157, no. 107666, 2020.
- [113] S. Konforty, M. Khmelnsky, I. Kressel, R. Klein, M. Tur, and J. Bortman, 'BEARING HEALTH MONITORING USING OPTICAL FIBER SENSORS', in *PHM Society European Conference*, Bilbao, 2016.
- [114] E. V GENUCHTEN and J. M. Á. L. V. A. R. E. Z. S. VAN EESBEEK, 'Multi-parameter Fibre Optic Sensing System for Remote Condition and Operation Monitoring of Gearbox Bearings in Rack and Pinion Jacking Systems', in *Structural health monitoring 2017*, 2017.
- [115] S. Group, 'youtube - Load sensing by light – SKF Fiber Optic Sensing'. [Online]. Available: https://www.youtube.com/watch?v=E-pSvTZr6Nk&ab_channel=SKFGroup.
- [116] B. Torres Górriz, 'Definición de las pautas y condiciones de monitorización, encapsulado y fijación de sensores de fibra óptica para la medida de deformación y temperatura en estructuras', Universitat Politècnica de València, Valencia, 2012.
- [117] R. Measures, 'Structural Monitoring with Fiber Optic Technology', in *eBook ISBN: 9780080518046*, 2002.

List of Publications

Journal Papers:

1. T. Grandal, A. Zornoza, S. Fraga, G. Castro, T. Sun and K. T. V. Grattan, "Laser Cladding-Based Metallic Embedding Technique for Fiber Optic Sensors," in *Journal of Lightwave Technology*, vol. 36, no. 4, pp. 1018-1025, 15 Feb.15, 2018, doi: 10.1109/JLT.2017.2748962.
2. T. Grandal, A. Zornoza, A. López, S. Fraga, T. Sun and K. T. V. Grattan, "Analysis of Fiber Optic Sensor Embedded in Metals by Automatic and Manual TIG Welding," in *IEEE Sensors Journal*, vol. 19, no. 17, pp. 7425-7433, 1 Sept.1, 2019, doi: 10.1109/JSEN.2019.2916639.

Conference Papers:

1. Tania Grandal and Sergio Fraga and Jose A. Vazquez and Ander Zornoza, "Technique for embedding fiber optics in metallic structures for smart material applications", 8th European Workshop On Structural Health Monitoring (EWSHM 2016), [Online]. Available <http://www.ndt.net/events/EWSHM2016>
2. T. Grandal, S. Fraga, and A. Zornoza, "Solar molten salt temperature monitoring with fiber optic sensors," in *Advanced Photonics 2016 (IPR, NOMA, Sensors, Networks, SPPCom, SOF)*, OSA Technical Digest (online) (Optica Publishing Group, 2016), paper SeM4D.5.
3. Tania Grandal, Sergio Fraga, Gemma Castro, Esteban Vazquez, Ander Zornoza, "Laser Brazing metallic embedding technique for fiber optic sensors," *Proc. SPIE 10323*, 25th International Conference on Optical Fiber Sensors, 103236S (23 April 2017); <https://doi.org/10.1117/12.2263974>
4. Tania GRANDAL, Sergio FRAGA, Gemma CASTRO, Esteban VAZQUEZ and Ander ZORNOZA, "Embebido de sensores de fibra óptica en metales mediante laser Brazing, Fiber optic sensor embedding on metals by laser Brazing", *OPTOEL 2017 – X Reunión Española de Optoelectrónica*, July 2017, Santiago de Compostela, Spain.
5. T. Grandal and A. Zornoza, "Smart metallic part manufacturing by laser-cladding based embedding of optical fiber sensors," in *Imaging and Applied Optics 2018 (3D, AO, AIO, COSI, DH, IS, LACSEA, LS&C, MATH, pcAOP)*, OSA Technical Digest (Optica Publishing Group, 2018), paper ATu3A.2. DOI: 10.1364/aio.2018.atu3a.2.
6. Tania Grandal, Sergio Fraga, Gemma Castro, Esteban Vazquez and Ander Zornoza, "Fibre Optic Sensor Embedded into Metals Using Low Cost TIG Welding and High Precision Laser Brazing", *STO-MP-AVT-305 – NATO Conference*, 2018-12. [Online] Available: <https://www.sto.nato.int/publications/STO%20Meeting%20Proceedings/STO-MP-AVT-305/MP-AVT-305-06.pdf>

